

Experimental and Theoretical Study of Particle Transport in the TCV Tokamak

THÈSE N° 4334 (2009)

PRÉSENTÉE LE 12 JUIN 2009
À LA FACULTÉ SCIENCES DE BASE
CRPP ASSOCIATION EURATOM
PROGRAMME DOCTORAL EN PHYSIQUE

ÉCOLE POLYTECHNIQUE FÉDÉRALE DE LAUSANNE

POUR L'OBTENTION DU GRADE DE DOCTEUR ÈS SCIENCES

PAR

Emiliano FABLE

acceptée sur proposition du jury:

Prof. O. Schneider, président du jury
Dr O. Sauter, directeur de thèse
Dr C. Angioni, rapporteur
Dr T. Hoang, rapporteur
Dr H. Weisen, rapporteur



ÉCOLE POLYTECHNIQUE
FÉDÉRALE DE LAUSANNE

Suisse
2009

Do we want to die here, like morons, on the back of a small shop?

Fight Club

No results... no results...

Max Cohen, π

Abstract (english)

The main scope of this thesis work is to compare theoretical models with experimental observations on particle transport in particular regimes of plasma operation from the **Tokamak à Configuration Variable** (TCV) located at CRPP–EPFL in Lausanne.

We introduce the main topics in Tokamak fusion research and the challenging problems in the **first Chapter**. A particular attention is devoted to the modelling of heat and particle transport.

In the **second Chapter** the experimental part is presented, including an overview of TCV capabilities, a brief review of the relevant diagnostic systems, and a discussion of the numerical tools used to analyze the experimental data. In addition, the numerical codes that are used to interpret the experimental data and to compare them with theoretical predictions are introduced.

The **third Chapter** deals with the problem of understanding the mechanisms that regulate the transport of energy in TCV plasmas, in particular in the electron Internal Transport Barrier (eITB) scenario. A radial transport code, integrated with an external module for the calculation of the turbulence-induced transport coefficients, is employed to reproduce the experimental scenario and to understand the physics at play. It is shown how the sustainment of an improved confinement regime is linked to the presence of a reversed safety factor profile.

The improvement of confinement in the eITB regime is visible in the energy channel *and* in the particle channel as well. The density profile shows strong correlation with the temperature profile and has a large local logarithmic gradient. This is an important result obtained from the TCV eITB scenario analysis and is presented in the **fourth Chapter**.

In the same chapter we present the estimate of the particle diffusion and convection coefficients obtained from density transient experiments performed in the eITB scenario.

The theoretical understanding of the strong correlation between density and temperature observed in the eITB is detailed in the **fifth Chapter**. Being the main topic of this work, it is given more space to introduce the basic theory and to compare the simulation results with the experimental data.

Impurity transport constitutes the topic of the **sixth Chapter**, where we demonstrate the physical mechanisms that can sustain a peaked carbon density profile in TCV L-mode plasmas.

Finally, the **seventh Chapter** summarizes the work done with conclusions and a discussion of the possibilities to further improve the results.

Keywords: Tokamak, transport barrier, confinement, turbulence, transport, heat, particles, electrons, pinch, gyrokinetic theory, impurity accumulation

Abstract (français)

Le but principal de ce travail de thèse est de comparer les prédictions des modèles théoriques avec les observations expérimentales pour le transport de particules dans les plasmas du **Tokamak à Configuration Variable** (TCV) situé au CRPP-EPFL à Lausanne. Nous présentons d'abord les principaux problèmes encore ouverts dans la recherche de fusion de tokamak dans le **premier Chapitre**. Une attention particulière est mise sur la modélisation du transport de la chaleur et de particules.

Dans le **deuxième Chapitre**, la partie expérimentale est présentée, y compris une vue d'ensemble des possibilités de TCV, un bref examen des systèmes diagnostiques, et une discussion des outils numériques utilisés pour analyser les données expérimentales. En outre, les codes numériques employés pour interpréter les données expérimentales et pour les comparer aux prévisions théoriques sont présentés.

Le **troisième Chapitre** traite le problème de comprendre le mécanisme qui règle le transport de l'énergie dans les plasmas de TCV, en particulier dans les scénarios avec la formation de barrières internes de transport d'électrons (eITB). Un code radial de transport intégré avec un module externe pour le calcul des coefficients de transport turbulent est utilisé pour reproduire le scénario expérimental et pour comprendre la physique en jeu. On montre comment le soutien d'un régime amélioré de confinement est lié à la présence d'un profil de facteur de sécurité renversé.

L'amélioration du confinement dans le régime eITB est évidente dans le canal d'énergie et dans le canal de particules car le profil de densité montre une forte corrélation avec le profil de température et a un gradient normalisé local élevé. Ceci est un important résultat obtenu à partir de l'analyse d'eITB de TCV et est présenté dans le **quatrième Chapitre**. Dans le même chapitre nous présentons l'estimation des coefficients de diffusion et de convection pour les particules en analysant des évolutions transitoires de densité obtenues dans des eITBs.

La compréhension théorique des observations montrées dans le Chapitre 4 est détaillée dans le **cinquième Chapitre**. Etant le cœur de cette thèse, on lui est dédié plus d'espace pour présenter la théorie de base et pour comparer les résultats des simulations aux données expérimentales présentées dans le Chapitre précédent.

Le transport d'impuretés constitue la matière du **sixième Chapitre**, où nous clarifions les mécanismes physiques qui soutiennent un profil piqué de densité du carbone dans des plasmas de TCV en L-mode sans ou avec chauffage électronique additionnel.

Enfin, le **septième Chapitre** récapitule le travail effectué et discute des possibilités pour améliorer encore les résultats.

Mots clés: Tokamak, barrière de transport, confinement, turbulence, transport, chaleur, particules, électrons, convection, théorie gyrocinétique, accumulation d'impuretés

Contents

1	Introduction to fusion-oriented transport physics	1
2	Transport simulations for TCV plasmas	5
2.1	Introduction	5
2.2	Experimental framework	6
2.2.1	The TCV Tokamak	6
2.2.2	Main diagnostics	6
2.2.3	ECH system	8
2.2.4	Analyzing experimental data	9
2.2.5	TCV plasma scenarios	10
2.3	Theoretical tools	13
2.3.1	The ASTRA code	13
2.3.2	Test of ASTRA for TCV plasmas	18
2.3.3	The gyrokinetic and the gyrofluid paradigms	20
2.4	Summary	30
3	Heat transport in TCV eITBs	33
3.1	Introduction	33
3.2	ASTRA–GLF23 modelling	33
3.2.1	Gyro–Bohm or ‘isothermal’ scaling ?	34
3.3	Comparison with TCV L–mode plasmas	35
3.3.1	Ohmic L–mode, no ECH	35
3.3.2	Ohmic L–mode, with ECH	36
3.3.3	Remarks on the benchmark	40
3.4	Modeling TCV eITB plasmas	41
3.4.1	Experimental dataset	41
3.4.2	Simulations of eITBs with ASTRA+GLF23–I	43
3.5	Summary	46

4	Particle transport in TCV eITBs: experimental results	49
4.1	Introduction	49
4.2	Steady-state scenarios	49
4.2.1	Static database	49
4.2.2	Confinement properties	51
4.2.3	n_e barrier structure	52
4.2.4	Sensitivity to local current profile details	53
4.3	Transient analysis	55
4.3.1	Non-harmonic transient analysis	55
4.3.2	Harmonic transient analysis	57
4.3.3	Experimental evaluation of D and V	57
4.4	Summary	63
5	Theoretical study of electron particle transport in TCV plasmas and eITBs	65
5.1	Introduction	65
5.2	Basic equations	65
5.2.1	Neoclassical particle flux	66
5.2.2	Turbulent particle flux	67
5.2.3	Stationary condition	67
5.3	Linear gyrokinetic theory of particle transport	70
5.3.1	Physics of the pinch coefficients	72
5.3.2	Choice of the quasi-linear rule	75
5.4	Understanding the behavior of density peaking in standard scenarios	76
5.4.1	Base case and spectrum	77
5.4.2	Dependence of $[R/L_n]_{\text{stat}}$ on temperature gradients	81
5.4.3	Dependence of $[R/L_n]_{\text{stat}}$ on collisionality and temperatures ratio	83
5.4.4	Interpretation of experimental data with a collisionality scan	85
5.4.5	Dependence of $[R/L_n]_{\text{stat}}$ on magnetic shear	88
5.5	Interpretation of the eITB density profile behavior	90
5.5.1	Base case and turbulence spectrum	91
5.5.2	Dominant thermodiffusive contribution	92
5.5.3	$s - \alpha$ TEM stabilization effect	94
5.5.4	Effect of finite collisionality	98
5.5.5	Impurities effect	99
5.5.6	Comparison with the experiment	101
5.6	Summary	104

6	Impurity particle transport in TCV L-modes	107
6.1	Introduction	107
6.2	Stationary carbon transport in TCV L-modes	107
6.2.1	Current scan in TCV Ohmic L-mode discharges	109
6.2.2	Detailed parameters analysis	112
6.3	Theoretical analysis	114
6.3.1	Calculation of stationary values	115
6.3.2	Neoclassical contributions	116
6.3.3	Linear gyrokinetic impurity transport coefficients	118
6.4	Interpretation of the experimental behavior	120
6.4.1	Detailed transport analysis	120
6.4.2	Comparison with experimental regime	125
6.5	Summary	126
7	Conclusions	127
7.1	Main considerations	127
7.2	Heat transport analysis of the eITB scenario	127
7.3	Particle transport in the eITB scenario: experimental results	128
7.4	Particle transport theory	129
7.5	Particle transport theory: interpretation of the eITB scenario	130
7.6	Particle transport theory: interpretation of carbon behavior in TCV L-modes	131
7.7	Open issues	132

Chapter 1

Introduction to fusion-oriented transport physics

Transport physics is a fundamental and very complex research domain, spanning from atmospheric modeling to semiconductors. It assesses the capabilities of a given physical system to displace mechanical and thermodynamical quantities like energy, momentum, velocity, particles, and so on. In particular, it is important to have a correct prediction of the gains/losses and thus the capability of a system to retain or evacuate a certain amount of, for example, energy, with respect to exchanges with the external environment. In addition, transport physics allows the scientist to calculate and to predict profiles, i.e. the spatial variation of local values of the relevant quantities, and their evolution in time. In the domain of thermonuclear fusion, transport physics is applied to understand the phenomena that take place in the core of a Tokamak, the toroidal device designed to magnetically confine the high temperature plasma. The main goal of the fusion-oriented scientific community is to obtain a steady-state self-sustained burning plasma to produce low-cost and safe electrical energy from thermonuclear reactions. The burning plasma reactor has become, from a mere tool to study fundamental plasma physics, a real necessity for future times due to the strong increase in energy demand we are facing nowadays, and the need to cut with polluting and/or dangerous energy sources. The next generation of fusion reactors, like ITER (acronym for **I**nternational **T**hermonuclear **E**xperimental **R**eactor) [1, 2], is designed explicitly to show the public opinion that the production of energy through nuclear fusion is feasible.

This objective has been pursued since the realization that a magnetically confined ensemble of deuterium and tritium ions can be pushed to sufficiently high temperatures to react and produce helium and energetic neutrons via nuclear fusion reactions. The confinement scheme should be able to maintain the quasi-neutral ensemble of ions and electrons in steady-state conditions without appreciable use of an external energy source. Indeed, the main limitation to an achievable steady-state energy-producing reactor is, altogether with some technological limitations regarding the plasma-facing components

due to high edge temperatures, the fact that a large external energy source is needed in order to successfully confine the plasma. This last point is crucial since, for the realization of a fusion reactor for commercial use, it is necessary that the ratio between released and input energies, called Q factor, satisfies $Q \gg 1$. This requires the hot particles to stay in the core of the plasma for a sufficiently long time to perform a relevant number of thermonuclear reactions. Indeed the core should have the same reactants concentration in time, and not become polluted by inert reaction products (essentially ionized He), or edge-ablated impurities. These problems are at the center of the studies of plasma physics in the domain of confinement and transport. The transport channels can be divided in two main categories: the energy channel and the particle channel.

Physicists have since the sixties discovered that different mechanisms regulate energy and particle transport. In particular it has been observed that inside the tokamak, radial transport is caused at a very basic level by cross-field collisional transport, where collisions are provided by Coulomb scattering between charged particles. However collisional transport in a toroidal device (called *neoclassical* transport, [3]) would result in levels of transport that are far inferior to the ones observed in the core of Tokamak plasmas. Experimental observations of core confinement degradation give rates of energy and particle cross-field diffusion that are $\sim 10^1 - 10^2$ times larger than what is predicted by neoclassical transport. On the other hand, it has been known since the development of fluid dynamics that growing instabilities can form in unfavorable regions of a dynamical system. For example, the Rayleigh–Taylor instability amplifies small perturbations of an interface between two fluids at different densities, provided there is a net force perpendicular to the interface whose sign is the same as the density gradient. In a similar way, in a magnetically confined toroidal plasma, different kinds of fluid and kinetic instabilities can be excited due to the presence of magnetic field curvature and finite gradients of the plasma density and temperature profiles [4]. The presence of plasma microinstabilities results in a turbulent state that strongly enhances radial cross-field transport of energy and particles. However improved core confinement regimes, where turbulence activity is reduced or almost completely suppressed, have been found in many tokamaks ([5, 6, 7] and references therein).

The effect of turbulence on the equilibrium plasma profiles is highly non-trivial with regards to the dependence of the amplitude of radial diffusion on the plasma equilibrium parameters, the magnetic geometry, and the fact that turbulence can act also as a *source* of plasma profile gradients. For example it enables inward convection of particles that can balance outward diffusion and sustain a finite gradient even in the absence of core particle source [8]. Nevertheless this is consistent with the second law of thermodynamics [9], because the sustainment of a peaked density profile is indirectly provided by the coupling with the temperature and current profiles, thus it is not possible in the absence

of an external power source that sustains the temperature and the current profiles via an external inductive source or a radio-frequency generated current drive. The fact that turbulence can provide an inward convection of particles can give rise to a problem since core pollution by impurity accumulation and helium ash retention are dramatic limitations to the performance of the tokamak plasma.

Different theoretical models, which are based on the assumption of a developed turbulent state, have been proposed to interpret the experimental observations on particle transport, like the 'TEP' model [10, 11, 12], or a model based on particle diffusion in energy phase space [13]. Actually, as we will discuss in this work, a self-consistent gyrokinetic model can be shown to incorporate, derived from first principles, all these partial models. In addition to collisional neoclassical transport and turbulence-driven transport, other phenomena linked to Magneto-Hydro-Dynamic (MHD) macro-instabilities like the Neoclassical Tearing Mode (NTM) [14], sawtooth crashes [15] or fishbones [16] can have a strong effect on transport and thus on plasma profiles. Other models are based on completely different arguments like profiles 'universality', see Ref. [17] and references therein. The complexity of plasma transport physics can be very high. Nevertheless, it is possible to understand the separate mechanisms and compare theoretical predictions with experimental observations through detailed study of the local characteristics of plasma profiles and their time traces. In this perspective, we will introduce and discuss the tools that allow us to perform local analysis of the transport phenomena observed in the Tokamak core, showing in detail the different capabilities of the employed theoretical models and numerical codes.

The experiments that allow us to perform comparison with theoretical models have been performed on the TCV Tokamak. Its main characteristics, diagnostics, and the powerful electron cyclotron heating and current-driving capabilities will be briefly presented. Following the experimental tools, we will present the main codes used to perform the theoretical interpretation of experimental data. We employ a dynamical radial transport code for the calculation of time scales, magnetic equilibrium, and plasma profiles. This code is coupled with the required modules for the calculation of MHD instabilities and neoclassical transport coefficients. In addition, two numerical codes are used for the calculation of turbulence related quantities and the assessment of the effect of turbulence-induced transport on the plasma profiles in the view of performing an in-depth study of the electron Internal Transport Barrier (eITB) scenario. The ITB scenario has been proposed for ITER operation in the advanced phases. Thus, the key results obtained in this thesis work could be helpful to predict the outcomes in future experiments. Indeed we will present general results on particle transport theory that can help in understanding existing experiments. We also dedicate some space to the study of impurity transport in TCV L-modes and analyze the basic mechanisms that provide the observed carbon

impurity peaking in that scenario.

Although the main scope of the present thesis is to deal with particle transport theory and comparison with the experimental observations, we present some results on heat transport simulations for TCV plasmas, in particular for the eITB scenario, to show that the same fundamental mechanism acts synergetically to enhance both energy and particle confinement.

Chapter 2

Transport simulations for TCV plasmas

2.1 Introduction

Transport modeling of the Tokamak plasma core is a challenging issue and requires several tools to be employed to reach the specific goals. Although in general, with the help of the system symmetries, the global transport problem can be reduced to one spatial dimension, namely along the radial cross-field direction, the transport itself is known to be driven by phenomena that intrinsically develop on two, even three, dimensions, covering several disparate time and length scales. Nevertheless there are several advantages arising from these scales separation. The cross-field transport that is observed on confinement time scales can be modeled with global radial transport codes. The transport sources, i.e. particle and energy fluxes, are calculated with external modules that consider phenomena happening at a much faster time scale. This is possible since these phenomena are caused by plasma microinstabilities (turbulence), which are the main responsible for the observed fluxes, that act on length scales of order of the Larmor radius and on time scales of the order of the ion sound transit time. For the same reason they can be studied independently from the phenomena acting on equilibrium scales, with powerful codes that clarify their behavior.

In this Chapter we first introduce the TCV tokamak, its heating capabilities and the relevant plasma diagnostics. Then we present the main plasma scenarios, in particular the electron Internal Transport Barrier scenario (eITB). The theoretical tools that will be used to analyze global and local transport properties are introduced and discussed. These tools can be used either to interpret the experimental observations or to predict the behavior of plasma parameters in artificial parameters scan similar to the experimental values.

Parameters	Symbol	Value
Major radius	R_0	0.88 m
Minor radius	a	0.25 m
Nominal aspect ratio	$A = R_0/a$	3.4
Vacuum vessel elongation	κ_{TCV}	3
Maximum plasma current	I_p	1.2 MA
Maximum central magnetic field	B_0	1.54 T
Maximum loop voltage	V_{loop}	10 V
Discharge duration		< 4 s
edge plasma elongation	κ_a	0.9 - 2.82
edge plasma triangularity	δ_a	(-0.8) - (+0.9)

Table 2.1: *Main TCV parameters.*

2.2 Experimental framework

We start by describing the TCV Tokamak, the relevant diagnostics from which data are extracted, and the Electron Cyclotron system. We briefly present the numerical tools used to analyze the experimental data. Finally we present the eITB scenario and its characteristics.

2.2.1 The TCV Tokamak

TCV, acronym for Tokamak à Configuration Variable, is located at the Centre de Recherches en Physique des Plasmas (CRPP), is an axisymmetric toroidal confinement machine with the peculiarity of being versatile in obtaining disparate shapes for the plasma column to study their stability properties [18]. The main design parameters of the machine are shown in Table 2.1, while figure 2.1 shows a schematic view of TCV. From the parameters table we can see that the geometry in particular is characterized by the low aspect ratio ($\epsilon(a/2) \approx 0.12$).

2.2.2 Main diagnostics

The TCV diagnostic system is composed of different components to measure the main plasma parameters and obtain core profiles of the relevant quantities. The diagnostics can be divided in categories depending on the type of data they provide.

For the purpose of performing transport simulations of TCV plasmas, the main diagnostics used in this work are: the magnetic coils to reconstruct the magnetic equilibrium, the Thomson Scattering system to measure core density and temperature profiles of electrons, a system of 14 vertical chords of the Far InfraRed (FIR) interferometer to simultaneously cross-check the Thomson Scattering measurements and to reconstruct the electron density

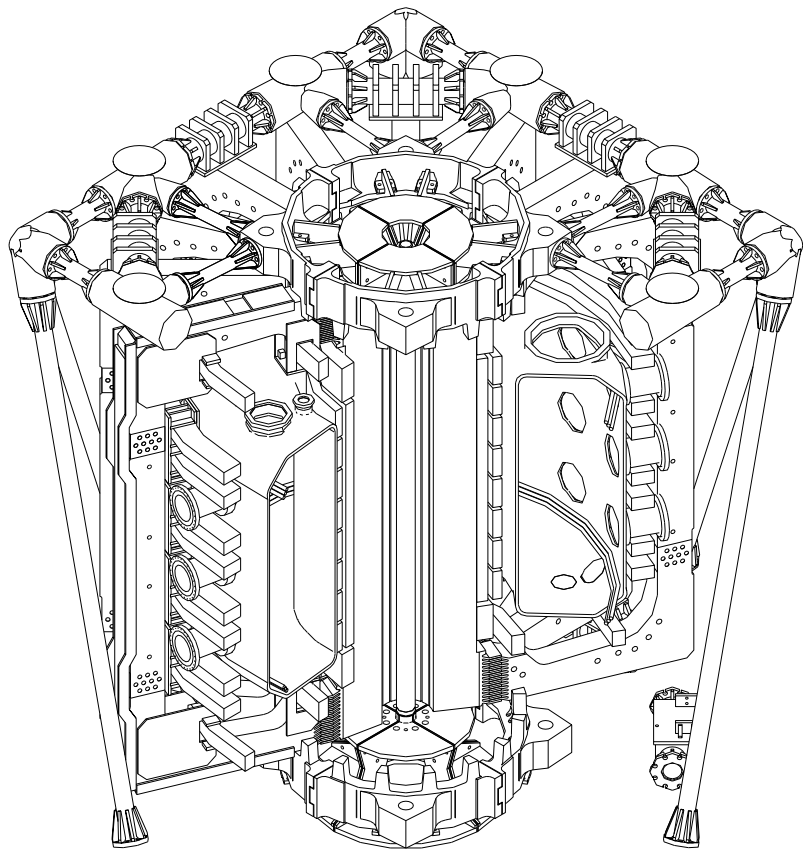


Figure 2.1: *The TCV vessel: main structure and coils.*

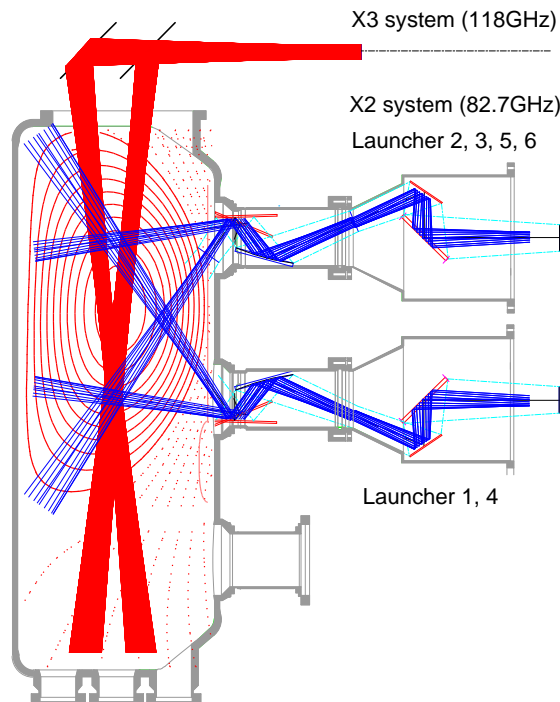


Figure 2.2: *Poloidal cross-section of the TCV vessel. The X2 and X3 ECH launching systems and ray paths are shown.*

evolution on a fast time scale, a Charge Exchange Resonant Scattering (CXRS) diagnostic to measure the main ions and impurity density and temperature profiles, a Compact Neutral Particle Analyzer (CNPA) to estimate the ion temperature distribution function, a system of multiple fast X-ray cameras to map the spatio-temporal evolution of the plasma energy content, and a recently installed Phase Contrast Imaging (PCI) diagnostic to measure small-scale fluctuations and obtain information on plasma turbulence.

2.2.3 ECH system

TCV is equipped with an ECH system characterized by its flexibility [19]. It is designed to cover a large portion of the poloidal cross section, as it is required to be used with the wide variety of plasma shapes created in the vessel. The toroidal injection angles can be changed, allowing the generation of substantial electron cyclotron current drive (ECCD), either in co or in counter directions. The plasma scenarios we are interested in are heated through the 2nd harmonic cyclotron resonance in the extraordinary mode X2. The TCV ECH system provides two clusters of three gyrotrons operating at the second harmonic frequency, $f_{2ce} = 82.7$ GHz. The nominal power for each gyrotron is 500 kW, resulting in a total available RF power of 3 MW. The pulse duration is limited by the window heat load at about 2 s.

In figure 2.2 the X2 system launchers geometry is shown in the poloidal plane of the TCV vessel. Each launcher has two degrees of freedom. One provides steering of the microwave beam in a fixed plane, changing the poloidal injection angle, even during the discharge, allowing experiments with a sweep of the power deposition location. The other degree of freedom allows the rotation of the sweep plane between discharges, permitting experiments with different amounts of ECCD.

2.2.4 Analyzing experimental data

The main scope of the work is to compare predictions from theory-based numerical codes with experimental observations. Thus, an important part of the work is to select reliable data and to process them to be used for the theoretical analysis. Since the present work deals with heat and particle transport, the relevant quantities that are subject to the main analysis are the density and temperature profiles of electrons and ions.

Electron temperature and density from Thomson Scattering

The Thomson Scattering system of TCV consists of three YAG lasers firing high power pulses, each one with a frequency of ~ 16 Hz. They can be fired alternatively to obtain profiles with a sampling frequency of ~ 50 Hz, although this modality requires high density plasmas, or simultaneously to obtain good quality measurements in low density plasmas. The acquisition of the scattered light is done by means of 25 detectors aligned in the vertical direction at a distance of 0.92 meters from the torus axis. The detectors are symmetrically displaced above and below the equatorial plane $z = 0$ and they are distanced by ~ 3 cm, thus covering almost the whole height of the vessel. From each scattering measurements the electron temperature T_e and density n_e can be calculated and mapped on the radial direction assuming constant quantities on a magnetic flux surface. To improve the time and spatial precision it is possible to perform slow vertical movements of the plasma column provided the core parameters are kept constant. With this technique T_e and n_e are obtained with more accuracy.

Interferometry

In the context of the study of particle transport, subject of chapter 4 and chapter 5, a particular attention will be devoted to the study of transient phenomena to characterize the relevant time scales. However the Thomson Scattering system has a low time sampling, not suited for transient analysis. An alternative source of density profiles comes from the inversion of the FIR data. The FIR interferometer consists of 14 vertically oriented equi-spaced lines of sights traversing the plasma, horizontally placed from $R = 0.64$ m to $R = 1.12$ m, thus covering the radial extension of most of TCV plasmas. The in-vessel

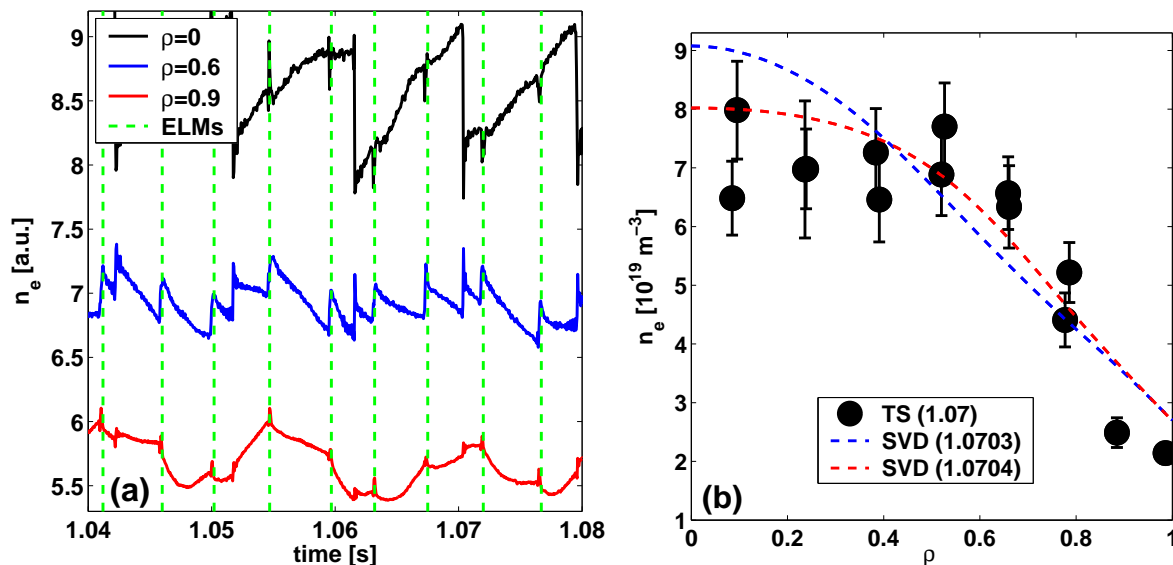


Figure 2.3: *a)* Example of SVD inversion for an ELMy H-mode discharge in TCV. ELM events are marked with vertical dashed green lines. ρ is a radial coordinate defined as $\rho = \sqrt{\psi/\psi_{r=a}}$, where ψ is the poloidal magnetic flux; *b)* For the same discharge, comparison of fitted Thomson density (black solid) and density profiles obtained from SVD (dashed) around the sawtooth crash at $t = 1.0703$ s (blue dashed before crash, red dashed after crash). Four topos are used for this case.

laser lines are compared with an external reference line and thus the line-integrated density can be evaluated from the fringe counts. From these measurements, the local profile can be reconstructed by means of different inversion methods.

In this work we adopt the SVD method proposed by Furno *et al.* [20]. It will be employed to reconstruct the dynamical evolution of the density profile on time scales relevant to estimate the magnitude of diffusion and convection. In figure 2.3(a) we show how the SVD inversion of FIR measurements leads to a high-sampling time reconstruction of the density profile evolution. We plot the time traces of the electrons density at three different radial locations. The selected discharge #24474 is an ELM-y H-mode plasma with both core sawtooth activity (with an inversion radius $\rho_{\text{inv}} \approx 0.6$) and edge ELM activity. The ELM events are identified by vertical dashed lines, while the sawtooth crashes are clearly visible on the density trace at $\rho = 0$. In figure 2.3(b) we compare the Thomson density profiles (TS in the legend) at the time $t \sim 1.07$ s with two SVD-inverted profiles (SVD in the legend) before and after the sawtooth crash.

2.2.5 TCV plasma scenarios

TCV is capable of operating in a disparate variety of plasma conditions producing a rich zoology of scenarios, ranging from Ohmic L-modes to ECH heated H-modes to electron Internal Transport Barriers (eITBs). As we have seen in subsection 2.2.3, the ECH system

is particularly suited for experiments with strong electron heating and where a large fraction of non-inductive current drive is needed. This allows to obtain regimes where a strong increase in core electron energy confinement is reached, substituting the inductive Ohmic current drive with an off-axis deposited EC drive, such that the current profile becomes hollow and an internal transport barrier in the electron temperature (eITB) is formed [21].

The eITB scenario is very useful to perform fundamental physics studies in a steady-state regime with strong gradients. In fact, both the electron temperature and density profiles show a drastic change in their gradients when going into the barrier region [22]. We can distinguish different types of eITB scenarios, depending on the heating/current-drive configuration. In this work we will concentrate on the fully non-inductive scenario. Another scenario obtained often in TCV is called **Improved Core Electron Confinement (ICEC)** and it is produced injecting central counter ECCD to obtain a total current profile that is slightly off-axis. In this case the Ohmic component is large and a strong heating is delivered on-axis. This scenario will not be addressed here. However it has been studied previously in Ref. [23] where more details on it can be found.

eITB fully non-inductive scenario

The fully non-inductive scenario is obtained substituting the centrally peaked Ohmic current with an off-axis EC co-current drive (co-CD). In this scenario the Ohmic transformer can still be used as an actuator to drive central current perturbations to test the barrier sensitivity to small changes in the core magnetic shear and q profiles [24]. Under these conditions, the current profile is characterized by being hollow and peaked off-axis. An additional central heating and/or counter-current (cnt-CD) component can be added to enhance the barrier. In this type of plasma the reachable total current I_p is limited by the capabilities of the ECCD system to values of $I_p \approx 80 \div 120$ kA. Indeed, it has been found that it can be sustained mostly by the gradients-driven bootstrap current [25], up to 100% in some cases as shown in Refs. [19, 26, 27].

To give an idea of the main parameters evolution during and after the formation of the fully non-inductive eITB scenario we choose an example from the eITB database. In figure 2.4(a) we show the poloidal cross-section of the TCV vessel and eITB plasma discharge #21655 (the LCFS is drawn in solid green). The off-axis co-CD components are drawn as green and blue rays and the additional central heating component is drawn as a red ray. In figure 2.4(b) we plot the time traces of some global quantities for the same discharge. The formation of the barrier is shown by the strong rapid increase in the figure of merit H_{RLW} , defined as the ratio between the experimental electron energy confinement time $\tau_{\text{Ee}}^{\text{EXP}}$ and the scaling law for the same parameter obtained with the Rebut-Lallia-Watkins model [28] $\tau_{\text{Ee}}^{\text{RLW}}$: $H_{\text{RLW}} = \tau_{\text{Ee}}^{\text{EXP}} / \tau_{\text{Ee}}^{\text{RLW}}$. This parameter is known to be a good

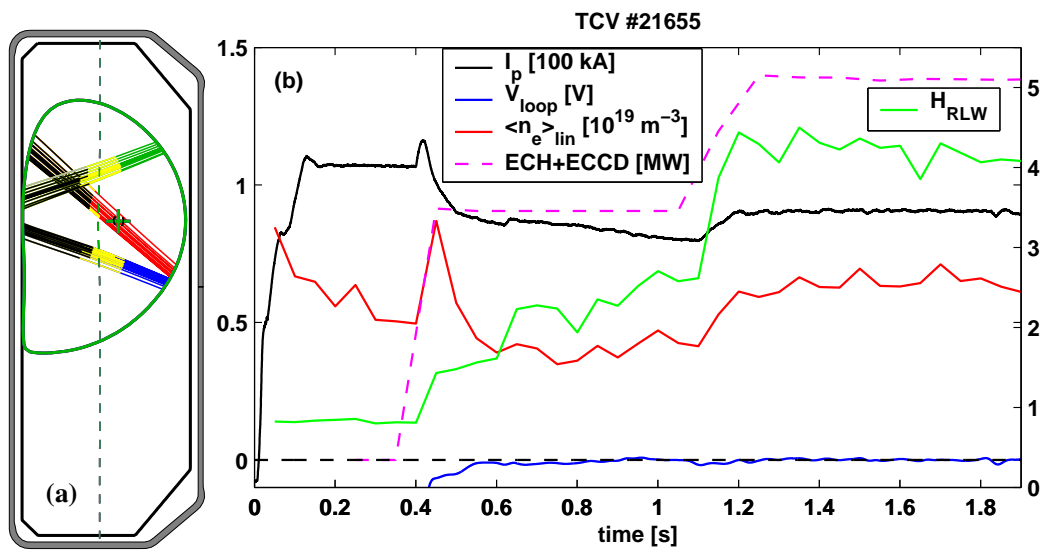


Figure 2.4: a) Poloidal cross-section of the TCV vessel with fully non-inductive eITB plasma of discharge #21655 at $t = 1.5$ s (represented through the LCFS drawn in solid green). The ECH-ECCD rays configuration is also shown: the green and blue rays are the off-axis co-CD components to drive the non-inductive current, the red ray is the central ECH component to enhance the barrier performance; b) Time traces of total plasma current I_p , edge loop voltage V_{loop} , line averaged electron density $\langle n_e \rangle_{lin}$, and total ECH+ECCD power for same discharge #21655. The barrier formation is visible in the increase of the figure of merit H_{RLW} from ~ 1 to ~ 4 as the loop voltage drop to zero and the additional central heating is imposed around $t \approx 1.1$ s.

scaling parameter for the energy confinement in TCV L-mode plasmas. It is of order ~ 1 in Ohmic L-mode plasmas but it can increase up to ~ 6 for strong eITBs, indicating a large improvement in the core energy confinement.

2.3 Theoretical tools

Once the experimental data are processed and mapped on a unique radial coordinate, they can be inserted in a transport code to simulate the global behavior of the plasma and compare the outcomes of the simulation with the experimental observations. In this work different numerical tools will be used:

- 1) The dynamical transport code **ASTRA** [29] will be used to simulate the behavior of the electron temperature and to reproduce the eITB characteristic profile observed in the fully non-inductive scenario.
- 2) Turbulence codes: used to analyze properties of steady-state profiles, they are devoted to understand the mechanisms sustaining the observed profiles.

The latter are employed to understand the behavior of the plasma in terms of micro-turbulence driven fluxes. To model these phenomena, a class of codes constructed around the gyrokinetic theory are adopted. They are both fully kinetic (gyrokinetic codes) or derived in a fluid paradigm (gyrofluid codes).

Since in this thesis work we will concentrate on the study of transport fluxes and equilibrium profiles, we distinguish between the two main sources of transport: **neoclassical** transport and **turbulence-driven** transport. Neoclassical transport is taken into account using available formulas from the literature. Turbulence-driven transport is investigated by means of gyrokinetic and gyrofluid codes. In all the cases, both sources of transport are taken into account and the relative importance will be discussed.

2.3.1 The ASTRA code

The modelling of a dynamical plasma is a very complex issue due to many different aspects and phenomena that accompany the evolution of the plasma as a system. However, different considerations or approximations allow to model the relevant phenomena of interest, in this case cross-field transport on confinement time scales, in a simplified geometry. The ASTRA code as it is employed here is used to model 1D radial transport of heat and particles provided the sources and the boundary conditions with a fixed plasma magnetic boundary. A detailed description of the code can be found in Ref. [29]. Here we report the fundamental equations that are useful to understand the following. We note now that in the version of ASTRA used here, the neoclassical transport coefficients are implemented according to fitting formulas described in Refs. [30, 31].

Magnetic equilibrium and current

The plasma magnetic equilibrium is reconstructed at each time step by means of the Grad–Shafranov equation with a three-moments approximation, i.e. to each flux surface three degrees of freedom are assigned, which are linked to the geometrical parameters elongation κ , triangularity δ and mid–plane radial position. The plasma boundary, i.e. the LCFS, that closes the equation, is represented with these formulas with experimental boundary values for the geometrical parameters:

$$\begin{aligned} R &= R_0 + \Delta + a [\cos \theta - \delta \sin^2 \theta] \\ z &= \Delta_z + a\kappa \sin \theta \end{aligned} \quad (2.1)$$

where Δ is the LCFS Shafranov–shift and Δ_z the vertical displacement. The experimental values of κ , δ , a , Δ and Δ_z are retrieved from the magnetic equilibrium reconstruction performed by the code LIUQE [32]. Once the flux surfaces are computed, the flux functions ψ (poloidal flux) and Φ (toroidal flux) and the metric coefficients are calculated.

The safety factor profile $q(\rho)$ is given by the well known equation $q = \frac{d\Phi}{d\psi}$ and the total plasma current density, expressed as the averaged parallel component $j_{\parallel} = \langle \mathbf{j} \cdot \mathbf{B} \rangle / B_0$, is calculated as the sum of the resistive inductive contribution σE_{\parallel} , the bootstrap current j_{BS} , and the external non–inductive sources (for example RF current–drive) j_{CD} :

$$j_{\parallel} = \sigma E_{\parallel} + j_{\text{BS}} + j_{\text{CD}} \quad (2.2)$$

This equation is also used in ASTRA for the radial diffusion equation of the poloidal magnetic flux ψ with j_{BS} and j_{CD} as external sources. The bootstrap current j_{BS} is evaluated with the neoclassical coefficients reported in Ref. [30].

The magnetic shear s is calculated as $s = r/q \, dq/dr$ and it is positive for monotonic q profiles but reverses sign in the core for reversed q profiles obtained for example when $E_{\parallel} = 0$ and a strong j_{CD} is injected off–axis.

When running ASTRA one has to be careful that the value of the total current density j_{\parallel} does not become too low near the magnetic axis. In that case the magnetic equilibrium solver does not converge anymore and the code crashes. To avoid this problem, which sometimes arises when simulating the fully non–inductive eITB cases, we adjust the profile with a small ad–hoc residual component that preserves a non–vanishing on–axis value of j_{\parallel} . The problem itself is due to the fact that when $j_{\parallel}(\rho \rightarrow 0) \rightarrow 0$ then $q(\rho \rightarrow 0) \rightarrow \infty$, the metric coefficients become infinite and the transport equations are no more solvable.

Heat transport

The transport of energy is modelled by the following 1D flux–surface averaged equation:

$$\frac{1}{V'} \frac{\partial(V' n_j T_j)}{\partial t} + \frac{1}{V'} \frac{\partial}{\partial \rho} (V' g_1 Q_j) = P_j \quad (2.3)$$

where $V' = \partial V / \partial \rho$ is the flux–surface enclosed volume radial derivative, T_j is the j^{th} species local temperature, $g_1 = \langle |\nabla \rho| \rangle$ is a metric coefficient, Q_j is the local heat flux, and P_j the local power density source.

The radial coordinate ρ is an arbitrary flux surface label but in the following we will employ specific definitions: (the square root of) the normalized poloidal flux $\rho_\psi = \sqrt{\psi / \psi_{r=a}}$, the normalized enclosed volume $\rho_V = \sqrt{V / V_{r=a}}$, the normalized toroidal flux $\rho_\Phi = \sqrt{\Phi / \Phi_{r=a}}$. Throughout the following we will employ mainly the volume–related coordinate ρ_V as it is closely related to the real space cylindrical–like radial coordinate r . In some cases the poloidal magnetic flux label ρ_ψ will be used. In all the formulas and equations, the radial coordinate will be always left 'unspecified' and indicated with the symbol ρ , being implicitly defined as ρ_V if not stated differently.

The heat flux Q_j appearing in equation (2.3) is expressed by:

$$Q_j = -n_j T_j \frac{g_2}{g_1} \sum_i \chi_j^i G_j^i \quad (2.4)$$

where $g_2 = \langle |\nabla \rho|^2 \rangle$ is another metric coefficient, χ_j^i is the heat transport coefficient of species j relative to the thermodynamical force i given by $G_j^i = \left(\frac{\partial T_j}{T_j \partial \rho}, \frac{\partial n_j}{n_j \partial \rho}, \dots \right)$.

Here we neglect the small contribution $3/2 \Gamma_j T_j$ coming from energy convection due to a finite particle flux Γ_j . We also neglect the so–called heat pinch, i.e. any off–diagonal contribution appearing in equation (2.4), thus leaving only the diagonal thermodynamical force $\frac{\partial T_j}{T_j \partial \rho}$ to give $Q_j = -n_j \chi_j \frac{g_2}{g_1} \frac{\partial T_j}{\partial \rho}$. The (only diagonal) heat transport coefficients χ_j are provided by neoclassical theory–based formulas implemented in the code, and by an external module for the turbulence–driven flux calculation. The time evolution of the temperature is thus self–consistently calculated inserting the external power source as from the experiment and initiating the simulation with the experimental profiles.

At stationary state, i.e. when $\partial / \partial t = 0$, the temperature profile is given by the solution of the following differential equation:

$$\frac{\partial T_j}{\partial \rho} = -\frac{1}{V' n_j \chi_j g_2} \int_0^\rho P_j dV \quad (2.5)$$

In fact, from the experimental measurements of temperature and density, and provided the magnetic equilibrium and the absorbed power, one can evaluate a 'power balance' heat transport coefficient, for example for electrons, as:

$$\chi_e^{\text{PB}} = -\frac{1}{V' \frac{\partial T_e}{\partial \rho} n_e g_2} \int_0^\rho P_e dV \quad (2.6)$$

In general the electron absorbed power P_e is calculated as the sum of the Ohmic power, the absorbed ECH power and the equipartition power loss:

$$P_e = P_{\text{ECH}} + P_{\text{OH}} - P_{\text{EQ}} \quad (2.7)$$

The radiated power loss, diagnosed with the bolometers, is negligible in TCV as well as other minor sources/sinks of energy.

For the ions, a formula similar to 2.6 is used, but only the equipartition power is retained in the ion power source P_i since no other ions heating source is presently installed in TCV:

$$P_i = P_{\text{EQ}} \quad (2.8)$$

Particle transport

The particle continuity equation is analogous to equation (2.3):

$$\frac{1}{V'} \frac{\partial V' n_j}{\partial t} + \frac{1}{V'} \frac{\partial}{\partial \rho} (V' g_1 \Gamma_j) = S_j \quad (2.9)$$

where now n_j is the local density, Γ_j the local particle flux, and S_j the local particle source. The particle flux is decomposed in the following way:

$$\Gamma_j = -n_j \left(D_j \frac{g_2}{g_1} \frac{\partial n_j}{n_j \partial \rho} - V_j \right) \quad (2.10)$$

where the diagonal term is proportional to the density logarithmic gradient through the diffusion coefficient D_j , and the off-diagonal contributions are contained in the convection velocity V_j .

In TCV plasmas the core particle sources have been estimated to be very small [33] and eventually important only in the very edge region $\rho_V \gtrsim 0.9$, which allows us to assume $S_j \approx 0$ for the core region. In this case, contrary to heat transport, where the steady-state ($\partial/\partial t = 0$) transport coefficient χ_j can be evaluated with a power balance technique, see equation (2.6), in the case of particle transport the steady-state condition reads

$$\Gamma_j = 0 \quad (2.11)$$

Therefore, D_j and V_j cannot be evaluated independently. However, from equation (2.10) and equation (2.11), their ratio is found to be related to the density logarithmic gradient:

$$\frac{g_1}{g_2} \frac{V_j}{D_j} = \frac{\partial n_j}{n_j \partial \rho} \quad (2.12)$$

To separate diffusion and convection in an unambiguous way, we performed experiments where density transients are triggered and D_j and V_j are evaluated separately solving equation (2.9).

Initial and boundary conditions

Current evolution – With regards to the initial and boundary conditions for the current density profile, different possibilities can be chosen. In fact, ASTRA allows to impose

either the total plasma current I_p or the edge loop voltage $V_{\text{loop}}^{\text{LCFS}}$. For the fully non-inductive cases we find better to use the boundary condition $V_{\text{loop}}^{\text{LCFS}} = 0$, while in all the other cases we fix the current $I_p = I_p^{\text{EXP}}$. A check that the self-consistent current and loop voltage are close to the experimental values is done for every case to insure stationarity. The initial condition on the current density profile (or alternatively on the q profile) does not matter so much and we decide to use the LIUQE q profile, even if the real q profile is reversed. The current density will diffuse according to the Ampere's law and thus ASTRA will converge to the self-consistent steady-state within a few current evolution characteristic times.

Temperature evolution – The initial electron temperature is provided by the Thomson Scattering measurements:

$$T_e(\rho, t = 0) = T_e^{\text{EXP}}(\rho) \quad (2.13)$$

The ion temperature profile, if available, is provided by the CXRS diagnostic. However most of the time the ion temperature measurements are absent and thus we utilize a simple procedure to provide an initial T_i : it is fitted as a linear function of the electron temperature with central and edge scaling factor. That is:

$$T_i(\rho, t = 0) = T_e^{\text{EXP}}(\rho, t = 0) \left[\left(\frac{T_e}{T_i} \right)_0 (1 - \rho) + \left(\frac{T_e}{T_i} \right)_b \rho \right] \quad (2.14)$$

where the central $\left(\frac{T_e}{T_i} \right)_0$ and boundary $\left(\frac{T_e}{T_i} \right)_b$ values are chosen by the user.

The boundary conditions are chosen to fix the simulated values to the experimental values:

$$T_j(\rho_b, t) = T_j^{\text{EXP}}(\rho_b) \quad (2.15)$$

where the 'boundary' ρ_b can be chosen to be smaller than the edge value $\rho = 1$.

Density evolution – We choose to simulate the density of electrons, main ions (deuterium, $Z = 1$) and one impurity (carbon, $Z = 6$). The initial values for the three densities are provided by the electron density measurements from Thomson Scattering or FIR (via SVD inversion) and the value of the effective charge Z_{eff} . In practice we have:

$$n_e(\rho, t = 0) = n_e^{\text{EXP}} \quad (2.16)$$

$$n_i(\rho, t = 0) = n_e^{\text{EXP}} \left(\frac{6 - Z_{\text{eff}}}{5} \right) \quad (2.17)$$

$$n_C(\rho, t = 0) = n_e^{\text{EXP}} \left(\frac{Z_{\text{eff}} - 1}{30} \right) \quad (2.18)$$

The boundary conditions for densities follow the same rule as for that of the temperature, equation (2.15). However in most of the performed simulations the densities are kept fixed and no evolution is allowed. The reason is that we concentrate on temperature evolution for the dynamical studies and on steady-state regimes for the study of density profiles.

2.3.2 Test of ASTRA for TCV plasmas

We now show how the code works presenting several simulations of some TCV plasmas using exclusively experimental data. In this sense we concentrate on checking the self-consistent magnetic equilibrium and compare it with the reconstruction obtained from the LIUQE code, used routinely for the mapping of Thomson Scattering measurements on the flux surface coordinate ρ , for different cases. For these simulations, the electron temperature T_e is allowed to evolve according to equation (2.3), using the power balance χ_e from formula (2.6). The current density j_{\parallel} is calculated according to formula (2.2). The core MHD-driven instabilities, sawtooth crashes in this case, are taken into account in the simulations with the aid of a Fortran90 sawtooth module [34], based on the Kadomtsev–Porcelli model [35]. The densities are kept fixed as well as the ion temperature. The EC current drive is modelled by the Fokker–Planck code CQL3D as done in Ref. [36].

Ohmic L-mode plasmas

We perform ASTRA simulation of Ohmic sawtoothing discharge #28359 at $t = 1$ s. In figure 2.5(a) we compare the radial profile of T_e [keV] from both the Thomson Scattering measurements and from the ASTRA prediction, showing also the power balance χ_e^{PB} [m^2/s]. In figure 2.5(b) we compare the result for the q profile between LIUQE and ASTRA, together with the total j_{\parallel} [MA/m^2] and the bootstrap j_{BS} [MA/m^2] current densities. Note that the LIUQE initial q profile is lower than 1 for a large portion of the radial interval and thus a cycle of sawtooth crashes takes place to recover $q \geq 1$.

Ohmic L-mode ECH heated plasma

In figures 2.6(a,b) we show the simulation results for ECH heated Ohmic discharge #24883, taking the experimental profiles at $t = 1.8$ s. The ECH power is injected at $\rho_V \approx 0.35$, plotted in figure 2.6(a) as a dashed green line. The total injected power is $\int P_{\text{ECH}} dV = 1.7$ MW. In figure 2.6(b) we show again the current density and the safety factor profiles compared to the LIUQE reconstruction.

Fully non-inductive eITB plasma

We take as an eITB example discharge #29859 at time $t = 1.5$ s, for which the total current is $I_p \approx 95$ kA. The current scenario is the fully non-inductive scenario with off-axis co-CD and a negligible Ohmic component. In figure 2.7 we show the result of the ASTRA simulation for the electron temperature T_e in figure 2.7(a) and for the q profile and current densities in figure 2.7(b). Note that now the total current density has an additional component, namely the ECRF driven current density j_{CD} .

It is interesting to observe, in figure 2.7(b), the difference between the q profile predicted

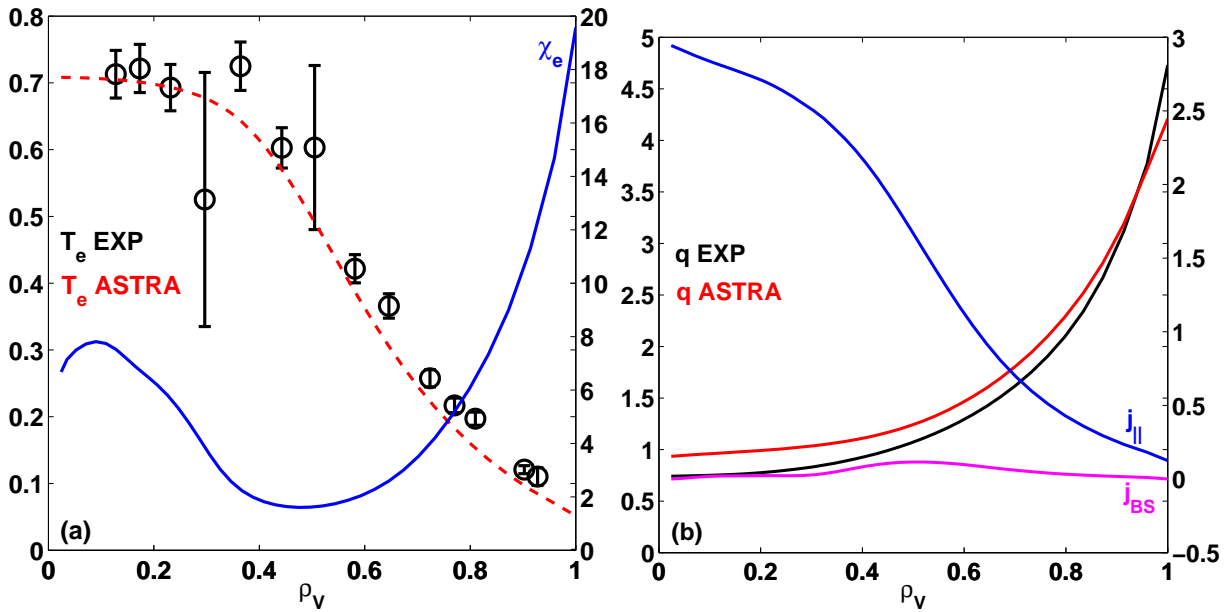


Figure 2.5: a) Simulation outcomes for #28359 at $t = 1$ s, comparing T_e (shown in keV) from Thomson Scattering (black, left y-axis) and the ASTRA result (red, left y-axis), together with the power balance heat transport coefficient χ_e^{PB} (blue, right y-axis) in m^2/s ; b) Comparison of q profiles from LIUQE (black) and ASTRA (red) on the left y-axis. The reconstructed total current density j_{\parallel} in MA/m^2 (blue) and bootstrap component j_{BS} in MA/m^2 (magenta) are plotted on the right y-axis.

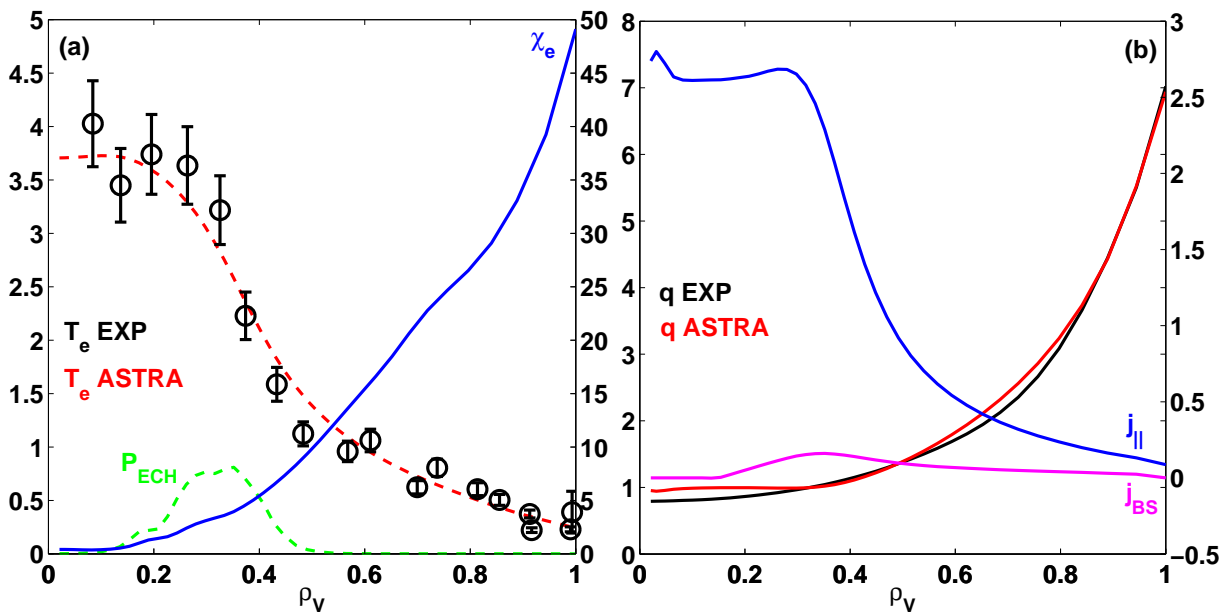


Figure 2.6: a) Simulation outcomes for #24883 at $t = 1.8$ s, with the same logic as in figure 2.5. Here we plot also the absorbed ECH power density profile in arbitrary units (dashed green); b) Comparison of q profiles and current densities as in figure 2.5.

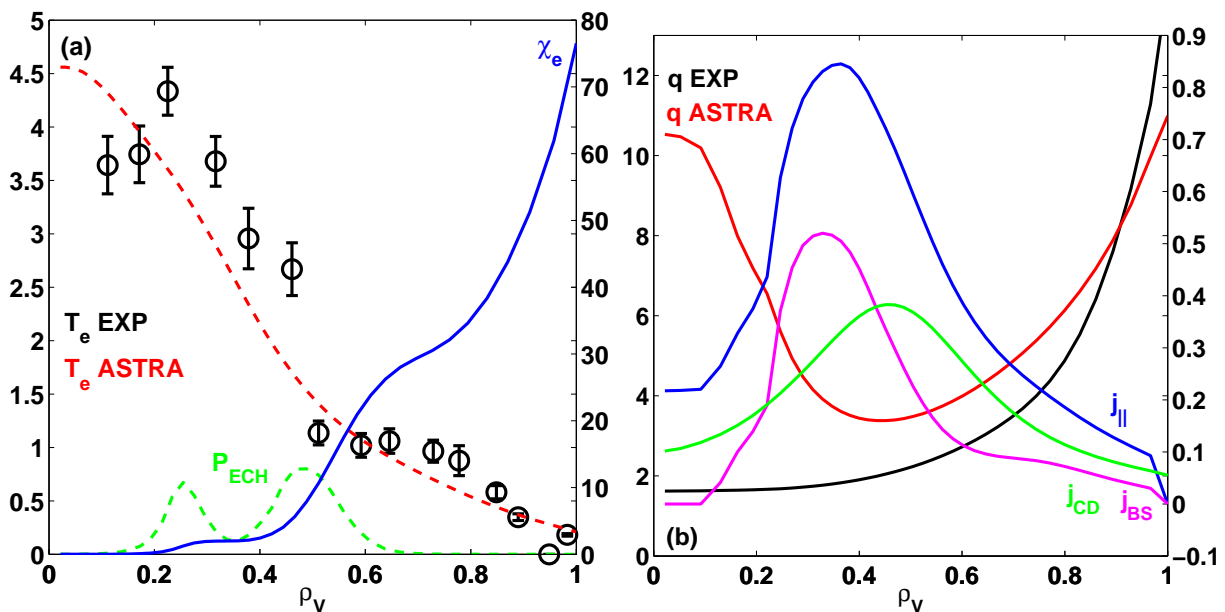


Figure 2.7: a) Simulated eITB discharge #29859 at $t = 1.5$ s: Thomson and ASTRA T_e with absorbed ECH power density P_{ECH} ; b) q profiles and current densities. Here we show also the current drive component j_{CD} (green).

by ASTRA (red) and the q profile reconstructed by LIUQE (black). The first is reversed and has a minimum around $\rho_V \sim 0.4$ whereas LIUQE gives a monotonic q profile.

In this discharge, during the eITB phase, the bootstrap current fraction f_{BS} is about 45% and the ECCD fraction f_{CD} around 50%. In the experimental scenario the Ohmic current vanishes as the Ohmic transformer is set to zero current slope. In the simulation a 5% of the current is still inductive as a vanishing Ohmic current would cause the current density at the axis to go to zero and thus the code would not converge anymore.

2.3.3 The gyrokinetic and the gyrofluid paradigms

The Tokamak geometry and the plasma magnetic and kinetic equilibria are such that electrostatic (or electromagnetic) microinstabilities can develop, spreading to form a turbulent state that provides a large source of energy and particle transport. Plasma microinstabilities are destabilized by the interplay between the unfavorable magnetic curvature in the low field side of the Tokamak and the presence of steep equilibrium gradients in the thermodynamic fields, i.e. temperature and density.

These microinstabilities are usually characterized by their fast time scale ($\sim R/v_{th}^i$ the ion sound transit time) and their short length scale ($\sim \rho_i$ the ion Larmor radius) compared to the equilibrium time ($\sim \tau_E$) and length scales ($\sim R$). However, the time scale $\tau_{turb} \sim R/v_{th}^i$ is much longer than the cyclotron time scale $\tau_{turb} \gg (m_i, m_e)/(eB)$, allowing to average over the faster gyro-motion. The theoretical framework developed from first

principle (statistical) kinetic equations, introducing these characteristic time and length scales separation, is called the 'gyrokinetic theory'. If a fluid closure is introduced to represent the plasma as a thermodynamical system, 'averaging' details over the phase space, then the theory is called 'gyrofluid'. The ultimate goal of these two paradigms is to describe plasma turbulence such that a reliable calculation of transport fluxes is possible. In principle the gyrokinetic theory is more complete as it contains single-particle kinetic effects. However, as done in fluid dynamics for example, to fasten calculation time it is easier to stick to a fluid model (gyrofluid in the Tokamak case), whose drawback is the loss of kinetic effects and the relative arbitrariness in the choice of the fluid closure.

In this work we employ tools that have been developed in both the gyrokinetic and the gyrofluid frameworks. In some cases these tools can be integrated in ASTRA to dynamically simulate the plasma evolution due to the background turbulent activity. To this purpose, the Gyro-Landau-Fluid **GLF23** code [37] is employed in ASTRA for dynamical simulations. The terminology 'Gyro-Landau-Fluid' means that GLF23 employs a gyro-averaged fluid paradigm that allows the user to perform very fast calculation of turbulence in the linear regime, using a complicated mixing-length rule to emulate the non-linear saturation phase, but it retains kinetic Landau damping in the fluid closure in the form of a dissipative heat flux [38]. This code will be used predominantly for heat transport studies, although it can also provide predictions on particle transport as for example done in Ref. [39].

In addition, we employ the powerful **GS2** gyrokinetic code [40] to analyze in detail the properties of turbulence in the linear phase for different plasma parameters scans. It will be shown that relevant information about the dominant microinstabilities and the induced transport can be obtained from this code. It will be used mainly for the study of steady-state particle transport presented in chapter 5 and in chapter 6.

To proceed in a proper logical order, we present first the fundamental gyrokinetic theory and the GS2 code, and then the gyro-Landau-fluid model as implemented in GLF23.

The gyrokinetic equation and GS2

Gyrokinetic theory is founded on the assumption that the kinetic of Tokamak plasma micro-turbulence follows the physics contained in the Vlasov equation with the addition of a proper collision operator. The basic assumption is that the relevant time and length scales must be much larger than the cyclotron time and length scale as previously discussed. In particular all the fluctuating field \tilde{X} (which equilibrium value is X_0) and parameters must be such that they obey the fundamental gyrokinetic ordering:

$$\frac{\tilde{X}}{X_0} \sim \frac{k_{\parallel}}{k_{\perp}} \sim \frac{\omega_{\text{turb}}}{\Omega_{\text{cyclo}}} \sim \frac{1}{k_{\perp} L_0} \sim \frac{\rho_i}{L_0} \ll 1 \quad (2.19)$$

where L_0 is a typical equilibrium length scale. This ordering allows to treat the gyro-motion as a very fast time scale that can be averaged out. The resulting guiding-center approximation for the particle trajectory leads to the standard form of the gyrokinetic equation [41]:

$$\frac{\partial f}{\partial t} + \frac{d\mathbf{R}}{dt} \cdot \nabla f + \frac{dv_{\parallel}}{dt} \frac{\partial f}{\partial v_{\parallel}} = C(f) \quad (2.20)$$

where $f(\mathbf{R}, v_{\parallel}, v_{\perp}, t)$ is the single-particle distribution function, \mathbf{R} is the particle guiding center position and v_{\parallel}, v_{\perp} respectively the particle velocity along and perpendicular to the magnetic field lines. $C(f)$ is the collision operator. The trajectory of the guiding center position \mathbf{R} is determined by the particle drifts caused by the presence of an electromagnetic field in a toroidal geometry. Its evolution equation is given by:

$$\frac{d\mathbf{R}}{dt} = v_{\parallel} \frac{\mathbf{B}}{|\mathbf{B}|} + \tilde{\mathbf{v}}_{\mathbf{E} \times \mathbf{B}} + \mathbf{v}_{\perp}^d \quad (2.21)$$

where $\tilde{\mathbf{v}}_{\mathbf{E} \times \mathbf{B}}$ is the $\tilde{\mathbf{E}} \times \mathbf{B}$ drift induced by the fluctuating electric field $\tilde{\mathbf{E}}$, and \mathbf{v}_{\perp}^d is the perpendicular drift associated with the curvature of the magnetic field lines. At the moment we neglect the magnetic fluctuations. The electromagnetic field (\mathbf{E}, \mathbf{B}) is self-consistently evaluated with Maxwell's equations which close the problem.

Equation (2.20) contains nonlinearities in the last two terms at the left. These are classified as the perpendicular nonlinearity (term $\frac{d\mathbf{R}}{dt} \cdot \nabla f$) and the parallel nonlinearity (term $\frac{dv_{\parallel}}{dt} \frac{\partial f}{\partial v_{\parallel}}$). It can be shown, through a simple scales separation argument, that the first one is dominant, while the second does not play a major role [42] except on confinement time scales as inferred in recent works [43]. The perpendicular nonlinearity arises from the advection of the perturbed part of f , i.e. \tilde{f} , by the perturbed $\tilde{\mathbf{E}} \times \mathbf{B}$ velocity, namely $\tilde{\mathbf{v}}_{\mathbf{E} \times \mathbf{B}} \cdot \nabla \tilde{f}$. For our purposes we will neglect the nonlinear interactions and study the properties of turbulence and transport in the linear phase. On the other hand, the nonlinear term is fundamental to obtain turbulence saturation values and fluxes amplitudes. This can be done in the linear framework introducing mixing length arguments and it will be done in the following.

From now on we will focus on the linearized gyrokinetic equation for \tilde{f} , namely the perturbed part of $f = \tilde{f} + f_0$, where f_0 is the equilibrium distribution function:

$$\frac{\partial \tilde{f}}{\partial t} + \frac{d\tilde{\mathbf{R}}}{dt} \cdot \nabla f_0 + \frac{d\mathbf{R}_0}{dt} \cdot \nabla \tilde{f} + \frac{d\tilde{v}_{\parallel}}{dt} \frac{\partial f_0}{\partial v_{\parallel}} + \frac{dv_{\parallel 0}}{dt} \frac{\partial \tilde{f}}{\partial v_{\parallel}} = C(\tilde{f}) \quad (2.22)$$

Note that $\frac{d\mathbf{R}_0}{dt} \cdot \nabla \tilde{f}$ contains the macroscopic gyrocenter drifts and $\frac{dv_{\parallel 0}}{dt} \frac{\partial \tilde{f}}{\partial v_{\parallel}}$ represents the parallel mirror force that provides particle trapping. From this equation one can immediately see that the source of turbulence is given by the resonance between the advection of the perturbation by the macroscopic drifts in the presence of gradients of the

equilibrium fields.

The derivation of the non-linear electromagnetic gyrokinetic equation for a toroidal axisymmetric configuration from equation (2.20) is given in Ref. [44]. We show here the resulting equation in its electrostatic, linearized, collisionless form:

$$\left(\frac{\partial}{\partial t} + v_{\parallel} \nabla_{\parallel} + \omega_d \right) \tilde{f} = \frac{Ze}{T} F_0 (-v_{\parallel} \nabla_{\parallel} - \omega_d + \omega_*) \langle \tilde{\Phi} \rangle_g \quad (2.23)$$

where \tilde{f} is the fluctuating part of the distribution function f , such that $f = F_0 + \tilde{f}$, F_0 is the equilibrium distribution function (usually assumed Maxwellian), and $\langle \tilde{\Phi} \rangle_g$ is the 'gyro-averaged' electrostatic potential fluctuation. ∇_{\parallel} is the parallel gradient operator, ω_d is the magnetic curvature drift frequency operator, which contains poloidal and radial derivatives, and ω_* is the diamagnetic drift frequency operator. Taking a simple magnetic equilibrium with concentric shifted-circles surfaces, their definitions are:

$$\begin{aligned} \nabla_{\parallel} &= \frac{1}{Rq} \left(q \frac{\partial}{\partial \phi} - \frac{\partial}{\partial \theta} \right) \\ \omega_d &= -\frac{1}{v_{\text{th}}^2} \left(v_{\parallel}^2 + \frac{v_{\perp}^2}{2} \right) \frac{T}{ZeBR^2} \left(\frac{\cos \theta}{\rho} \frac{\partial}{\partial \theta} + \sin \theta \frac{\partial}{\partial \rho} \right) \\ \omega_* &= \frac{T}{ZeBR^2} \left[\frac{1}{n} \frac{\partial n}{\partial \rho} + \left(\frac{E}{E_{\text{th}}} - \frac{3}{2} \right) \frac{1}{T} \frac{\partial T}{\partial \rho} \right] \frac{\partial}{\rho \partial \theta} \end{aligned} \quad (2.24)$$

where Z is the species to electron charge ratio, e the electron charge, n is the species density, T the species temperature, E the particle energy and v_{th} , E_{th} are respectively the particle thermal velocity and thermal energy. The radial coordinate ρ is defined here as the local aspect ratio, or normalized minor radius, $\rho = r/R$.

Equation (2.23) is fully described when the initial and boundary conditions are known. At each time step its solution is defined on a 4D plane, two spatial dimensions $\rho - \theta$, and two phase space dimensions $v_{\parallel} - v_{\perp}$. Note also that it is a global problem, due to the presence of radial coupling in ω_d , meaning that the full radial interval must be solved consistently. However equation (2.23) can be strongly simplified if the dominant microinstabilities are ballooning modes [45, 48] with high toroidal number n , for which the relation $k_{\parallel} \ll k_{\perp}$ holds. This relation can be easily understood as $T/(ZeBR^2) \sim v_{\text{th}} \rho_i / R^2$ and as such the perpendicular wavenumber must scale as $1/\rho_i$ to balance parallel damping $\sim v_{\text{th}}/R$. Ballooning means that the instability develops mainly on the plasma low field side and its radial extension is much smaller than the equilibrium length scales. In this case the perturbation can be decomposed into the parallel and perpendicular components with completely different length scales. The formal procedure is discussed in Ref. [46]. Equation (2.23) can thus be reduced to a 3D differential equation (1D spatial and 2D in velocity space):

$$\left(\frac{\partial}{\partial t} + v_{\parallel} \nabla_{\parallel} + i\omega_d \right) \tilde{f} = \frac{Ze}{T} F_0 (-v_{\parallel} \nabla_{\parallel} - i\omega_d + i\omega_*) J_0 \tilde{\Phi} \quad (2.25)$$

with now $\nabla_{\parallel} = -1/(Rq)\partial/\partial\theta$ while ω_d and ω_* become algebraic operators:

$$\begin{aligned}\omega_d &= -\frac{1}{v_{\text{th}}^2} \left(v_{\parallel}^2 + \frac{v_{\perp}^2}{2} \right) \frac{T}{ZeBR} [\cos\theta + (s\theta - \alpha \sin\theta) \sin\theta] k_y \\ \omega_* &= \frac{T}{ZeBR} \left[\frac{1}{n} \frac{\partial n}{\partial \rho} + \left(\frac{E}{E_{\text{th}}} - \frac{3}{2} \right) \frac{1}{T} \frac{\partial T}{\partial \rho} \right] k_y\end{aligned}\quad (2.26)$$

where $k_y = nq/(R\rho)$ is the poloidal wavenumber and J_0 is the zero-order Bessel function arising from Fourier decomposition of the gyro-averaging operator $\langle \dots \rangle_g$, with argument $J_0(k_{\perp} v_{\perp}/v_{\text{th}})$, $k_{\perp} = \rho_i \sqrt{k_y^2 + k_x^2}$, $k_x = k_y s\theta$. The angle θ is no more the poloidal angle but it is here an extended field-aligned coordinate that represents the extension of the ballooning mode on the magnetic field lines. Note that linearly the single modes with toroidal wavenumber n are not coupled due to axial symmetry (i.e. $e^{in\phi}$ is an eigenvector), while poloidal harmonics are coupled through the perpendicular drift ω_d . The definition for ω_d , valid in the low aspect ratio limit for a shifted circles magnetic equilibrium, shows that the magnetic curvature drift operator becomes a function of the magnetic shear s and of the Shafranov-shift parameter α . Note also that $\omega_d(\theta = 0)$ is positive for electrons and negative for ions. The same is true for the density-driven term in ω_* as, for peaked profiles, $\frac{1}{n} \frac{\partial n}{\partial \rho} < 0$.

The drawback of using the first-order ballooning representation as done here is that the problem becomes radially localized to 'zero-dimensional' and thus no information on non-local or global effects are retained except from the appearance of the magnetic shear s . This approximation becomes invalid when the magnetic shear approaches zero as for example near the magnetic axis or near q_{min} when the q profile is reversed. Nevertheless, around the $s = 0$ flux surface the turbulence modelling equations can still be represented with a ballooning formalism but to higher radial order [47]. Indeed slab modes can be important in that region. In fact, it has been recently shown that the $s = 0$ surface can host slab-like Electron Temperature Gradient (ETG) modes that could provide an important source of transport for reversed q -profile scenarios [49]. In this work no attempt to use the higher order formalism is done, and in this perspective we will restrain to simulation of cases with $|s| \gtrsim 0.2$.

We now adopt the 'main ion' normalization, i.e. we normalize time and length scales to respectively the ion transit time and Larmor radius ρ_i . Equation (2.25) is then rewritten in normalized form:

$$\left(\frac{\partial}{\partial t} + v_{\parallel} \nabla_{\parallel} + i\omega_d \right) \tilde{f} = Z\tau F_0 (-v_{\parallel} \nabla_{\parallel} - i\omega_d + i\omega_*) J_0 \tilde{\Phi} \quad (2.27)$$

and for ω_d and ω_* :

$$\begin{aligned}\omega_d &= - \left(v_{\parallel}^2 + \frac{v_{\perp}^2}{2} \right) \frac{k_y \rho_i}{Z\tau} [\cos \theta + (s\theta - \alpha \sin \theta) \sin \theta] \\ \omega_* &= \frac{k_y \rho_i}{Z\tau} \left[\frac{1}{n} \frac{\partial n}{\partial \rho} + \left(\frac{E}{E_{th}} - \frac{3}{2} \right) \frac{1}{T} \frac{\partial T}{\partial \rho} \right]\end{aligned}\quad (2.28)$$

where $\tau = T_i/T$ is the main ions to species temperature ratio. Note that the Maxwellian average of ω_d is

$$\omega_{d0} = \int F_0 \omega_d = -2 \frac{k_y \rho_i}{Z\tau} [\cos \theta + (s\theta - \alpha \sin \theta) \sin \theta] \quad (2.29)$$

which can be useful to put in evidence the velocity-dependent part in the form

$$\omega_d = \frac{1}{2} \left(v_{\parallel}^2 + \frac{v_{\perp}^2}{2} \right) \omega_{d0} \quad (2.30)$$

An alternative form of equation (2.25) is conveniently obtained substituting \tilde{f} with a sum of the adiabatic part $-Z\tau F_0 J_0 \tilde{\Phi}$ and the non-adiabatic part \tilde{g} :

$$\tilde{f} = \tilde{g} - Z\tau F_0 J_0 \tilde{\Phi} \quad (2.31)$$

The resulting equation that describes the evolution of \tilde{g} is

$$\left(\frac{\partial}{\partial t} + v_{\parallel} \nabla_{\parallel} + i\omega_d \right) \tilde{g} = Z\tau F_0 \left(\frac{\partial}{\partial t} + i\omega_* \right) J_0 \tilde{\Phi} \quad (2.32)$$

The other piece of the physical system is provided by Maxwell's laws which, in the case of ion-scale electrostatic microinstabilities, are simplified down to the gyro-averaged quasi-neutrality condition

$$\sum_i Z_i \tilde{n}_i = \sum_i Z_i \tilde{n}_i^{\text{pol}} \quad (2.33)$$

with the gyro-center density \tilde{n}_i given by

$$\tilde{n}_i = \int J_{0i} \tilde{f}_i d\mathbf{v} \quad (2.34)$$

and the polarization density \tilde{n}_i^{pol} , produced by finite Larmor radius effects, is given by

$$\tilde{n}_i^{\text{pol}} = Z_i \tau_i \left[1 - \int J_{0i}^2 F_{0i} d\mathbf{v} \right] \tilde{\Phi} = Z_i \tau_i [1 - \Gamma_{0i}] \tilde{\Phi} \quad (2.35)$$

where $\Gamma_{0i} = I_0(b_i)e^{-b_i}$, I_0 is the modified Bessel function of order zero, and $b_i = (k_{\perp} \rho_{Li})^2$. It is easy to see that for electrons, at the ion scale, $\Gamma_{0e} \approx 1$ and the polarization density can be neglected in first approximation.

The system described by equations (2.32) and (2.33) is then solved to find the evolution

of the quantities \tilde{g} and $\tilde{\Phi}$. It is then possible to calculate the cross-field flux Γ_X for a thermodynamic field X obtained as a moment of \tilde{g} :

$$\Gamma_X \sim \langle \tilde{X} \tilde{v}_{E \times B}^r \rangle \quad (2.36)$$

where $\tilde{v}_{E \times B}^r$ is the radial component of the fluctuating $\mathbf{E} \times \mathbf{B}$ velocity. Because $\tilde{v}_{E \times B}^r \propto \tilde{\Phi}$ and, in the linear regime, $\tilde{X} \propto \tilde{\Phi}$, it is found that the flux is defined only if the value of $|\tilde{\Phi}|^2$ is known. This is not possible in the linear regime since $\tilde{\Phi}$ is exponentially growing without any saturation mechanism. However, the usual mixing length argument approximates the saturated value of $|\tilde{\Phi}|^2$ with $(\gamma / \langle k_{\perp}^2 \rangle)^2$ where γ is a characteristic inverse linear time scale and $\langle k_{\perp} \rangle_{\theta}$ a characteristic perpendicular inverse correlation length, given in the linear regime by the ballooning averaged perpendicular wavenumber [50].

The GS2 code calculates, for a given set of plasma equilibrium parameters, the fastest growing instability, according to equation (2.32), and the resulting linear normalized flux, from equation (2.36), defined as $\Gamma_X / |\tilde{\Phi}|^2$, which is a meaningful quantity for linear calculations.

The gyro–fluid paradigm and GLF23

The gyro–fluid equations are derived from the ballooning gyrokinetic equation presented before, assuming a particular closure for the hierarchy of moments equations, such that some kinetic effects, first of all Landau damping, are retained. With this respect, the equations obtained with the closure that contains Landau damping effects are called gyro–Landau–fluid equations. The mathematical method to achieve this goal has been introduced for the first time in Ref. [38]. The GLF23 code itself is derived following that scheme and the basic equations are shown and discussed in detail in Refs. [51] and [37]. Here we discuss some of the model basic assumptions:

- The ion species are considered as a whole and averaged over phase space while the electrons are split into the trapped and passing components in phase space, i.e. divided into two sub–species. For the trapped particles a simple bounce–averaged approximation is used, neglecting the parallel motion and keeping only the magnetic curvature operator on the left–hand side of equation (2.23). The passing electrons are assumed to be massless such that they are quasi–adiabatic. Non–adiabaticity is provided by collisional coupling with trapped electrons and by electromagnetic effect, which are in any case neglected here;
- The geometrical magnetic model is the shifted–circles $s - \alpha$ equilibrium.
- The mixing length formula used in GLF23 for the saturated value of $|\Phi|^2$ is:

$$|\Phi|^2 = C \left(\frac{\gamma_{\text{net}}^{1/2} \gamma_{\text{d}}^{1/2}}{k_x k_y} \right)^2 \quad (2.37)$$

where C is an amplitude parameter that is chosen to fit results from non-linear simulations, $\gamma_{\text{net}} = \gamma - \gamma_{\text{ExB}}$, $\gamma_d = 0.2(3/2)|\omega_d|\tau^{-1}$ and k_x, k_y are respectively the radial and the poloidal wavenumbers.

Using equation (2.37), the particle and heat transport coefficients are calculated according to equation (2.36) as shown below, see Ref. [37], equations (9a), (10a) and (11a).

Electron heat transport coefficient

$$\chi_e^{\text{GLF}} = c_s \left(\frac{\rho_s^2}{a} \right) \frac{L_{\text{Te}}}{a} \sum_k \Im \left[\left| \frac{\tilde{\Phi}_{\text{Max}}}{\tilde{\Phi}_k} \right|^2 k_y (3/2) (\tilde{P}_k^t + \tilde{N}_k^u + \tilde{T}_k^u)^* \tilde{\Phi}_k \right] \quad (2.38)$$

Ion heat transport coefficient

$$\chi_i^{\text{GLF}} = c_s \left(\frac{\rho_s^2}{a} \right) \frac{L_{\text{Ti}}}{a} \sum_k \Im \left[\left| \frac{\tilde{\Phi}_{\text{Max}}}{\tilde{\Phi}_k} \right|^2 k_y (3/2) \left(\frac{1}{3} \tilde{P}_{\parallel k}^i + \frac{2}{3} \tilde{P}_{\perp k}^i \right)^* \tilde{\Phi}_k \right] \quad (2.39)$$

Particle diffusivity

$$D_{\text{GLF}} = c_s \left(\frac{\rho_s^2}{a} \right) \frac{L_{\text{Ni}}}{a} \sum_k \Im \left[\left| \frac{\tilde{\Phi}_{\text{Max}}}{\tilde{\Phi}_k} \right|^2 k_y \tilde{N}_k^{i*} \tilde{\Phi}_k \right] \quad (2.40)$$

Note the evident gyro-Bohm nature [48], i.e. the scaling with $c_s \rho_s^2 \sim T_e^{3/2}$, of the transport coefficients dimensional factor.

As it is clear from these equations, no distinction is done between diffusion and convection, such that these are 'effective' diffusivities obtained from a flux to gradient ratio. So, for example, the particle diffusivity from equation (2.40) should be used in equation (2.10) with the (turbulent part of the) convection velocity V set to zero. To discriminate between diffusion and convection in GLF23 one should be able to separately evaluate the diagonal and off-diagonal contributions to the flux. This will be done specifically to study particle transport in chapter 5.

Linear spectrum and fluxes: conventions

We now establish some conventions on the calculation of turbulence linear spectrum and induced quasi-linear fluxes, independently of the use of either codes.

Lengths are normalized to R , the geometrical average of the major radius of the local flux surface. The reference temperature is the main ions temperature T_i . The energy unit for the normalization of the electrostatic potential Φ is eT_e . The normalization units for the

Sign	Mode type	Acronym
$\omega_R > 0$	Trapped Electron Mode	TEM
	Electron Temperature Gradient Mode	ETG
$\omega_R < 0$	Ion Temperature Gradient Mode	ITG

Table 2.2: Mode frequency sign convention.

mode complex frequency is R/c_s where c_s is the ion sound speed $c_s = \sqrt{T_i/m_i}$ given in m/s. The wavenumbers are normalized in units of the ion Larmor radius ρ_i .

The mode complex frequency ω is composed of the growth rate γ (positive for an unstable mode) and the pulsation (here called 'frequency' in the following) ω_R . The latter is **positive** for modes rotating in the electron diamagnetic direction and **negative** for modes rotating in the ion diamagnetic direction. This convention is summarized in table 2.2. Note that this convention is opposite to the one used in GS2.

Given the spectrum and the fields fluctuations, the respective radial flux can be calculated as in equation (2.36). More precisely, given two real space fluctuations 'density' $n(\mathbf{x})$ and a 'radial velocity' $u(\mathbf{x})$ functions of the real space coordinate \mathbf{x} (time dependence is intended implicitly), the local 'flux' Γ of particles is obtained from

$$\Gamma = \frac{1}{\Delta} \int_{\Delta} n(\mathbf{x})u(\mathbf{x})d\mathbf{x} \quad (2.41)$$

where Δ is a domain sufficiently large to cover several correlation lengths, such that $\int_{\Delta} (n, u)d\mathbf{x}$ is statistically zero. We represent each perturbation $X = (n, u)$ with a Fourier series:

$$X = \sum_{\mathbf{k}} \tilde{X}_{\mathbf{k}} e^{i\mathbf{k}\cdot\mathbf{x}} \quad (2.42)$$

where the wavenumber \mathbf{k} spans from $-\infty$ to $+\infty$ for each component. The reality of the perturbations imposes $\tilde{X}_{-\mathbf{k}} = \tilde{X}_{\mathbf{k}}^*$. Applying some basic Fourier theorem, the flux calculated in equation (2.41) becomes:

$$\Gamma = \sum_{\mathbf{k}} \tilde{n}_{\mathbf{k}} \tilde{u}_{\mathbf{k}}^* \quad (2.43)$$

If we now assume the three-dimensional perturbation to be periodic in two dimensions (x, y) we can use the representation:

$$X(x, y, z) = \sum_{k_y=-\infty..+\infty} \sum_{k_x=-\infty..+\infty} \left[\tilde{X}_{k_y, k_x}(z) e^{i(k_y y + k_x x)} \right] \quad (2.44)$$

In this case the flux is given by:

$$\Gamma = \sum_{k_y=-\infty..+\infty} \sum_{k_x=-\infty..+\infty} \frac{1}{\Delta z} \int \left[\tilde{n}_{k_y, k_x} \tilde{u}_{k_y, k_x}^* \right] dz \quad (2.45)$$

An alternative representation is obtained choosing an expansion of the type:

$$X(x, y, z) = \Re \sum_{k_y=0..+\infty} \sum_{k_x=-\infty..+\infty} \left[\tilde{X}_{k_y, k_x}(z) e^{i(k_y y + k_x x)} \right] \quad (2.46)$$

In this case the flux is given by:

$$\Gamma = \frac{1}{2} \Re \sum_{k_y=0..+\infty} \sum_{k_x=-\infty..+\infty} \frac{1}{\Delta_z} \int \left[\tilde{n}_{k_y, k_x} \tilde{u}_{k_y, k_x}^* \right] dz \quad (2.47)$$

The relation of this formalism with the ballooning representation in axisymmetric systems is obtained substituting x, y, z with the usual field-aligned coordinates set [52]: radial coordinate $x = r$, perpendicular-to-the-field-lines coordinate $y = R(\phi + q\theta)$, and 'parallel' (or generalized poloidal coordinate) $z = r\theta$ (with $\Delta_z = 2\pi r$). In our case, working with the linear gyrokinetic equation in the zero order ballooning expansion, we derive the particle flux substituting for $\tilde{u} = \tilde{v}_{E \times B}^r$ in equation (2.45):

$$\Gamma = \Gamma_0 \sum_{\mathbf{k}} \Re \left(i k_y \rho_i \tilde{n}_{\mathbf{k}} \tilde{\Phi}_{\mathbf{k}}^* \right) \quad (2.48)$$

where Γ_0 is a proper dimensional factor and $\mathbf{k} = (k_y, 0)$, with k_y spanning from zero to k_y^{\max} . The z dependence and its integral is implicitly stated. In the linear phase, the fluctuation \tilde{X} is proportional to the electrostatic perturbation $\tilde{\Phi}$. Thus

$$\Gamma = \Gamma_0 \sum_{\mathbf{k}} |\tilde{\Phi}_{\mathbf{k}}|^2 \Re (i k_y \rho_i A_{\mathbf{k}}) = -\Gamma_0 \sum_{\mathbf{k}} k_y \rho_i |\tilde{\Phi}_{\mathbf{k}}|^2 \Im (A_{\mathbf{k}}) \quad (2.49)$$

where $A_{\mathbf{k}} = \frac{\tilde{X}_{\mathbf{k}} \tilde{\Phi}_{\mathbf{k}}^*}{|\tilde{\Phi}_{\mathbf{k}}|^2}$. The quantity ' $\Im(A_{\mathbf{k}})$ ' is called the 'phase-shift' (one for each wavenumber \mathbf{k}) and it is the only meaningful flux-related quantity in a linear calculation. In fact, $|\Phi|^2$ is not known and thus the actual value of the flux has to be approximated choosing a closure for the saturation value $|\Phi^2|$, as discussed above and done for example in GLF23 as from equation (2.37).

The summation appearing in formula (2.49) can be rewritten with the mode with the largest $|\Phi^2|$:

$$\Gamma = -\Gamma_0 |\tilde{\Phi}|_{\text{Max}}^2 \sum_{\mathbf{k}} k_y \rho_i \left| \frac{\tilde{\Phi}_{\mathbf{k}}}{\tilde{\Phi}_{\text{Max}}} \right|^2 \Im (A_{\mathbf{k}}) \quad (2.50)$$

The choice of the summation components and of the weights $\left| \frac{\tilde{\Phi}_{\mathbf{k}}}{\tilde{\Phi}_{\text{Max}}} \right|^2$ can be done in different ways depending on the quasi-linear rule employed. GLF23 has its own quasi-linear rule and it will be kept the same for the following simulations. For example the Weiland model [53] has also a particular choice of the quasi-linear rule. When using GS2, in the linear mode, we will adopt different quasi-linear rules. One example is proposed by Jenko

et al. [54], i.e. only the mode that has the highest value of the mixing length estimate $\gamma / \langle k_{\perp}^2 \rangle$ is kept. Note that the sum $\sum_{\mathbf{k}}(\dots)$ appearing in equation (2.50) requires the choice of equispaced k_y s, otherwise it should be replaced by $\sum_{\mathbf{k}}(\dots)\Delta k_y \rho_i$.

In this work the lowest order of the small aspect ratio expansion for the shifted-circles geometry is employed, which means that no dependence of ω_d , see equation (2.28), and in turns of the turbulence properties, on the elongation and triangularity is kept. In this respect, we do not cover the problem of the turbulence-driven transport dependence on plasma shape. Indeed plasma shape, and more recently the triangularity δ , has been shown to have strong effects on core transport [55].

Note that GLF23 calculates fluid fields and thus the quantity \tilde{X} directly (for example pressure, or density, fluctuations), while GS2, being a kinetic code, calculates the distribution function from equation (2.32) and then heat, particle and parallel velocity fluxes are evaluated with the proper phase space integral.

2.4 Summary

This Chapter has been devoted to the introduction of the main tools that will be used in the following analysis. First, the TCV Tokamak is presented with particular emphasis on the ECH/ECCD capabilities. The possibility to study scenarios with high core gradients is guaranteed by the improved eITB regime obtainable in TCV plasmas with different ECH/ECCD schemes. The most used scenario is the fully non-inductive operation with off-axis co-CD injection and zero current slope in the Ohmic transformer. In these conditions, the total current is sustained by the ECCD current and the bootstrap current only.

The numerical tool **ASTRA** [29] is then introduced. It is a radial transport code that allows to simulate a discharge evolution and to test different models for heat and particle transport. The code is tested on different TCV discharges with experimental input parameters to take confidence with the results.

The effect of turbulence on transport is modelled by gyrokinetic and gyrofluid codes **GS2** [40] and **GLF23** [37] respectively. Each one has its own capabilities and limitations. We have shown that the gyrokinetic code, in the linear version, is a powerful tool to accurately evaluate the phase shift, i.e. the flux normalized to the fluctuation amplitude, and the turbulence properties taking into account kinetic effects. It will be used for detailed study of stationary particle transport in chapter 5 and chapter 6. The gyro-Landau-fluid code GLF23 can predict turbulence-driven fluxes through a choice of the quasi-linear rule, tuned on non-linear simulations results, and its fluid approach allows rapid calculations and its use as a module to ASTRA. It will be used for heat transport studies of TCV

discharges.

Chapter 3

Heat transport in TCV eITBs

3.1 Introduction

We present now the integration of the experimental data into the transport code ASTRA [29] to simulate the behavior of the temperature profile in different TCV plasma scenarios. We employ the GLF23 [37] code to calculate the heat transport coefficients for electrons χ_e and for ions χ_i .

The main goal is to simulate and to understand the physics of the formation of the eITB in TCV via the gyrofluid modelling and to elucidate the role of local confinement amelioration due to the reversal of the safety factor profile. First we will benchmark the code on standard L-modes to evidence the eventual limitations of the model and then we will try to simulate the eITB scenario.

3.2 ASTRA–GLF23 modelling

In subsection 2.3.2 we have introduced the ASTRA code as the main tool to simulate TCV plasmas and to retrieve a more reasonable magnetic equilibrium than just simply relying on the LIUQE code. However, up to now it was run only in the 'experimental mode', i.e. without any model for the transport coefficients.

In this section we want to model some TCV discharges using first–principles based transport coefficients to try to understand the physical mechanisms behind a certain scenario. The modelling paradigm that we will employ to simulate the TCV discharges is the following:

- 1) The ASTRA transport code is run with experimental profiles as initial conditions;
- 2) The initial condition for the magnetic equilibrium is provided by the LIUQE code;
- 3) The electron temperature is evolved assuming a theoretically computed heat transport coefficient;
- 4) Densities are kept fixed;
- 5) The simulations are run for a time sufficient to reach a self–consistent steady–state

checking the spatial constancy of the loop voltage. In the case sawteeth are present the steady-state condition is checked outside the mixing radius;

6) We neglect here the ion temperature evolution and concentrate on electron heat transport;

7) The boundary condition is fixed at $\rho_V = 0.8$.

The transport coefficients are respectively called: χ_e^{PB} for the power balance coefficient and χ_e^{GLF} for the coefficient calculated by GLF23 as in formula (2.38). The neoclassical contribution to the heat transport coefficient will be called χ_e^{NEO} and it is calculated according to Ref. [56]. Thus the theoretical heat transport coefficient χ_e^{TH} is given by:

$$\chi_e^{\text{TH}} = \chi_e^{\text{NEO}} + \chi_e^{\text{GLF}} \quad (3.1)$$

3.2.1 Gyro-Bohm or 'isothermal' scaling ?

Before we start to simulate different TCV cases with the system ASTRA-GLF23, we find instructive to discuss the agreement between the coefficient shown in formula (2.38) and the experimental value to assess the validity of the gyro-Bohm scaling. In this perspective we define an alternative coefficient which has no explicit T_e dependence (hence we call it 'isothermal' scaling):

$$\chi_e^{\text{GLF-I}} = \chi_e^{\text{GLF}} \left(\frac{T_e(\rho_0)}{T_e(\rho)} \right)^{3/2} \quad (3.2)$$

such that $\chi_e^{\text{GLF-I}}(\rho_0) = \chi_e^{\text{GLF}}(\rho_0)$, and ρ_0 will be chosen case to case to have the best fit with the experimental χ_e^{PB} .

The reason to introduce this 'isothermal' scaling is that the explicit gyro-Bohm scaling appearing in formula (2.38) produces a reduction in χ_e^{GLF} when going towards the edge due to a decrease in T_e . However this reduction should be overcome by the strong increase of the normalized term $\propto \chi_e^{\text{GLF}}/T_e^{3/2}$. We will see later that indeed the GLF23 calculations give a coefficient that does not grow towards the edge, meaning the $T_e^{3/2}$ effect is too strong, and in net contrast to what is seen in the experiment. Another reason to eliminate the explicit T_e dependence is that the scaling provided by formula (3.2) is somewhat similar to the RLW scaling used to simulate TCV plasmas in Ref. [23], subsection 3.6.2, formula (3.39). Note that indeed this rescale of χ_e^{GLF} with $T_e(\rho_0)$, where ρ_0 is now arbitrary, brings us back into the semi-empirical domain, while the intention was to compare 'first-principals based' calculations with the experiment. At this point this is the best that can be done to match the theoretical predictions with the experimental observations, and no further investigation will be done at this stage, but it is worth to mention that the correct coefficient could be retrieved if, instead of renormalizing to $T_e^{3/2}$, the mixing length estimate was changed to produce a stronger increase of χ_e^{GLF} towards the edge, for example modifying the rule to account for the nonlinear q dependence observed in past

Current [kA]	Discharge	Time [s]
320	28395	1.3
200	29765	0.8
110	30078	0.4

Table 3.1: *Simulated L-mode discharges with Ohmic heating.*

works (for example in Ref. [57]).

In the following we will test both the GLF23 model as expressed in formula (3.1) over the whole radius and the modified GLF23-I model as expressed in the formula below:

$$\chi_e^I = \chi_e^{\text{NEO}} + \chi_e^{\text{GLF-I}} \quad (3.3)$$

3.3 Comparison with TCV L-mode plasmas

We start by comparing the power balance electron heat transport coefficient χ_e^{PB} with the theoretical coefficients χ_e^{TH} , χ_e^I for some L-mode steady-state plasmas with and without auxiliary ECH heating.

3.3.1 Ohmic L-mode, no ECH

Several L-mode plasmas with Ohmic heating are chosen such to have different total plasma current I_p as shown in table 3.1. The results of the simulation for the self-consistent steady-state electron temperature profile T_e and for the electron heat diffusivity χ_e are shown in figures 3.1, 3.2 and 3.3.

Discharge #28395 is a high-current sawtoothing L-mode plasma with an inversion radius of $\rho_{\text{inv}} \approx 0.5$. For this reason the power balance χ_e^{PB} in figure 3.1(b) becomes very high for $\rho_V \lesssim 0.5$, where the sawteeth are dominating the transport.

From figure 3.1(a) we see that both the GLF23 and GLF23-I models give a T_e that is in good agreement with the experimental profile, although from figure 3.1(b) we note that only the modified GFL23-I χ_e^I is able to reproduce the χ_e^{PB} in the outer region $\rho_V \gtrsim 0.7$. The neoclassical contribution χ_e^{NEO} is practically negligible for $\rho_V \gtrsim 0.4$.

With regard to the underlying turbulence, the code predicts a dominant ITG in the region $0.4 \lesssim \rho_V \lesssim 0.8$ while it changes to TEM near the edge (compare with table 2.2).

Discharge #29765 is an intermediate-current sawtoothing L-mode plasma with an inversion radius of $\rho_{\text{inv}} \approx 0.35$. In figure 3.2(a) we see that the GLF23 result is in poor agreement with the experimental profile for $\rho_V \gtrsim 0.6$, while the GLF23-I is correct all along the radial interval, due to the different behavior in the region $\rho_V \gtrsim 0.6$. Again χ_e^{NEO} is negligible except near the axis. In this case the dominant instability is predicted to be a TEM on the whole radial interval.

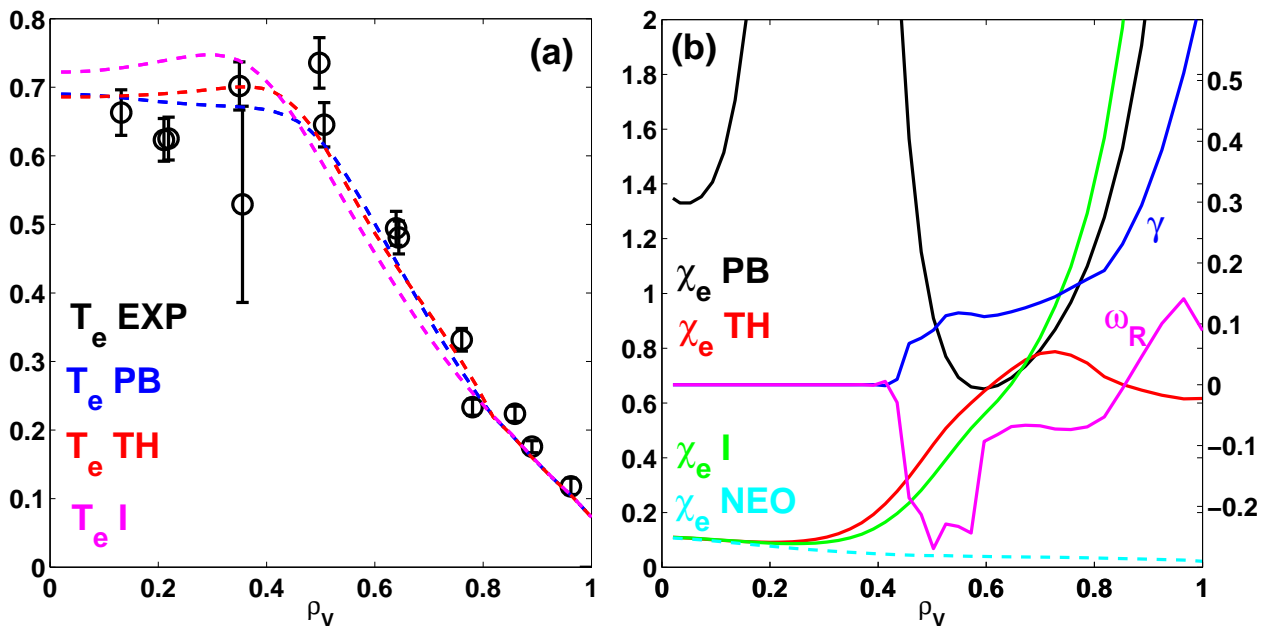
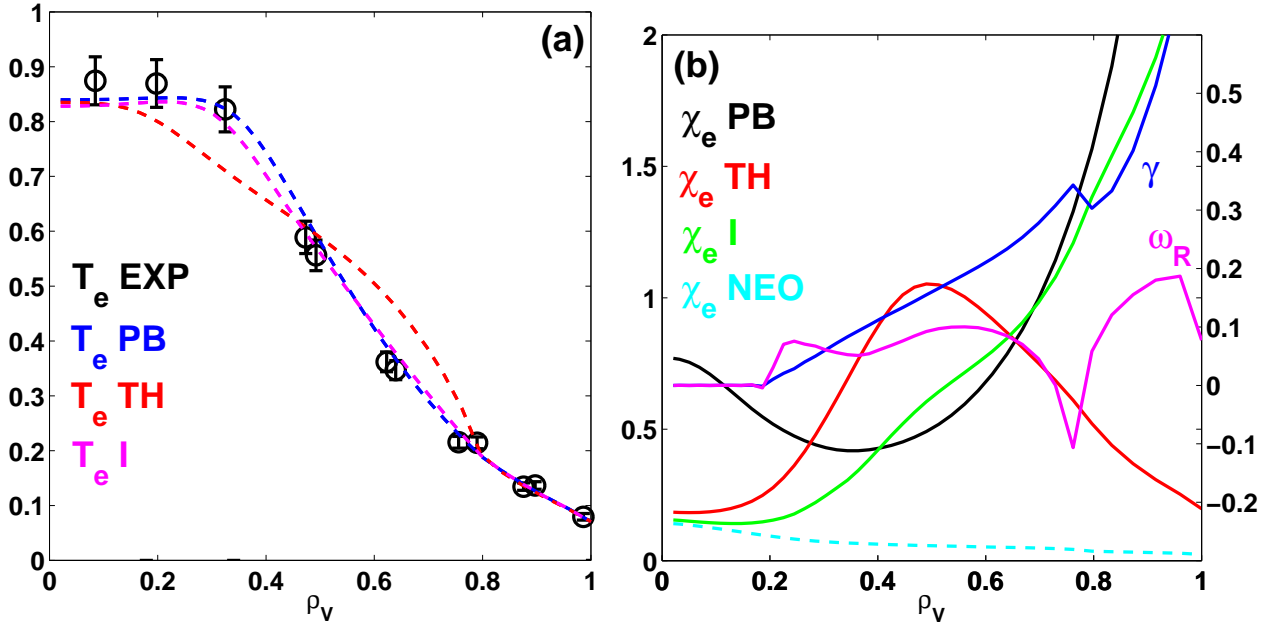
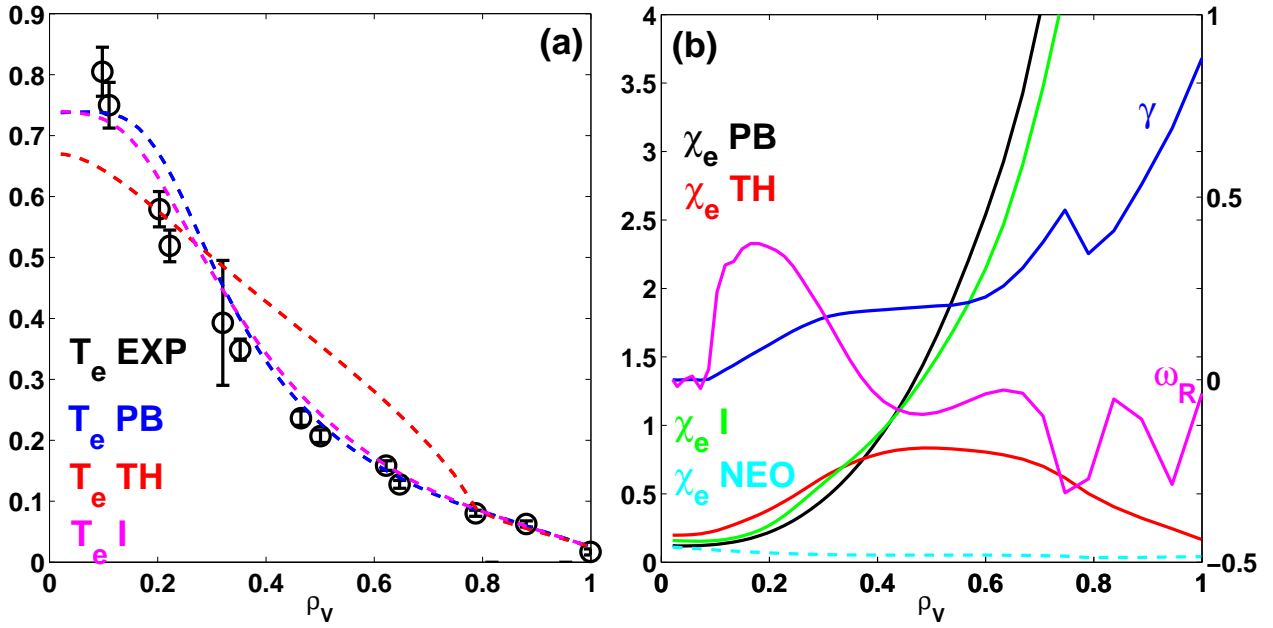


Figure 3.1: a) Comparison of temperature profiles in keV for $I_p = 320$ [kA] discharge #28395 at $t = 1.3$: experimental (black with error bars), calculated using the power balance χ_e^{PB} (dashed blue), calculated using the GLF23 model χ_e^{TH} (dashed red), calculated using the modified GLF23-I model (dashed magenta); b) The heat transport coefficients in m^2/s provided by: power balance χ_e^{PB} (black), theoretical with GLF23 χ_e^{TH} (red), theoretical with GLF23-I χ_e^{I} (green) and the neoclassical contribution χ_e^{NEO} (dashed cyan). In blue and magenta on the right axis we plot respectively the most unstable mode growth rate γ and the rotational frequency ω_R as provided by GLF23, in units of c_s/a .

The last discharge analyzed for the current scan is at low-current with very small sawteeth. The results in figure 3.3(a) show that the GLF23 model is not able to reproduce the experimental profile while the modified GLF23-I model is in very good agreement with it. The reason is visible from figure 3.3(b), where we clearly see that GLF23 deviates significantly from the power balance χ_e^{PB} for $\rho_V \gtrsim 0.4$, while inside this value it is somewhat higher. The dominant mode is predicted to be a TEM in the core while there is a competition of TEM and ITG near the edge. The modified model catches the behavior of the experimentally-evaluated χ_e and thus represents a good model for these cases.

3.3.2 Ohmic L-mode, with ECH

Additional EC heating is injected and the deposition location ρ_{ECH} is varied along the radial direction for a fixed current $I_p = 220$ kA, see table 3.2. The ECH power is delivered with four gyrotrons divided in two clusters, each one aimed at a different radial position. Each gyrotron delivers about 450 kW, such that the total power is ~ 2 MW. We thus expect the Ohmic power to be negligible from where the power is deposited outward, and a strong increase in χ_e with respect to the Ohmic cases.


 Figure 3.2: $I_p = 200$ kA discharge #29765 at $t = 0.8$ s [See caption of figure 3.1].

 Figure 3.3: $I_p = 110$ kA discharge #30078 at $t = 0.4$ s [See caption of figure 3.1].

Power(1) [MW]	Power(2) [MW]	$\rho_{\text{ECH}}(1)$	$\rho_{\text{ECH}}(2)$	Discharge	Time [s]
1.5	0.5	0.5	0.8	25409	1.1
1	1	0.5	0.8	25409	1.95
2.0	—	0.5	—	24883	1.8

 Table 3.2: Simulated *L*-mode discharges with ECRF heating.

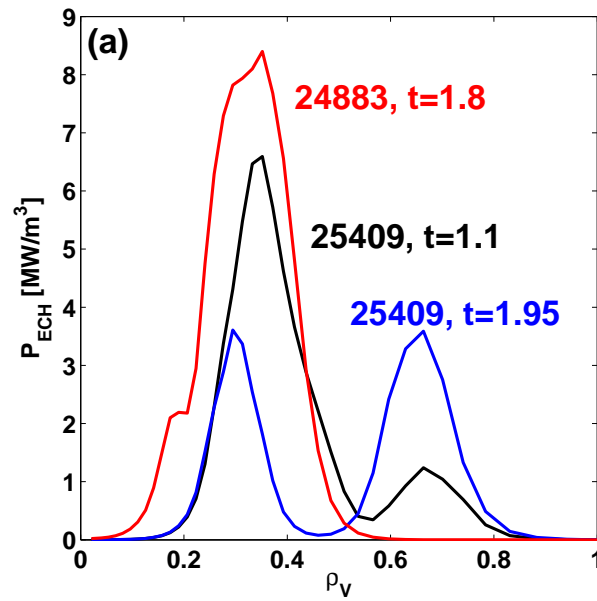


Figure 3.4: *ECH deposition profiles for the three cases of table 3.2.*

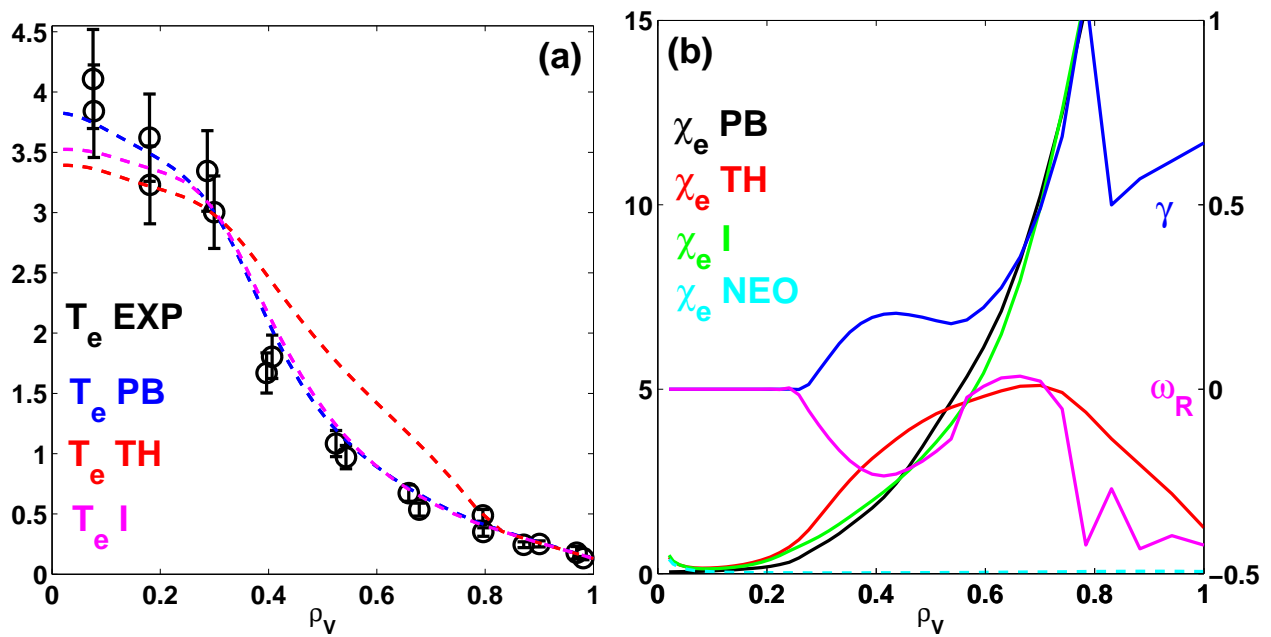


Figure 3.5: *ECH discharge #25409 at $t = 1.1$ s [See caption of figure 3.1].*

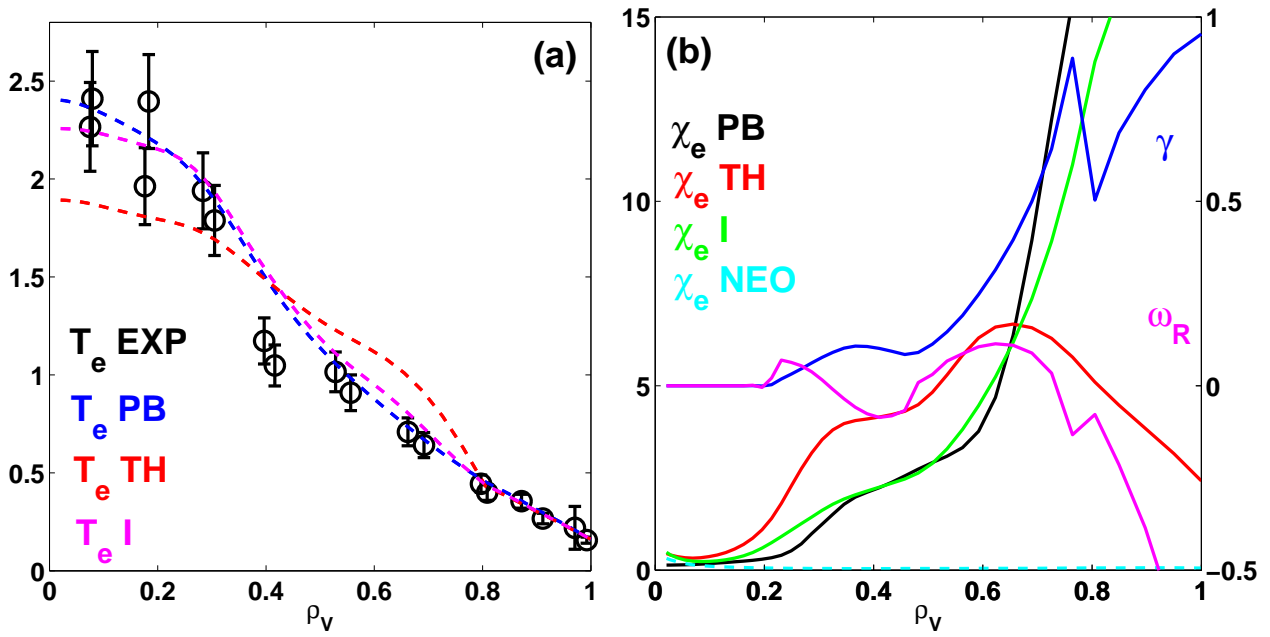


Figure 3.6: ECH discharge #25409 at $t = 1.95$ s [See caption of figure 3.1].

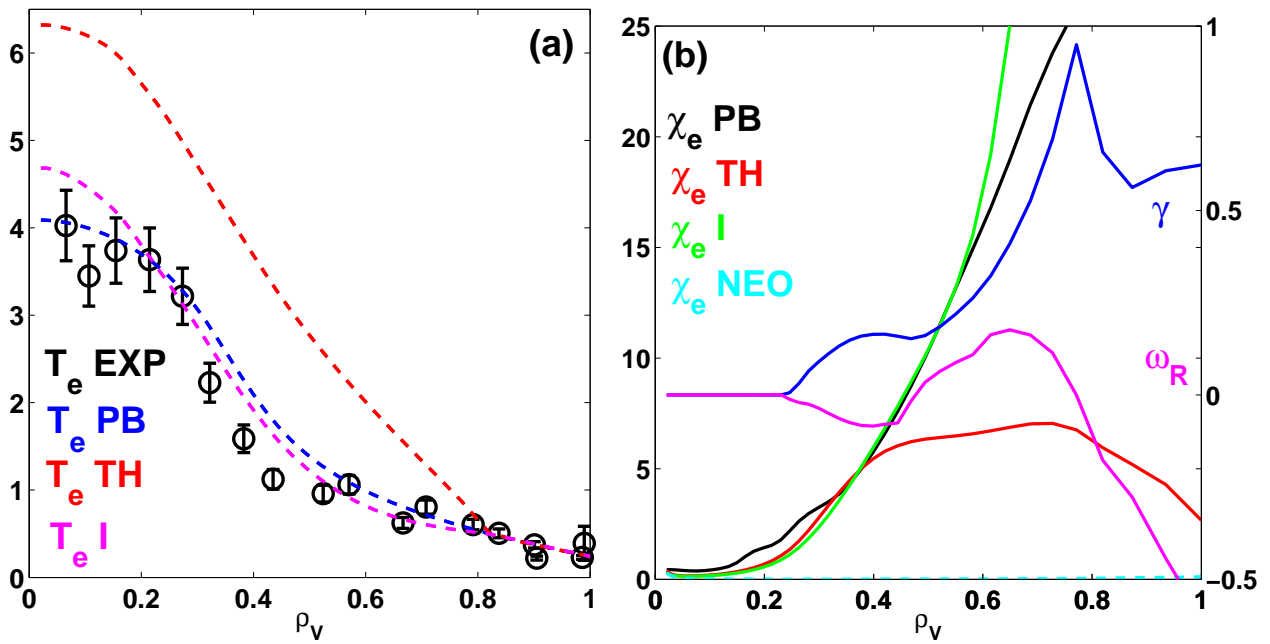


Figure 3.7: ECH discharge #24883 at $t = 1.8$ s [See caption of figure 3.1].

In figures 3.5, 3.6 and 3.7 we show the results as previously done for the Ohmic cases. Again we clearly see that the modified GLF23 model captures the main radial profile of the heat transport coefficient while the original GLF23 model underestimates the transport in the outer region, thus predicting larger stationary temperature gradients.

3.3.3 Remarks on the benchmark

From the simulations performed in the previous subsections some general remarks on the use of GLF23 in calculating the heat diffusivity, and on the results themselves, can be done. Already from the very first case shown in figure 3.1, but generally as seen in all the other cases, different regions can be identified in the plasma depending on the type of transport observed and the agreement between the model predictions and the experimental data. In particular, we can identify:

- (1) A central region, close to the magnetic axis, where $\chi_e \sim \chi_e^{\text{NEO}}$; however this region is eventually dominated by sawtooth-driven transport if the $q = 1$ surface is present;
- (2) A core region, $0.3 \lesssim \rho_V \lesssim 0.6$, where turbulence-driven transport (and, again, the eventually sawtooth-driven transport) becomes dominant over the neoclassical transport and the turbulence is sustained by toroidal instabilities like the ITG and/or the TEM. In this region the GLF23 model seems to give, depending on the case, reasonable agreement with the experimental data;
- (3) An outer region where turbulence-driven transport is the sole responsible for the observed flux, but the type of turbulence is not easily recognizable or identifiable, as the GLF23 model fails to reproduce the experimental flux, generally having the opposite trend/slope. However we have shown that the modified GLF23 model, i.e. where the explicit gyro-Bohm scaling has been eliminated, reproduces very well the coefficient χ_e in this region. This seems to suggest either that turbulence can still be imagined as dominated by toroidal instabilities but some (non-linear) mechanism is responsible for the disappearance of the gyro-Bohm scaling, which in turns indicate that the turbulence is more of a 'global' nature than a local one (remember that the GLF23 model is based on a local ballooning expansion as seen in subsection 2.3.3), or that the mixing-length estimate done in GLF23 does not work over the whole radial interval.

An interesting remark about the fact that a simple rescale, with $T_e^{3/2}$ of the GLF23 transport coefficient is in good agreement with the experimental diffusivity can be drawn in the view of the following studies on particle transport (chapter 5). As we will see, the steady-state density profile is determined by a balance of diffusion and convection in a way such that it is not important what 'absolute values' the diffusivity and the convection have. What only counts is the 'phase-shift', i.e. the phase relation between the fluctuations, which does not depend on the mixing-length formula nor on the 'normalization

scaling' such as the gyro-Bohm scaling appearing in local gyrokinetic theory. This means that, as soon as the modified GLF23 model we discussed before is in good agreement with experimental results, we can safely assume that gyrokinetic theory can be used to analyze particle transport in the plasma from the simulation boundary up to the core $\rho_V \sim 0.2$.

(4) The very edge region, $\rho_V \gtrsim 0.8$, where either experimental data are not available/reliable or the simulation becomes difficult. It has been chosen not to simulate this region anyway, since the boundary conditions as well as coupling to the SOL region become important as well.

3.4 Modeling TCV eITB plasmas

We now use the ASTRA-GLF23 system to simulate and try to understand the formation and sustainment of steady-state eITBs in the TCV fully non-inductive scenario. We first introduce the experimental data and the relevant quantities that are used for the following analysis, then we will present the simulations results.

3.4.1 Experimental dataset

In subsection 2.2.5 we have introduced the eITB scenarios that can be produced in TCV plasmas. We have discussed the global features of the fully non-inductive scenario, where a steady-state barrier is created by means of the reversal of the q profile which is beneficial in locally reducing transport around the q_{\min} surface [58]. We will discuss later on the theoretical interpretation of this phenomenon.

We have seen that fully non-inductive means that the current profile is sustained exclusively by the ECCD component and the bootstrap current driven by the strong core gradients of temperature and density. A small Ohmic perturbation is eventually added to test the barrier sensitivity to the current profile.

In this context we study three cases of fully non-inductive eITB with positive ('counter'-barrier), null and negative ('pro'-barrier) Ohmic perturbations added when the barrier is already formed.

Discharges #25957, #25956, #25953

These three eITB discharges are characterized by the same plasma parameters, except for the application of a V_{loop} perturbation that is co-current for #25957, null for #25956, and counter-current for #25953 (Ref. [24] for details).

The main physical quantities characterizing these three shots are evaluated during the steady-state eITB without perturbation, and near the 'foot' of the barrier:

$$I_p \approx 90 \text{ kA}, q_{95} \approx 12, \langle n_e \rangle_V \approx 1.1 \times 10^{19} \text{ m}^{-3}, Z_{\text{eff}} \sim 3.5, \nu_{\text{eff}}(\rho_V \approx 0.4) \sim 0.02, R/L_{\text{Te}} \approx 24, R/L_n \approx 10.$$

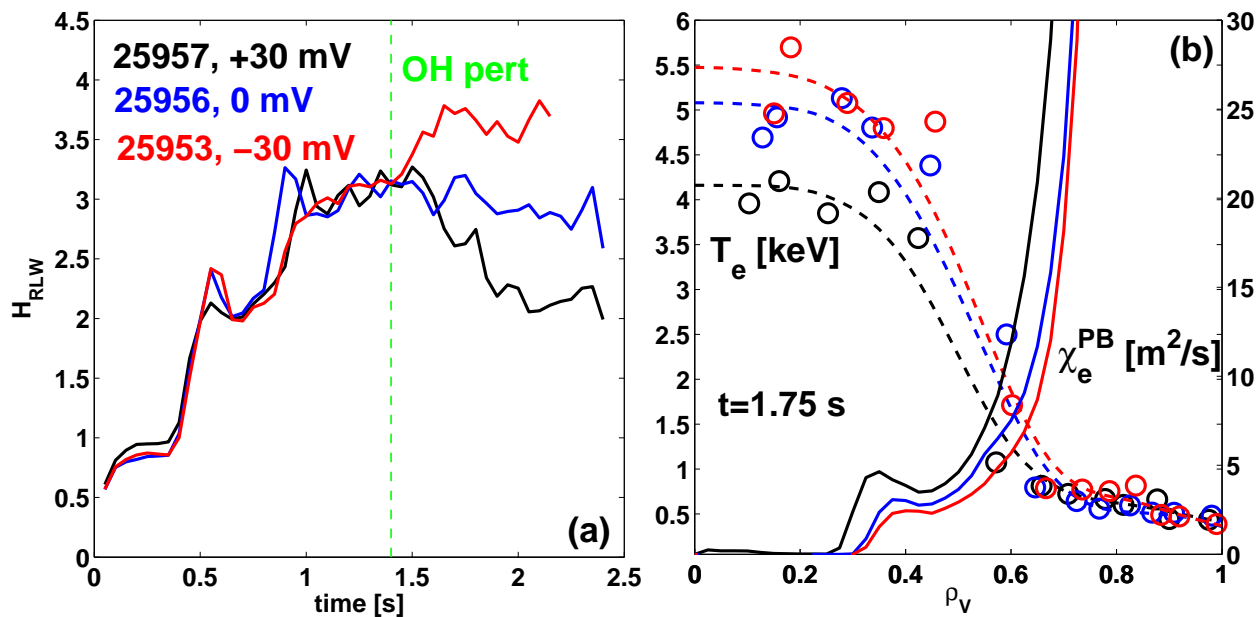


Figure 3.8: *a)* Evolution of the figure of merit H_{RLW} for three eITB plasmas where an Ohmic current perturbation is added at $t = 1.4$ s respectively of $\delta V_{loop} = +30$ mV (black), no perturbation (blue), and $\delta V_{loop} = -30$ mV (red); *b)* Comparison of the T_e profiles in keV at $t = 1.75$ s, after the barrier is eventually enhanced (red) or depressed (black) by the current perturbation. On the right axis we plot the power balance heat diffusivities χ_e^{PB} in m²/s at the same time step.

In figure 3.8(a) we show the time evolution of the H_{RLW} parameter, which represents a global figure of merit for the barrier performance with respect to the TCV L-mode scaling, for the three cases. At $t = 1.4$ s the Ohmic perturbation is applied resulting in either an enhancement of the barrier (counter-current perturbation of $\delta V_{loop} = -30$ mV, red curve) or a degradation of the core confinement (co-current perturbation of $\delta V_{loop} = +30$ mV, black curve). The blue curve without Ohmic perturbation is the reference case with a $H_{RLW} \approx 3$, typical value for many TCV eITBs.

The effect of the perturbation on the confinement is visible in figure 3.8(b) where we show the T_e profiles at $t = 1.75$ s together with the heat diffusivities obtained from power balance calculations. We note that the T_e profiles are identical in the outer region $\rho_V \gtrsim 0.6$, while the core values in the region $\rho_V \lesssim 0.4$ are higher for the red curve, intermediate for the blue curve, and lower for the black curve, indicating an important change in the local normalized gradient $\partial \log(T_e) / \partial \rho$ at constant power (the contribution of the perturbed Ohmic power is negligible). The last observation is confirmed by the behavior of the heat diffusivities plot on the right axis: at $\rho_V \approx 0.5$ the case with negative perturbation (red) has the lowest χ_e^{PB} , while the case with positive perturbation (black) has the highest value of χ_e^{PB} .

We will assess the understanding of this phenomenon in the next subsection.

3.4.2 Simulations of eITBs with ASTRA+GLF23-I

From the simulation results obtained in the previous section, we chose to simulate the eITB cases using only the modified GLF23-I model.

For the cases to be simulated, the experimental ion temperature profiles are not available. They will be modelled with formula (2.14), using a central value of $\left(\frac{T_e}{T_i}\right)_0$ such as to have a central $T_i \approx 0.6$ keV, consistent with many observations from ECH discharges with available CXRS measurements, and an edge value of $\left(\frac{T_e}{T_i}\right)_b = 1$. In any case the ion temperature profile (and the density profile) will be kept fixed during the simulation. The key mechanism that allows the sustainment of an eITB, as we have already discussed before, is the appearance of a q_{\min} surface with core reversal of the sign of the magnetic shear. In a recent paper [59] this experimental evidence has been connected to the influence of a negative magnetic shear and high values of the α parameter, representative of the pressure profile effect on the Shafranov-shift, on the turbulence properties. In particular, negative magnetic shear and high α values can reverse the precessional drift of trapped electrons causing a strong decrease in the TEM growth rate, hence its stabilization [60]. We remind that TEM-dominated turbulence is usually associated with the observation of a strong outward electron heat transport [61]. The GLF23 model should be able to catch this property of a reversed q profile scenario through its dependence on s and α on the magnetic curvature drift frequency as expressed in formula (2.28).

The simulations will be based on the reference case #29859 which is identical to discharge #25959 but for which the ECCD contribution for the steady-state unperturbed phase has been calculated with CQL3D. The perturbation δV_{loop} will be imposed *during* the simulation, instead of simulating three different discharges which is less precise with regard to the focusing on one specific parameter effect. To perform this V_{loop} scan in a precise way, we rather prefer to impose the total plasma current I_p as the boundary condition for the current profile and perform a scan in the total ECCD current I_{CD} . In this manner the total current is conserved and the resulting V_{loop} depends on I_{CD} through the relation $I_{\text{OH}} = I_p - I_{\text{CD}} - I_{\text{BS}}$.

Simulation results

In figure 3.9 we show the simulation results for the test case with the I_{CD} scan mentioned above. Figure 3.9(a) shows the steady-state T_e profiles from: experimental data (black circles with error bars), simulated from power balance χ_e^{PB} (dashed black), and simulated with the modified GLF23 model in colored solid lines, each one characterized by a defined ECCD fraction indicated in the plot in percentage of the total current. Each case is simulated up to steady-state conditions to ensure that the result is not just due to the temporal evolution of the temperature profile.

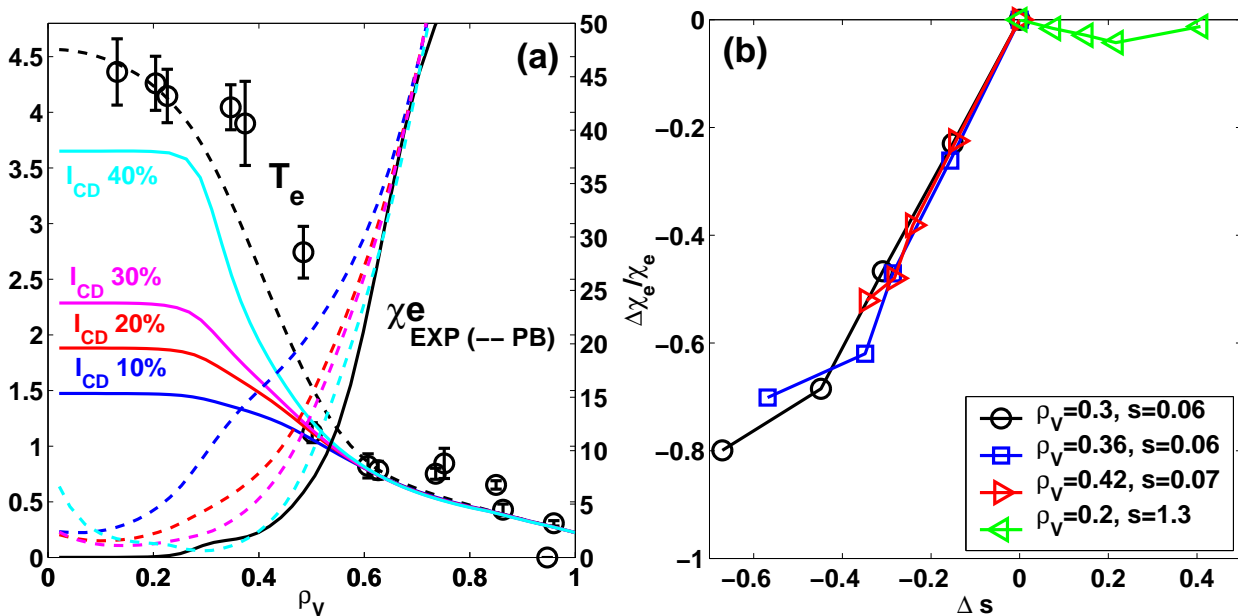


Figure 3.9: *a)* Steady-state T_e profiles in keV for the ASTRA-GLF23 simulation of *e*ITB discharge #29859, $t = 1.5$ s, using the modified GLF23 model, formula (3.2), where four different ECCD currents are used (show in percentage with respect to the total current). In black: experimental data with error bars and simulated with power balance χ_e^{PB} in m^2/s (dashed black). On the right y -axis: calculated χ_e^{I} (dashed colours) compared to χ_e^{PB} (solid black); *b)* Relative variation $\Delta\chi_e/\chi_e$ versus magnetic shear variation Δs for four different radial positions. Shown are also the values of magnetic shear s at the four radial positions for the case with $I_{\text{CD}} = 10\%$.

The simulated T_e becomes more accurate when increasing the I_{CD} fraction because the heat transport coefficient χ_e is reduced accordingly. However quantitative agreement is not robust as during the simulation, when I_{CD} fraction is 40%, the barrier undergoes unstable numerical oscillations due to the large current hole near the axis and the sensitivity of confinement to the local changes in the q profile.

In figure 3.9(b) we plot the relative variation $\Delta\chi_e/\chi_e$ obtained as the difference of each χ_e for each different I_{CD} content, divided by the initial χ_e , versus the magnetic shear variation Δs for different radial positions inside and outside the barrier. Each curve is obtained with points ordered with increasing I_{CD} fraction. Increasing I_{CD} content reduces the magnetic shear to negative values. We can clearly see that the heat transport coefficient follows almost linearly the decrease of magnetic shear, such that, for example at $\rho_V \sim 0.36$, there is a $\sim 60\%$ of reduction of the heat transport when magnetic shear is reduced by -0.3 down to negative values. The experimental evidence of confinement dependence on the local magnetic shear has been discussed extensively in Refs. [24, 58].

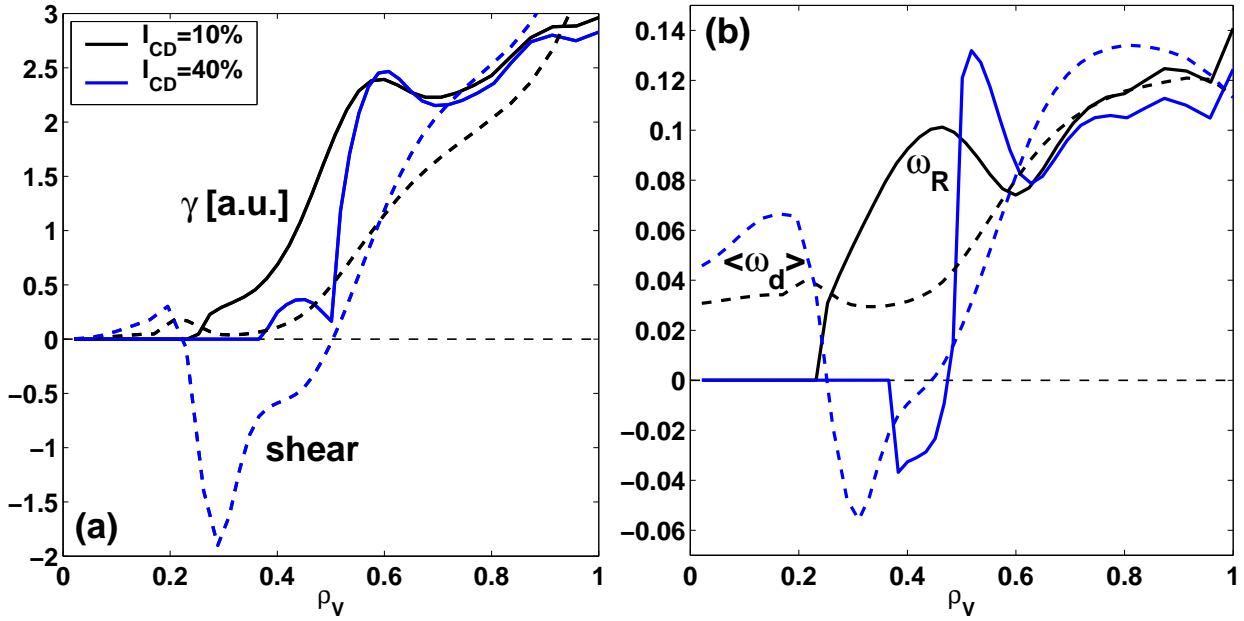


Figure 3.10: *a)* Radial profiles of the growth rate (in units of c_s/a) of the most unstable mode at $k_y \rho_i = 0.1$ (solid lines) and of the magnetic shear (dashed lines) for two values of the I_{CD} fraction; *b)* For the same mode, profiles of the real frequency ω_R (in units of c_s/a) (solid) and the average magnetic curvature drift frequency ω_d (in units of c_s/a) (dashed).

Role of the magnetic shear on TEMs

The physical mechanism behind the suppression of heat transport and the achievement of an improved confinement can be undisclosed looking at the behavior of the dominant microinstabilities as magnetic shear is decreased.

In figure 3.10(a) we plot the radial profile of the growth rate γ of the mode located at $k_y \rho_i = 0.1$ together with the magnetic shear for two values of the I_{CD} fraction. We see the correlation between the reversal of the magnetic shear which attains large negative values with the decrease of the growth rate of the mode, which is almost stabilized, in the region of negative shear $0.2 \lesssim \rho_V \lesssim 0.5$. In figure 3.10(b) we plot, for the same mode and the same values of I_{CD} fraction, the real frequency ω_R and the average magnetic curvature drift ω_d .

First note that for low I_{CD} content, i.e. for positive shear, the mode is a TEM (positive ω_R) all along the radial interval, and the average ω_d is positive. Going to higher I_{CD} content, and thus to negative magnetic shear, the TEM branch has now been stabilized (with a residual ITG in the interval $0.35 \lesssim \rho_V \lesssim 0.5$) due to the decrease (and even reversal in sign) of the average ω_d up to $\rho_V \sim 0.6$. This also means that in the eITB region transport is mainly due to modes residing in a wavenumber interval shifted to higher values of $k_y \rho_i$, thus producing a lower transport level.

We can identify the mechanism for confinement improvement in fully non-inductive eITBs

in the TEM stabilization due to a decrease in $\langle \omega_d \rangle$, caused by its almost linear dependence on magnetic shear and the Shafranov–shift parameter α . This mechanism has been discussed in detail and compared to results from a global code in Ref. [59].

3.5 Summary

In this Chapter we have shown the results of heat transport modelling for TCV plasmas in different scenarios using the GLF23 transport model coupled to the ASTRA transport code.

We have found that the GLF23 model predictions are in strong disagreement with the experimental results in the outer plasma region, where a decrease in the predicted heat transport coefficient found by the code, whereas the experimental coefficient increases. We have assessed the question of whether this could be related to the intrinsic gyro–Bohm scaling of the model, which provides a radial dependence on $T_e^{3/2}$, giving a lowering of χ_e in the outer plasma region, in contrast with the experimental radial trend. To correct this disagreement we have modified the GLF23 model replacing the local gyro–Bohm scaling with a ‘global’ scaling where the $T_e^{3/2}$ is now evaluated at one radial location and kept fixed on the whole interval. However the observed discrepancy might be as well related to the choice of the mixing–length rule in GLF23. The model is then used to simulate Ohmic L–mode scenarios, either with a current scan or with a ECH power deposition scan. In all the cases there is good agreement between the calculated T_e profile and the experimental one using the modified GLF23 model.

The eITB fully non–inductive scenario and its properties of improved core heat transport is introduced through a set of discharges where confinement is shown to be strongly dependent on the local value of the magnetic shear. To understand this behavior we have employed the modified GLF23 model coupled to ASTRA. A series of simulations have been performed at different values of the non–inductive current drive fraction. The results show that a better confinement is achieved when the off–axis co–CD content increases and thus the current profile becomes more hollow with a consequent decrease of magnetic shear towards more negative values. A fairly good agreement has been found between the calculated T_e and the experimental T_e for realistic values of I_{CD} , using the modified GLF23, although the ASTRA transport code starts to show numerical instabilities at that point due to the very low central current density. The reason behind the confinement improvement is the decrease of the heat transport coefficient with decreasing magnetic shear to negative values.

The basic mechanism is then elucidated tackling the behavior of the background microinstabilities which are shown to decrease in amplitude as shear is decreased to negative values. In particular, the TEM which is responsible for the high levels of electron heat

transport observed in standard L-modes, is strongly suppressed by negative magnetic shear through the decrease and/or reversal of the magnetic curvature drift frequency, decoupling trapped electron motion from the mode evolution.

Chapter 4

Particle transport in TCV eITBs: experimental results

4.1 Introduction

This Chapter shows the new results obtained during this Thesis work in particle transport for TCV eITBs, from the experimental point of view. We will present the behavior of the density profile in eITBs obtained with fully non-inductive current source or with partial inductive source, and even in the case of strong inductive source for the ICEC discharges described in subsection 2.2.5.

These results have been presented in Ref. [62, 22], and show that a peaked density profile with non negligible core gradient can be sustained despite the strong central electron heating delivered to maintain the barrier. This behavior is somewhat different than the behavior observed in Ohmic L-mode plasmas with ECH deposition, where the density profile is observed to decrease its logarithmic gradient with respect to the case without ECH [63].

The physical reason for this difference will be discussed in chapter 5, while here we will focus mainly on the experimental results for steady-state and transient particle transport observations.

4.2 Steady-state scenarios

We focus mainly on the fully non-inductive eITB scenario presented in subsection 2.2.5 and study the steady-state regimes.

4.2.1 Static database

To appreciate the steady-state properties of particle transport in TCV eITBs, we start from showing the behavior of the normalized electron density logarithmic gradient R/L_n

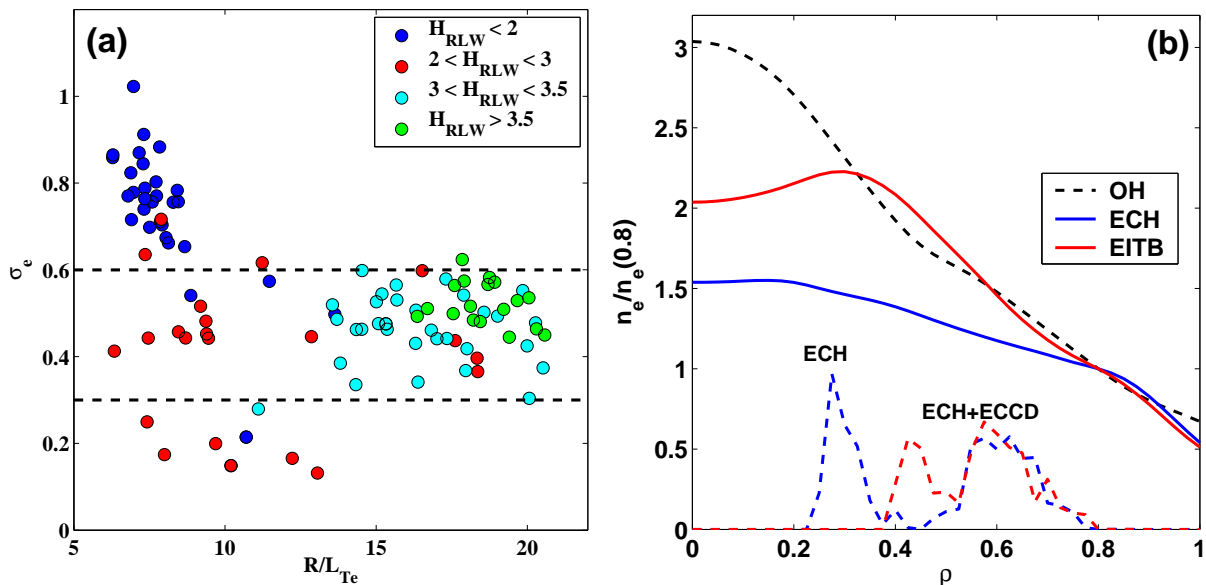


Figure 4.1: a) Steady-state database of normalized electron density to temperature logarithmic gradient ratio $\sigma_e = 1/\eta_e = L_{Te}/L_n$ versus R/L_{Te} for different value of the figure of merit H_{RLW} ; b) Comparison of density profiles normalized to the value at $\rho = 0.8$ for: Ohmic phase (black dashed), ECH without barrier (blue), and with an eITB (red).

for different discharges and different heating/current-drive schemes. To discriminate between standard L-modes and developed eITBs we use the figure of merit H_{RLW} .

About 200 time slices from steady-state conditions of 21 discharges have been taken into consideration using profile data obtained with the Thomson Scattering diagnostic, both for electron temperature and density profiles. Radially dependent quantities are averaged over the region $0.3 < \rho < 0.6$. For all the fully developed eITBs, the maximum of the electron temperature normalized gradient is located in this region. The parameter range covered in the database is: $I_p \sim 70 - 120$ kA, $P_{EC} = 0.9 - 2.3$ MW, $\rho_{EC} \sim 0.3 - 0.7$, $q_{95} \sim 8 - 17$ and $\langle n_e \rangle_V \sim 0.2 - 1.1 \cdot 10^{19} \text{ m}^{-3}$. In these plasmas the effective collisionality is low, i.e. $\nu_{eff} \sim 10^{-2}$, where $\nu_{eff} \equiv \nu_{ei}/(c_s/R)$, with ν_{ei} being the electron-ion collision frequency, c_s the ion sound velocity and R the average curvature radius of local flux surface. In figure 4.1(a) we show the quantity $\sigma_e = 1/\eta_e = L_{Te}/L_n$ versus R/L_{Te} for different values of H_{RLW} . While at low values of H_{RLW} and R/L_{Te} , typical of an Ohmic heated plasma, R/L_n and R/L_{Te} are essentially independent, at high values of H_{RLW} , the ratio of the two length scales, represented by σ_e , approaches a value around $\sigma_e \sim 0.35 - 0.5$, indicating a strong coupling of the density and the temperature profiles (a similar results has been found for FTU eITBs and reported in Ref. [64]). However, for moderate values of $R/L_{Te} \sim 10$ and without the formation of an eITB, i.e. when $H_{RLW} \lesssim 2.5$, the density profile can be flatter than in the ohmic phase as in that case $\sigma_e \sim 0.2$ (red points around $R/L_{Te} \sim 10$ for example). The flattening of the density profile with ECH is already a

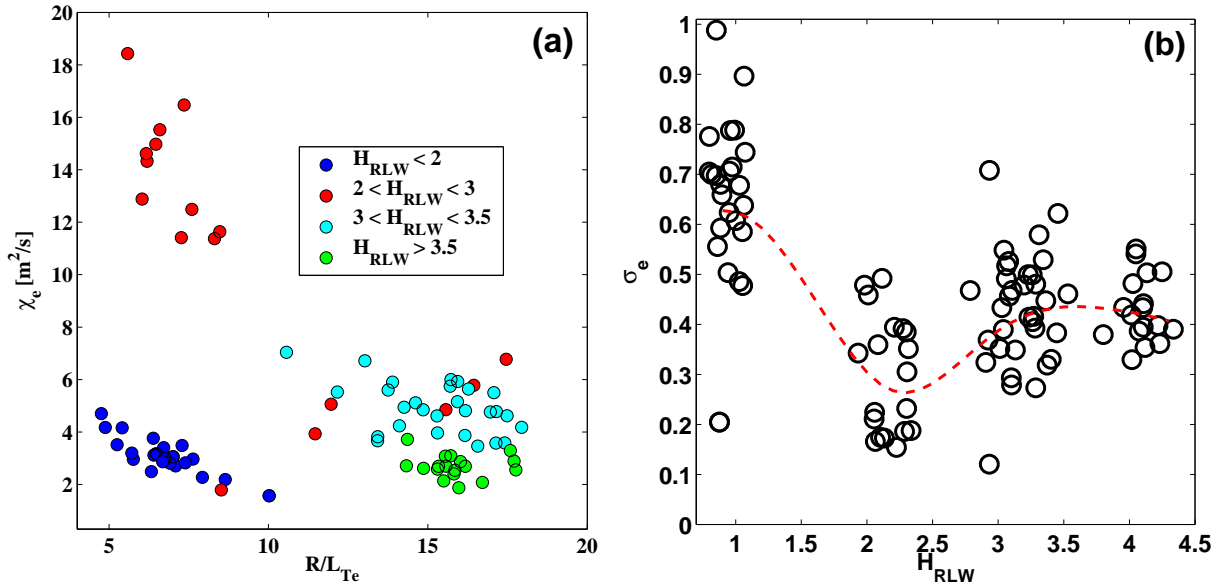


Figure 4.2: a) Power balance χ_e [m^2/s] versus R/L_{Te} for different H_{RLW} intervals (in the legend); b) σ_e versus H_{RLW} for the static database with a spline fit (dashed line).

well known result Ref. [63] and for TCV plasmas it is documented in Ref. [65]. However, the eITB scenario is completely different as in that case the density profile can present a local normalized gradient even larger than the one present in the Ohmic phase as shown in figure 4.1(b), where we plot three density profiles for:

- 1) the Ohmic phase (black dashed);
- 2) a ECH plasma without eITB (solid blue);
- 3) an eITB with the same ECH configuration as 2) but different current-driving scheme (solid red).

4.2.2 Confinement properties

In the previous subsection we showed that for improved confinement regimes with $H_{RLW} \gtrsim 3$ there is a correlation between R/L_n and R/L_{Te} such that the ration $\sigma_e = L_{Te}/L_n \sim 0.45$. Let us now look into more details at the confinement properties of the eITB scenario using the static database.

In figure 4.2(a) we plot the electron heat transport coefficient χ_e (in m^2/s) obtained from power balance versus R/L_{Te} for different intervals in H_{RLW} . The radial variables are averaged in the interval $0.5 < \rho_\psi < 0.65$. We see that the eITB scenario has the same χ_e as for the Ohmic heating scenario but with a doubling of the stationary R/L_{Te} , meaning a strong improvement in the local confinement. On the contrary, for ECH discharges without eITB, χ_e strongly increases at fixed R/L_{Te} , indicating a stiff behavior and a poor confinement, represented in the figure by the points with $\chi_e \sim 14$ and $R/L_{Te} \sim 7$.

In figure 4.2(b) we show again σ_e but now versus H_{RLW} for all the cases, together with a

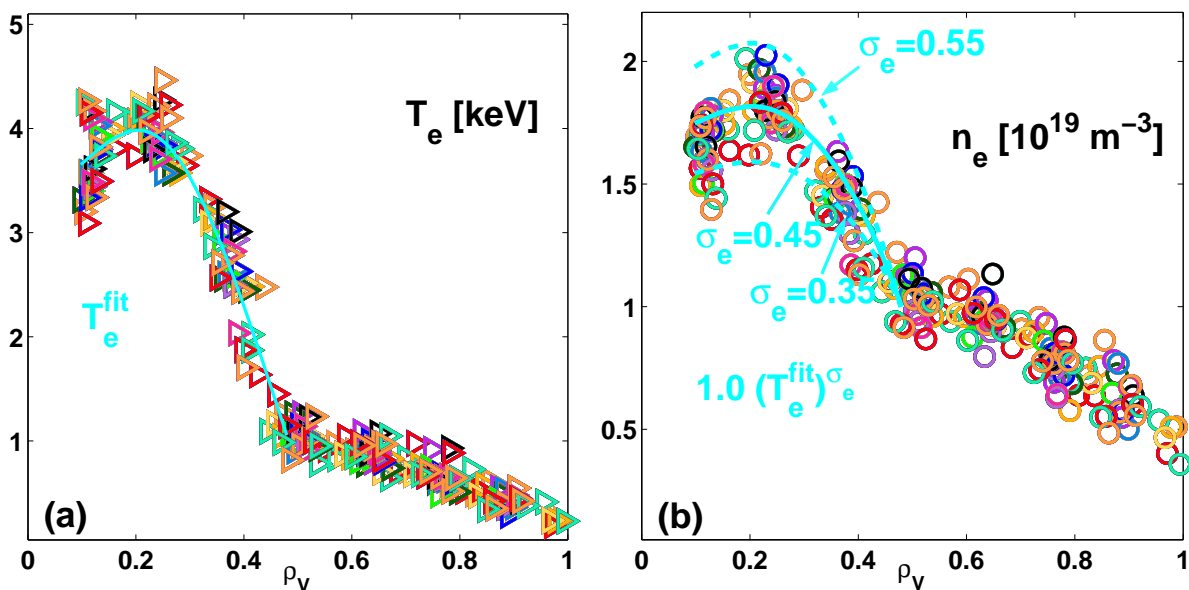


Figure 4.3: a) Temperature profile from Thomson Scattering diagnostic from discharge #29948 with fit (solid line) in the barrier region; b) Density profile together with fit proportional to $T_e^{\sigma_e}$ where the best fit is obtained with $\sigma_e = 0.45 \pm 0.1$.

spline fit (dashed line) to look at the main trend. We note that there is a strong profile flattening when moving from the Ohmic cases at $H_{RLW} \sim 1$ to the ECH cases without barrier at $H_{RLW} \sim 2 \div 2.5$, which have a high χ_e and the same R/L_{Te} . On the contrary, the barrier regime at $H_{RLW} \gtrsim 3$ has a strong density peaking provided by $\sigma_e \sim 0.45$ and a high R/L_{Te} , and this time χ_e is at low values.

We thus conclude that there is a correlation between the fact that confinement is improved in the eITB scenario and the appearance of a density barrier correlated with the temperature barrier with a ratio of $L_{Te}/L_n \sim 0.45$.

4.2.3 n_e barrier structure

To evidence the barrier structure and demonstrate the strong correlation between T_e and n_e we have used a particular experimental technique aimed at this goal. The plasma undergoes a slow vertical displacement (2.5 cm/0.7 s for $1.1 < t < 1.9$ s, which is slow compared with the time scale of all relevant plasma processes) to allow the Thomson Scattering diagnostic, which operates on fixed vertical points, to sample intermediate radii. The aiming of the EC launchers is modified to follow the vertical movement. In figure 4.3(a,b) we show all the points in the interval $1.1 < t < 1.9$ s for the T_e and n_e profiles. In figure 4.3(a) we plot the experimental T_e points versus ρ_V with a fit in the barrier region (solid line). In figure 4.3(b) we plot the n_e profile together with a fit proportional to $T_e^{\sigma_e}$. We see that in the barrier region the best fit is obtained with $\sigma_e \sim 0.45 \pm 0.1$ consistently with the results from the database shown in figure 4.1(a). The

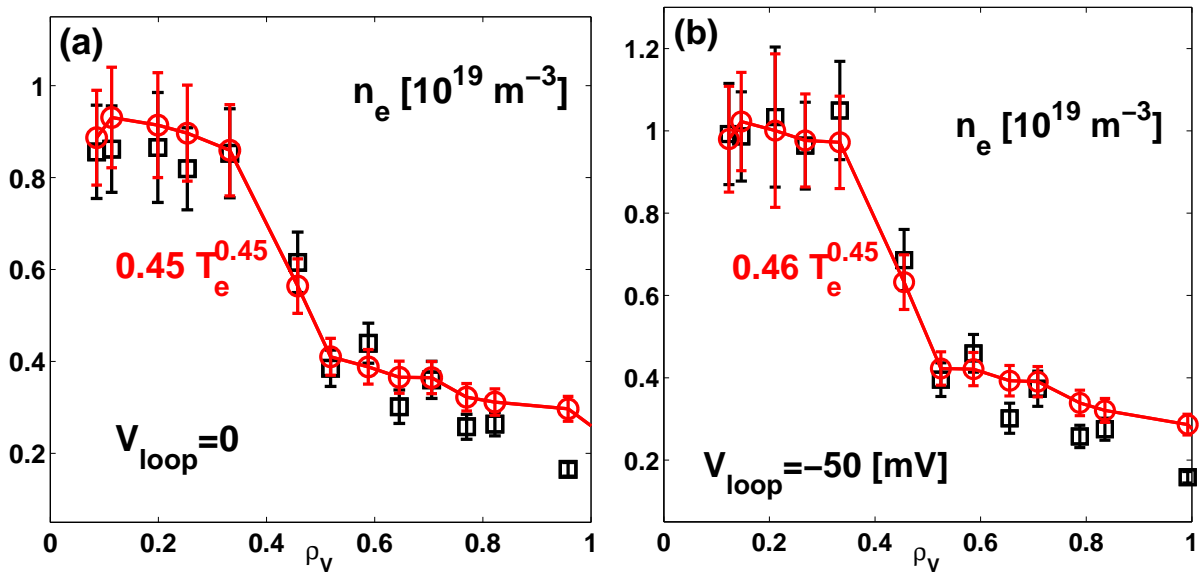


Figure 4.4: a) Experimental stationary n_e profile (black) with error bars for eITB discharge #25956 compared with the profile of $0.45T_e^{0.45}$ with error bars (red); b) The same for eITB discharge #25953 which has a small Ohmic current component.

rapid change in the density gradients inside and outside the foot of the barrier ($\rho_V \gtrsim 0.5$) is consistent with a rapid change in the local confinement properties. Outside the foot of the barrier, the density profile follows the usual properties of ECH L-mode plasmas.

4.2.4 Sensitivity to local current profile details

In subsection 4.2.1 we noted that the particular correlation between density and temperature length scales appears in the eITB regime, i.e. when local confinement is strongly improved. We now show that the relation between R/L_n and R/L_{T_e} given by $\sigma_e \approx 0.45$ is not sensitive on the local characteristics of the current profile, only requiring that the local confinement stays in the eITB regime. In figure 4.4(a) we plot the stationary density profile for fully non-inductive eITB discharge #25956 together with the profile of $\sim T_e^{0.45}$. The fit is in good agreement with the experimental profile in the barrier region between the foot ($\rho_V \sim 0.5$) and the top ($\rho_V \sim 0.3$). In figure 4.4(b) we compare now the density profile with the fit from the same function $\sim T_e^{0.45}$ for eITB discharge #25953 which has the same characteristics of discharge #25956 but with the addition of a small Ohmic current component of $V_{\text{loop}} = -50$ mV to enhance the core q profile reversal and have more negative magnetic shear. Again the fit with $\sigma_e = 0.45$ is in good agreement with the experimental profile in the barrier region, although the maximum of R/L_n has increased from ≈ 10 to ≈ 12 .

We already said that in TCV plasmas, this improvement of local confinement is obtained in fully non-inductive eITBs through q profile reversal and the creation of a core region

Discharge	Ohmic component [mV]
29863	+90
29859,29867	0
29866	-30
25957	+30
25956	0
25953	-30
29852	-60

Table 4.1: Ohmic current components.

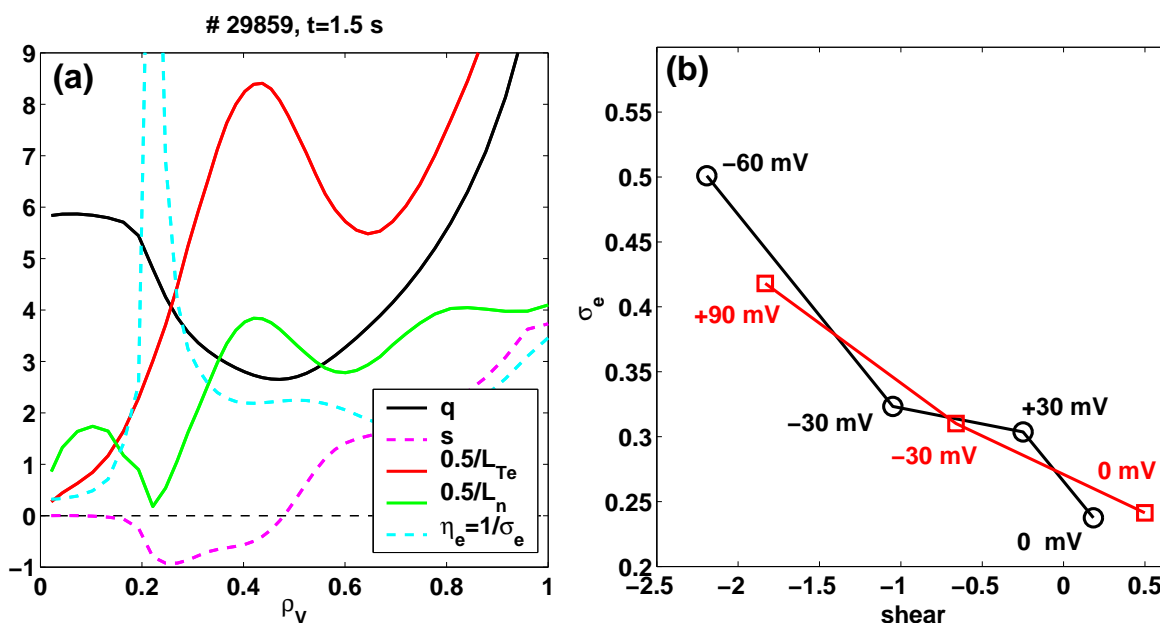


Figure 4.5: *a)* Simulation results for stationary eITB discharge #29859 at $t = 1.5$ s for q , s , L_{Te} , L_n , and $\eta_e = 1/\sigma_e$; *b)* σ_e versus shear for several discharges with similar heating and current drive but different Ohmic current components.

with $s \lesssim 0$. Unfortunately in TCV no direct measurement of q is possible and only transport simulations with equilibrium reconstruction allows to study the current properties of the eITB scenario.

In a recent work [66] a series of discharges, which have similar EC heating and current drive profiles, but different Ohmic residual components, have been simulated with ASTRA to retrieve the stationary current profile. Their Ohmic components are shown in table 4.1. Note that #29863 and #25957 have positive Ohmic components, resulting in a final monotonic q profile. Discharges #29859 – #25956 are two fully non-inductive eITBs, and #29866 – #25953 – #29852 are eITBs enhanced by a more negative magnetic shear driven by the negative Ohmic component.

In figure 4.5(a) we show the results of the simulation for fully non-inductive discharge

#29859. We plot the radial profiles of q , s , the two inverse length scales $1/L_{Te}$ and $1/L_n$, and of the parameter $\eta_e = 1/\sigma_e$. For the fully non-inductive barrier the q profile has a minimum of $q_{\min} \approx 2.7$ located at $\rho_V \sim 0.47$ and the ratio of the two length scales is $\sigma_e = L_{Te}/L_n \sim 0.45$ in the region where $s \lesssim 0$. We now compare, in figure 4.5(b), the value of σ_e for the whole dataset of table 4.1 around the position where $1/L_{Te}$ is maximum. We find that this value is decreasing with increasing magnetic shear, and it is minimal for the monotonic q profile cases. This is also consistent with the improved confinement with decreasing magnetic shear also shown in Ref. [66].

4.3 Transient analysis

No hints on the levels of diffusivity D and convection velocity V can come from the analysis of steady-state regimes as already seen from equation (2.12). In this perspective different experiments have been carried out to obtain transients or oscillations in the density profile inside the barrier and separately estimate the values of D and V [67, 68]. These experiments consist in either gas puffing from the edge and studying the resulting density evolution or performing ECH modulation to drive regular coupled temperature/density oscillations.

First it is useful to discuss the general methodology employed to evaluate diffusion and convection from the experimental profile evolution.

4.3.1 Non-harmonic transient analysis

The full electron particle continuity equation with explicit flux expression is given by:

$$\frac{\partial V_0' n_e}{\partial t} + \frac{\partial}{\partial \rho} V_0' \left(-g_2 D \frac{\partial n_e}{\partial \rho} + g_1 V n_e \right) = 0 \quad (4.1)$$

where V_0' is the flux surface enclosed volume radial derivative.

Because the density transients are usually quite fast and the time sampling of the Thomson Scattering diagnostic is not sufficient to obtain a meaningful result, we employ the SVD technique described in subsection 2.2.4 to reconstruct the density profile temporal evolution with sufficient time resolution.

After some algebra we arrive at these expressions:

$$\begin{aligned}
y(\rho, \delta t) &= A(\rho)x(\rho, \delta t) + B(\rho) \\
y &= \frac{1}{V_0'g_2n_e} \int_0^\rho \frac{\partial V_0'n_e}{\partial t} d\rho \\
A &= D \\
x &= \frac{\partial n_e}{n_e \partial \rho} \\
B &= -\frac{g_1}{g_2}V
\end{aligned} \tag{4.2}$$

where the assumptions that during the time interval δt over which the expression is valid the diffusivity and convection velocity and the magnetic equilibrium do not change. Formulas (4.2) allow to evaluate $D(\rho)$ and $V(\rho)$ for each δt chosen with a linear fit.

This is the case if the species under consideration is in very small concentration (trace species) like for example impurity traces in the bulk. However this is not true for electrons, for which D and V depend on the plasma parameters in a very complicated way. We thus expect this procedure to be valid for electrons only when the perturbation is very small compared to the equilibrium density, or if the perturbation itself does not change dramatically the mechanism that provides D and V . If the perturbation is too strong or if the plasma parameters that change strongly affect the physical mechanism behind D and V , then this procedure is not valid anymore. We will see in the different examples that this can happen.

A simplification of equations (4.2) occurs if, at steady-state and without source, i.e. when $\partial/\partial t \sim 0$, the relation $\partial \log n_e / \partial \rho^{\text{steady}} D - g_1/g_2 V = 0$ holds, i.e. if D and V do not change when going from before to after the perturbation, and the initial and final steady-state are the same. In this case we can rewrite the system (4.2) as:

$$\begin{aligned}
y(t) &= D [x(t) - x_0] \\
y &= \frac{1}{V_0'g_2n_e} \int_0^\rho \frac{\partial V_0'n_e}{\partial t} d\rho \\
x &= \frac{\partial n_e}{n_e \partial \rho} \\
x_0 &= \left[\frac{\partial n_e}{n_e \partial \rho} \right]_{\text{steady}}
\end{aligned} \tag{4.3}$$

Where now we evaluate a D that minimizes the error

$$\epsilon = \int_{\delta t} |y(t) - D [x(t) - x_0]| dt \tag{4.4}$$

over the interval δt during which the density evolves due to the perturbation. Then the convection velocity is evaluated simply as $V = x_0 D g_2 / g_1$.

4.3.2 Harmonic transient analysis

We want also to show a simplified method, although it will not be used in the following, that can be used if the density evolution follows a periodic pattern, for example if the profile undergoes quasi-sinusoidal oscillations. In this case it is possible to simplify the procedure shown above and obtain averaged estimates for the averages of D and V over the oscillations period.

Starting again from equation (4.1), we substitute the density with a simple harmonic function:

$$n_e(\rho, t) = n_0(\rho) + A(\rho) \cos(\omega t + \phi(\rho)) \quad (4.5)$$

where n_0 is the equilibrium density profile, A is the amplitude of the oscillatory perturbation, ω is the oscillation frequency (imposed), and ϕ the phase. In this equation the time enters only in the term ωt , while n_0 , A and ϕ are functions of the radial coordinate ρ .

We thus obtain the following linear system:

$$\begin{aligned} \mathbf{M}_{11}D(\rho) + \mathbf{M}_{12}V(\rho) &= \mathbf{N}_1 \\ \mathbf{M}_{21}D(\rho) + \mathbf{M}_{22}V(\rho) &= \mathbf{N}_2 \end{aligned} \quad (4.6)$$

where the matrix \mathbf{M} has the following elements:

$$\mathbf{M} = \begin{pmatrix} A' \cos \phi - A\phi' \sin \phi & -\frac{g_1}{g_2} A \cos \phi \\ -A' \sin \phi - A\phi' \cos \phi & \frac{g_1}{g_2} A \sin \phi \end{pmatrix} \quad (4.7)$$

and for \mathbf{N} :

$$\mathbf{N} = -\frac{\omega}{V'g_2} \begin{pmatrix} \int_0^\rho A \sin \phi V' d\rho \\ \int_0^\rho A \cos \phi V' d\rho \end{pmatrix} \quad (4.8)$$

Since A , ω and ϕ can be calculated fitting the experimental data with function (4.5), D and V can be evaluated by inversion of linear system (4.6). Note that, inserting expression (4.5) in equation (4.1), we obtain the additional condition $n'_0 D - g_1/g_2 n_0 V = 0$ which must be satisfied independently for consistency. As we said for the non-harmonic analysis, this method is valid until the perturbation does not change the plasma properties that affect D and V .

4.3.3 Experimental evaluation of D and V

We now employ the analysis method shown in subsection 4.3.1 to assess the levels of diffusion and convection present inside the eITB.

#32681: eITB with Ar gas puffing in deuterium plasma

The first case that we analyze is fully non-inductive eITB discharge #32681. In figure 4.6(a) we plot the experimental time traces of some quantities for this discharge.

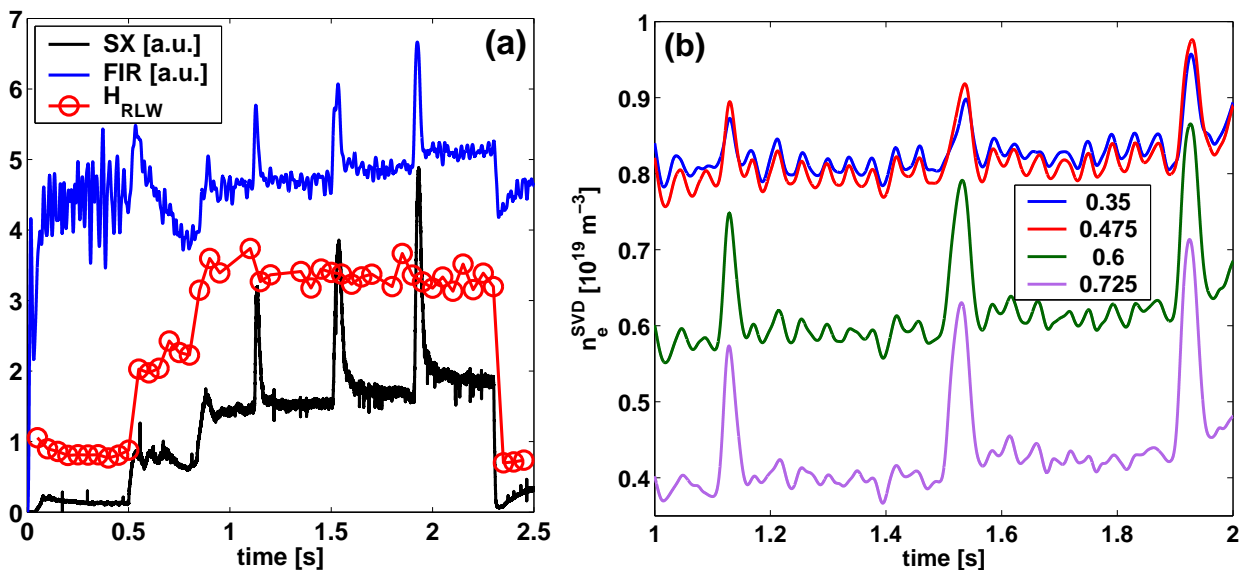


Figure 4.6: *a)* Experimental time traces for discharge #32681: X-ray signal (black), line integrated density (blue) and eITB figure of merit H_{RLW} (red circles); *b)* Time traces of electron density at different radial locations in ρ_ψ (in the legend) obtained with the SVD inversion technique. The traces are zoomed in the interval where the three Ar gas puffs are applied, respectively at $t = 1.1$ s, $t = 1.5$ s and $t = 1.9$ s.

From both the X-rays signal and the figure of merit H_{RLW} we see that an eITB appears at $t \sim 0.9$ s and stays up to the end of the EC phase at $t = 2.4$ s with a $H_{\text{RLW}} \sim 3$. During the eITB phase three edge argon gas puffs are applied at $t = 1.1$ s, $t = 1.5$ s and $t = 1.9$ s, resulting in strong perturbations of the electron (and deuterium for ambipolarity) density profile. To investigate the effects of the gas puff on the local characteristics of the density profile and to estimate the diffusivity and convection velocity we first perform an inversion of the FIR line integrated density signal with the SVD technique. The result for the evolution of the reconstructed density profile is shown in figure 4.6(b) for four radial positions. The plot is zoomed in the time interval $1 < t < 2$ s to show the clear effect of the three Ar gas puffs on the density.

We now concentrate on one of the Ar puffs to show the details of the density evolution. In figure 4.7(a) we show the time traces of the quantities $-x$ and y of system (4.2) together with the quantity $y - D(x - x_0)$ (called 'NL role' in the figure) from system (4.3) which gives an idea on the deviation of D and V from their respective steady-state values. All the quantities are evaluated at $\rho_\psi = 0.6$. First we note that during the evolution of the perturbation, the value of $-\partial \log n_e / \partial \rho$ decreases down to a minimum and then goes back to the equilibrium value, indicating an overall local flattening of the profile during the perturbation. On the other hand, the 'Flux' term $y = \frac{1}{V_0' g_2 n_e} \int_0^\rho \frac{\partial V_0' n_e}{\partial t} d\rho$ undergoes a complete oscillation between a positive maximum and a negative minimum. This means that relation $y = D(x - x_0)$ is valid only for the initial phase of the evolution where the

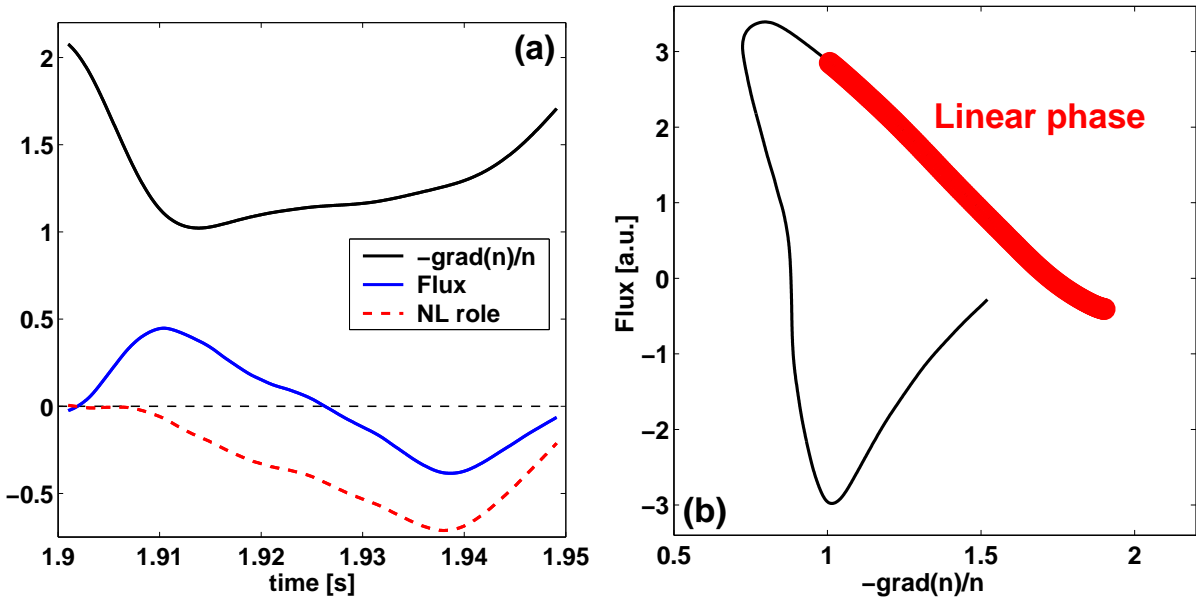


Figure 4.7: a) Time traces of $|x| = -\partial \log n_e / \partial \rho$ (' $-\text{grad}(n)/n$ ') and y ('Flux') of expression equation (4.3) for the gas puff at $t = 1.9$ s, evaluated at $\rho_\psi = 0.6$. Shown also is the differential error $\partial \epsilon / \partial t$ ('NL role') derived from equation (4.4); b) Contour of the 'Flux' term y versus $-\partial \log n_e / \partial \rho$ (' $-\text{grad}(n)/n$ ') for the same puff. Shown also is the linear phase where a diffusion coefficient can be evaluated.

flux and the gradient increase together through a proportionality factor (the diffusivity D). In later phases the system becomes non-linear and a simple positive-definite relation between flux and gradient can not be found. This is put in evidence in figure 4.7(b) where we plot the contour of the phase plot 'Flux' versus $\partial \log n_e / \partial \rho$ which clearly shows the strongly non-linear behavior of the system. However, a first linear phase can be identified (large red curve) where a diffusion coefficient D can be effectively calculated.

Tackling the linear phase for each puff we evaluate averaged $\langle D \rangle$ and $\langle V \rangle$ which we show in figure 4.8(a). We also compare the profiles for D against χ_e^{PB} and we note that we almost have $D/\chi_e \lesssim 0.25$ in the barrier region where $1/L_{\text{Te}}$ peaks. Note also the values of D in the barrier region ($\rho_\psi \sim 0.6$) which are of order $D \sim 0.45$ m²/s, while for the convection velocity we have an inward directed $V \sim -4$ m/s, giving an equivalent stationary R/L_n of $-RV/D \approx 8$.

We now compare the value of D found with this calculation with the diffusivity induced by neoclassical transport. In figure 4.8(b) we show the ratio D_{neo}/D for different values of Z_{eff} , where the other parameters, taken from the experimental data, are kept fixed. We clearly see that neoclassical transport is negligible, therefore suggesting that the eITB region is still dominated by turbulent transport although at lower levels than in the standard L-mode scenario with ECH heating.

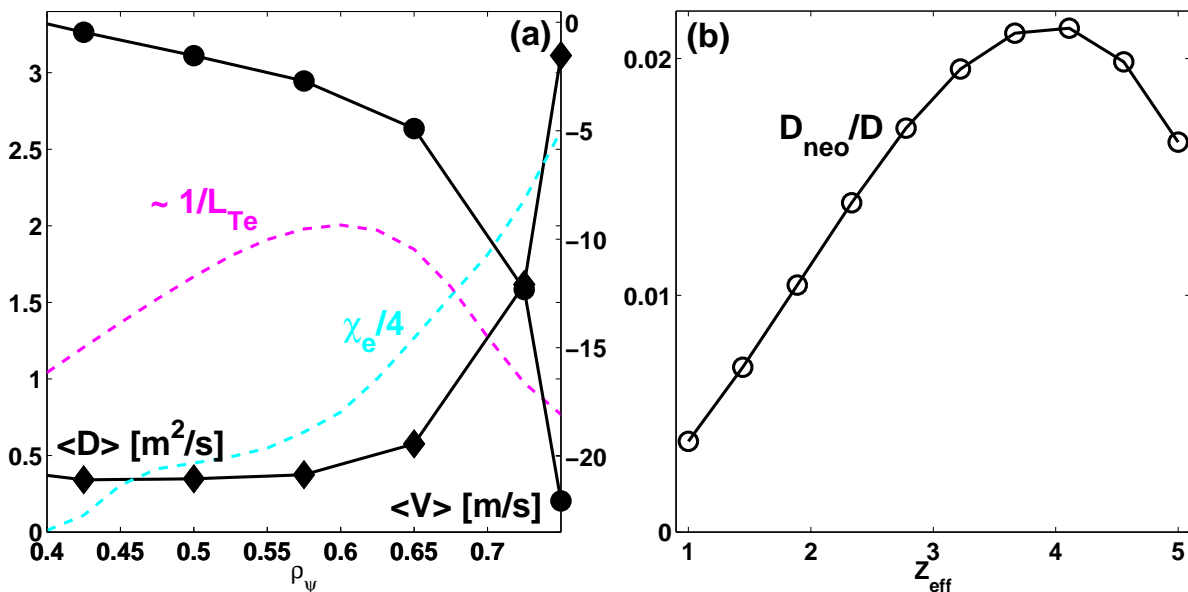


Figure 4.8: a) Calculated $\langle D \rangle$ (averaged over the three puffs, diamonds, left y-axis) and $\langle V \rangle$ (circles, right y-axis) versus ρ_ψ . Shown also are χ_e^{PB} scaled by 4 (cyan dashed, left y-axis) and the scaled inverse temperature length scale (magenta dashed, left y-axis); b) Ratio between the neoclassical diffusivity D_{neo} and the estimated diffusivity D at $\rho_\psi = 0.6$ as a function of Z_{eff} .

Comparison with an Ohmic case

The non-linear evolution of the flux versus the local gradient shown in figure 4.7(b) is not a general observation for TCV plasmas. In fact it depends on the strength of the perturbation and can be different in other cases with different modulation methods. For example for Ohmic L-mode discharge #26694, where the density perturbation is caused by small amplitude current modulation, the flux-gradient relationship is completely linear and can be represented with equation (4.1) with D and V constants in time. To show the difference between the eITB case shown previously and this L-mode Ohmic scenario we estimate D and V also for the latter.

Discharge #26694 has a total current $I_p \sim 110$ kA, line averaged $\langle n_e \rangle \sim 0.8$ [10^{19} m^{-3}], and central $T_e \sim 0.8$ keV. Current modulation is applied for a certain time interval resulting in a small perturbation of the density profile. In figure 4.9 we show the flux-gradient relationship for this Ohmic example for the radial position $\rho_\psi = 0.5$ where many oscillations have been taken into account. It is clear that a linear relationship appears and a diffusivity and a convection velocity can be estimated to be $D \sim 1.2$ [m^2/s] and $V \sim -8$ [m/s]. Note that the gradient excursion during the oscillations is $|\Delta(\partial \log n_e / \partial \rho)| \sim 0.4$, while in the eITB case of figure 4.7(b) it is $|\Delta(\partial \log n_e / \partial \rho)| \sim 1.25$, which also means that the oscillations in the Ohmic case would stay in the 'linear phase' of the eITB case. The full D and V profiles, obtained with the same technique for each radial point, are shown

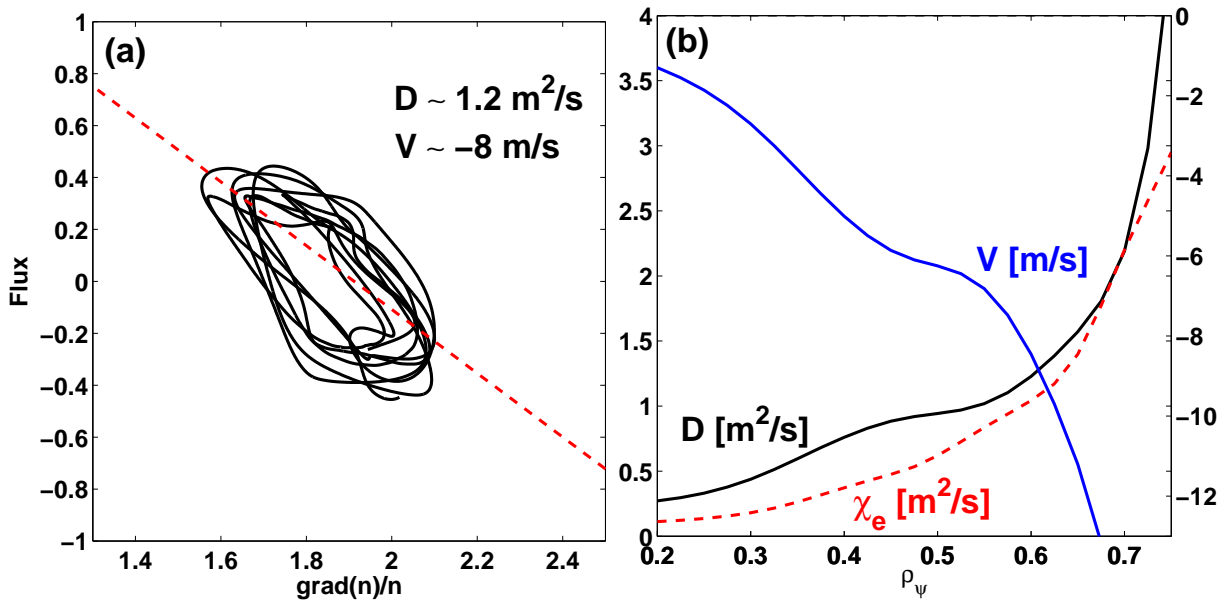


Figure 4.9: a) Relation between flux and density logarithmic gradient for #26694 during the density modulation phase at $\rho_\psi = 0.6$. The fit on the experimental data (dashed line) gives the estimation for $D \sim 1.2 \text{ [m}^2/\text{s]}$ and $V \sim -8 \text{ [m/s]}$; b) For the same discharge, estimated profiles of D (black) and V (blue), compared to the profile of χ_e (red dashed).

in figure 4.9(b), where we also compare the diffusion coefficient D with the heat transport coefficient χ_e , the two being of the same order, namely $D \sim \chi_e$ over the considered radial interval.

#33235: eITB with ECH modulation and MHD oscillations

We analyze another eITB discharge similar to #32681, where now the centrally injected ECH power is sinusoidally modulated with a frequency of 10 Hz. During the eITB phase MHD modes are also observed with frequency and amplitude oscillating during the ECH modulation period, and which continue after the modulation is stopped and the power is kept constant. We can look at the interplay of the two, the ECH modulation and the MHD oscillations, in figure 4.10(a), where we plot the time traces for the 'Flux' term and for $-\partial \log n_e / \partial \rho$, at $\rho_\psi = 0.6$, in a time interval that contains both the types of oscillations. The ECH modulation is applied between $1.4 < t < 1.8$ s, while a high-frequency MHD mode is already present before and intermittent weak high and strong low frequency modes are observed from $t = 1.4$ s without interruption up to the end of the eITB phase at $t = 2.4$ s. Note that the density logarithmic gradient oscillates from $t = 1.4$ s on with a slightly higher amplitude in the ECH+intermittent MHD phase, namely the ECH power modulation would provide a small perturbation while the MHD mode is the main responsible for the density oscillations and local deformations of the profile. The eITB is at its strongest point when $-\partial \log n_e / \partial \rho \sim 2.5$, where we observe a $H_{\text{RLW}} \sim 3.2$. To esti-

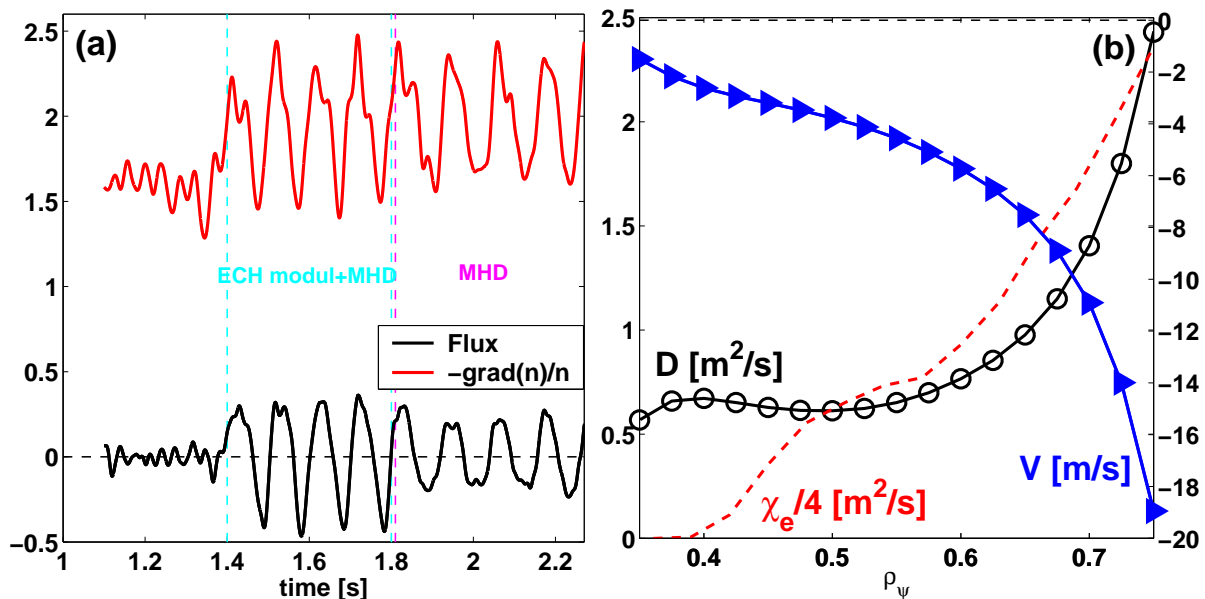


Figure 4.10: *a)* Time traces of the flux term and of the logarithmic density gradient at $\rho_\psi = 0.6$. We evidence the two phases, the first with simultaneous ECH modulation and MHD oscillations (cyan) and the second with only MHD oscillations (magenta); *b)* Radial profiles of estimated D (circles, left y -axis) and V (diamonds, right y -axis) evaluated for the ECH modulation phase when the MHD mode is absent. Shown also is the electrons heat transport coefficient χ_e scaled by 4 (dashed, left y -axis).

mate the eITB diffusivity without the spurious effect of the low frequency MHD mode we analyze the flux–gradient relationship only in the time intervals where the low frequency MHD signal is weak, i.e. when the gradient is restoring at large negative values but has not yet attained the minimum.

The resulting D and V are shown in figure 4.10(b) together with the electron heat transport coefficient χ_e . In the barrier region, $\rho_\psi \sim 0.6$, the values of the coefficients are $D \sim 0.6 \text{ m}^2/\text{s}$ and $V \sim -5 \text{ m/s}$, in agreement with the order of magnitudes found for the cases analyzed previously.

Relevance of neoclassical transport

From the results presented before we can argue that for the eITB, in the barrier region, neoclassical transport is negligible compared to turbulent transport, in particular near the maximum of the normalized gradients. Note that for this scenario no contribution from the Ware pinch is expected since $V_{\text{loop}} \approx 0$.

The estimated $D/D_{\text{neo}} \sim 50$ suggests that the observed correlation between n_e and T_e in the eITB is due to turbulence effects, which will be studied in details from the theoretical point of view in the next Chapter. However neoclassical transport might be important in the very core, near to the magnetic axis, i.e. from $\rho_V \sim 0.2$ inwards. It is also interesting

Discharge,type	χ_e [m ² /s]	D [m ² /s]	V [m/s]
26694, OH	≈ 1	≈ 1.2	≈ -8
32681, eITB	≈ 3	≈ 0.45	≈ -4
33235, eITB+modul	≈ 3.2	≈ 0.65	≈ -6

Table 4.2: Calculated χ_e , diffusion coefficient D , and convection velocity V for the three discharges analyzed in this Section, taken at $\rho_\psi = 0.6$.

to look at the heat and particle transport relationship through the $D - \chi_e$ relation which seems to provide $D \sim \chi_e$ for the Ohmic case and $D = a\chi_e$, with $a \sim 0.1 \div 0.25$, for the eITB case. From this last observation we can conclude that in the eITB scenario the particle diffusivity is reduced, as well as the energy diffusivity, to lower values, still much higher compared to the neoclassical values. In addition, it seems that in the eITB scenario the particle diffusivity is reduced by a higher factor, with respect to the Ohmic case, compared to the reduction of the heat transport diffusivity. However this last result needs more investigation and it should not be considered as a definitive statement on heat and particle transport relationship for these scenarios. To summarize the results we show the estimated values for χ_e , D and V for the three discharges analyzed before in table 4.2. Note that each coefficient is subjected to errors arising from the calculation of the density profiles and their gradients, thus they give more an indication of the order of magnitudes and not on the precise values.

4.4 Summary

In this Chapter we have presented novel results on particle transport characteristics observed during the fully non-inductive eITB scenario achieved in TCV, either in stationary or in transient regime.

The static database, i.e. the collection of profiles data during stationary phases, shows a peculiar correlation between the electron density and the electron temperature profiles for fully developed eITBs with high values of H_{RLW} . This correlation is such that, in the eITB region, the two normalized gradients are related by $R/L_n \sim 0.45R/L_{Te}$. In addition, the spatial structure of the density profile closely resembles that of the temperature profile, indicating the creation of a barrier in the particle transport channel. Through a fine spatial scan with the Thomson Scattering diagnostic we have confirmed the barrier structure on both T_e and n_e and the relation $n_e \sim T_e^{0.45}$ inside the barrier. The effect of this link between the temperature and density is to provide a peaked electron density profile despite the strong external ECH heating applied. This peaking can be even higher than the one observed in the Ohmic phase due to the large temperature gradients achieved in the eITB. There is an indication that this behavior is linked to the improvement of

local confinement through the reversal of the q profile and the appearance of a negative magnetic shear region. In fact it is shown that the ratio L_{Te}/L_n decreases with increasing magnetic shear in the presence of strong ECH heating, namely when the barrier is weakened.

The analysis of transient phenomena is then carried out to estimate the particle diffusivity and convection velocity for the eITB scenario. Two cases are taken into consideration: a stationary eITB perturbed by edge argon gas puffs, and a stationary eITB with central ECH power modulation. A standard Ohmic L-mode case is also considered to compare the result with the eITB scenario. In all the cases we find that, at mid-radius, the levels of energy and particle diffusivity are well above the neoclassical level, although in the eITB case the values themselves are lower than in the Ohmic case, indicating that turbulent transport is still the main source of both heat and particle transport inside the eITB. We also find that the linear flux-gradient relationship with constant diffusivity breaks down for strong plasma perturbations as observed in the case of edge gas puffing.

Chapter 5

Theoretical study of electron particle transport in TCV plasmas and eITBs

5.1 Introduction

In the previous Chapter we have discussed the novel experimental results obtained in TCV fully non-inductive eITB scenario in the framework of electron particle transport. These results have not been studied yet from the point of view of theoretical understanding and that is the topic that we want to assess here. In particular we search to clarify the physical mechanisms that provide the observed behavior and the striking differences between standard L-mode scenarios and the eITB scenario [69].

We start by presenting the general theoretical formulation of particle transport for the core of Tokamak plasmas to evidence the role of the different sources of transport and to justify the following assumptions and calculations. The gyrokinetic theory of particle transport is presented in detail and the transport coefficients for electrons will be calculated and discussed for several cases. The numerical evaluation of the stationary density gradient and of the pinch coefficients is performed with the GS2 code [40] presented in subsection 2.3.3. If not stated differently, the code will be employed in the electrostatic, linear version with $s - \alpha$ magnetic equilibrium and fully kinetic ions and electrons. The application of this model will first be the understanding of density peaking behavior observed in different Tokamaks in standard scenarios like L or H modes with/without auxiliary heating. Then, the interpretation of the eITB behavior will be presented.

5.2 Basic equations

Electron particle transport is regulated by the fundamental particle continuity equation, which we write for an axisymmetric system in the flux-surface averaged coordinate system assuming an equilibrium with circular flux surfaces, and defining $\rho = r/R$ where ρ is the minor radius measured on the equatorial plane and R is the local flux-surface magnetic

axis major radius:

$$\frac{1}{V'} \frac{\partial(V'n_e)}{\partial t} + \frac{1}{RV'} \frac{\partial}{\partial \rho} (V'\Gamma) = S_e \quad (5.1)$$

This equation allows to calculate the density profile n_e once the expression for the (electron particle) flux Γ is known. The flux Γ can be written as the sum of different physical processes:

$$\Gamma = \Gamma_{\text{neo}} + \Gamma_{\text{turb}} + \Gamma_{\text{MHD}} + \dots, \quad (5.2)$$

where Γ_{neo} is the flux described by neoclassical transport, Γ_{turb} the flux induced by microinstabilities and turbulence, Γ_{MHD} the flux provided by MHD phenomena like sawteeth or NTMs, and so on. The different physical mechanisms can also interact in a non-linear way, thus invalidating the expression of the flux as a linear sum of processes. However the issue of taking into account the highly complex interplay between, for example, a MHD island and the local micro-instabilities [70] it is outside the scope of this work. In the following we will thus neglect any interaction between different sources of transport and we will consider only the neoclassical and the turbulent terms in the flux, neglecting any other source.

5.2.1 Neoclassical particle flux

From neoclassical theory, the flux can be shown to be composed by two main contributions [3]: one is proportional to the neoclassical diffusivity and scales with the electron poloidal Larmor radius and collisionality, namely the diagonal and off-diagonal contributions arising from density and temperature gradients, the other is proportional to the toroidal electric field and scales with the plasma resistivity, namely the Ware pinch. Thus we write the neoclassical flux as:

$$\Gamma_{\text{neo}} = -D_{\text{neo}} n_e \frac{1}{R} \left(\frac{\partial \log n_e}{\partial \rho} + C_{\text{T}}^{\text{neo}} \frac{\partial \log T_e}{\partial \rho} + C_{\text{ni}}^{\text{neo}} \frac{\partial \log n_i}{\partial \rho} + C_{\text{Ti}}^{\text{neo}} \frac{\partial \log T_i}{\partial \rho} \right) + n_e W_p \quad (5.3)$$

where D_{neo} is the neoclassical diffusivity, $C_{\text{T}}^{\text{neo}}, C_{\text{Ti}}^{\text{neo}}$ the neoclassical thermodiffusion coefficients, $C_{\text{Ni}}^{\text{neo}}$ is another off-diagonal coefficients, and W_p is the Ware pinch [71]. The various quantities are available from analytical or numerical formulas or codes which can be run very fast. In this respect neoclassical transport can be seen as a well understood contribution.

In the following we will be using the formulas reported in Ref. [31]. In general it is seen that, at mid-radius, the electron neoclassical diffusivity is very low, of order $D_{\text{neo}} \sim 10^{-2}$ m²/s, while typical values of the estimated heat transport coefficients are ranging from $\chi_e \sim 0.1 \div 10$ m²/s, depending on the heating scheme and the confinement properties. In the previous Chapter we also showed that, for the eITB region, $D/D_{\text{neo}} \sim 10 \div 10^2$, allowing us to neglect the contribution of the term proportional to D_{neo} in equation (5.3).

The remaining term proportional to the Ware pinch, namely $W_p n_e$, is calculated with formulas provided by Ref. [31] and Ref. [30].

The Ware pinch itself can be shown to be given by

$$W_p = F(f_t, Z_{\text{eff}}, \nu_*) \frac{E_{\parallel}}{B_{\theta}} \propto -\frac{V_{\text{loop}}}{B_{\theta}} \quad (5.4)$$

where $F(f_t, Z_{\text{eff}}, \nu_*)$ is a function of the trapped particle fraction f_t , the effective charge Z_{eff} and the neoclassical collisionality ν_* . We expect the Ware pinch to play a role in the core region of inductive current driven plasmas, while for the fully non-inductive driven plasmas we expect $W_p \propto V_{\text{loop}} \approx 0$ and no effect from the neoclassical source.

5.2.2 Turbulent particle flux

As we showed in subsection 2.3.3, the turbulent flux is given by the correlation of the fields fluctuations, as from equation (2.36). We rewrite the turbulent particle flux definition as:

$$\Gamma_{\text{turb}} = \langle \tilde{n}_e \tilde{v}_{E \times B}^r \rangle \quad (5.5)$$

where \tilde{n}_e is the fluctuating density perturbation and $\tilde{v}_{E \times B}^r$ is the radial component of the fluctuating $\mathbf{E} \times \mathbf{B}$ velocity. As we will derive from first principles in Section 5.3, the turbulent particle flux can be written analogously to the neoclassical flux:

$$\Gamma_{\text{turb}} = -D_{\text{turb}} n_e \frac{1}{R} \frac{\partial \log n_e}{\partial \rho} + n_e V_{\text{turb}} \quad (5.6)$$

where D_{turb} is the turbulent particle diffusivity coefficient and V_{turb} is the turbulent particle convection velocity.

5.2.3 Stationary condition

We assume stationary conditions, i.e. $\partial/\partial t = 0$ and solve (5.1):

$$\Gamma = \frac{1}{V'} \int_0^{\rho} V' S_e R d\rho \quad (5.7)$$

The flux will be a function of the density and of its normalized gradient: $\Gamma = \Gamma(n_e, R/L_n)$. Thus equation (5.7) gives the self-consistent stationary density profile provided the proper boundary condition.

We shall ignore here every other mechanism but neoclassical transport and turbulent transport on which we focalize, thus equation (5.7) becomes:

$$\Gamma_{\text{neo}} + \Gamma_{\text{turb}} = \frac{1}{V'} \int_0^{\rho} V' S_e R d\rho \quad (5.8)$$

Substituting the expressions for Γ_{neo} and Γ_{turb} from equations (5.3) and (5.6) in equation (5.8) we can evaluate the stationary density logarithmic gradient as:

$$\left[-\frac{\partial \log n_e}{\partial \rho} \right]_{\text{stat}} = -\frac{RV_{\text{turb}}}{D} + \frac{D_{\text{neo}}}{D} C_{\text{T}}^{\text{neo}} \frac{\partial \log T_e}{\partial \rho} - \frac{RW_{\text{p}}}{D} + \frac{R}{n_e DV'} \int_0^\rho V' S_e R d\rho \quad (5.9)$$

where $D = D_{\text{neo}} + D_{\text{turb}}$.

We now make some assumptions to concentrate on the turbulence-induced part of the sustained density gradient, namely $-V_{\text{turb}}/D$:

- We neglect core particle sources imposing $S_e = 0$. This assumption is generally valid in the core of Tokamak plasmas except in the presence of NBI heating or pellet injection. However neither is present in TCV;
- We assume that neoclassical diffusivity is negligible with respect to turbulent diffusivity, i.e. $D_{\text{turb}} \gg D_{\text{neo}}$. This is a realistic assumption for electron transport in plasmas where core turbulence is not completely suppressed;
- We assume that $|V_{\text{turb}}| \gg |W_{\text{p}}|$, which is particularly true for cases where the loop voltage is small, for example for a high electron temperature plasma or for fully non-inductive discharges. However, in Ohmic plasmas at low temperature, the contribution from the Ware pinch can be important and should be taken into account. Since it is always directed inwards and it is not so sensitive on plasma parameters, it is possible to take it into account in a straightforward manner. For the eITB scenarios that we want to study, the assumption of negligible Ware pinch is valid due to the vanishing or very small edge loop voltage.

With these assumptions, equation (5.9) simplifies to:

$$\left[-\frac{\partial \log n_e}{\partial \rho} \right]_{\text{stat}} = -\frac{RV_{\text{turb}}}{D_{\text{turb}}} \quad (5.10)$$

This equation states that the stationary density profile is tailored by the existence of a turbulent convection mechanism. Note that when $V_{\text{turb}} < 0$ (inward convection) the profile has a negative slope and thus is peaked, while for $V_{\text{turb}} > 0$ (outward convection) the profile is hollow.

In the following we introduce the quantity $R/L_n = -\partial \log n_e / \partial \rho$. Then the steady-state condition equation (5.10) becomes:

$$\left[\frac{R}{L_n} \right]_{\text{stat}} = -\frac{RV_{\text{turb}}}{D_{\text{turb}}} \quad (5.11)$$

Now we show how the $V_{\text{turb}}/D_{\text{turb}}$ term appears from first principles in linear gyrokinetic theory and how it can be calculated.

Addition of the Ware pinch

The stationary condition 5.10, which takes into account turbulent transport only, can be used with the addition of the Ware pinch without too much complication. Taking

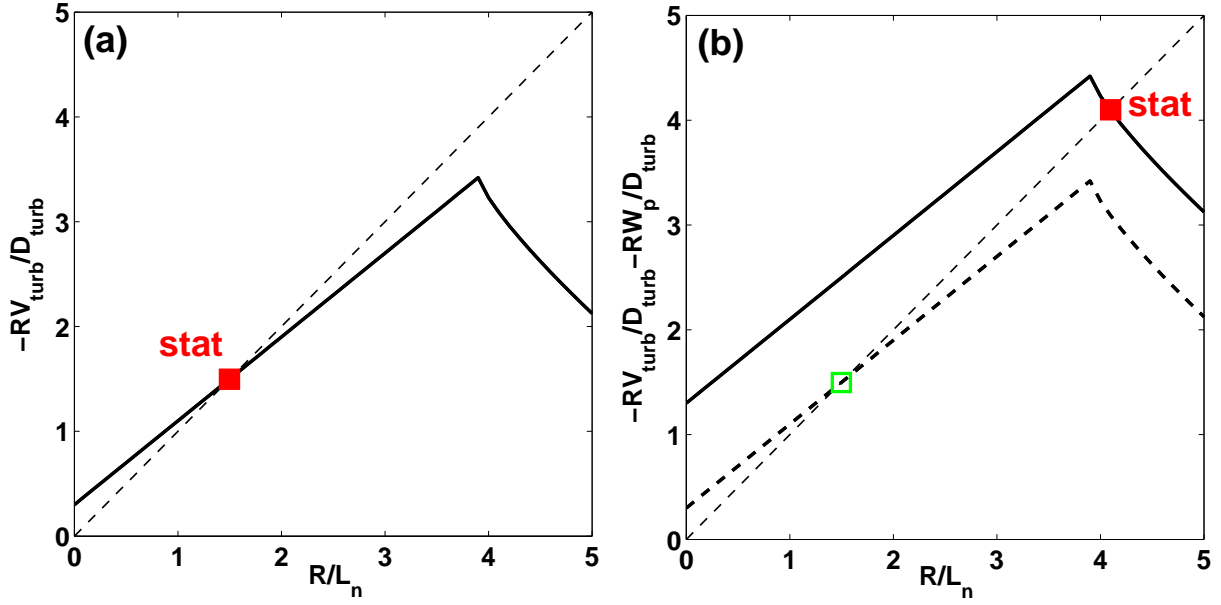


Figure 5.1: a) $-RV_{\text{turb}}/D_{\text{turb}}$ versus R/L_n (solid), the stationary point (full square) is obtained at the intersection of the y s with the diagonal; b) Same plot but with the addition of the Ware pinch term $-RW_p/D_{\text{turb}}$. The new stationary point is shifted upwards along the diagonal. The old stationary point is indicated by an empty square.

again formula (5.9), and assuming $D_{\text{neo}} \ll D_{\text{turb}}$, and no sources, we obtain ($R/L_n = -\partial \log n_e / \partial \rho$)

$$\left[\frac{R}{L_n} \right]_{\text{stat}} = -\frac{RV_{\text{turb}}}{D_{\text{turb}}} - \frac{RW_p}{D_{\text{turb}}} \quad (5.12)$$

which can be written

$$\left[\frac{R}{L_n} \right]_{\text{stat}} = \frac{R^{\text{turb}}}{L_n} - \frac{RW_p}{D_{\text{turb}}} \quad (5.13)$$

It is then possible to evaluate the first term of the right hand side with gyrokinetic theory as a function of R/L_n and then one can find the total stationary logarithmic gradient by numerically solving this equation where the Ware pinch contribution is inserted with an ad-hoc value for D_{turb} . This procedure is valid only if the newly calculated $\left[\frac{R}{L_n} \right]_{\text{stat}}$ does not modify the value of D_{turb} itself. This is equivalent to satisfy the condition $\Gamma_{\text{turb}} + W_p n_e = 0$ assuming that Γ_{turb} is a non-linear function of R/L_n with fixed D_{turb} and $V_{\text{turb}} = f(R/L_n)$, see formula (5.6).

We show an example of this procedure in figures 5.1(a,b). In figure 5.1(a) we plot an example of the function $-RV_{\text{turb}}/D_{\text{turb}}$ versus R/L_n . If there is no Ware pinch then the stationary condition 5.10 is satisfied at the intersection of this curve (solid) with the diagonal (dashed); the intersection is shown in the plot as a full square with 'stat'. In this case the value is $[R/L_n]_{\text{stat}} = 1.5$.

If we now add the Ware pinch, assuming $W_p = -1$ m/s and $D_{\text{turb}} = 1$ m²/s, the plot

is modified to the one shown in figure 5.1(b). The solid curve is the total function $-RV_{\text{turb}}/D_{\text{turb}} - RW_p/D_{\text{turb}}$ while the dashed curve is just $-RV_{\text{turb}}/D_{\text{turb}}$. The new intersection (full square with 'stat') is now located at $\left[\frac{R}{L_n}\right]_{\text{stat}} = 4.1$. In this case the new stationary state is not just the old plus 1 because of the non-trivial dependence of $V_{\text{turb}}/D_{\text{turb}}$ on R/L_n , which is typical of bulk species. Indeed, for a passive species (in very small concentration) pinch sources 'add-up' in a linear way as there is no influence of this species on turbulence itself. Note that the addition of the Ware pinch is straightforward when evaluating $V_{\text{turb}}/D_{\text{turb}}$ and not Γ_{turb} only. However, this requires at least two simulations for each case to evaluate the two constants of the relation $\Gamma_{\text{turb}} \propto A\partial\log n_e/\partial\rho + B$, where $RV_{\text{turb}}/D_{\text{turb}} = -B/A$.

In a similar way also core sources could be added to the model.

5.3 Linear gyrokinetic theory of particle transport

In subsection 2.3.3 we derived the normalized linear ballooning electrostatic gyrokinetic equation for a generic species in equation (2.27). We rewrite it here for sake of clarity, again without collisional operator:

$$\left(\frac{\partial}{\partial t} + v_{\parallel}\nabla_{\parallel} + i\omega_d\right)\tilde{g} = Z\tau F_0 \left(\frac{\partial}{\partial t} + i\omega_*\right) J_0\tilde{\Phi} \quad (5.14)$$

We introduce now the symbol L_H which stands for the linear operator of the homogenous part $L_H = \left(\frac{\partial}{\partial t} + v_{\parallel}\nabla_{\parallel} + i\omega_d\right)$, and we explicit the density and temperature gradients dependence of ω_* to rewrite equation (5.14) as:

$$L_H\tilde{g} = Z\tau F_0 \left[\frac{\partial}{\partial t} + i\frac{k_y\rho_i}{Z\tau}\frac{\partial\log n}{\partial\rho} + i\frac{k_y\rho_i}{Z\tau}\left(\frac{E}{E_{\text{th}}} - \frac{3}{2}\right)\frac{\partial\log T}{\partial\rho}\right] J_0\tilde{\Phi} \quad (5.15)$$

We formally define the inverse operator L_H^{-1} of L_H , such that the equality $L_H^{-1}(L_H\tilde{g}) = \tilde{g}$ is valid for every solution \tilde{g} . We then write the formal solution to equation (5.15) as:

$$\begin{aligned} \tilde{g} = & Z\tau F_0 L_H^{-1} \left(\frac{\partial}{\partial t} J_0\tilde{\Phi}\right) + ik_y\rho_i F_0 L_H^{-1} \left(J_0\tilde{\Phi}\right) \frac{\partial\log n}{\partial\rho} \\ & + ik_y\rho_i F_0 \left(\frac{E}{E_{\text{th}}} - \frac{3}{2}\right) L_H^{-1} \left(J_0\tilde{\Phi}\right) \frac{\partial\log T}{\partial\rho} \end{aligned} \quad (5.16)$$

The non-adiabatic part of the density fluctuation \tilde{n} is defined by the phase-space integral $\tilde{n}^{\text{non-adiab}} = \int J_0\tilde{g}d^3v$. The adiabatic part does not contribute to the turbulent flux Γ_{turb} , which can now be written substituting the expressions in formula (5.5):

$$\Gamma_{\text{turb}} = \Gamma_0 \sum_k \Re \left[ik_y\rho_i \tilde{\Phi}_k^* \int J_0\tilde{g}_k d^3v \right] = \Gamma_0 \sum_k \left[A_k \frac{\partial\log n}{\partial\rho} + B_k \frac{\partial\log T}{\partial\rho} + C_k \right] \quad (5.17)$$

where $\Gamma_0 = n_i v_{\text{th}} (\rho_i/R)^2$ is a dimensional factor, and the three constants A_k , B_k and C_k are defined as:

$$\begin{aligned} A_k &= -(k_y \rho_i)^2 \Im \left[i \tilde{\Phi}_k^* \int J_0 F_0 L_H^{-1} \left(J_0 \tilde{\Phi}_k \right) d^3 v \right] \\ B_k &= -(k_y \rho_i)^2 \Im \left[i \tilde{\Phi}_k^* \int J_0 F_0 \left(\frac{E}{E_{\text{th}}} - \frac{3}{2} \right) L_H^{-1} \left(J_0 \tilde{\Phi}_k \right) d^3 v \right] \\ C_k &= -Z \tau k_y \rho_i \Im \left[\tilde{\Phi}_k^* \int J_0 F_0 L_H^{-1} \left(\frac{\partial}{\partial t} J_0 \tilde{\Phi}_k \right) d^3 v \right] \end{aligned} \quad (5.18)$$

Comparing with formula (5.6), we can identify the two transport mechanisms driven by turbulence:

$$\begin{aligned} D_{\text{turb}} &= -\frac{R\Gamma_0}{n} \sum_k A_k \\ V_{\text{turb}} &= \frac{\Gamma_0}{n} \left(\sum_k B_k \frac{\partial \log T}{\partial \rho} + \sum_k C_k \right) \end{aligned} \quad (5.19)$$

where it can be shown that D_{turb} is positive definite, thus providing outward diffusion, whereas V_{turb} can be negative, i.e. inward directed, or positive, i.e. outward directed, depending on the details of turbulence. Note also that turbulent convection is composed of two separate mechanisms: thermodiffusion, which depends on diffusion in particle energy space and provides a pinch proportional to the temperature gradient [13, 72], and another pinch mechanism. We thus define the two pinch coefficients as:

$$\begin{aligned} C_{\text{T}} &= -\frac{\sum_k B_k}{\sum_k A_k} \\ C_{\text{P}} &= -\frac{\sum_k C_k}{\sum_k A_k} \end{aligned} \quad (5.20)$$

to rewrite turbulent convection as $V_{\text{turb}} = -D_{\text{turb}} \frac{1}{R} \left(C_{\text{T}} \frac{\partial \log T_e}{\partial \rho} - C_{\text{P}} \right)$. Looking back at the stationary condition expressed by equation (5.10), it can now be written:

$$\left[-\frac{\partial \log n_e}{\partial \rho} \right]_{\text{stat}} = C_{\text{T}} \frac{\partial \log T_e}{\partial \rho} - C_{\text{P}} \quad (5.21)$$

It is clear now that turbulence can effectively sustain a peaked density profile in absence of core sources and neoclassical transport due to the two mechanisms identified in thermodiffusion (C_{T}) and the other convection pinch term C_{P} . As we said for the convection velocity V_{turb} , C_{T} and C_{P} provide an inward directed pinch when they have negative values, and provide an outward directed pinch in the opposite case. These two coefficients are defined in terms of the solution of the gyrokinetic equation, which depends on the equilibrium profiles and their gradients. In this sense equation (5.21) is a non-linear

equation for the self-consistent value of the stationary $\partial \log n / \partial \rho$. One can solve numerically equation (5.21) performing a scan in $\partial \log n / \partial \rho$ and finding the value that satisfies equation (5.21), or alternatively the condition $\Gamma_{\text{turb}} = 0$.

The steady-state condition can be rewritten using R/L_n :

$$\left[\frac{R}{L_n} \right]_{\text{stat}} = -C_T \frac{R}{L_{\text{Te}}} - C_P \quad (5.22)$$

When searching for this condition, a scan in R/L_n is performed. Let us call the input parameter R/L_n^{In} . Formula (5.22) can be applied anyway to calculate a

$$\left[\frac{R}{L_n} \right]^{\text{Out}} = -C_T \frac{R}{L_{\text{Te}}} - C_P \quad (5.23)$$

where C_T and C_P are functions of R/L_n^{In} . The difference $R/L_n^{\text{Out}} - R/L_n^{\text{In}}$ is proportional to the particle flux, such that if $R/L_n^{\text{Out}} - R/L_n^{\text{In}} > 0$ there is a net inward flux, while if $R/L_n^{\text{Out}} - R/L_n^{\text{In}} < 0$ there is a net outward flux. The flux vanishes when $R/L_n^{\text{Out}} = R/L_n^{\text{In}}$. Note that this point is a stable solution if

$$\left[\frac{dX^{\text{Out}}}{dX^{\text{In}}} \right]_{\text{steady}} < 1 \quad (5.24)$$

where $X = R/L_n$. Namely, the local slope at the stationary point must not be higher than the 45° degrees diagonal.

In the linear model derived from equation (5.14) the perturbation $\tilde{\Phi}$, for unstable modes, has an exponential growth $\sim e^{\gamma t}$, such that the saturated state at equilibrium, in the non-linear regime, is not known. However from formulas (5.19), it is possible to see that C_T and C_P are products of ratios of transport fluxes, the saturation value for each single $\tilde{\Phi}$ is not needed, but their ratio is sufficient. Indeed, if only one single toroidal mode is chosen, then the two coefficients become independent on the value of $\tilde{\Phi}$.

5.3.1 Physics of the pinch coefficients

We now study in details the physics contained in the two pinch coefficients C_T and C_P making simplifying assumptions which do not undermine the possibility of understanding the basic mechanisms. As we said in the introduction, we focalize our attention on electron transport.

We split the phase space in the passing and trapped particle regions, introducing the geometrical trapped particle fraction $f_t(\rho) = \sqrt{1 - \frac{B_{\text{min}}(\rho)}{B_{\text{max}}(\rho)}}$. For trapped particles, we can assume a bounce averaged ($\langle \dots \rangle_b$) equation with no parallel component, i.e. $\langle k_{\parallel} v_{\parallel}^{\text{trap}} \rangle_b = 0$, such that phase space is reduced to the particle energy E . For passing particles we assume fast motion along the field lines, i.e. $|k_{\parallel} v_{\parallel}^{\text{pass}}| \gg |\partial/\partial t|, |\omega_d|$.

These two assumptions on the particles phase space, which strongly simplify the calculations, have the drawback of eliminating the possibility of studying the physics of the barely trapped particles, whose bounce averaged potential is not the same as the deeply trapped particles. In addition, they can experience Landau damping and be influenced by parallel dynamics. Note that this limitation is intrinsic to fluid models where a kinetic description can be approached but not reproduced genuinely. For example, an effort to take into account the influence of parallel dynamics on trapped particles in a fluid model has been done in the new TGLF model [73] which is an improvement of the GLF23 model. The derivative operator ∇_{\parallel} as well as every quantity that depends on θ is replaced with an averaged value obtained substituting $\theta \rightarrow \delta\theta$ where $\delta\theta$ is the characteristic extension of the mode along the field line ballooning coordinate. The time evolution operator $\partial/\partial t$ is replaced with its Fourier transform $-i\omega$ where $\omega = \omega_{\text{R}} + i\gamma$ is the mode complex frequency. With this simplifications, the linear operator L_H becomes an algebraic operator. We focus on one single toroidal mode $k_y \rho_i$ for simplicity. After some straightforward algebra the two pinch coefficients C_{T} and C_{P} can be analytically reduced to these expressions:

$$\begin{aligned}
 C_{\text{T}} &= \frac{f_t \left[\int_0^{+\infty} dE \left(\sqrt{E} e^{-E} \frac{\gamma(E-3/2)}{\gamma^2 + (\omega_{\text{R}} - \omega_{\text{d0}} \frac{E}{2})^2} \right) \right] + \frac{(1-f_t)}{4} \frac{1}{Mk_{\parallel}}}{f_t \left[\int_0^{+\infty} dE \left(\sqrt{E} e^{-E} \frac{\gamma}{\gamma^2 + (\omega_{\text{R}} - \omega_{\text{d0}} \frac{E}{2})^2} \right) \right] - \frac{(1-f_t)}{2} \frac{1}{Mk_{\parallel}}} \\
 C_{\text{P}} &= -\tau \frac{\omega_{\text{d0}}}{k_y \rho_i} \frac{f_t \left[\int_0^{+\infty} dE \left(\frac{E}{2} \sqrt{E} e^{-E} \frac{\gamma}{\gamma^2 + (\omega_{\text{R}} - \omega_{\text{d0}} \frac{E}{2})^2} \right) \right] - \frac{(1-f_t)\omega_{\text{R}}}{\pi M k_{\parallel}}}{f_t \left[\int_0^{+\infty} dE \left(\sqrt{E} e^{-E} \frac{\gamma}{\gamma^2 + (\omega_{\text{R}} - \omega_{\text{d0}} \frac{E}{2})^2} \right) \right] - \frac{(1-f_t)\omega_{\text{d0}}}{\pi M k_{\parallel}}} \quad (5.25)
 \end{aligned}$$

where the quantity $M = \sqrt{\tau(m_i)/(m_e)} \sim 60$ for $\tau = T_i/T_e = 1$. We now study different details of the physics contained in these two expressions.

Pure passing electron pinch at $f_t = 0$

If we assume only passing electrons, which can be the case for pure ETG turbulence, formulas (5.25) reduce to:

$$\begin{aligned}
 C_{\text{T}} &= -\frac{1}{2} \\
 C_{\text{P}} &= -\tau \frac{\omega_{\text{R}}}{k_y \rho_i} \quad (5.26)
 \end{aligned}$$

Namely: thermodiffusion (C_{T}) provides an inward directed pinch that correlates density and temperature with the simple relation $n_e \propto T_e^{1/2}$ [13]. Note that incidentally this value 1/2 is found in another model [17] and it also seems to fit the data of edge profiles from H-modes in ASDEX Upgrade [75]. The other pinch contribution C_{P} is proportional to the mode real frequency, i.e. it provides an inward directed pinch for TEM dominated turbulence (see table 2.2) and an outward directed pinch for ITG dominated turbulence;

its role is decreased if $\tau = T_i/T_e \ll 1$, for example for strongly EC heated discharges where $T_e \gg T_i$. The pure passing electron pinch C_P is analogous to the impurity pinch driven by parallel dynamics found in Ref. [74].

Pure trapped electron pinch at $f_t = 1$

In the opposite extreme, namely when there are no passing electrons, C_T and C_P are given by:

$$\begin{aligned}
 C_T &= \frac{\int_0^{+\infty} dE \sqrt{E} e^{-E} \frac{\gamma(E-3/2)}{\gamma^2 + (\omega_R - \omega_{d0} \frac{E}{2})^2}}{\int_0^{+\infty} dE \sqrt{E} e^{-E} \frac{\gamma}{\gamma^2 + (\omega_R - \omega_{d0} \frac{E}{2})^2}} \\
 C_P &= -\tau \frac{\omega_{d0}}{k_y \rho_i} \frac{\int_0^{+\infty} dE \frac{E}{2} \sqrt{E} e^{-E} \frac{\gamma}{\gamma^2 + (\omega_R - \omega_{d0} \frac{E}{2})^2}}{\int_0^{+\infty} dE \sqrt{E} e^{-E} \frac{\gamma}{\gamma^2 + (\omega_R - \omega_{d0} \frac{E}{2})^2}} \quad (5.27)
 \end{aligned}$$

In this case, both coefficients are derived from energy phase space integrals with fundamentally different kernels. For C_T , the kernel is proportional to $E - 3/2$, which means that the sign of C_T can change depending on the resonant denominator, i.e. depending on the value of ω_R . For C_P the kernel is positive definite, which means C_P is always inward directed when the average ω_{d0} is positive, which is the case for standard monotonic q profile scenarios.

We evaluate numerically the two coefficients to show the strong dependence on the mode real frequency ω_R . In figure 5.2 we show the plots of C_T and C_P to evidence their strong dependence on the mode real frequency ω_R and their behavior versus the type of mode. The fixed parameters are $\tau = 1$, $k_y \rho_i = 0.12$, $\omega_{d0} = 0.3$. In figure 5.2(a) we see that C_T is inward directed in ITG turbulence and attains its minimum value (read: maximum inward pinch) at $\omega_R \sim 0$, where ITG and TEM coexist at similar growth rates. In TEM turbulence C_T becomes smaller in absolute value and can change sign, i.e. change direction from inwards to outwards, with increasing ω_R in the TEM regime. There is also a dependence on the mode growth rate γ , showing that if the mode becomes less unstable the inward pinch is increased. The behavior of C_P is shown in figure 5.2(b), where we see that, as expected, it is always inward directed. It provides a stronger pinch in TEM dominated turbulence. Note that, from formula (5.21), C_T enters in the stationary profile together with $\partial \log T_e / \partial \rho$, which means that at large values of the temperature logarithmic gradient the contribution from C_P can become negligible. Note also that the curvature drift ω_d enters in both the coefficients. In particular one sees that increasing the average ω_{d0} , the two pinch coefficients are increased in absolute value in an almost linear proportionality. This means that, through the shear dependence of ω_d , see formula (2.26), we could expect a proportionality between the magnetic shear and the stationary density logarithmic gradient.

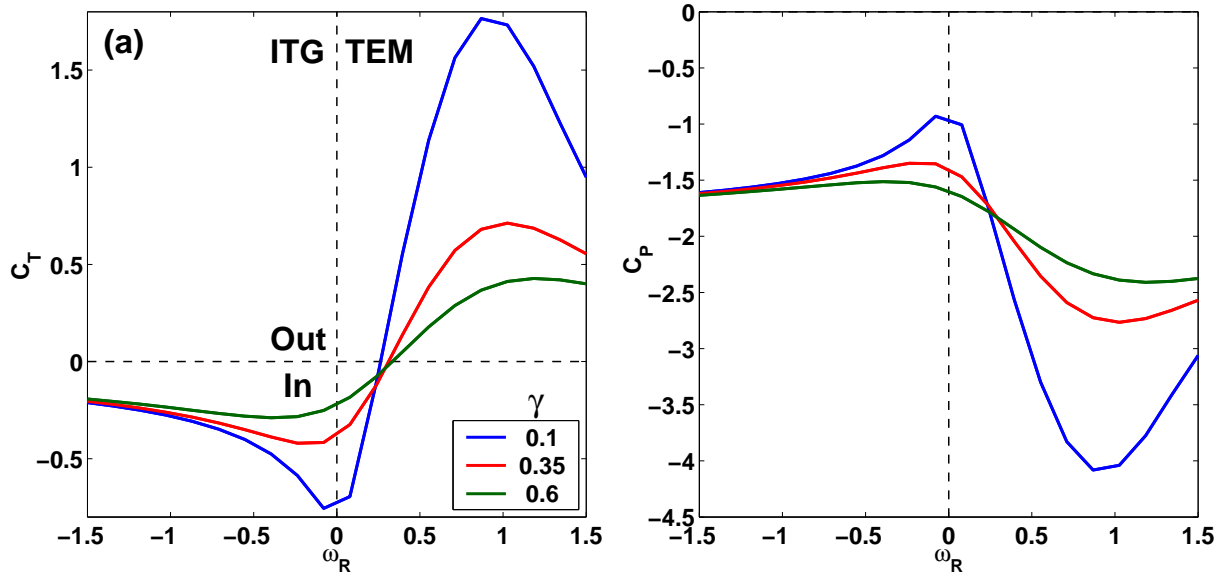


Figure 5.2: a) Thermodiffusion coefficient C_T for the pure trapped electrons case plotted versus the mode real frequency ω_R and for three values of the growth rate γ ; b) Same plot for the other pinch contribution C_P .

General situation for $0 < f_t < 1$

In the core of Tokamak plasmas, both passing and trapped electrons exist due to the poloidal angle dependence of the magnetic field on a fixed flux surface. For the general case, the pinch will be carried by both kind of particles in different proportions. Due to the fast motion of passing electrons along field lines, we can expect their pinch to be small compared to the trapped electrons pinch for cases with weak non-adiabaticity of passing electrons. This is visible in formulas (5.25) where we see that the passing electrons contribution, proportional to $1 - f_t$ scales with $|\omega/(Mk_{\parallel})|$ compared to the trapped electrons contribution. The value of M for deuterium plasmas is ~ 60 . However the role of passing electrons can become important either if k_{\parallel} is strongly decreased, for example if the magnetic shear approaches zero, or if the scaling $|\omega/(Mk_{\parallel})| \ll 1$ breaks down, for example in the presence of collisions [76].

5.3.2 Choice of the quasi-linear rule

It is evident from formulas (5.18) that one can extract the saturation value $|\tilde{\Phi}_k(0)|^2$ from $\tilde{\Phi}_k$ to rewrite the coefficients as, for example, $A_k = |\tilde{\Phi}_k(0)|^2 \alpha_k$ where α_k contains terms of the type $\tilde{\Phi}_k(\theta)/|\tilde{\Phi}_k(0)|$. The coefficient α_k is thus well defined in the linear stage, and

the values of $|\tilde{\Phi}_k(0)|^2$ can be extracted to rewrite the pinch coefficients as:

$$\begin{aligned} C_T &= -\frac{\sum_k |\tilde{\Phi}_k(0)|^2 \beta_k}{\sum_k |\tilde{\Phi}_k(0)|^2 \alpha_k} \\ C_P &= -\frac{\sum_k |\tilde{\Phi}_k(0)|^2 \gamma_k}{\sum_k |\tilde{\Phi}_k(0)|^2 \alpha_k} \end{aligned} \quad (5.28)$$

where β_k and γ_k are the $|\tilde{\Phi}_k(0)|^2$ -normalized B_k and C_k respectively. The linear model provides the values for α_k , β_k and γ_k , while the $|\tilde{\Phi}_k(0)|^2$ have to be given *a posteriori* with ad-hoc expressions. In this context, different *quasi-linear* rules, i.e. the choice of $|\tilde{\Phi}_k(0)|^2$, can be used. For a rule to be more or less adherent to the real turbulent state, it has to be compared to the result from non-linear simulations.

In the following we will adopt the rule proposed in Ref. [54]: we choose to retain only the mode that has the highest value of $\gamma / \langle k_\perp^2 \rangle$, which corresponds to choosing $|\tilde{\Phi}_k(0)|^2$ as a delta function located at the $k_y \rho_i$ with the highest value of $\gamma / \langle k_\perp^2 \rangle$. Other rules could be adopted, for example as the rule used in GLF23 and shown in equation (2.37), or the rule proposed in Ref. [77] which prescribes $|\tilde{\Phi}_k(0)|^2 \propto e^{4k_y \rho_i - 8(k_y \rho_i)_{\max}}$ for $k_y \rho_i < (k_y \rho_i)_{\max}$ and $|\tilde{\Phi}_k(0)|^2 \propto e^{-4k_y \rho_i}$ for $k_y \rho_i > (k_y \rho_i)_{\max}$ where $(k_y \rho_i)_{\max}$ is the $k_y \rho_i$ at which $\gamma / \langle k_\perp^2 \rangle$ is maximum. This last rule is based on results from both non-linear simulations and experimental measurements on core plasma turbulence. Note that, while the rules based on sum over powers of $\gamma / \langle k_\perp^2 \rangle$ maintain a memory of the linear spectrum, the rule proposed in Ref. [77] reflects the idea that there is a mechanism that, in the non-linear stage, smoothes out turbulence towards a universal spectrum, with a simple exponential decay, independently of the details of the spectrum in the linear stage (except for the position of the maximum which is still calculated on $\gamma / \langle k_\perp^2 \rangle$). This last statement is reported to be consistent with findings from both non-linear simulations and from experimental measurements. However no general conclusion can be drawn as these cases do not cover a large parameters set.

The choice of the quasi-linear rule is particularly important for particle transport as different parts of the $k_y \rho_i$ spectrum can have opposite signs in the flux, i.e. in either B_k and C_k of the convection velocity given in the second of formulas (5.19), and thus the sum can drastically change result depending on the weight given to the different $k_y \rho_i$ modes.

5.4 Understanding the behavior of density peaking in standard scenarios

Before applying linear gyrokinetic theory to the interpretation of the eITB scenario, we want to show how this model works for well known scenarios like the Ohmic L/H mode. Several theoretical models have been proposed to interpret experimental results in differ-

ent scenarios, for example Refs. [72, 63, 80, 78, 79]. Each work deals with a particular observation about steady-state particle transport.

In this context we use the linear gyrokinetic model to understand the different observations as the manifestation of an underlying coherent mechanism arising from turbulence.

5.4.1 Base case and spectrum

We adopt the following set of parameters which resemble a typical monotonic q profile plasma obtained in TCV and other machines:

- aspect ratio of $\epsilon = 0.125$, representing mid-radius for most of the existing Tokamaks;
- normalized inverse length scales $R/L_{Te} = R/L_{Ti} = 9$;
- $T_e = T_i$, no collisions $\nu_{\text{eff}} = \nu_{ei}R/(\sqrt{2}v_{th}^i) = 0$, no impurities $Z_{\text{eff}} = 1$;
- safety factor $q = 1.4$ and magnetic shear $s = 0.8$, while the Shafranov-shift parameter α is calculated self-consistently assuming $n_e = 10^{19} \text{ m}^{-3}$ and $T_e = 0.5 \text{ keV}$ with a $B_0 = 1.44 \text{ T}$.

The density normalized inverse length scale R/L_n is scanned to find the steady-state point and a spectrum in $k_y\rho_i$ is calculated for each single case in the range $0.08 < k_y\rho_i < 1.5$.

In figures 5.3(a,b) we show the result for the turbulence properties for this case: most unstable mode growth rate γ and real frequency ω_R versus $k_y\rho_i$ in figure 5.3(a), and turbulence spectrum for the mixing length parameter $\gamma/ < k_{\perp}^2 >$ and for the phase shift $\tilde{\Gamma}_k$ which is defined as the turbulent particle flux Γ_{turb} , for each single mode, normalized to $|\tilde{\Phi}_k(0)|^2$ since $\Gamma_{\text{turb}}/|\tilde{\Phi}_k(0)|^2$ is the only meaningful quantity in a linear model.

Each curve in figures 5.3(a,b) is obtained with a different R/L_n as input to the code. First of all, we note that there are two completely different type of modes present along the $k_y\rho_i$ axis. At long wavelengths, for $k_y\rho_i \lesssim 0.7$ the dominant mode is an ITG, which frequency becomes more negative going to lower values of R/L_n and to higher values of $k_y\rho_i$. However, a TEM can become dominant at $k_y\rho_i \sim 0.1$ for high values of R/L_n . In general this is the effect of TEM destabilization by R/L_n . For $k_y\rho_i \gtrsim 0.7$ the dominant mode is rotating in the electron diamagnetic direction but it is stabilized by increasing R/L_n . Its structure is different from the modes located at longer wavelength as we can see from figures 5.4(a,b), where we compare the mode structure along the ballooning angle θ for some mixed $R/L_n - k_y\rho_i$ cases. While for low values of $k_y\rho_i$, shown in figure 5.4(a), the mode is essentially located between $-\pi < \theta < \pi$, for $k_y\rho_i = 0.9$, shown in figure 5.4(b), there are important structures occupying a large interval in θ , indicating an elongated mode. The mode associated with these structures has its growth rate reduced by increasing R/L_n .

Looking now at the transport properties of these modes, shown in figure 5.3(b), we see that for all the R/L_n cases, the spectrum for $\gamma/ < k_{\perp}^2 >$ (solid lines) peaks at $k_y\rho_i \sim 0.1$

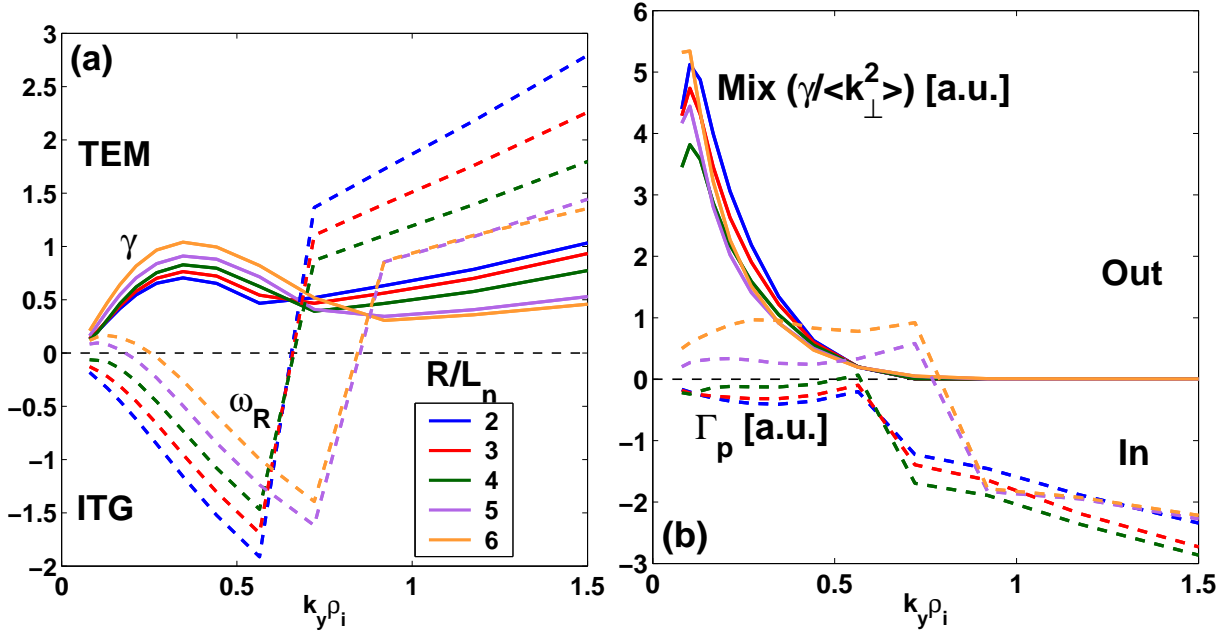


Figure 5.3: a) Growth rate γ (solid) and real frequency ω_R (dashed), both in units of v_{th}^i/R , of the most unstable mode for each $k_y \rho_i$, for different values of R/L_n (in the legend). Indicated also is the type of mode according to the sign convention: a positive ω_R is a TEM, while a negative ω_R is an ITG; b) The same type of plot for the mixing length parameter $\gamma / \langle k_\perp^2 \rangle$ ('Mix', solid) and for the phase shift $\tilde{\Gamma}_k$ (Γ_p in the plot, dashed), i.e. the turbulent particle flux Γ_{turb} of each single mode normalized to the respective $|\tilde{\Phi}_k(0)|^2$. Indicated also is the direction of the flux according to the sign convention: a positive flux is outward directed and a negative flux is inward directed.

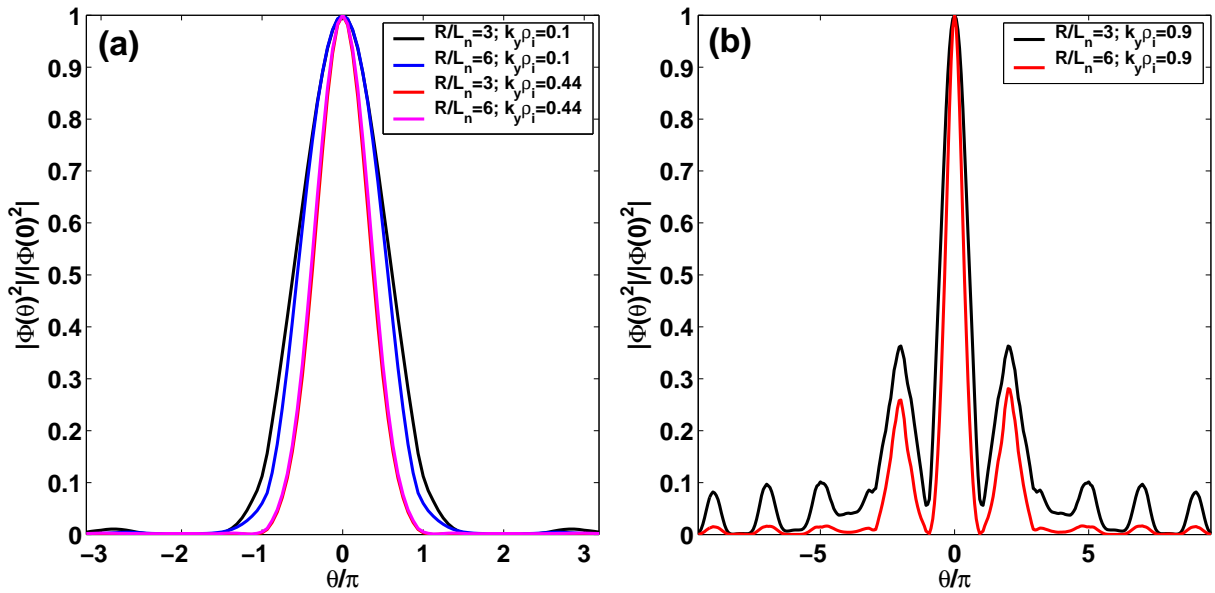


Figure 5.4: a) Mode structure for $|\tilde{\Phi}/\tilde{\Phi}_k(0)|^2$ along the ballooning angle θ in units of π for four cases (in the legend) at low values of $k_y \rho_i$; b) The same plot for two cases at high values of $k_y \rho_i$.

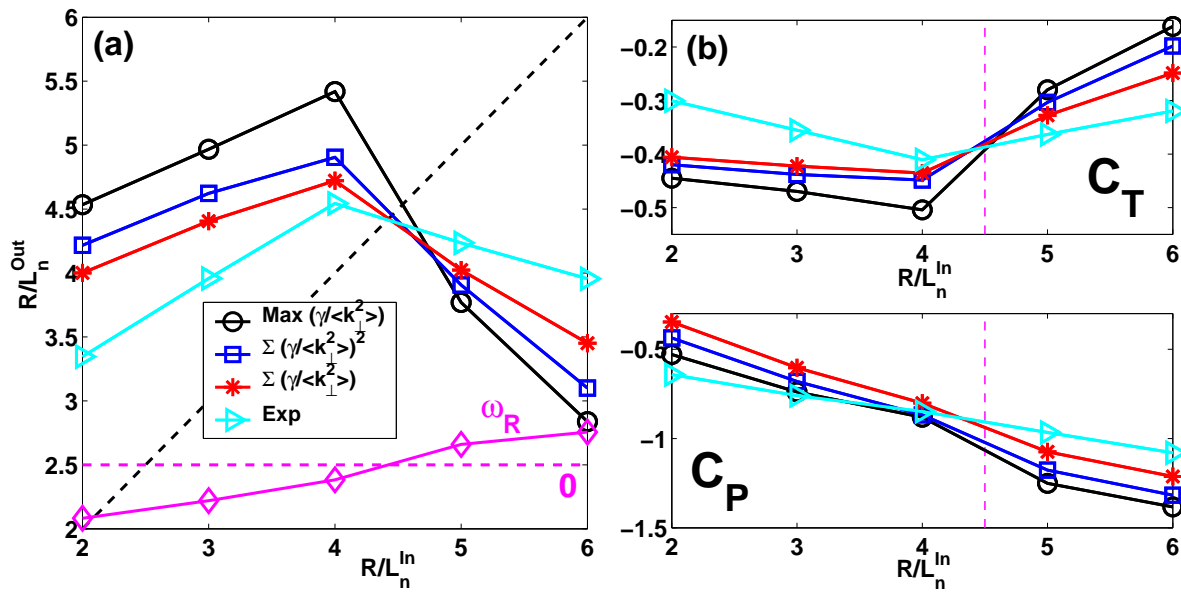


Figure 5.5: a) R/L_n^{Out} , as calculated from formula (5.23), versus R/L_n^{In} evaluated with different quasi-linear rules (in the legend). The intersection with the diagonal line gives the steady-state R/L_n . The frequency ω_R of the mode with the highest value of $\gamma / \langle k_{\perp}^2 \rangle$ is also shown (diamonds) plotted with the reference zero line (horizontal dashed line); b) Pinch coefficients C_T and C_P . Shown also is the stationary value obtained from plot (a) as a dashed vertical line.

and decreases down to negligible values already at $k_y \rho_i \sim 0.6$. The spectrum does not change significantly for different R/L_n .

If we now consider the induced particle normalized flux, or 'phase-shift' (dashed lines), we see that the long and short wavelengths behave differently:

- for $k_y \rho_i \lesssim 0.6 - 0.7$ the phase-shift is almost constant with respect to $k_y \rho_i$ but it strongly depends on the value of R/L_n as it is inward directed for $R/L_n \leq 4$ and becomes outward directed for $R/L_n \geq 5$;
- for $k_y \rho_i \gtrsim 0.7$ the phase-shift is inward directed and becomes more negative with increasing $k_y \rho_i$, while it shows little dependence on the value of R/L_n .

From the flux behavior shown in figure 5.3(b) we can expect the steady-state $[R/L_n]_{\text{stat}}$ to be located between 4 and 5. We calculate it finding the condition $\Gamma_{\text{turb}} = 0$ using different rules for the sum over the spectrum.

In figure 5.5(a) we show the predicted R/L_n^{Out} , as calculated from formula (5.23), versus R/L_n^{In} , using different quasi-linear rules for the calculation of C_T and C_P , see formulas (5.28). The rules employed are in the order: retaining only one mode where $\gamma / \langle k_{\perp}^2 \rangle$ peaks (circles), sum using $|\tilde{\Phi}_k(0)|^2 \propto (\gamma / \langle k_{\perp}^2 \rangle)^2$ (squares), sum using $|\tilde{\Phi}_k(0)|^2 \propto \gamma / \langle k_{\perp}^2 \rangle$ (stars) and sum using the prescription of Ref. [77] (right triangles) where $|\tilde{\Phi}_k(0)|^2 \propto e^{-C k_y \rho_i}$. It is interesting to see that, despite the four rules being different in weighting over the wavenumber spectrum, the predicted stationary point is almost

the same for all and it is $[R/L_n]_{\text{stat}} \sim 4.5$. Note also that all the identified stationary points are stable, when looking at condition (5.24), and that the behavior of R/L_n^{Out} versus R/L_n^{In} can be divided in two regions at low and high values of R/L_n^{In} , and that the stationary point is located in between. In figure 5.5(a), we also show the behavior of the real frequency ω_R of the mode with the highest $\gamma / \langle k_{\perp}^2 \rangle$ versus R/L_n^{In} (diamonds) with its own reference zero line (horizontal dashed). Note that the frequency changes sign from negative (meaning a dominant ITG mode) at low R/L_n^{In} to positive (meaning a dominant TEM) at high R/L_n^{In} . The region where $\omega_R \sim 0$, namely where ITG and TEM coexist at similar growth rates, is also the region where the stationary point is located.

To understand the mechanisms that drive this behavior we look now at the two pinch coefficients C_T and C_P shown in figure 5.5(b), plotted versus R/L_n^{In} . Here we show also the stationary value at $[R/L_n]_{\text{stat}} = 4.5$ to check the behavior of the two coefficients at that point.

The thermodiffusion coefficient C_T , figure 5.5(b) on the top, is directed inwards on all the R/L_n^{In} range, but it is more negative, i.e. provides a stronger inward pinch, for $R/L_n^{\text{In}} < 4.5$, reaching its highest absolute value near the stationary point. Relating this behavior to the behavior of ω_R as shown in figure 5.5(a), we see that the predictions from subsection 5.3.1, in particular as from figure 5.2(a), are recovered. The same is true for C_P , both with regards to the magnitude and the fact that it increases in absolute value going to TEM dominated turbulence.

The final result, namely the stationary $[R/L_n]_{\text{stat}}$, is thus an interplay between the role of the thermodiffusive pinch which is inward directed and maximized in absolute value at $\omega_R \sim 0$, it becomes small in absolute value in TEM dominated turbulence, and the contribution from C_P which becomes more important in TEM dominated turbulence. However, if R/L_{Te} is high, C_P is expected to become negligible compared to $C_T R/L_{Te}$ and thus the stationary point would be dictated by the ITG–TEM transition.

We said before that for high $k_y \rho_i$ modes the transport properties are different. However their role is minimal when using quasi-linear rules where $|\tilde{\Phi}_k(0)|^2$ rapidly decays with $k_y \rho_i$. In this sense we do not expect a strong difference between different rules of this kind, as can be seen from figure 5.5(a) looking at the circles, squares and stars. A more important difference can arise if the spectrum of $|\tilde{\Phi}_k(0)|^2$ decays slowly as for example using the rule of Ref. [77] (right triangles in the figure). Nevertheless for this case the stationary point is almost the same.

In the following parameters scan we will concentrate only on the stationary point, again looking at the basic mechanisms and the effect of using different quasi-linear rules.

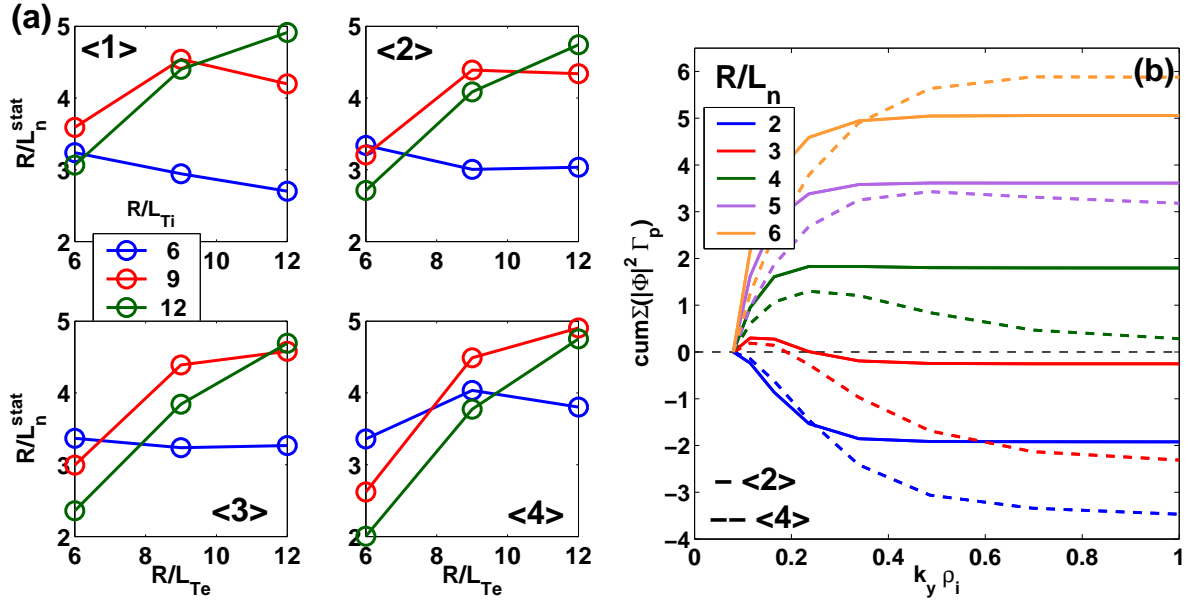


Figure 5.6: a) Stationary R/L_n for different values of R/L_{Te} (x axis) and R/L_{Ti} (legend). Each subplot shows the result of a different rule (see text); b) Cumulative total flux for the case with $R/L_{Te} = 12$ and $R/L_{Ti} = 6$, plotted versus $k_y \rho_i$ for the R/L_n scan, using rules < 2 > (solid) and < 4 > (dashed).

5.4.2 Dependence of $[R/L_n]_{\text{stat}}$ on temperature gradients

We employ the same parameters as the base case but we perform a parameters scan in R/L_{Te} and R/L_{Ti} to show the dependence of $[R/L_n]_{\text{stat}}$ on the two temperature length scales. For this scan the wavenumbers are retained in the interval $0.08 < k_y \rho_i < 1$. In figure 5.6(a) we show the predicted $[R/L_n]_{\text{stat}}$ versus R/L_{Te} for three values of R/L_{Ti} , using the four rules presented before, respectively: < 1 > retains only the mode where $\gamma / < k_{\perp}^2 >$ peaks, < 2 > is the sum using $|\tilde{\Phi}_k(0)|^2 \propto (\gamma / < k_{\perp}^2 >)^2$, < 3 > is the sum using $|\tilde{\Phi}_k(0)|^2 \propto \gamma / < k_{\perp}^2 >$, and < 4 > is the sum using $|\tilde{\Phi}_k(0)|^2 \propto e^{-C k_y \rho_i}$ as in Ref. [77]. Several interesting observations can be drawn from these results:

- 1) The different rules present different details on the predicted $[R/L_n]_{\text{stat}}$. Again this is due to the different weights given to the wavenumbers, as shown in figure 5.6(b). Here we plot the cumulative flux, i.e. $\propto \sum_{k=0.08}^{k=k_y \rho_i} [|\tilde{\Phi}_k(0)|_k^2 \tilde{\Gamma}_k]$, versus $k_y \rho_i$, for rules < 2 > (solid lines) and < 4 > (dashed lines), for the case with $R/L_{Te} = 12$ and $R/L_{Ti} = 6$, for different values of R/L_n . For $R/L_n < 5$ the inward directed contribution coming from high values of $k_y \rho_i$ is relevant for rule < 4 > while it is small for rule < 2 >. The effect is to shift $[R/L_n]_{\text{stat}}$ to higher values for rule < 4 >;
- 2) Looking at figure 5.3(a), rule < 1 >, one can note that $[R/L_n]_{\text{stat}}$ is maximized, at fixed R/L_{Ti} , when $R/L_{Ti}/R/L_{Te} \approx 1$. This is also visible in rules < 2 > and < 3 > although with less evidence as other modes are taken into account. For rule < 4 > this dependence

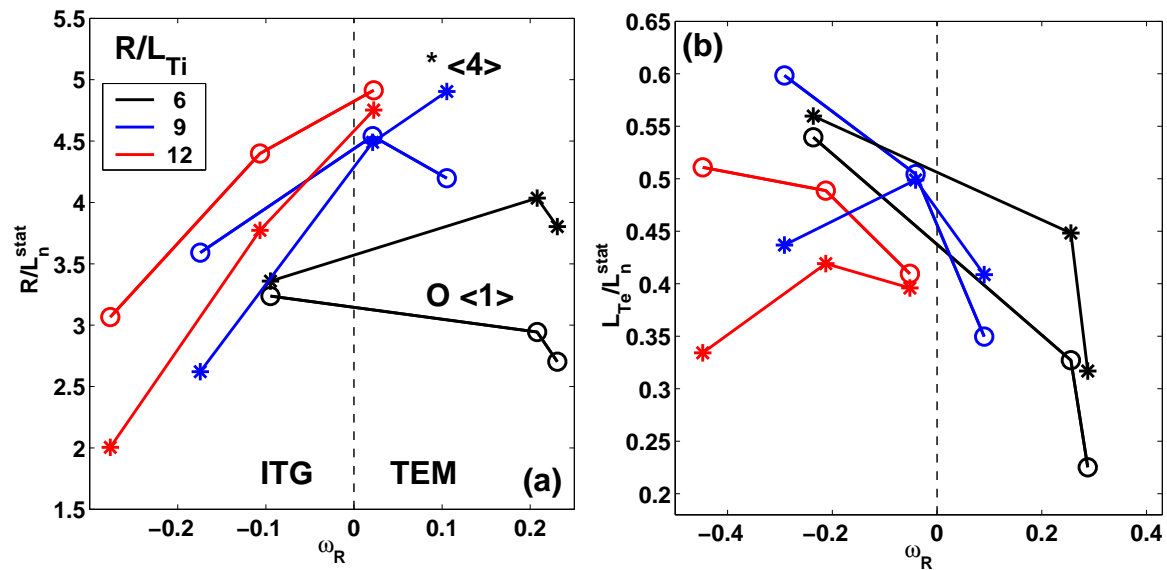


Figure 5.7: a) $[R/L_n]_{\text{stat}}$ for rules $\langle 1 \rangle$ (circles) and $\langle 4 \rangle$ (stars) versus ω_R of the mode with highest $\gamma / \langle k_{\perp}^2 \rangle$; b) Same plot for L_{Te}/L_n^{stat} .

on $R/L_{Ti}/R/L_{Te}$ can be observed on the local slope $d[R/L_n]_{\text{stat}}/dR/L_{Te}$ but not on the value of $[R/L_n]_{\text{stat}}$ itself;

3) The mechanism that gives this behavior can be understood looking at the behavior of $[R/L_n]_{\text{stat}}$ versus the real frequency of the dominant mode. In figures 5.7(a,b) we plot respectively $[R/L_n]_{\text{stat}}$ and L_{Te}/L_n^{stat} for the $R/L_{Te} - R/L_{Ti}$ scan, and for rules $\langle 1 \rangle$ and $\langle 4 \rangle$, versus ω_R of the mode with highest $\gamma / \langle k_{\perp}^2 \rangle$ at the value of $[R/L_n]_{\text{stat}}$ of rule $\langle 1 \rangle$. In figure 5.7(a), as expected, we see that $[R/L_n]_{\text{stat}}$ increases going from ITG to the ITG–TEM transition region where $\omega_R \sim 0$, while it decreases going into the TEM region. The behavior is also visible in rule $\langle 4 \rangle$ although there is no clear reduction in the TEM branch. However, looking at L_{Te}/L_n^{stat} , figure 5.7(b), which gives a direct indication on the strength of the thermodiffusive pinch, we see that the thermodiffusive contribution is decreased going into the TEM regime also for rule $\langle 4 \rangle$.

Collecting all these observations we can make a first general conclusion from this collisionless $R/L_{Te} - R/L_{Ti}$ scan, namely that $[R/L_n]_{\text{stat}}$ will be maximized, at fixed R/L_{Ti} , when $R/L_{Te} \approx R/L_{Ti}$, which also gives, for the mode with highest $\gamma / \langle k_{\perp}^2 \rangle$, $\omega_R \approx 0$. However the details of the dependences and the values can moderately change depending on the quasi-linear rule employed, especially if a relevant weight is given to high $k_y \rho_i$ numbers where the flux is found to be inward directed for all the cases.

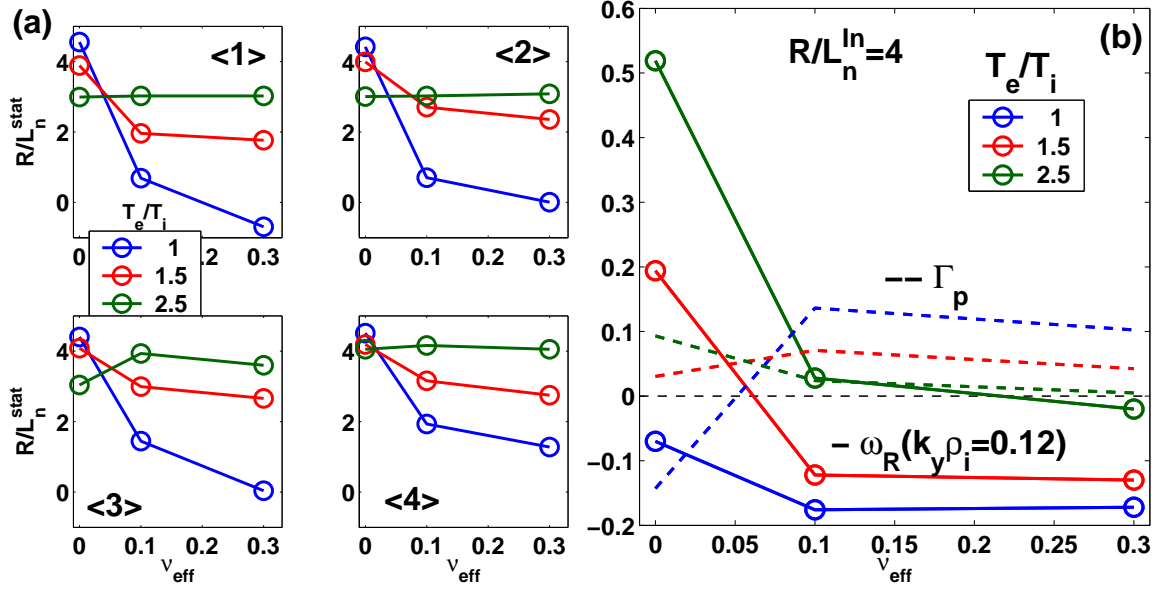


Figure 5.8: *a)* Plot similar to 5.6(a) but for the $\nu_{\text{eff}} - T_e/T_i$ scan; *b)* Mode real frequency ω_R (solid) and phase shift $\tilde{\Gamma}_k$ (dashed) for wavenumber $k_y \rho_i = 0.12$ plotted versus ν_{eff} for the case with $R/L_n^{\text{In}} = 4$ and for three values of T_e/T_i .

5.4.3 Dependence of $[R/L_n]_{\text{stat}}$ on collisionality and temperatures ratio

We adopt the same base case parameters as in subsection 5.4.1 with $0.08 < k_y \rho_i < 1$. We scan the temperature ratio T_e/T_i and the effective collisionality ν_{eff} . In figure 5.8(a) we present the results for the stationary $[R/L_n]_{\text{stat}}$ as done in the previous subsection in figure 5.6(a). $[R/L_n]_{\text{stat}}$ is shown versus ν_{eff} for the different T_e/T_i values and each subplot shows the result for a different quasi-linear rule. The main observation that can be drawn from this scan is that the local normalized density gradient is strongly reduced by increasing collisionality for $T_e/T_i \lesssim 1$, while for $T_e/T_i \gg 1$ the density peaking is not modified by collisionality (in some cases it can even be slightly increased). This strong collisionality-driven flattening effect at $T_e/T_i \approx 1$ is relaxed when more modes are taken into account as can be seen from the curve at $T_e/T_i = 1$ which attains negative values for rule < 1 > but stays positive for rule < 4 >. Again this is due to the inward directed contribution from high $k_y \rho_i$ modes. The reduction of $|V_{\text{turb}}/D_{\text{turb}}|$ with collisionality has also been reported in Ref. [80], and collisionality itself seems to be the most important parameter for general density scalings in H-modes plasmas of several machines [81].

The positive effect of T_e/T_i at high ν_{eff} and the reason why collisionality influences the density peaking in a negative way can be understood from figure 5.8(b) where we plot the real frequency ω_R (solid) and the respective phase shift $\tilde{\Gamma}_k$ (dashed) for the mode at $k_y \rho_i = 0.12$ versus ν_{eff} for the three values of T_e/T_i , at a fixed $R/L_n^{\text{In}} = 4$. For all the ν_{eff} , increasing T_e/T_i pushes the frequency from ITGs towards TEMs. This effect is larger at

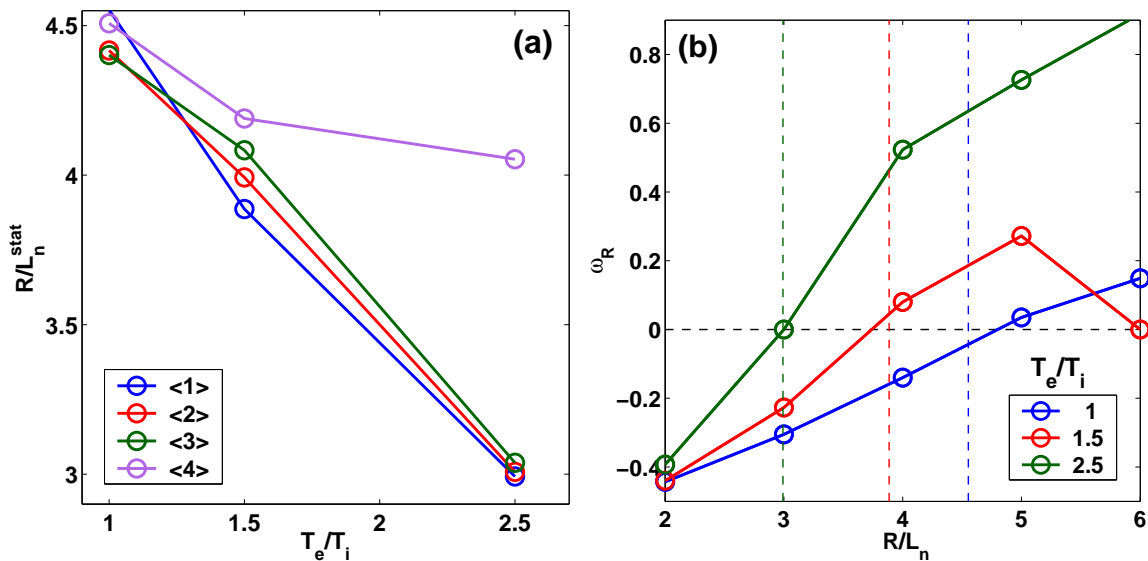


Figure 5.9: a) $[R/L_n]_{\text{stat}}$ versus T_e/T_i for the case with $\nu_{\text{eff}} = 0$, obtained with different quasi-linear rules; b) Mode real frequency ω_R for wavenumber $k_y \rho_i = 0.12$ plotted versus R/L_n for three values of T_e/T_i (legend).

low ν_{eff} . With regards to the flux sign, we see that at low ν_{eff} it is inward directed for low T_e/T_i , i.e. in ITG, and becomes outward directed increasing T_e/T_i , i.e. going to TEMs. At high ν_{eff} the flux becomes outward directed and the magnitude increases as T_e/T_i is decreased, i.e. as ω_R goes more into the ITG mode. This picture explains why ν_{eff} causes a density profile flattening at low T_e/T_i as an effect of an outward directed contributions from ITG modes. We will see later what is the main mechanism behind this effect.

We focus now on the collisionless case, for which we see that $[R/L_n]_{\text{stat}}$ is slightly decreased with increasing T_e/T_i . In figure 5.9(a) we put this in evidence by plotting $[R/L_n]_{\text{stat}}$ versus T_e/T_i for the case at $\nu_{\text{eff}} = 0$ and for the four rules. $[R/L_n]_{\text{stat}}$ decrease with T_e/T_i . The reason is shown in figure 5.9(b), where we show the real frequency ω_R for the mode at $k_y \rho_i = 0.12$ versus R/L_n . The dashed vertical lines indicate the position of $[R/L_n]_{\text{stat}}$. We see that the mode changes from an ITG to a TEM at lower R/L_n with increasing T_e/T_i . Consequently the stationary point adjusts itself to relocate near $\omega_R \approx 0$. This effect of R/L_n limitation due to TEM destabilization is the same that has been discussed in subsection 5.4.2. This effect has also been observed in low collisionality plasmas where the density profile is flattened by application of core ECH in TCV [65] and in ASDEX Upgrade [63].

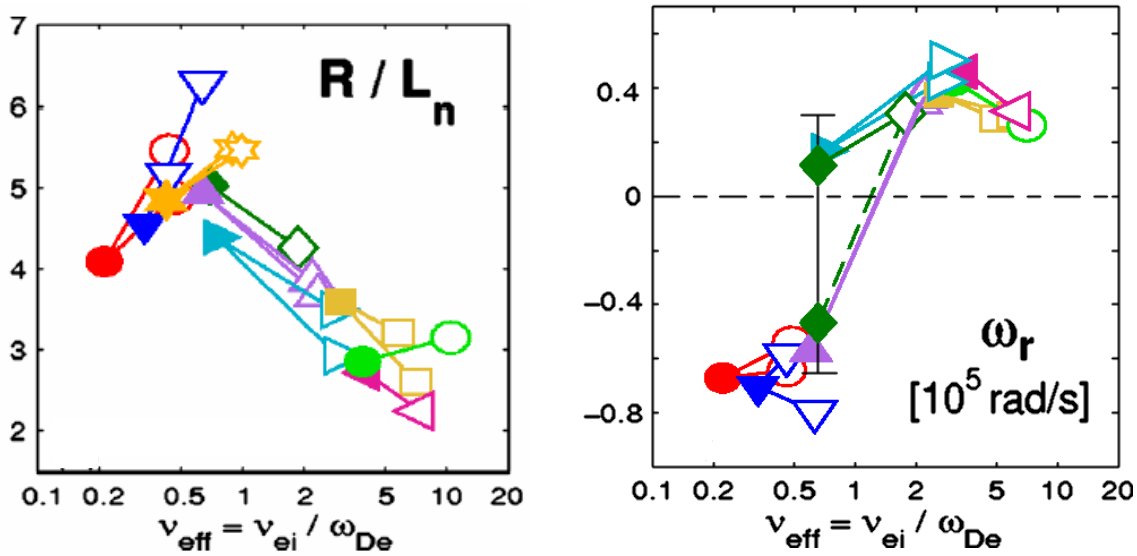


Figure 5.10: Figure taken from Ref. [82]. Note that in the right plot ω_r is in fact $-\omega_R$, which means that negative values indicate a TEM, while positive values indicate an ITG, opposite to our convention.

5.4.4 Interpretation of experimental data with a collisionality scan

We employ the results presented in the previous subsections 5.4.2 and 5.4.3 to interpret observations from experimental data observed in the ASDEX Upgrade Tokamak. In particular we refer to the results presented in Ref. [82], figure 3 on page 3, which we report here in figure 5.10. On the left of this figure we see a collection of stationary points of R/L_n shown as a collisionality scan for different ASDEX Upgrade L and H modes. On the right, the most unstable mode frequency for a fixed $k_y \rho_i$ is shown, calculated for each R/L_n point. In this plot ω_r is in fact $-\omega_R$, which means that a negative value of ω_r indicates a TEM, and a positive value indicates an ITG. We see that the mode changes from a TEM to an ITG increasing ν_{eff} , and that the maximum in R/L_n in the left figure is located at the ν_{eff} where the mode frequency changes sign.

We use now the quasi-linear model discussed in this Chapter to help us in understanding this behavior. To this purpose we perform a $\nu_{\text{eff}} - T_e/T_i$ scan employing a single toroidal mode $k_y \rho_i = 0.13$, with the other parameters kept fixed at the same values as the base case except for the choice: $R/L_{Te} = 10$, $R/L_{Ti} = 6$. The parameter scan is done in the intervals $0 \leq \nu_{\text{eff}} \leq 0.15$ and $T_e/T_i = 1.2 \div 2.2$. Note that the definition of ν_{eff} in figure 5.10 is such that in our parameter scan we actually scan a $0 \leq \nu_{\text{eff}} \lesssim 1$ according to the definition in figure 5.10.

In figure 5.11(a) we present the results of the code for $[R/L_n]_{\text{stat}}$ (circles), plotted versus $-\omega_R$. The arrow indicates that increasing collisionality, at fixed T_e/T_i , moves the fre-

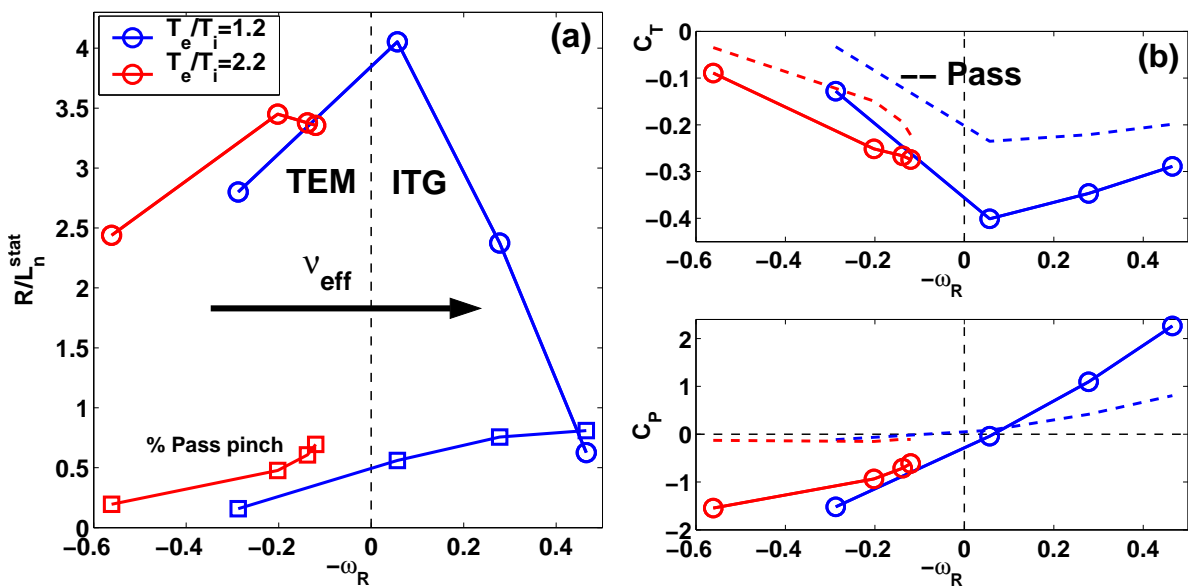


Figure 5.11: *a)* $[R/L_n]_{\text{stat}}$ (circles) versus $-\omega_R$ for the $\nu_{\text{eff}} - T_e/T_i$ scan. The arrow indicates the direction of increasing ν_{eff} . Also shown the passing electron pinch fraction (squares) limited to 0 – 1; *b)* Pinch coefficients C_T (top, circles) and C_P (bottom, circles) versus $-\omega_R$ for the same scan. In dashed we show their respective passing electrons contributions.

quency to the right. It is clear that the code is capable of reproducing the experimental behavior qualitatively, if the result is plotted versus ω_R (and not versus ν_{eff}) as ν_{eff} is only one of the many parameters that influence ω_R but the pinch is essentially driven by ω_R . As expected from previous results, the highest peaking is obtained near $\omega_R \approx 0$, i.e. when ITG and TEM coexist at similar growth rates. In addition, increasing ν_{eff} has also the effect of increasing the fraction of the pinch carried by passing electrons, as shown by the squares ('% Pass pinch') which values go from $\sim 10\%$ in the collisionless case to $\sim 80\%$ at $\nu_{\text{eff}} = 0.15$. Note that at $T_e/T_i = 2.2$, the stationary points are located more into the TEM branch, and that for those points an increase in ν_{eff} has a positive effect on the stationary peaking [83]. We also see that the code predicts a faster drop of density peaking with collisionality than what observed in the experiment. This can be due to the fact that we are taking only the mode with highest $\gamma / \langle k_{\perp}^2 \rangle$ for the transport analysis while it has been shown recently that a full spectrum up to the short wavelength region with $k_y \rho_i \gtrsim 1$ has to be taken into account to recover a reasonable $[R/L_n]_{\text{stat}}$ [84].

To clarify the mechanisms that provide the behavior shown in figure 5.11(a), we evaluate now the two pinch coefficients C_T and C_P . They are shown in figure 5.11(b) (the dashed lines are the respective contributions from the passing electrons).

- C_T : the thermodiffusion coefficient is inward directed and maximized in absolute value near $\omega_R \approx 0$ where it has the value $C_T \approx -0.4$. It decreases both into the TEM and into the ITG branch, however the decrease is stronger and more rapid in the TEM branch as

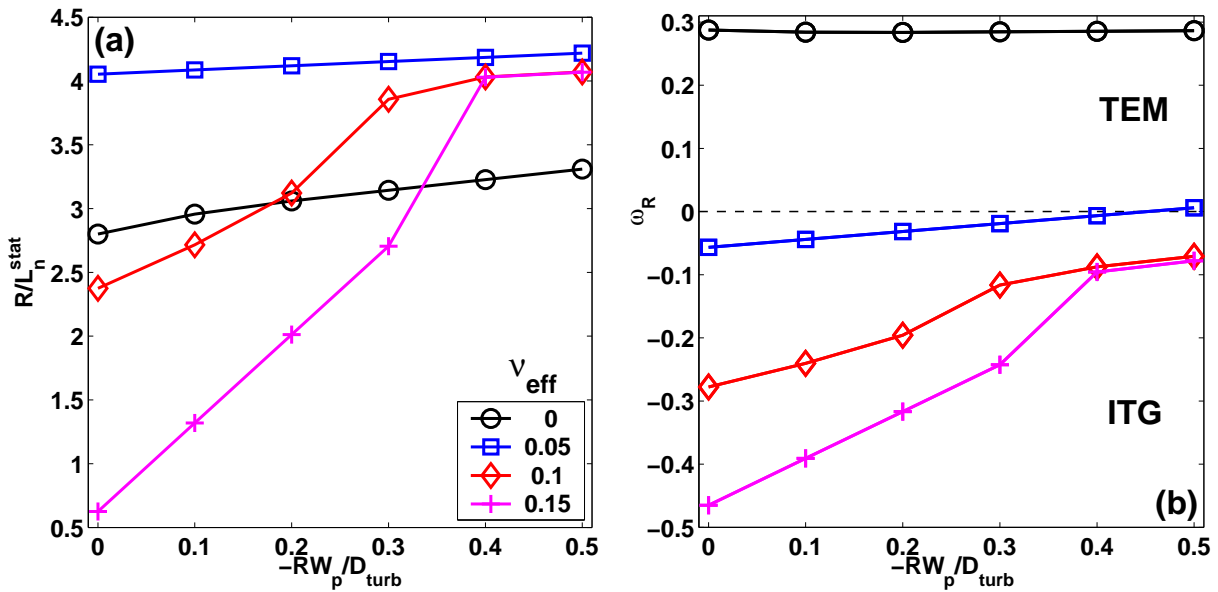


Figure 5.12: a) Stationary R/L_n as a function of the Ware pinch-driven term $-RW_p/D_{\text{turb}}$ for different values of ν_{eff} . $T_e/T_i = 1$ for this plot; b) Same plot but for the frequency ω_R corresponding to the stationary state.

expected from the analysis of subsection 5.3.1;

- C_P : this pinch coefficient is inward directed and important into the TEM branch and compensates the drop of $|C_T|$ in this regime ($C_P \sim -2$). It is interesting to note that it changes sign and becomes outward directed in the ITG branch, providing a strong outward contribution that almost balances the inward contribution of C_T , giving the observed $[R/L_n]_{\text{stat}} \approx 0$ at high ν_{eff} . We already showed in subsection 5.3.1 that the passing electrons part of C_P is proportional to ω_R and can thus provide an outward pinch in ITG. However, in this case we see that not all the outward contributions are from passing electrons, but a part is also carried by trapped electrons. It can be shown that this effect is mainly due to barely trapped electrons for which the parallel dynamics is still important. Note that the increase of C_P to large positive values in ITG could be less rapid and less strong if more modes are taken into account as mentioned before.

Ware pinch effect

We now insert the Ware pinch as shown in subsection 5.2.3 to see what is its effect depending on the turbulence regime. For the scan performed in this subsection we find the new stationary state assuming different values for the term $-RW_p/D_{\text{turb}}$ which has to be added to R/L_n^{Out} .

The results are shown in figure 5.12(a) for the stationary state $[R/L_n]_{\text{stat}}$ and in figure 5.12(b) for the value of ω_R corresponding to the stationary state. Each figure shows the respective quantity plotted versus the Ware pinch driven term $-RW_p/D_{\text{turb}}$ for dif-

ferent values of ν_{eff} . All the cases reported have $T_e/T_i = 1$. Note that for TCV typical parameters in low current Ohmic L-modes, we estimate $-RW_p/D_{\text{turb}} \approx 0.5 \div 1$ at $\rho_\psi \sim 0.3$. It is interesting to note that in TEM dominated turbulence, and near the transition between the two modes, i.e. for $\omega_R \gtrsim 0$ (circles and squares), the inclusion of the Ware pinch does not modify in a substantial way either the value of $[R/L_n]_{\text{stat}}$ or the value of ω_R . In the case of strongly ITG dominated turbulence at $W_p = 0$ (diamonds and crosses), the inclusion of the Ware pinch has an important effect as it rapidly increases both $[R/L_n]_{\text{stat}}$ and ω_R . If the Ware pinch is substantial, it will tend to push the stationary value up to the ITG→TEM transition, where it will stop to cause any further increase due to the strong change in the slope of the function. It is interesting to remember that this effect has in fact already been observed and discussed in Ref. [79] and it is believed to be the mechanism for the creation of a density barrier in positive magnetic shear scenarios with off-axis ICRH.

Another characteristic of the Ware pinch effect on the stationary R/L_n is that, as it can be seen for the crosses in figure 5.12, the relative change $\delta [R/L_n]_{\text{stat}}$ due to the application of a certain Ware pinch $-RW_p/D$ can be much larger than $-RW_p/D$ itself, due to the particular functional form of $V_{\text{turb}}/D_{\text{turb}}$. This delicate topic will be inspected in more detail in chapter 6.

5.4.5 Dependence of $[R/L_n]_{\text{stat}}$ on magnetic shear

We adopt the same base case parameters as in subsection 5.4.1 with $0.08 < k_y \rho_i < 1$. We scan the magnetic shear s and the safety factor q around the base case parameters. In addition, we perform the same scan with modified parameters $\nu_{\text{eff}} = 0.15$, $R/L_{Te} = 10$ and $R/L_{Ti} = 6$ to check the effect of collisions.

We show the results for the stationary state in figures 5.13(a,b), where we plot $[R/L_n]_{\text{stat}}$ versus magnetic shear for three values of q , adopting the four quasi-linear rules presented in subsection 5.4.2. In the collisionless case, shown in figure 5.13(a), the stationary density logarithmic gradient increases monotonically with increasing magnetic shear, and its value does not show any relevant dependence on q . In addition, the result does not change using different quasi-linear rules. This dependence is consistent with the findings of Ref. [85] from LHCD experiments in JET, and of Ref. [86] from LHCD experiments in Tore Supra, although in those cases $T_e \gg T_i$.

When collisions are non-negligible, this dependence can be completely destroyed, as shown in figure 5.13(b), where the same scan is done but with $\nu_{\text{eff}} = 0.15$, $R/L_{Te} = 10$ and $R/L_{Ti} = 6$. Now the stationary density peaking decreases with increasing magnetic shear and its value shows also some sensitivity on the rule employed. As in the collisionless case, there seems to be no significant dependence on q .

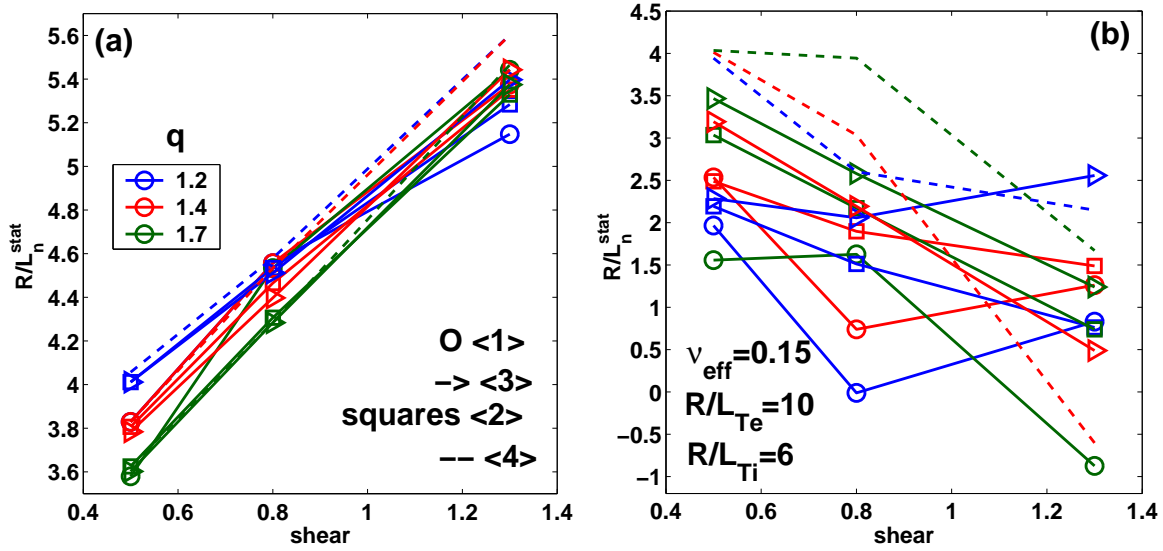


Figure 5.13: a) $[R/L_n]_{\text{stat}}$ versus magnetic shear for three values of q (in legend) and for $\nu_{\text{eff}} = 0$, $R/L_{\text{Te}} = R/L_{\text{Ti}} = 9$. Each symbol represents a different quasi-linear rule, see subsection 5.4.2; b) Same plot but with modified parameters: $\nu_{\text{eff}} = 0.15$, $R/L_{\text{Te}} = 10$ and $R/L_{\text{Ti}} = 6$.

To understand this striking difference between the collisionless and the collisional cases, we plot the results from the two scans for the case with $q = 1.4$, and for rule < 1 >, versus ω_R in figure 5.14(a). It is clear that the two scans fall in completely different frequency ranges and this explains also the different shear dependence.

In the collisionless case the stationary state is located near $\omega_R \approx 0$ and the influence of the shear s on $[R/L_n]_{\text{stat}}$ is through the ω_d term in the pinch coefficients. ω_d contains a contribution proportional to s . In the collisional case, the stationary state is located in the ITG branch and the shear has a big effect on the frequency itself, moving the stationary state deeper into the ITG regime as shear is increased. As we saw in the previous subsection, going deeper into the ITG regime with collisions causes a strong flattening of the density profile.

We can also look at the phase space contribution to the particle flux to observe this difference between collisionless and collisional scans. In figure 5.14(b), we plot the differential phase shift $d\tilde{\Gamma}_k/d\lambda$, in arbitrary units, versus the pitch angle parameter λ , for the stationary points shown in figure 5.14(a). The passing/trapped electrons boundary is located at $\lambda = 1 - \epsilon = 0.88$. For the collisionless case (solid lines) the passing electrons carry a very small outward contribution. All the flux is essentially carried by the trapped particles, for which the inward/outward directed contributions are redistributed in λ depending on the value of the magnetic shear. In any case there is balance between inward and outward directed fluxes to obtain the stationary condition. In the collisional case (dashed lines) the trapped electrons move outwards as a whole, but they are balanced by the passing

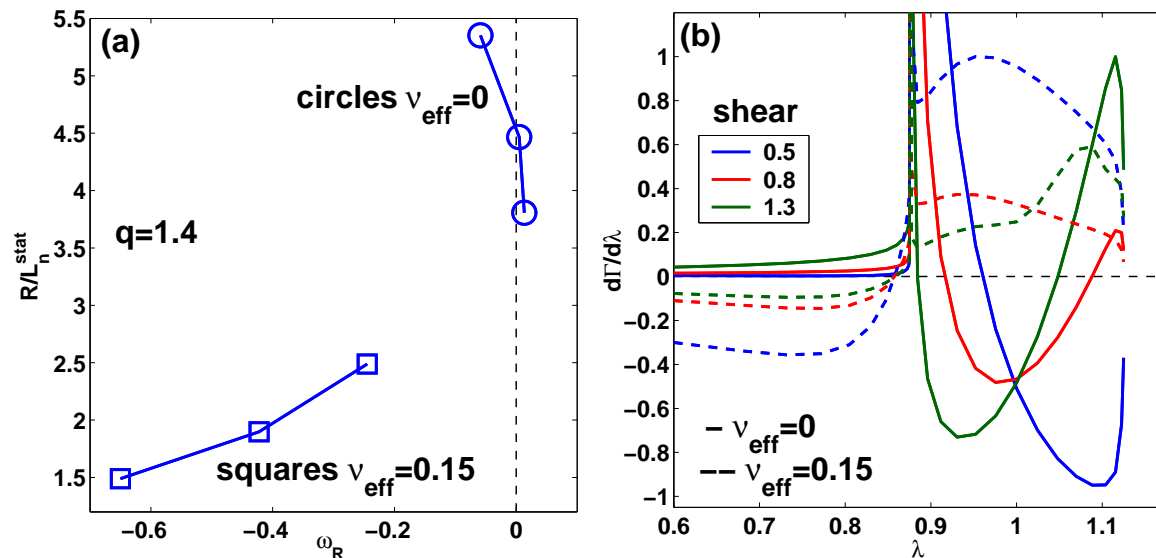


Figure 5.14: a) $[R/L_n]_{\text{stat}}$, from rule $\langle 1 \rangle$, plotted versus ω_R of the mode with highest value of $\gamma/\langle k_{\perp}^2 \rangle$, for the case with $q = 1.4$, for both the base case scan and the modified scan; b) Differential phase shift $d\tilde{\Gamma}_k/d\lambda$ versus pitch angle parameter λ for the cases shown in a).

electrons which now contribute with a relevant inward directed flux.

We can conclude that the different behavior between the collisionless case and the collisional case is due to a different distribution of carried flux in phase space and its dependence on the mode frequency and on magnetic shear. However a more detailed study on these dependencies has to be done to make specific comparisons between these predictions and the observations of shear dependence of density peaking in collisional plasmas.

5.5 Interpretation of the eITB density profile behavior

In the previous sections we have applied the quasi-linear gyrokinetic model to explore the behavior of the density logarithmic gradient in scenarios with monotonic q profiles and moderate gradients. We have seen that the model is able to qualitatively reproduce different experimental observations and to clarify the background physical mechanisms in term of the two pinch coefficients C_T and C_P . The eITB scenario can be analyzed as well, with the difference that now the core q profile is reversed, the magnetic shear s is negative, and the equilibrium gradients reach very high values. It is clear that the gyrokinetic code used here cannot provide any result for the region near $s \approx 0$ as the zeroth-order ballooning approximation is not valid there.

In the following we will analyze several effects and separate details that add up to the observed density barrier and allow us to understand the behavior shown in chapter 4.

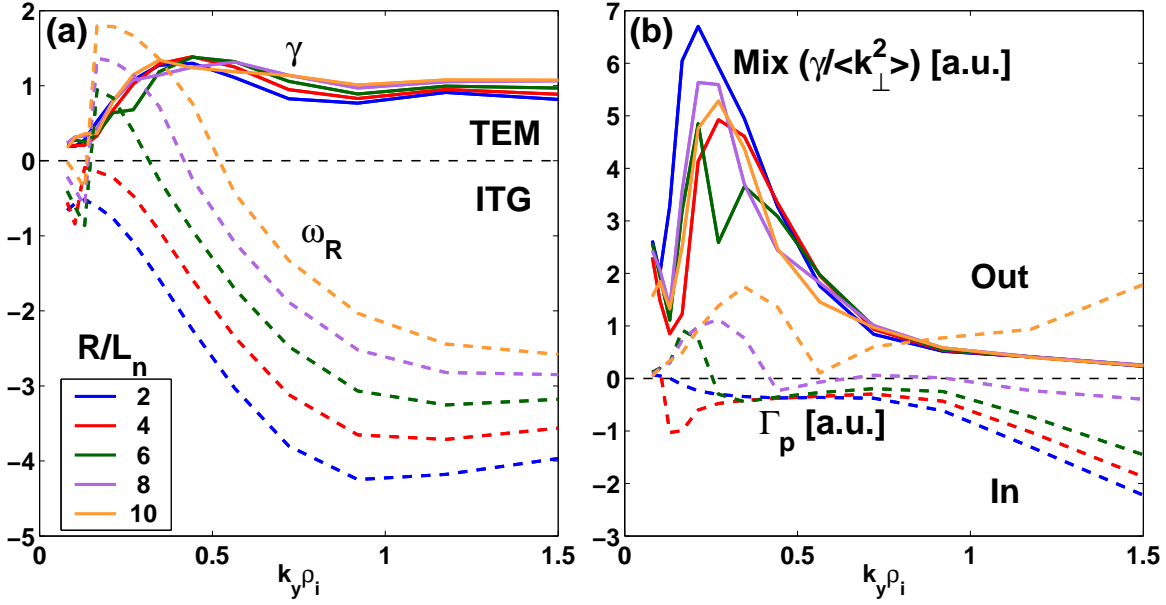


Figure 5.15: a) Growth rate γ (solid) and real frequency ω_R (dashed) of the most unstable mode for each $k_y \rho_i$, for different values of R/L_n (in the legend); b) Mixing length parameter $\gamma / \langle k_\perp^2 \rangle$ ('Mix', solid) and phase shift $\tilde{\Gamma}_k$ (dashed).

5.5.1 Base case and turbulence spectrum

As for the monotonic q profile case, we define here a base case on which we perform different parameters scan:

- aspect ratio of $\epsilon = 0.125$;
- $R/L_{Te} = 20$, $R/L_{Ti} = 0.8R/L_{Te}$, $\nu_{\text{eff}} = 0$, $Z_{\text{eff}} = 1$;
- safety factor $q = 2.8$ and magnetic shear $s = -0.7$, while the Shafranov–shift parameter α is calculated self-consistently assuming $n_e = 0.9 [10^{19} \text{ m}^{-3}]$ and $T_e = 1.5 \text{ keV}$ with $B_0 = 1.44 \text{ T}$.

For the eITB scenario studied here T_i , and consequently R/L_{Ti} , is not known from the experiment. However an average value for T_i can be grossly estimated from CNPA measurements and will be set such that $T_e/T_i = 2.5$. With regards to R/L_{Ti} , its importance will be assessed in dedicate scans.

As done for the previous scenario, the density normalized inverse length scale R/L_n is scanned to find the steady–state point and a spectrum in $k_y \rho_i$ is calculated for each single case in the range $0.08 < k_y \rho_i < 1.5$. We report the results in figure 5.15(a,b) as done for the monotonic q profile scenario, see figure 5.4.1. Some differences with respect to the first scenario studied can be seen. In this case we see that the mode frequency ω_R is bigger in absolute value, and that no high $k_y \rho_i$ ETG–like mode is now present. In addition we see that the turbulence spectrum is shifted to higher $k_y \rho_i$, such that the maximum $\gamma / \langle k_\perp^2 \rangle$ is located at $k_y \rho_i \approx 0.23$. This peak is also less pronounced with respect to the monotonic

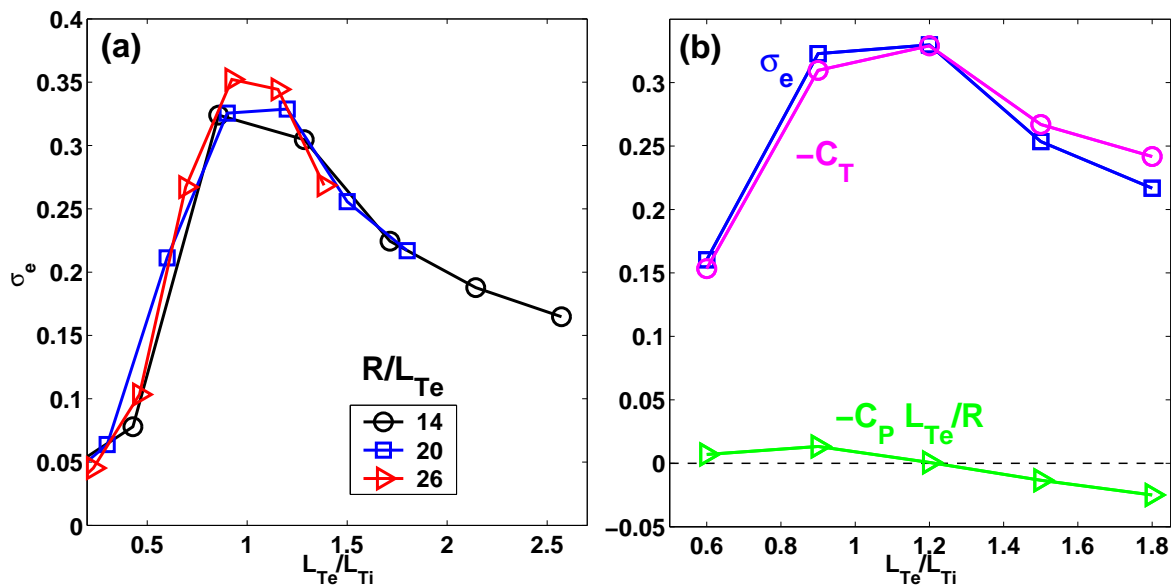


Figure 5.16: a) Stationary σ_e versus L_{Te}/L_{Ti} for different values of R/L_{Te} ; b) σ_e for the case with $R/L_{Te} = 20$ decomposed in its thermodiffusion contribution $-C_T$ and the other pinch contribution $-C_P L_{Te}/R$.

q profile case.

The stationary values of R/L_n for this base case are computed to be $[R/L_n]_{stat} = 4.7$; 5.4; 5.7; 5.4, respectively for rules $\langle 1 \rangle$, $\langle 2 \rangle$, $\langle 3 \rangle$, $\langle 4 \rangle$. We see that the main difference arises when using only one mode with respect to using more modes, but for more modes being employed, the different rules do not exhibit significant differences.

5.5.2 Dominant thermodiffusive contribution

We employ the base case parameters shown in the previous subsection to perform a double $R/L_{Te} - R/L_{Ti}$ scan using a single $k_y \rho_i = 0.23$. In figure 5.16(a) we show the result for the predicted stationary value of the parameter $\sigma_e = 1/\eta_e = [R/L_n]_{stat}/R/L_{Te}$ plotted versus the ratio of the two length scales L_{Te}/L_{Ti} , obtained varying R/L_{Ti} at fixed R/L_{Te} , for three values of R/L_{Te} . We see that σ_e is maximized at a value of $\sigma_e \approx 0.35$ when $L_{Te}/L_{Ti} \approx 1$, and that it decreases rapidly on the left for $L_{Te}/L_{Ti} \lesssim 1$, while it decreases slowly on the right for $L_{Te}/L_{Ti} \gtrsim 1$. The predicted σ_e is sustained almost entirely by the thermodiffusive pinch contribution C_T as shown in figure 5.16(b), where we plot again the stationary σ_e (squares) for the case with $R/L_{Te} = 20$ versus L_{Te}/L_{Ti} , decomposed in the two contributions $-C_T$ (circles) and $-C_P L_{Te}/R$ (triangles). The role of C_T is dominant and the other pinch contribution from C_P can be neglected in the region where σ_e has experimentally relevant values $\sigma_e \gtrsim 0.15$. The reasons are that: first $L_{Te}/R \ll 1$, second C_P depends on the average magnetic curvature drift ω_d which is decreased in value due to the presence of a small or negative magnetic shear compared to the monotonic q -profile

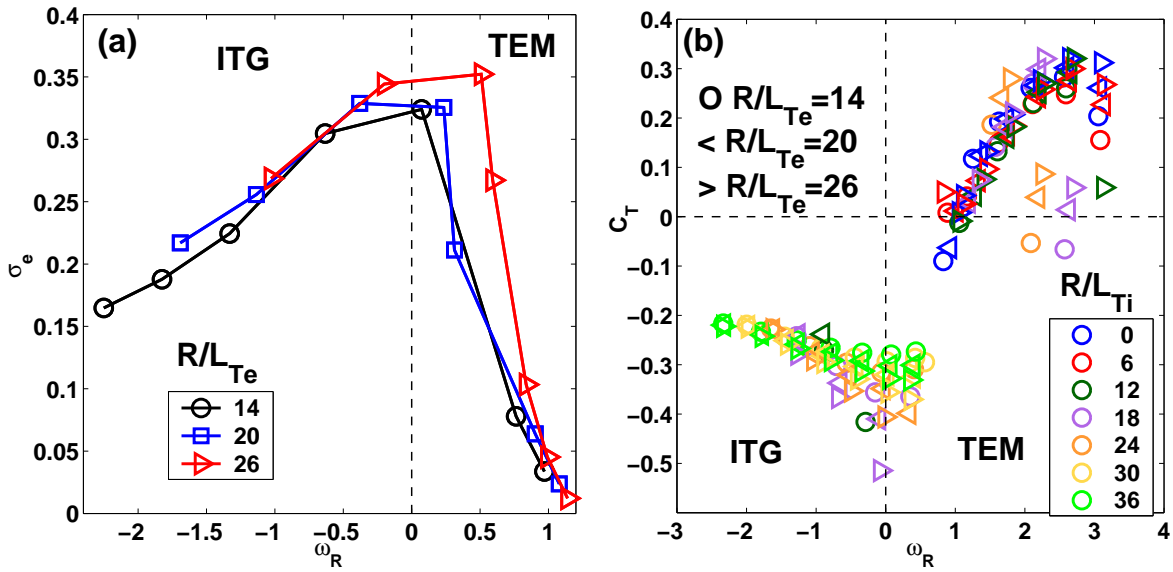


Figure 5.17: a) Stationary σ_e versus the mode real frequency ω_R ; b) Thermodiffusion coefficient C_T plotted versus ω_R for all the scan points.

scenario, and finally $T_e \gg T_i$.

To understand the behavior shown by σ_e when L_{Te}/L_{Ti} is far from unity, we plot it, in figure 5.17(a), versus the real frequency ω_R of the mode at $k_y \rho_i = 0.23$ corresponding to the stationary state. We recover again that the stationary state is maximized near $\omega_R \approx 0$. In addition, we again see how σ_e (i.e. $[R/L_n]_{\text{stat}}$) is strongly decreased in the TEM branch, while it decreases at a slower pace in the ITG branch.

We have just shown that the dominant contribution is the thermodiffusive part C_T . Its behavior is shown in figure 5.17(b) for all the scan points. We immediately see a strong similarity with figure 5.2(a), which allows us to understand the behavior of σ_e in figure 5.17(a).

We have previously discussed the role of TEM turbulence in limiting the increase of $[R/L_n]_{\text{stat}}$ due to a rapid decrease in the thermodiffusion pinch when TEM are dominant. However we see here that the $[R/L_n]_{\text{stat}}$ is reduced the more we go into the ITG regime. This is due to a slight decrease of C_T in the ITG branch. We find useful to make a simple sketch of the physical mechanism to clarify this point. In figure 5.18(a) we show three cases where the transition of the dominant mode from an ITG to a TEM happens at three different R/L_n^{In} . In figure 5.18(b) we show the pinch coefficient C_T which is a fixed function of the frequency ω_R , and which functional form is based on the previous results. Applying now the relation $R/L_n^{\text{Out}} = -C_T R/L_{Te}$ (we neglect C_P), where C_T is a function of ω_R and thus of R/L_n^{In} , we find the functional form of R/L_n^{Out} versus R/L_n^{In} which is shown in figure 5.18(c) for the three cases with different ITG \rightarrow TEM transition point. Note first that the maximum achievable $R/L_n^{\text{Out}} \approx 7.3$ and it is achieved at the R/L_n^{In} that

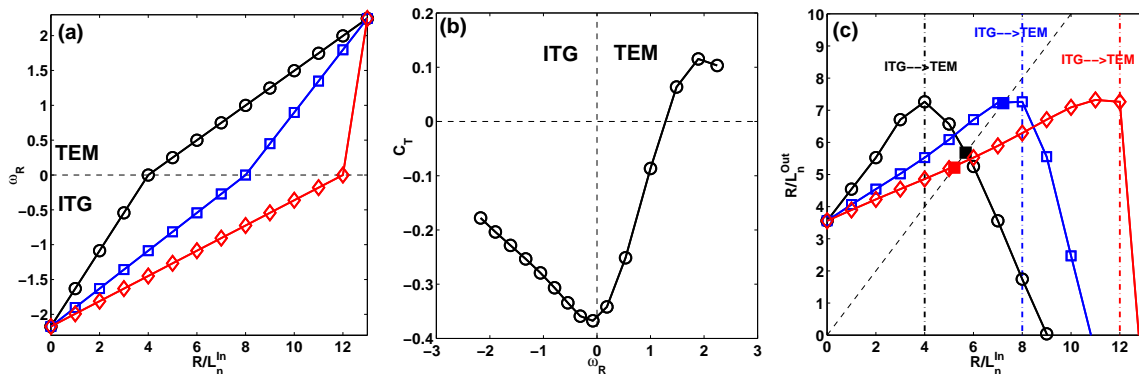


Figure 5.18: a) Different functional forms for ω_R as a function of R/L_n^{In} showing different ITG→TEM transition points; b) Functional form of C_T versus ω_R ; c) Resulting R/L_n^{Out} versus R/L_n^{In} which provide the stationary state depending on the relative position of the ITG→TEM transition point in R/L_n^{In} and the position of the maximal R/L_n^{Out} .

gives $\omega_R = 0$ and thus the minimum C_T . If we take the first case with $R/L_n^{\text{ITG} \rightarrow \text{TEM}} = 4$ (circles), we see that the maximum is in fact achieved before crossing the diagonal line. Because now C_T decreases rapidly in absolute value in the TEM branch, the stationary value will be lower than the maximal. We obtain $[R/L_n]_{\text{stat}} \approx 5.7$ and the respective turbulence regime has a dominant TEM. We take now the case with $R/L_n^{\text{ITG} \rightarrow \text{TEM}} = 8$ (squares). In this case the maximal value is reached near to the transition point, and the stationary value is now $[R/L_n]_{\text{stat}} \approx 7.2$, because the stationary state is at the transition where $\omega_R \approx 0$, and that is where C_T has the minimum negative value. In the third case, for which $R/L_n^{\text{ITG} \rightarrow \text{TEM}} = 12$ (diamonds), the stationary state is reached well before the transition point, which provides a lower stationary value of $[R/L_n]_{\text{stat}} \approx 5.2$.

This simplified picture explains the physical mechanism behind the maximization of the stationary R/L_n when ITG and TEM have similar amplitudes and no dominant mode can be defined. For this parameters scan, we find that the parameter that provides the $R/L_n^{\text{ITG} \rightarrow \text{TEM}}$ is $L_{\text{Te}}/L_{\text{Ti}}$, and we find that for $L_{\text{Te}}/L_{\text{Ti}} \lesssim 1$ the dominant mode in the stationary state is a TEM, while for $L_{\text{Te}}/L_{\text{Ti}} \gtrsim 1$, it is an ITG. The maximal $[R/L_n]_{\text{stat}}$ is thus located at $L_{\text{Te}}/L_{\text{Ti}} \approx 1$.

5.5.3 $s - \alpha$ TEM stabilization effect

In subsection 4.2.2 it has been shown that the eITB scenario is characterized by enhanced core confinement properties due to the reversal of the q profile and the appearance of a core region with magnetic shear $s \leq 0$. We now check if the code can reproduce this behavior via a double $s - q$ scan with the other parameters fixed at the base case.

In figure 5.19(a) we show the results for the stationary state $[R/L_n]_{\text{stat}}$ plotted versus

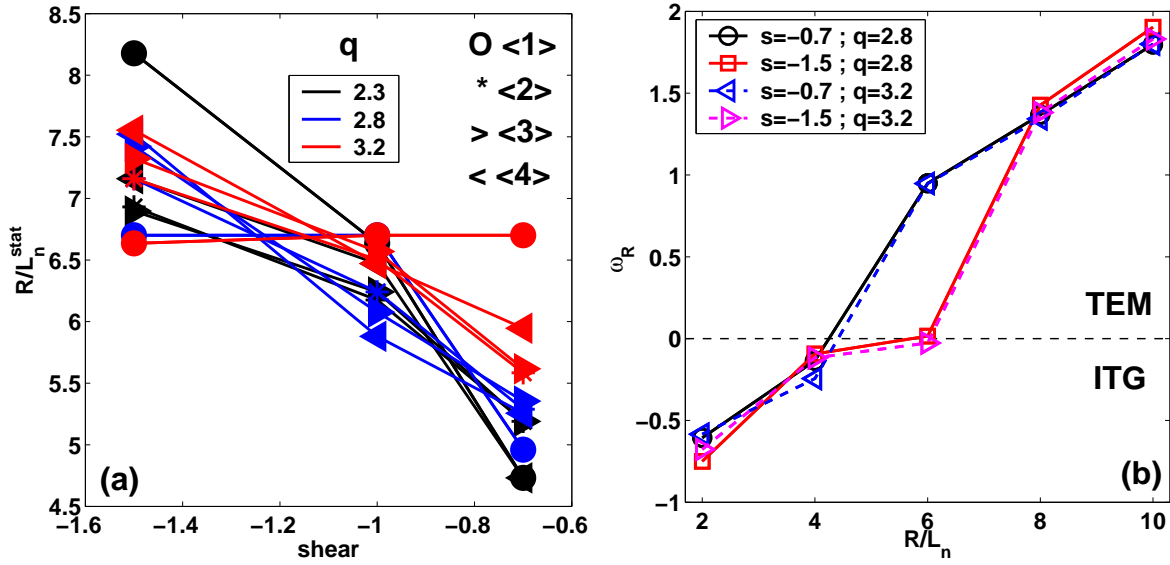


Figure 5.19: a) $[R/L_n]_{\text{stat}}$ plotted versus magnetic shear for three values of q and for the four quasi-linear rules (symbols); b) Real frequency ω_R of the mode at $k_y \rho_i = 0.18$ versus R/L_n for different combinations of shear and q (in the legend).

magnetic shear and for three values of q . We also show the differences between the four quasi-linear rules discussed before. It is interesting to observe how decreasing shear to more negative values and/or increasing q produces the effect of increasing the value of $[R/L_n]_{\text{stat}}$. As already seen for other cases, the values do not differ significantly using different rules. The highest value of $[R/L_n]_{\text{stat}}$ corresponds to a $\sigma_e \approx 0.4$, similar to the experimental value.

The mechanisms behind the stabilizing effect of s and q are several. First of all, as can be seen in figure 5.19(b), more negative shear and/or higher q provide an upshift in the value of R/L_n where the mode changes from an ITG to a TEM. This has a direct effect on the respective phase shift (or particle flux), shown with a similar plot in figure 5.20(a) for quasi-linear rule $\langle 2 \rangle$. Note how the particle flux crosses the zero at higher values in R/L_n according to the behavior of ω_R . As we discussed previously, this is due to the TEM becoming the dominant mode being the limiting factor to the increase of R/L_n .

The safety factor q enters into the gyrokinetic equation in two separate terms: in the parallel operator $k_{\parallel} \propto 1/q$ and in the magnetic curvature drift ω_d through $\alpha \propto q^2$. We show now that magnetic shear s and q do not enter in an 'independent' way in the stabilizing mechanism of TEMs but they are in fact merged in the magnetic curvature drift ω_d through the $s\theta - \alpha \sin \theta$ factor, equation (2.28). In subsection 3.4.2 we already presented a similar mechanism via gyro-Landau-fluid modelling of heat transport in the eITB. Here we obtain essentially the same result with gyrokinetic modelling. These results on $s - \alpha$ effect in the eITB modelling of particle transport have been reported in Ref. [87]. In figure 5.20(b) we plot the predicted $[R/L_n]_{\text{stat}}$, already shown in figure 5.19(a) versus

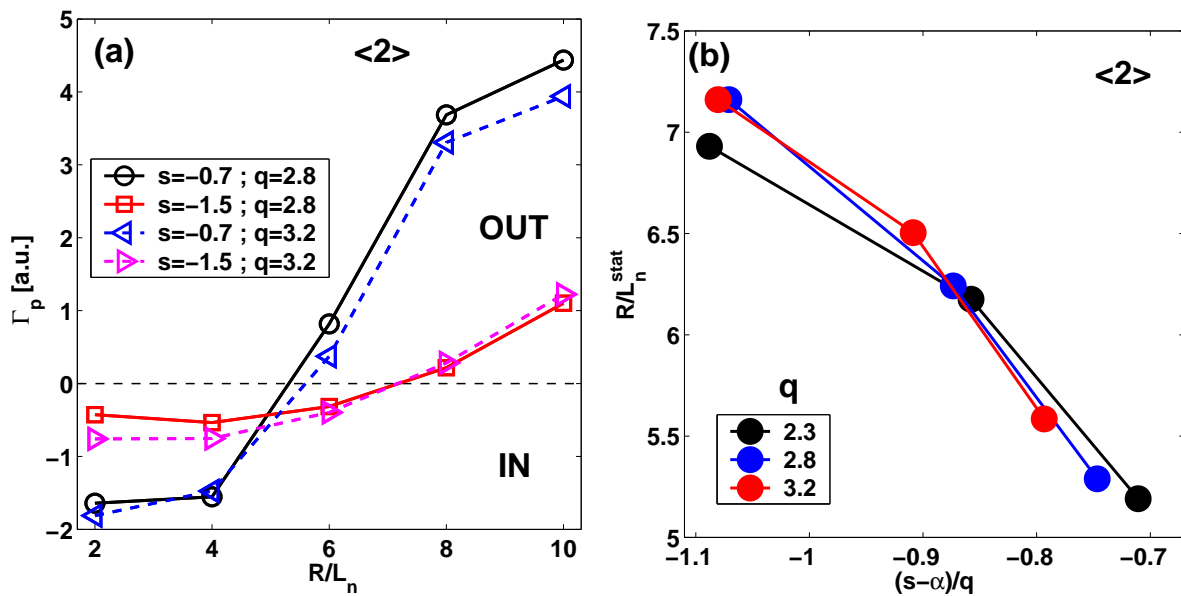


Figure 5.20: a) Phase shift $\tilde{\Gamma}_k$ (Γ_p in the plot) versus R/L_n for different combinations of shear and q obtained using quasi-linear rule $\langle 2 \rangle$; b) $[R/L_n]_{\text{stat}}$ versus $(s - \alpha)/q$ for the $s - q$ scan, obtained with quasi-linear rule $\langle 2 \rangle$.

shear, versus the parameter $(s - \alpha)/q$ for the case evaluated with quasi-linear rule $\langle 2 \rangle$ and the three values of q . Plotted versus this parameter, the points at same shear but different q become aligned. Namely, q has in fact a negative influence on the stability of TEM as it provides, through the k_{\parallel} term, a mechanism for TEM destabilization [59]. Increasing q , the final result will depend on the interplay between the less stabilizing $s/q \sim 1/q$ term (at fixed shear) and the more stabilizing $\alpha/q \sim q$ term. This is why in figure 5.19(a), the effect of q is evident on the points at $s = -0.7$ but it becomes small at $s = -1.5$.

We look into more details in the $s - \alpha$ combined effect here with a large $s - q$ scan with fixed parameters $R/L_{\text{Te}} = 20$, $R/L_{\text{Ti}} = 16$ and $R/L_n = 0.35R/L_{\text{Te}}$, for $k_y \rho_i = 0.23$. In figures 5.21(a,b,c,d) we show the results respectively for the growth rate γ (a), the frequency ω_R (b), the thermodiffusion coefficient C_T (c), and the other pinch coefficient C_P (d). To avoid a spurious effect coming from the k_{\parallel} term we fix the q entering in the parallel operator at a single value $q_{k_{\parallel}} = 2.8$. Note that the $s - q$ scan points fall on to one well defined curve when plotted against $(s - \alpha)$. As we already said this is also true if k_{\parallel} is allowed to change with q if we use the combined parameter $(s - \alpha)/q$.

Figure 5.21(a,b), γ and ω_R : the growth rate has a 'bell' shape with the maximum located around $(s - \alpha) \approx 1/2$, and decreases both on the left and on the right of this value. In the negative range of values of $(s - \alpha)$ the growth rate has a sharp drop until, for $(s - \alpha) \approx -2.5$, there is a well defined change in slope. Looking at the real frequency ω_R , we see that it indicates a dominant TEM (full symbols) in the positive range of $(s - \alpha)$,

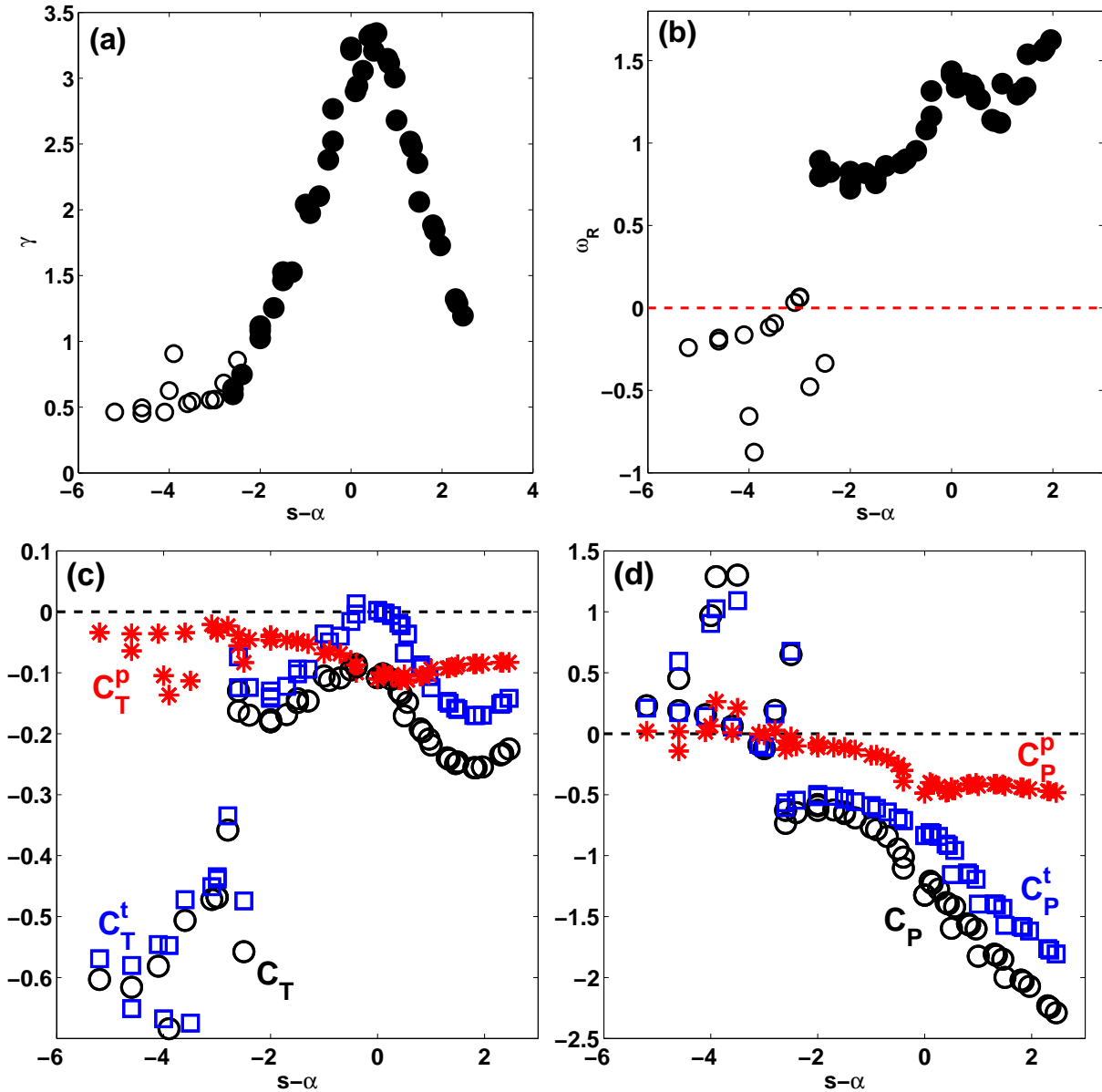


Figure 5.21: a) Most unstable mode growth rate γ for $k_y \rho_i = 0.23$ versus $s-\alpha$ (solid circles are TEM modes, empty circles are ITG modes) for a case with $R/L_{Te} = 20$, $R/L_{Ti} = 16$, $R/L_n^{\text{In}} = 6.1$; b) Most unstable mode real frequency ω_R versus $s-\alpha$, again divided into TEM branch (solid circles) and ITG branch (empty circles); c) Thermodiffusion coefficient C_T from trapped particles C_T^t (squares), from passing particles C_T^p (stars), and total (circles); d) Pure convection coefficient C_P , again with contributions from trapped (squares) and passing (stars) particles.

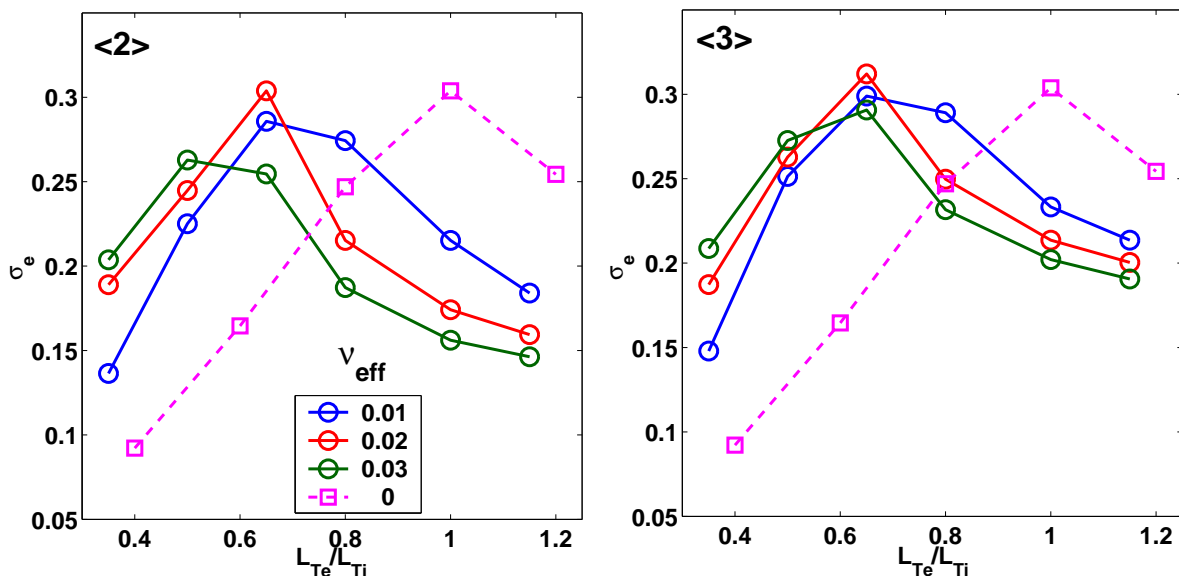


Figure 5.22: Stationary value of σ_e as a function of L_{Te}/L_{Ti} (where L_{Te} is kept fixed with $R/L_{Te} = 20$), for different values of the effective collisionality ν_{eff} . The two plots are obtained respectively with quasi-linear rules $\langle 2 \rangle$ and $\langle 3 \rangle$.

while it changes to an ITG (empty symbols) for $(s - \alpha) \lesssim -2.5$. We thus conclude that the TEM is strongly influenced by $(s - \alpha)$, and that for sufficiently negative values it is reduced in intensity such that the ITG can become the dominant mode.

Figure 5.21(c), C_T : the thermodiffusion coefficient is strongly linked to the mode type, and here we see that it is limited to values of ~ -0.1 in the TEM branch, while it jumps to values of ~ -0.6 in the ITG branch. Namely, decreasing $(s - \alpha)$ sufficiently can cause an abrupt increase in the density peaking due to the thermodiffusive contribution.

Figure 5.21(d), C_P : this coefficient has also a strong dependence on $(s - \alpha)$ through the curvature drift ω_d . We see that it attains low absolute values when $(s - \alpha)$ is sufficiently negative to obtain a strong stabilization of TEMs. This is also why this pinch contribution is negligible in the eITB negative shear scenario.

5.5.4 Effect of finite collisionality

The previous simulations have been done at zero collisionality. However the core of the eITB always presents a finite collisionality, even if it is of order $\nu_{eff} \sim 10^{-2}$. To tackle its effects we perform a double $\nu_{eff} - R/L_{Ti}$ scan on the base case.

The stationary σ_e is evaluated as a function of L_{Te}/L_{Ti} and shown in the two plot of figure 5.22, where each plot is obtained with a different quasi-linear rule, written in the top-left. The curves with circles are obtained at finite collisionality, and they are compared with the case at $\nu_{eff} = 0$ (squares). We see that a finite collisionality causes a shift of the curves to the left in the L_{Te}/L_{Ti} axis, indicating that we need a lower value

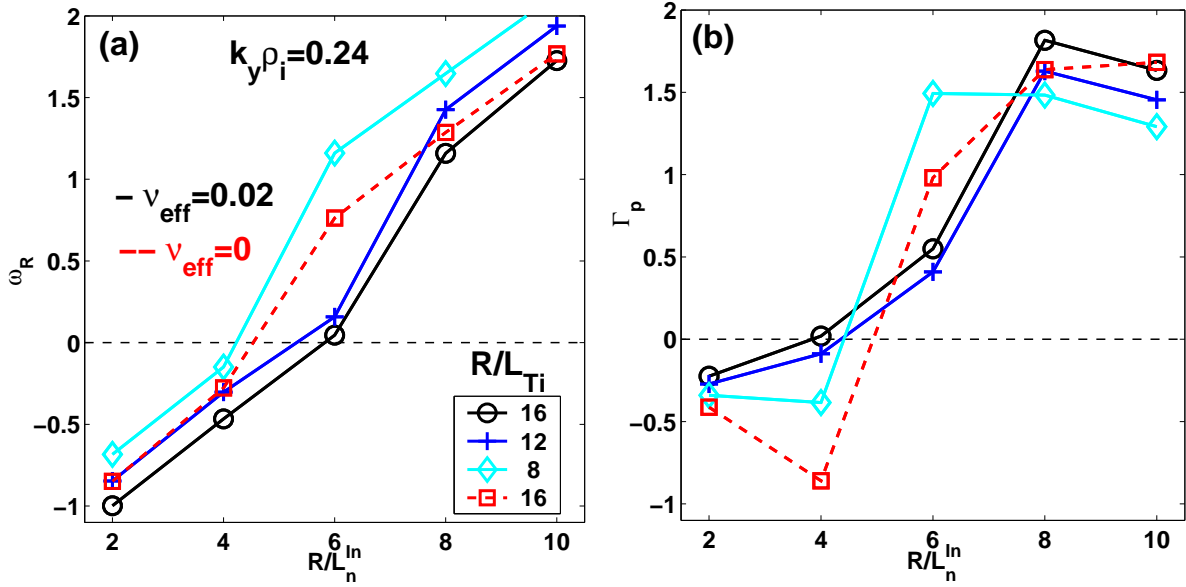


Figure 5.23: a) Mode frequency ω_R for wavenumber $k_y \rho_i = 0.24$ versus R/L_n^{In} for different values of R/L_{Ti} and ν_{eff} ; b) Same plot for the phase shift $\tilde{\Gamma}_k$ for wavenumber $k_y \rho_i = 0.24$.

of R/L_{Ti} at fixed R/L_{Te} to maximize the density peaking. In this case we find that at finite ν_{eff} , σ_e is maximized at $L_{\text{Te}}/L_{\text{Ti}} \approx 0.6$, while for $\nu_{\text{eff}} = 0$ we find $L_{\text{Te}}/L_{\text{Ti}} \approx 1$ for the maximum σ_e .

The reason can be understood remembering that the maximal σ_e is located near the ITG \rightarrow TEM transition point, i.e. where $\omega_R \sim 0$. This point, in the $R/L_{\text{Te}} - R/L_{\text{Ti}}$ parameters space, is located at $R/L_{\text{Ti}} \approx R/L_{\text{Te}}$, i.e. when the two modes drivers have the same strength. Collisionality, even at low levels, can have a significant effect in stabilizing TEM turbulence and thus pushing the ITG \rightarrow TEM transition point at higher values of R/L_n for the same R/L_{Te} and R/L_{Ti} , or at lower $L_{\text{Te}}/L_{\text{Ti}}$ at fixed R/L_n .

5.5.5 Impurities effect

Experimental data from X-rays collected from the core of TCV eITB plasmas show quite high estimations for the value of the effective charge Z_{eff} , which is observed to fluctuate in the range $1.5 \lesssim Z_{\text{eff}} \lesssim 3.5$, depending on the type of eITB plasma, on the wall conditions and on the accuracy of the estimation. Despite all the uncertainties, it is recognized that the carbon content in the core of the eITB is larger than in the Ohmic L-mode case.

We address this issue by performing a double parameters scan in Z_{eff} and R/L_{Ti} on the base case. We search for the stationary values of $[R/L_n]_{\text{stat}}$ and $[R/L_C]_{\text{stat}}$, obtained by matching both the conditions $\Gamma_{\text{turb}}^e = \Gamma_{\text{turb}}^C = 0$.

We perform these parameters scans at two values of ν_{eff} : $\nu_{\text{eff}} = 0$ and $\nu_{\text{eff}} = 0.02$, and using only one mode at $k_y \rho_i = 0.23$. We also set the magnetic shear to $s = -1$. In

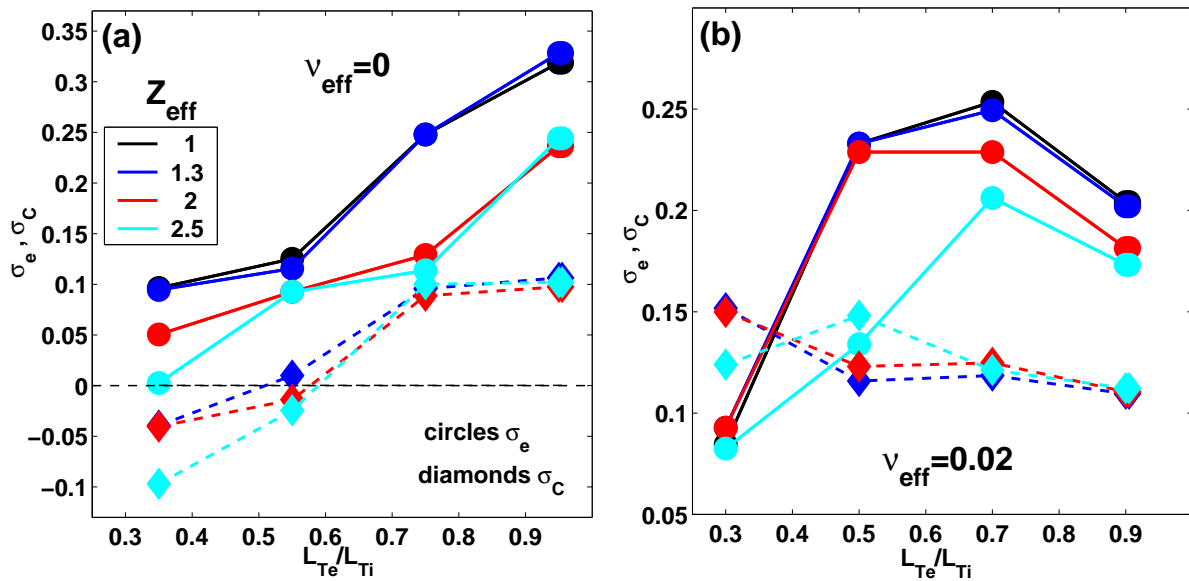


Figure 5.24: a) Stationary values of σ_e (solid, circles) and $\sigma_C = L_{Te}/L_C$ (dashed, diamonds) versus L_{Te}/L_{Ti} for different values of Z_{eff} , at $\nu_{eff} = 0$; b) Same plot obtained with $\nu_{eff} = 0.02$.

figures 5.24(a,b) we show the results of the simulations for the collisionless case in (a) and for the weakly collisional case with $\nu_{eff} = 0.02$ in (b). The key result from these plots is that the effect of carbon on the electron density peaking strongly depends on its charge concentration:

- when $Z_{eff} \lesssim 1.6$ there is no significant effect from the presence of carbon on the electron density peaking, i.e. carbon behaves as a passive species;
- when $Z_{eff} \gtrsim 1.6$ the presence of carbon reduces the value of the stationary electron density peaking at fixed L_{Te}/L_{Ti} ;
- the carbon density peaking is found to be lower than the electron density peaking for most of the scan points. Its dependence on Z_{eff} is not as large as the one shown by the electrons;
- The parametric dependence of σ_e versus L_{Te}/L_{Ti} is the same, although it seems to be shifted, such that at the same L_{Te}/L_{Ti} , σ_e is lower when Z_{eff} increases;
- σ_C increases with increasing L_{Te}/L_{Ti} in the collisionless case, it decreases at finite collisionality.
- The effect of finite collisionality is similar to the previously analyzed cases: the maximum σ_e is located at lower L_{Te}/L_{Ti} .

We conclude this part on the possible implications of these results for the interpretation of what the experiment shows: the impurity effect observed here suggests that, in the real plasma, the core carbon concentration should be limited to values of $Z_{eff} \lesssim 1.6$, otherwise there would be a relevant reduction of the stationary σ_e . Indeed in the experiments it

ρ_V	0.27	0.37	0.42	0.54	0.72	0.78
ϵ	0.07	0.1	0.12	0.16	0.21	0.23
q	3.9	3	2.7	2.9	4.4	5.2
shear	-0.9	-0.6	-0.5	0.9	1.8	2.1
R/L_{Te}	7.8	13.4	14.8	11.7	10.6	12.33
R/L_n^{EXP}	1.9	5.9	6.8	5.3	6.2	6.9
ν_{eff}	0.011	0.015	0.019	0.032	0.054	0.063
T_e/T_i	3.36	3.03	2.85	2.42	1.82	1.64

Table 5.1: *Experimental parameters from #29859 at $t = 1.5$ s.*

seems that $Z_{eff} > 2$ in the eITB, contradicting the last statement. This paradox is not clearly solved at the present times and requires more detailed study of the eITB scenario with high Z_{eff} concentration from both the experimental and theoretical point of view.

The physical mechanism behind the flattening effect driven by high impurity concentration can be seen in figure 5.25 where, for the case at $\nu_{eff} = 0$, we show the contours of ω_R plotted in the plane $R/L_n - Z_{eff}$ for different combinations of the parameters $R/L_C - R/L_{Ti}$. We see that the value of R/L_n where the mode changes from an ITG to a TEM, i.e. where ω_R crosses zero, is lower when increasing either Z_{eff} or R/L_C . Indeed, increasing R/L_{Ti} has a positive effect on the ITG→TEM transition point, pushing it upwards. The effect of a high impurity concentration is to have a destabilizing effect on TEMs, thus limiting the increase of $[R/L_n]_{stat}$ as already discussed before.

5.5.6 Comparison with the experiment

The gyrokinetic model has been applied previously to specific parameters scan to evidence the single details of the physical mechanism for the density barrier sustainment. However we want to compare the theoretical prediction against a realistic experimental case where all the parameters vary simultaneously.

We take as an example TCV eITB fully non-inductive discharge #29859 at $t = 1.5$ s, for which a discussion of the relevant profiles has already been presented in subsection 4.2.2. We analyze the stationary R/L_n at three radial positions for which the relevant parameters are given in table 5.1.

Note that both R/L_n and R/L_{Ti} are scanned to find the stationary state predicted by the code as a function of R/L_{Ti} and then we will compare the result with the experimental value indicated in the table. For this simulation no impurity is present, i.e. we assume $Z_{eff} = 1$. The results are shown in figures 5.26(a), for the stationary R/L_n , and in (b) for the stationary σ_e .

The model seems to reproduce the experimental trend along the radial interval although the value itself is underestimated. No relevant differences between the quasi-linear rules

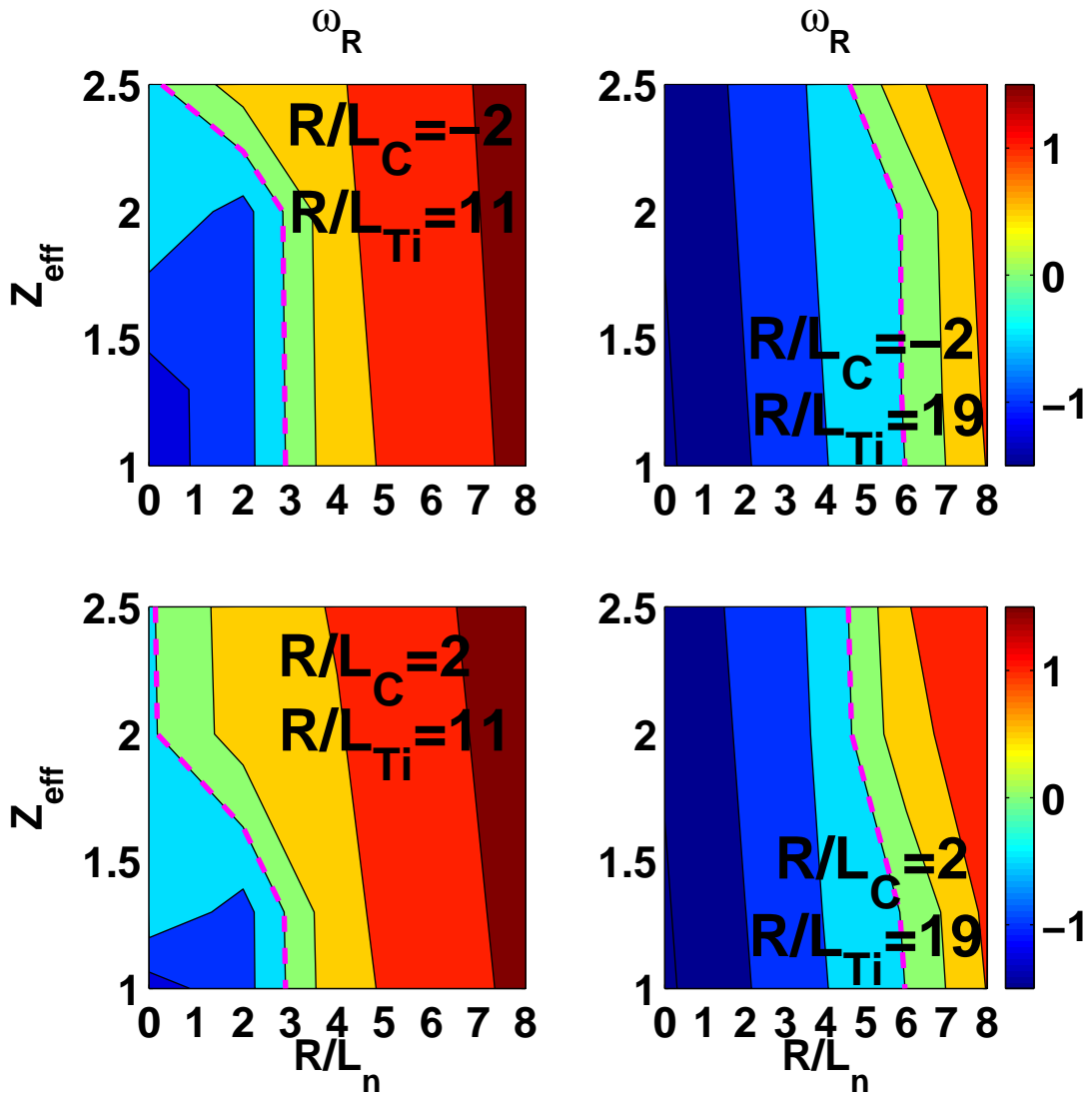


Figure 5.25: Values of the mode frequency ω_R as a function of R/L_n and Z_{eff} for different combinations of R/L_C and R/L_{Ti} . The dashed line identifies $\omega_R = 0$ where ITG and TEM have similar growth rates.

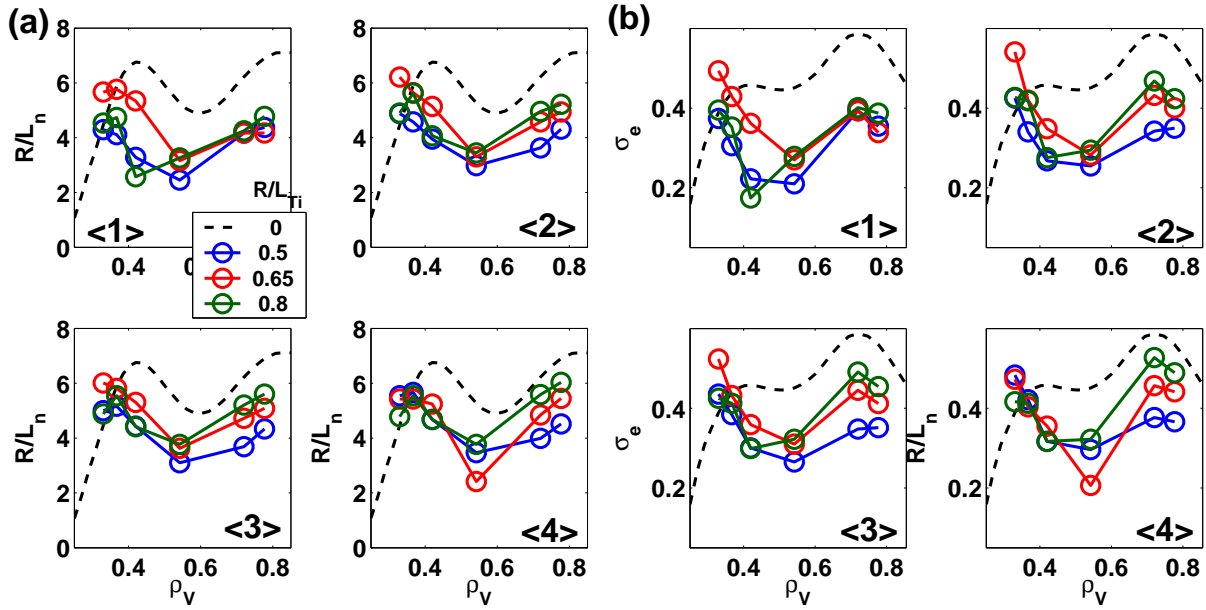


Figure 5.26: a) Simulated R/L_n profile (circles) for different values of L_{Te}/L_{Ti} (legend). The dashed line ('0' in the legend) is the experimental profile. Each subplot is obtained with a different quasi-linear rule; b) Same plots but for the stationary σ_e .

are observed. The value of L_{Te}/L_{Ti} modifies the result in the sense that $L_{Te}/L_{Ti} \approx 0.65$ provides the maximal σ_e inside the barrier, while it is $L_{Te}/L_{Ti} \approx 0.8$ that provides the result closest to the experimental value.

We look now at the behavior of turbulence outside and inside the barrier to understand in deeper details these results. In figure 5.27(a) we plot the spectrum of the mixing length estimate for $|\tilde{\Phi}_k(0)|^2$, using quasi-linear rule < 4 > and normalized to the value of $\gamma / \langle k_{\perp}^2 \rangle$, for the case with $L_{Te}/L_{Ti} = 0.65$ and at two radial locations $\rho_V = 0.37$ (circles), which is inside the barrier, and $\rho_V = 0.72$ (crosses), well outside the barrier. We see that for the radial location inside the barrier the spectrum peaks at a higher $k_y \rho_i$, resulting in a lower turbulence level in the long wavelength range $k_y \rho_i \approx 0.15$, usually the region where the peak is located for monotonic q profile cases.

In figure 5.27(b) we plot the radial profiles of the mode growth rate γ (circles and crosses) and frequency ω_R (right and left triangles) for the mode at $k_y \rho_i = 0.12$ (circles and right triangles) and for the mode at the $k_y \rho_i$ where the value of $|\tilde{\Phi}_k(0)|^2$ peaks (crosses and left triangles). The case is the same as figure 5.27(a). We can draw the following conclusions:

- The mode growth rate is strongly reduced in the long wavelength range inside the barrier $\rho_V \lesssim 0.45$;
 - This strong reduction is on the TEM branch, as we observe a residual ITG component;
 - Outside the barrier the turbulence is TEM dominated, particularly towards the edge;
- All these findings confirm the results obtained in chapter 3 in the case of the study of

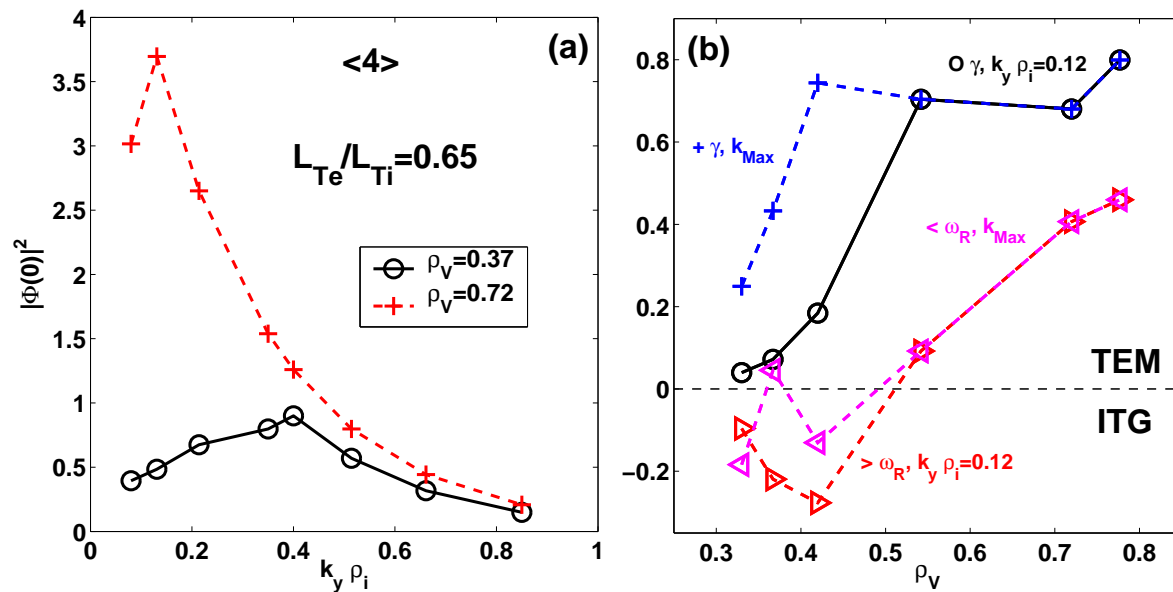


Figure 5.27: a) Spectrum of the mixing length estimate for $|\tilde{\Phi}_k(0)|^2$, from quasi-linear rule $\langle 4 \rangle$, versus $k_y \rho_i$ for the case with $L_{Te}/L_{Ti} = 0.65$, at two radial locations (legend); b) Radial profile of the growth rate γ (circles and crosses) and of the frequency ω_R (triangles) for the mode at $k_y \rho_i = 0.12$ (circles and right triangles) and for the mode at the $k_y \rho_i$ where the mixing length estimate for $|\tilde{\Phi}_k(0)|^2$ is maximal (crosses and left triangles).

electron heat transport inside the barrier. The appearance of a region with negative magnetic shear and high Shafranov-shift is beneficial on both the energy confinement, resulting in a higher value for $[R/L_{Te}]_{stat}$, and the particle confinement, resulting in a higher value for $[R/L_n]_{stat}$, through the reduction of TEM activity and the consequent decrease of the energy diffusivity together with an enhancement of the inward directed thermodiffusive particle pinch.

5.6 Summary

The theory of particle transport, in particular for stationary conditions, is reviewed and discussed in detail with regards to the transport driven by background turbulence. The model adopted is a quasi-linear model based on the linearized electrostatic gyrokinetic equation developed in the ballooning representation. We show how the two main mechanisms which provide the turbulent pinch arise naturally from the theory. These mechanisms are respectively thermodiffusion ($C_T R/L_{Te}$), driven by particle diffusion in energy phase space due to the turbulent field, and another convective term (C_P) which arises from the parallel and perpendicular particle drifts resonating with the turbulent potential fluctuations. The physics of these two pinch mechanisms is analyzed and shown to be different for passing and trapped particles due to the completely different drifts.

The model is then applied to study the physics of the turbulent pinch and the resulting

stationary state for several parameter scans to also interpret known experimental results. In particular we show how the theory can predict both the observation of a density profile flattening with increasing T_e/T_i at low collisionality and the flattening with increasing ν_{eff} at low values of T_e/T_i , with the observation of a maximal peaking at the ITG–TEM transition. These effects have been previously observed experimentally and interpreted from first–principles as discussed in Ref. [63]. We also show the non–trivial effect of adding the neoclassical Ware pinch, which could lead to a drastic change in both the stationary R/L_n , determined by $\Gamma_{\text{turb}} = 0$ only, and the turbulence properties.

The eITB scenario is then analyzed to interpret the experimental observations on the density profile behavior. The code predicts several of the observed features: a dominant thermodiffusive mechanism through C_T , the stabilizing effect of the magnetic shear, of the α parameter, and of a finite collisionality on the TEM to provide a higher density peaking. We also discussed the role of impurities through a carbon concentration scan, showing that when the impurity content increases, a reduction of the density peaking is observed due to a destabilization of the TEM, suggesting that the impurity content should be limited to moderate values to explain the density peaking observed in the experimental scenario. Finally we compare the model predictions against a real eITB discharge and we find a good qualitative agreement, although the code tends to underestimate the value of the stationary R/L_n with respect to the experimental value. However it correctly reproduces the improved confinement features that we already found for the heat transport studies.

Chapter 6

Impurity particle transport in TCV L-modes

6.1 Introduction

Impurity transport is another aspect of particle transport that has relevance for the performance of a Tokamak fusion plasma. In particular, it is necessary to know how the impurity density profile behaves depending on the other plasma parameters and on the operational scenario. In TCV, impurities are diagnosed with the CXRS diagnostic. Carbon is the main impurity due to the presence of graphite walls and CXRS measurements provide carbon density, temperature, and toroidal rotation profiles.

This chapter deals with the interpretation of the measurements of carbon density profiles observed in TCV L-mode plasmas with Ohmic heating, with a brief discussion of cases with auxiliary electron heating. In particular we assess the role of different transport sources to explain why at low total plasma currents, or high values of q_{95} , the carbon density profile shows a stronger peaking than the electron density profile. To accomplish this goal, we simultaneously model the electrons and the carbon ions behavior, showing how the interplay of turbulent transport, modelled with quasi-linear gyrokinetic theory as shown in the previous chapter, and neoclassical transport seem to explain all the experimental observations in a self-consistent and elegant way.

6.2 Stationary carbon transport in TCV L-modes

It has been reported that in TCV Ohmic L-mode discharges an accumulation of impurities, in particular carbon, is observed at low plasma currents [88, 89]. We briefly present here the experimental observations to understand the main issue. We then present in details some case to clarify the relevant parameters range. Before starting we acknowledge the fact that this phenomenon of impurity accumulation (in particular for high- Z impurities) in L-mode plasmas has also been reported in other machines [90, 91] and is

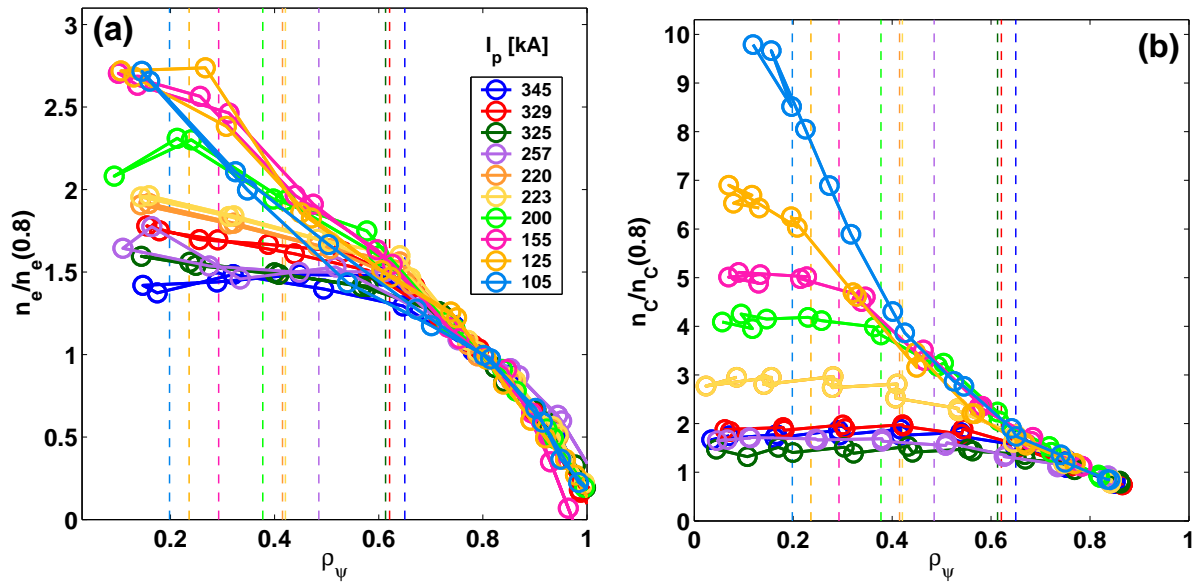


Figure 6.1: a) n_e profiles from raw data mapped on ρ_ψ for different values of the total plasma current I_p . The profiles are normalized to the value at $\rho_\psi \sim 0.8$. Shown also the position of the $q = 1$ surface estimated with the formula $\rho_{inv} \propto 1/I_p$ where q is the safety factor; b) Same plot for carbon density profiles n_C normalized to $n_C(\rho_\psi = 0.8)$.

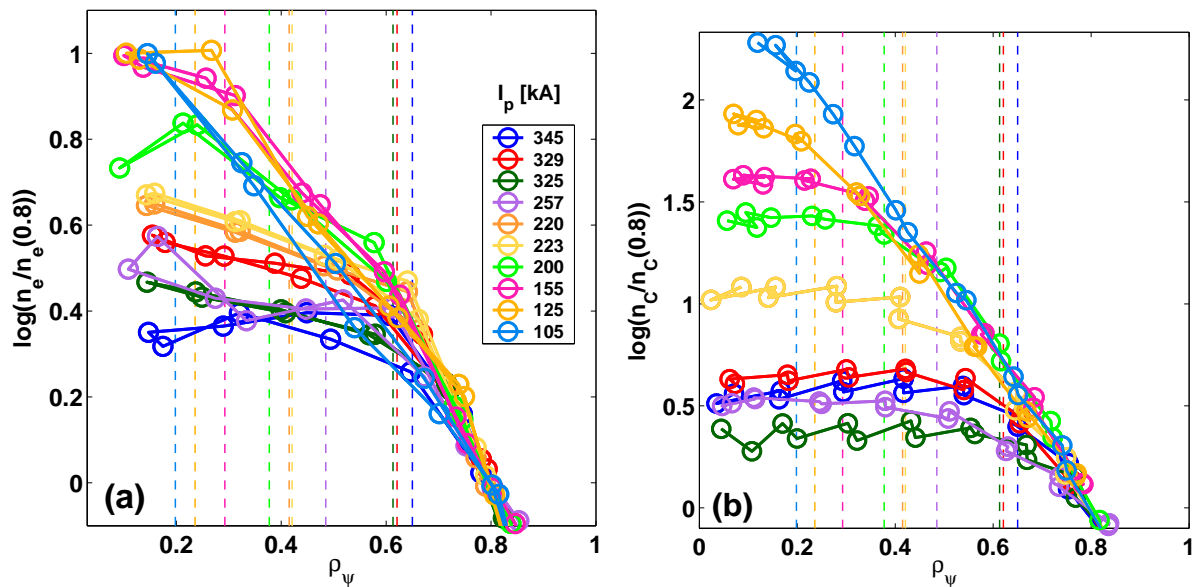


Figure 6.2: a,b) Same plots as in figure 6.1(a,b) but for the natural logarithm of the normalized densities.

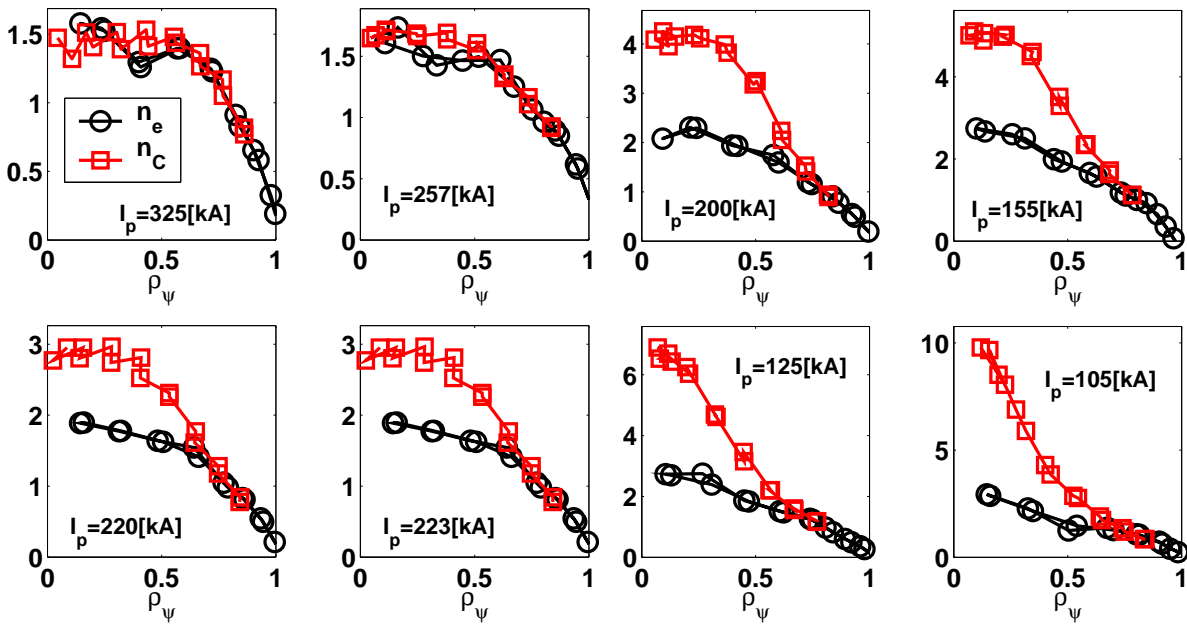


Figure 6.3: Comparison of normalized $n_e/n_e(0.8)$ and $n_C/n_C(0.8)$ profiles for different total plasma currents.

in general believed to be of a neoclassical nature.

6.2.1 Current scan in TCV Ohmic L-mode discharges

In figures 6.1(a,b) we show the electron n_e and carbon n_C density profiles normalized to their respective values at $\rho_\psi = 0.8$ for different plasma currents I_p indicated in the legend. All the points are taken from raw data and averaged over several profiles with the same current. We also show the position of the $q = 1$ surface with a dashed line of the corresponding color. The value of this radial position, ρ_{inv} , is produced with the simple formula $\rho_{\text{inv}} \propto 1/I_p$, which rudely approximates the experimental trend, where the proportionality constant is chosen to fit a case where the $q = 1$ surface location is known. The profiles with high currents and large sawteeth are strongly flattened up to the edge region and no significant difference is observed between the two species profiles. As current is reduced, the inversion radius moves inwards, and the profiles start to show different structures, in particular a certain degree of peaking is observed. For electrons this peaking is less pronounced as it can be seen in the two plots looking at the two curves representing $I_p = 155$ kA for example. It is also interesting to note that the profiles of both electron and carbon density, outside $\rho_\psi \approx 0.7$ are practically insensitive on the value of I_p , indicating a stiffness and a completely different regime with respect to the core region. To have a glance at the behavior of the profiles in terms of local gradients, we also show the natural logarithm of the normalized profiles, namely $\log [n_e/n_e(0.8)]$ and $\log [n_C/n_C(0.8)]$, in figure 6.2(a,b). Taking as an example the curve with $I_p = 155$ kA, we

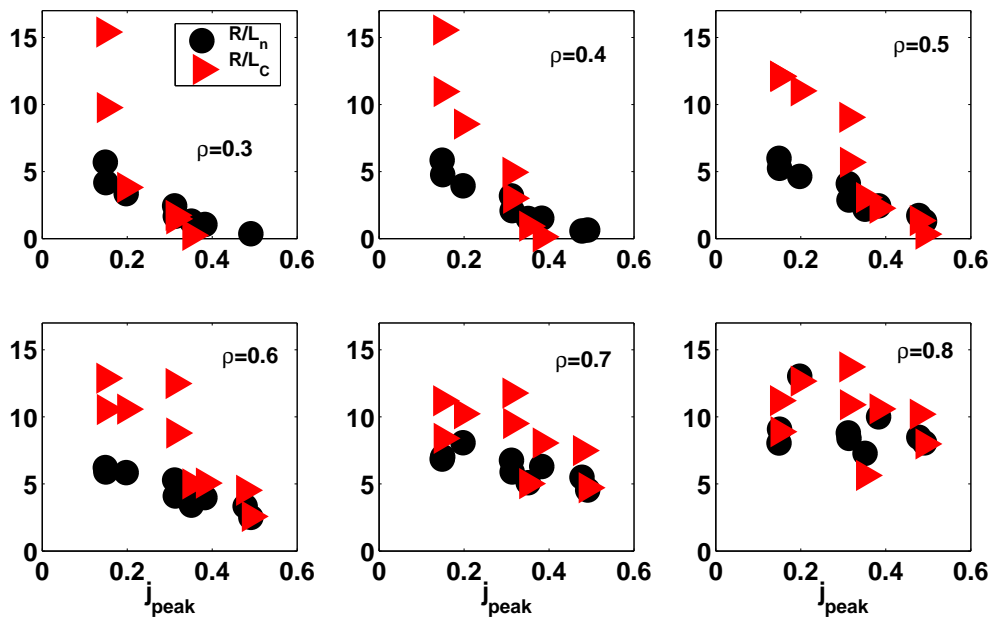


Figure 6.4: Normalized logarithmic gradients for electrons R/L_n (circles) and for carbon R/L_C (triangles) at different radial positions, plotted versus the current peaking parameter $j_{\text{peak}} = \langle j_q \rangle / j_0 q_0$ (see text).

can see that in the outer region $0.6 \lesssim \rho_\psi \lesssim 0.8$ the electrons and the carbon ions show a comparable local logarithmic density (slightly higher for carbon), while from $\rho_\psi \approx 0.6$ down to the inversion radius $\rho_{\text{inv}} \approx 0.3$ the carbon logarithmic gradient increases faster, displaying a larger normalized gradient.

We compare now more closely the electron and carbon density profiles to look at the differences along the radial interval. In figure 6.3 we present several subplots, each one reporting the normalized density profiles of n_e (circles) and n_C (squares) for a fixed plasma current. We see that for the highest currents of $I_p \sim 250 \div 300$ kA, the two profiles are similar with comparable gradients in the edge region. In the core region both profiles are flattened by sawteeth extending on a large radius.

For intermediate and low currents $I_p \lesssim 250$, sawteeth are smaller and the profiles can develop their natural gradients inside the core. In this regime we assist at this 'accumulation' phenomenon for which the carbon density gradient increases well above the electron density gradient for $\rho_\psi \lesssim 0.6$. However, in the edge region the two gradients seem to follow again without any dependence on the current. Decreasing the plasma current seems to have a stronger effect on carbon, for which the normalized profile reaches values of ~ 10 at $I_p \sim 100$ kA, while for the electrons the peaking does not increase specifically.

To appreciate the striking difference between the behavior of carbon and electrons with respect to plasma current, in figure 6.4 we plot the normalized logarithmic gradients of electrons, R/L_n , and for carbon, R/L_C , for different radial positions, versus the current

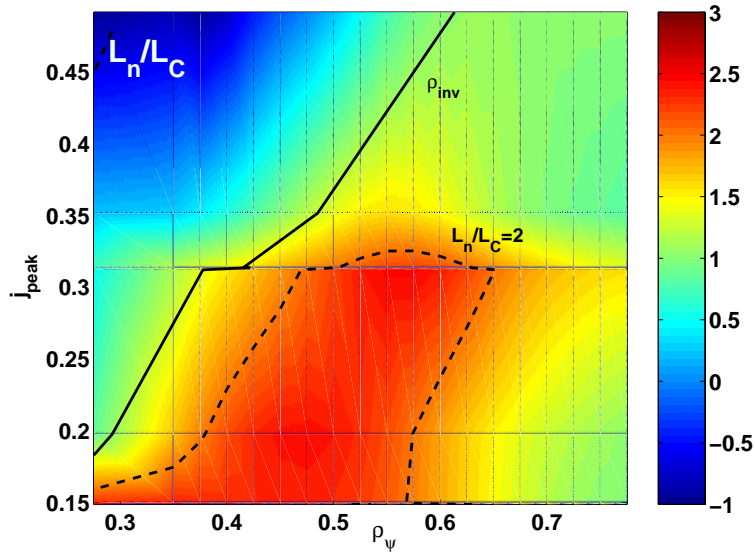


Figure 6.5: 2D color plot of electron to carbon density length scales ratio L_n/L_C plotted versus ρ_ψ (x -axis) and j_{peak} (y -axis). We show also the position of the sawtooth inversion radius ρ_{inv} versus j_{peak} (solid line), and the contour of the $L_n/L_C = 2$ line (dashed).

density peaking factor $j_{\text{peak}} = \langle jq \rangle / j_0 q_0$, where $\langle \dots \rangle$ is the surface integral and j_0, q_0 are respectively the on-axis current density and safety factor. Let us start for example from the first subplot of figure 6.4 which represents data from $\rho_\psi = 0.3$. At this position, transport is dominated by sawtooth activity until the current is sufficiently low to reduce the inversion radius down to $\rho_{\text{inv}} \lesssim 0.3$, which happens for $j_{\text{peak}} \sim 0.15$, such that only for the points below this value we have that $R/L_C > R/L_n$, and we find almost $R/L_C \sim 2R/L_n$. This behavior is the same up to $\rho_\psi \approx 0.6$. We observe that the 'detachment' of the carbon logarithmic gradient from the electrons logarithmic gradient happens at higher values of j_{peak} , namely we have that $R/L_C > R/L_n$ in the following ranges: $j_{\text{peak}} \lesssim 0.25$ for $\rho_\psi = 0.4$, $j_{\text{peak}} \lesssim 0.3$ for $\rho_\psi = 0.6$. As we will also see later, it is important to not interpret this kind of dependence on j_{peak} as a pure effect of local turbulent/neoclassical transport as this correlation is indeed provided by the global MHD instability: the sawtooth crash. We can elucidate this crucial point by showing a 2D plot of $L_n/L_C = (R/L_C)/(R/L_n)$ plotted versus j_{peak} on y -axis and ρ_ψ on x -axis, in figure 6.5. We also show the inversion radius position (solid line) and the contour of the value $L_n/L_C = 2$ (dashed line). We immediately see that the region where $R/L_C \sim 2R/L_n$ follows the position of the inversion radius, on the left of which no gradient is built. Note also that in the region $\rho_\psi \gtrsim 0.6$ the electrons and carbon have comparable normalized gradients $R/L_C \sim R/L_n$.

From these experimental observations we can conclude that the carbon density profile

behaves differently with respect to the electron density profile in the core of the plasma, when the core region is not affected by sawteeth, i.e. at low plasma currents, and in that case we observe $\partial \log n_C / \partial \rho \gtrsim \partial \log n_e / \partial \rho$ in the interval $0.3 \lesssim \rho_\psi \lesssim 0.6$. However, because the sawteeth behavior is strongly linked to the value of the plasma current itself, from these data it is not possible to assess if a real dependence of both $\partial \log n_e / \partial \rho$ and $\partial \log n_C / \partial \rho$ exists on I_p , or if only a dependence through the sawteeth activity appears and must be accounted for [93].

For the reasons discussed before, we now assess the theoretical model to interpret the two clear observations that:

- 1) At low currents, and in the core region, carbon shows a stronger peaking with almost double of the electron density logarithmic gradient;
- 2) In the edge region the two logarithmic gradients are comparable and they are not sensitive to the value of the total plasma current.

ECH effect at low current

When auxiliary ECH heating is applied in the center of the low current plasmas we can observe a strong flattening of both the electrons and the carbon density profiles. In figures 6.6(a,b) we show the normalized profile of electrons and carbon density for a case at $I_p \approx 120$ kA with (circles) and without (squares) auxiliary heating. In the former case the heating is applied on-axis with a total power of 1 MW. We see a flattening of both profiles, in particular on the carbon profile. This change in the local gradient is evident up to $\rho_\psi \approx 0.6$ while the outer region is essentially unaffected.

6.2.2 Detailed parameters analysis

We extract a set of two discharges from which the relevant plasma profiles are taken and analyzed to define the parameters range that we will use in the theoretical analysis. To avoid the problem arising from the core MHD activity we choose two low current plasmas for which the sawtooth activity is seen to be absent.

In figure 6.7(a) we show the electrons (circles, diamonds) and the carbon (squares, diamonds) density profiles normalized to the value at $\rho_\psi = 0.8$ for two discharges (#30487 and #30073) at low current ($I_p \sim 100$ kA), respectively Ohmically heated (solid) and with auxiliary central ECH heating of 0.9 MW total (dashed). The vertical thin dashed lines indicate the three spatial positions where the parameters are taken to be used for the simulations. These parameters, namely q , magnetic shear s , R/L_{Te} , R/L_{Ti} , T_e/T_i and ν_{eff} , are shown in figure 6.7(b) plotted versus the aspect ratio a/R for the Ohmic ('OH') and the ECH ('ECH') case. They are also summarized in table 6.1.

Looking at the parameters differences in figure 6.7(b) between the Ohmic and the ECH

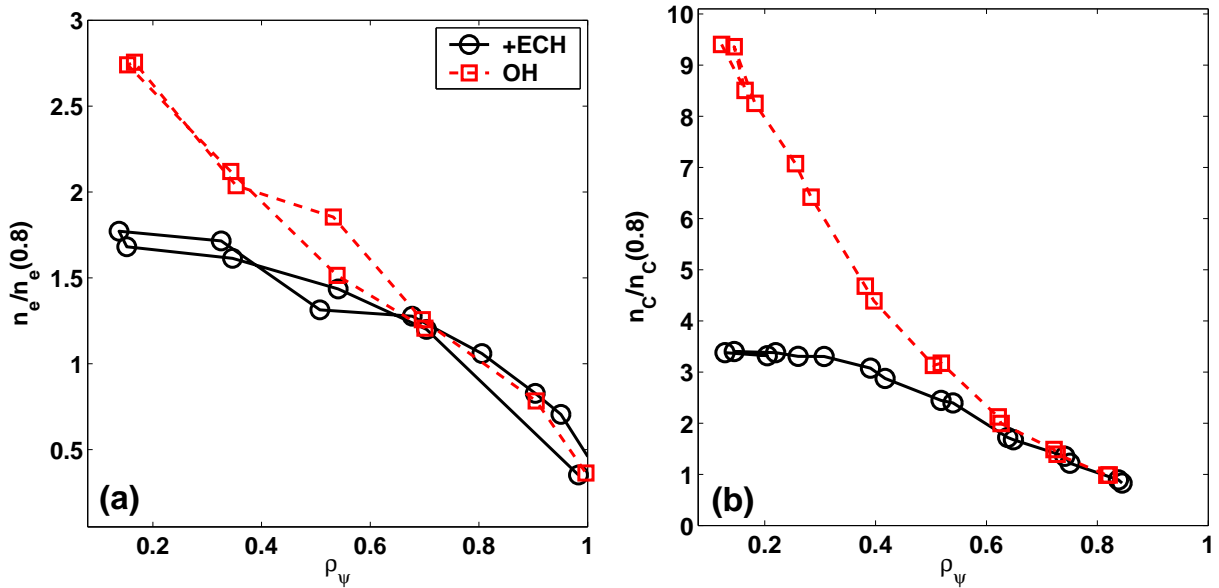


Figure 6.6: a) Normalized electron density profile with (circles) and without (squares) auxiliary ECH heating; b) Same plot for the carbon normalized density profile.

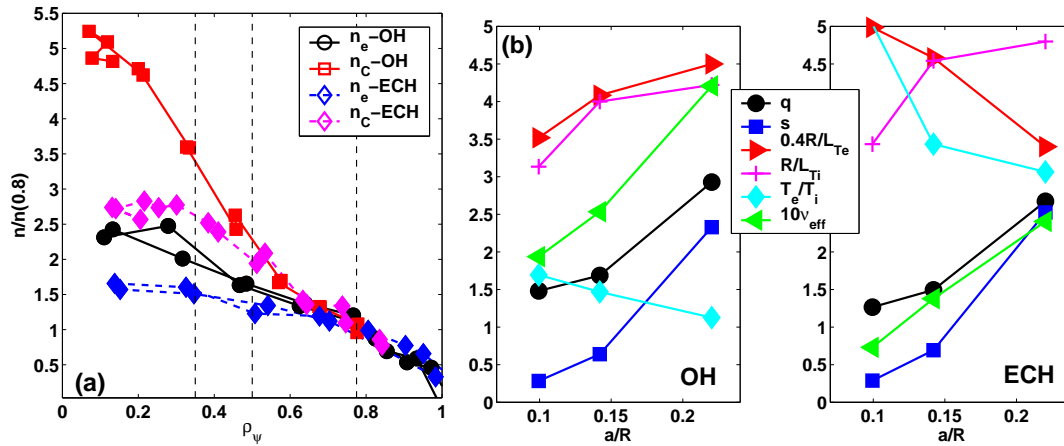


Figure 6.7: a) Normalized density profiles for electrons (circles, diamonds) and for carbon ions (squares, diamonds) for two low current discharges with Ohmic heating (solid) and with auxiliary ECH heating (dashed). The three vertical lines indicate the positions where the parameters are taken for the simulations; b) Values of the relevant parameters (names in the legend) plotted versus the local aspect ratio a/R for the two cases: with only Ohmic heating ('OH') and with auxiliary ECH heating ('ECH').

Case	1	2	3	4	5	6
Type	OH	OH	OH	ECH	ECH	ECH
ϵ	0.1	0.14	0.22	0.1	0.14	0.22
q	1.5	1.7	3	1.26	1.5	2.67
s	0.28	0.64	2.3	0.28	0.7	2.5
R/L_{Te}	7	8.2	9	12.5	11.4	8.5
R/L_{Ti}	3.1	4	4.2	3.4	4.5	4.8
T_e/T_i	1.7	1.5	1.1	5	3.4	3
ν_{eff}	0.2	0.25	0.42	0.07	0.14	0.24

Table 6.1: *Parameters set for the theoretical analysis to check for relevant dependencies.*

case we see that the most relevant changes are in the local temperature inverse length scale R/L_{Te} , which slightly increases at $a/R \approx 0.1 \div 0.14$ and decreases at $a/R \approx 0.22$, in the temperature ratio T_e/T_i , which strongly increases all along the considered radial interval, and in the effective collisionality ν_{eff} , which is reduced by a factor of about 2.

6.3 Theoretical analysis

We now discuss the theoretical tools that we adopt to interpret the experimental results just shown. Both neoclassical transport and turbulent transport will be taken into account for all the species: electrons, carbon C^{6+} ions and deuterium ions. The model adopted here is the same as the one used for electron particle transport and presented in Section 5.2 but with some modifications.

A scan in the electron density normalized gradient R/L_n is performed for each case. We take advantage of the low carbon concentration in these experimental scenario, i.e. $1.2 \lesssim Z_{\text{eff}} \lesssim 2$, corresponding to a charge concentration factor of $Zn_C/n_e \lesssim 20\%$ for carbon, to assume the carbon species as **passive**, which means that, while the curve for electrons of $[V_{\text{turb}}/D_{\text{turb}}]^e$, as a function of R/L_n , is calculated, the respective quantity $[V_{\text{turb}}/D_{\text{turb}}]^C$ for carbon is assumed to be independent of R/L_C , allowing us to perform only two simulations for each case to evaluate the zero of the linear function $\Gamma^C \propto \partial \log n_C / \partial \rho - [V_{\text{turb}}/D_{\text{turb}}]^C$. If the carbon species is not assumed to be passive, a full double scan in $R/L_n - R/L_C$ should be carried out. We have performed this calculation for a specific case and we confirmed that the presence of carbon does not alter significantly the turbulence properties for $Z_{\text{eff}} \lesssim 2$.

We now analyze separately the neoclassical and the turbulence-driven contributions to the particle transport of carbon impurity.

6.3.1 Calculation of stationary values

We employ the GS2 code to check what linear gyrokinetic theory predicts for electron and carbon density peaking in this kind of scenario. The total turbulent flux is obtained summing the spectrum over this range with weight (i.e. quasi-linear rule) $|\tilde{\Phi}_k(0)|^2 \propto (\gamma / \langle k_\perp^2 \rangle)^2$.

Adopting the procedure for the addition of the Ware pinch that we showed at the end of subsection 5.2.3 we could, in first approximation, define the stationary state for electrons and carbon ions density normalized gradient analogously as:

$$\begin{aligned} \left[\frac{R}{L_n} \right]_{\text{stat}} &= -\frac{RV_{\text{turb}}^e}{D_{\text{turb}}^e} - \frac{RW_p}{D_{\text{turb}}^e} \\ \left[\frac{R}{L_C} \right]_{\text{stat}} &= -\frac{RV_{\text{turb}}^C}{D_{\text{turb}}^C} - \frac{RV_{\text{neo}}^C}{D_{\text{turb}}^C} \end{aligned} \quad (6.1)$$

The factors V/D can be evaluated as functions of R/L_n and R/L_C by means of the linear gyrokinetic model for each species. Equation (6.1) was obtained assuming $D_{\text{neo}}^e \ll D_{\text{turb}}^e$ and $D_{\text{neo}}^C \ll D_{\text{turb}}^C$. The latter condition is not evident *a priori* and may not be true in realistic conditions. To avoid this approximation we use the fact that the ratio $D_{\text{turb}}^C/D_{\text{turb}}^e$ can be evaluated from the linear simulations. In addition we can approximate $D_{\text{turb}}^e \approx \lambda_D^e \chi_e$. In this way, and introducing λ_D^e , we can write the two stationary profiles as:

$$\begin{aligned} \left[\frac{R}{L_n} \right]_{\text{stat}} &= -\frac{RV_{\text{turb}}^e}{D_{\text{turb}}^e} \left(\frac{D_{\text{turb}}^e}{\lambda_D^e \chi_e} \right) - \frac{RW_p}{\lambda_D^e \chi_e} \\ \left[\frac{R}{L_C} \right]_{\text{stat}} &= -\frac{RV_{\text{turb}}^C}{D_{\text{turb}}^C} \frac{\delta_{eC} \lambda_D^e \chi_e}{D_{\text{neo}}^C + \delta_{eC} \lambda_D^e \chi_e} - \frac{RV_{\text{neo}}^C}{D_{\text{neo}}^C + \delta_{eC} \lambda_D^e \chi_e} \end{aligned} \quad (6.2)$$

where $\delta_{eC} = D_{\text{turb}}^C/D_{\text{turb}}^e$, $RV_{\text{turb}}^e/D_{\text{turb}}^e$ and $RV_{\text{turb}}^C/D_{\text{turb}}^C$ are evaluated from the linear gyrokinetic simulations and χ_e from experimental power balance considerations. The quantity in parenthesis, namely $D_{\text{turb}}^e/(\lambda_D^e \chi_e)$, is assumed to be ≈ 1 and will not be calculated.

Note that the only free parameter in this model is λ_D^e which gives the relationship between the unknown D_{turb}^e and the experimentally estimated χ_e . However in the literature we can find experimental estimates of this value, for example in Ref. [92] it is found $\lambda_D^e \approx 0.1$, while other studies assume $\lambda_D^e \approx 0.25 \div 1$. We note that to be fully self-consistent we may take λ_D^e , defined as $\lambda_D^e = D_{\text{turb}}^e/\chi_e^{\text{turb}}$, from the gyrokinetic simulations, and then assume $\chi_e^{\text{turb}} = \chi_e$. In this case there is no 'free' parameter except for the experimentally evaluated $\chi_e = \chi_e^{\text{PB}}$. In the following we will use this last model to have full consistency. The role of λ_D^e and of the Ware pinch for TCV L-mode Ohmic plasmas with/without ECH heating has been addressed, in an empirical way, in Refs. [94, 65, 95]. It was found that the Ware pinch alone can sustain the density peaking in Ohmic plasmas when $\lambda_D^e \approx 0.05 \div 0.1$ and in ECH plasmas when $\lambda_D^e \approx 0.01$. The latter clearly indicates that the Ware pinch

should not be relevant for electron heated discharges, while the result for Ohmic heated discharges is not conclusive as turbulent transport was neglected in that analysis. In the following we address both transport sources to clarify the mechanism at play in these Ohmic and ECH heated cases.

6.3.2 Neoclassical contributions

The neoclassical coefficients $D_{\text{neo}}^{\text{C}}$ and $V_{\text{neo}}^{\text{C}}$ are provided by different effects which role depends on the impurity collisional regime. In general the coefficients are composed by three contributions: classical [$D_{\text{CL}}, V_{\text{CL}}$], Pfirsch–Schluter [$D_{\text{PS}}, V_{\text{PS}}$], and Banana–Plateau [$D_{\text{BP}}, V_{\text{BP}}$]. Following Ref. [96], we want to discuss which could be the relevant one at play in our experimental cases. In fact, assuming only neoclassical transport, the impurity density profile n_{C} is provided by a relation of the type:

$$\frac{n_{\text{C}}}{n_{\text{C}}(0)} = \left(\frac{n_{\text{i}}}{n_{\text{i}}(0)} \right)^Z \left(\frac{T_{\text{i}}}{T_{\text{i}}(0)} \right)^{\alpha_1(Z)} \quad (6.3)$$

where $\alpha_1(Z)$ depend on the type of transport: for the classical transport $\alpha_1(Z) = Z-1$, for the Pfirsch–Schluter transport $\alpha_1(Z) \approx -(Z-1)/2$, and for the Banana–Plateau transport $\alpha_1(Z) \approx 3(Z-1)/2$. Now, including anomalous transport and assuming that anomalous transport contribute only with a finite diffusivity D but no convection, and assuming that the ratio between neoclassical and anomalous diffusivity is constant $\eta = D_{\text{neo}}^{\text{C}}/D$, we can modify equation (6.3) as:

$$\frac{n_{\text{C}}}{n_{\text{C}}(0)} = \left(\frac{n_{\text{i}}}{n_{\text{i}}(0)} \right)^{\eta Z} \left(\frac{T_{\text{i}}}{T_{\text{i}}(0)} \right)^{\eta \alpha_1(Z)} \quad (6.4)$$

We have estimated the η required to fit the experimental carbon profiles for the Ohmic case #30487 in the three different regimes. In practice we find that for the classical transport an $\eta \approx 0.3$ is required, for the Pfirsch–Schluter transport we need an $\eta \approx 1$, while for the Banana–Plateau transport we need an $\eta \approx 0.15$. Already from this rude estimate we see that the banana–plateau transport is the good candidate to explain the observed experimental profile without assuming a too large (eventually unphysical) ratio of neoclassical to anomalous diffusivity. The reason is that the ion temperature effect is strongly enhanced, and contributing with positive peaking, due to the power $15/2$ (for $Z = 6$). We thus speculate that the observed carbon accumulation at low current might be given by a strong inward neoclassical convection in the banana–plateau regime balancing the background turbulent diffusion, i.e. small effect from anomalous convection is expected. To corroborate this hypothesis we have estimated the dominant regime by looking at the value of the neoclassical collisionality ν_* for carbon. We find that up to $\rho_{\psi} \approx 0.5 \div 0.6$ the collisionality regime is the banana–plateau.

For the following analysis we take the same equations as in Ref. [96] for the classical diffusivity D_{CL} , the Pfirsch–Schlüter contribution D_{PS} , and the Banana–Plateau contribution D_{BP} . The latter is given by the approximate expression:

$$D_{\text{BP}} = 4.04q \frac{\sqrt{A_{\text{C}}} T_{\text{i}}^{3/2}}{RZ^2 B_0^2} \quad (6.5)$$

where q is the safety–factor, A_{C} the carbon atomic mass, and the ion temperature T_{i} is in keV. The actual equation for D_{BP} (and V_{BP}) is more complicated as it contains cross–species viscosities which have to be numerically evaluated, for example as it has been done for some cases using the STRAHL code [97] and it results in somewhat lower values of the convection term V_{BP} [89]. In fact, the neoclassical pinch V_{BP} found in Ref. [89] for other discharges similar to the ones analyzed here is about two–three times lower than the one estimated here. In this sense we intend the following results as *preliminary* with respects to more detailed calculations that will be pursued in the future. However, a paradoxical situation arises if both the anomalous *and* the neoclassical pinch are found insufficient to explain the experimental behavior, at least in the linear limit. We like to state that the results shown in the following, even if they show a discrete quantitative agreement, will have to be rechecked with more accurate calculations of the neoclassical pinch. Indeed we find that these results provide a sort of ‘upper bound’ to what one should need for the neoclassical pinch. In the following, for our purposes, we assume the simple estimate of equation (6.5), leaving more detailed study for the future. The neoclassical convection velocity V_{BP} is calculated as

$$V_{\text{BP}} = Z D_{\text{BP}} \left(\frac{\partial \log n_{\text{i}}}{\partial r} + \frac{3(Z-1)}{2Z} \frac{\partial \log T_{\text{i}}}{\partial r} \right) \quad (6.6)$$

The total carbon diffusivity and convection velocity are evaluated as sums of the three contributions. For electrons, we will take into account the Ware pinch in the way explained at the end of subsection 5.2.3. The neoclassical thermodiffusion–type convection will be neglected as it is proportional to the electron particle diffusivity.

For Ohmic discharge #30487, characterized by a $q_{95} = 4.7$, we report the profiles of the calculated neoclassical diffusivity $D_{\text{neo}}^{\text{C}} = D_{\text{CL}} + D_{\text{PS}} + D_{\text{BP}}$ and convection velocity $V_{\text{neo}}^{\text{C}}$ in figure 6.8 (solid lines), where we also show the electron heat transport coefficient χ_{e} calculated from power balance and the Ware pinch W_{p} . For this Ohmically heated case, at mid–radius, we find: $D_{\text{neo}}^{\text{C}} \approx 0.1$ [m²/s], $\chi_{\text{e}} \approx 1.5$ [m²/s], $V_{\text{neo}}^{\text{C}} \approx -5$ [m/s], $W_{\text{p}} \approx -0.4$ [m/s]. The electron neoclassical diffusivity is estimated to be $D_{\text{neo}}^{\text{e}} \sim 10^{-3}$ [m²/s] and will be neglected. The carbon neoclassical diffusivity is $\sim 0.1\chi_{\text{e}}$. The selected ECH case is discharge #30073 and the same parameters are shown in figure 6.8 in dashed lines. Note that χ_{e} is strongly increased in the outer region $\rho_{\psi} \gtrsim 0.5$, and that the neoclassical Ware pinch is strongly reduced in absolute value. For carbon: the neoclassical diffusivity is slightly increased and the neoclassical pinch is slightly reduced.

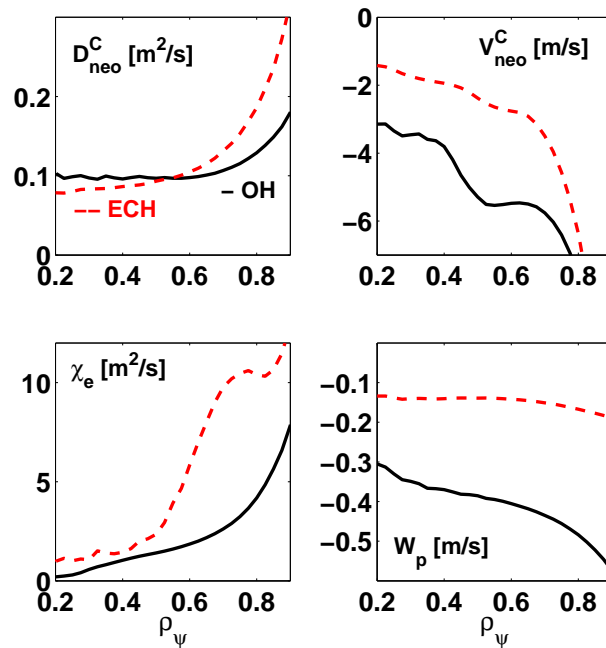


Figure 6.8: Radial profiles of the carbon neoclassical particle diffusivity $D_{\text{neo}}^{\text{C}}$, neoclassical convection $V_{\text{neo}}^{\text{C}}$, the electron heat transport coefficient from power balance χ_e and the Ware pinch W_p . The solid lines represents Ohmic discharge #30487 at $t = 1.35$ s, while the dashed lines pertain to ECH discharge #30073 at $t = 1.31$ s.

6.3.3 Linear gyrokinetic impurity transport coefficients

The carbon impurity pinch term $[V_{\text{turb}}/D_{\text{turb}}]^{\text{C}}$ can be shown to have a form analogous to the one for electrons, see equation (5.21):

$$[V_{\text{turb}}/D_{\text{turb}}]^{\text{C}} = -C_{\text{T}}^{\text{C}} g_1 \frac{\partial \log T_i}{\partial \rho} + \frac{C_{\text{P}}^{\text{C}}}{R} \quad (6.7)$$

where $g_1 = \langle |\nabla \rho| \rangle$ is a metric coefficient. The two pinch coefficients C_{T}^{C} and C_{P}^{C} have been evaluated analytically and numerically for different type of impurities in Ref. [80] and Ref. [98]. Qualitative agreement with experimental trends has been found and reported in Ref. [99].

The thermodiffusion contribution has a coefficient C_{T}^{C} which scales as $1/Z$ and thus is expected to be small for carbon with respect to deuterium. The other coefficient C_{P}^{C} is composed of a contribution coming from the magnetic curvature drift, analogous to the C_{P} from trapped electrons, and of another contribution that remains finite at large Z and scales as $1/q$, it is inward directed in ITG dominated turbulence and outward directed in TEM dominated turbulence. However, this contribution is limited in amplitude and is not expected to explain the large gradients observed in the low current plasmas in TCV. In figures 6.9(a,b) we show the range of variation of these two pinch coefficients for carbon. We plot C_{T}^{C} in figure 6.9(a) and C_{P}^{C} in figure 6.9(b) versus the most unstable mode real

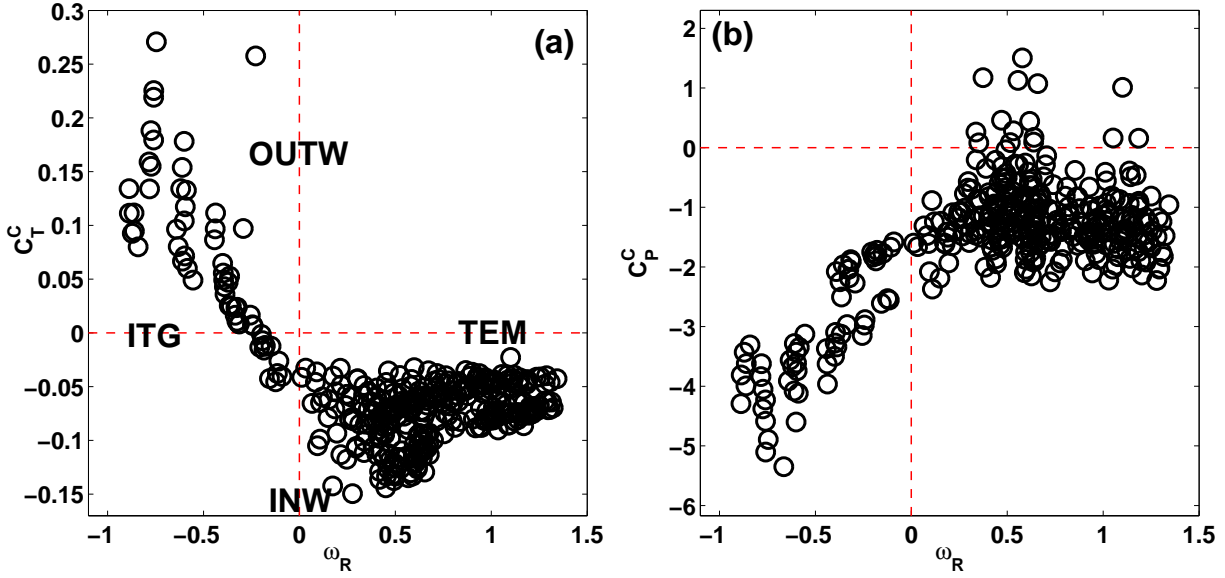


Figure 6.9: a) Carbon thermodiffusion coefficient C_T^C versus ω_R for the most unstable mode at $k_y \rho_i = 0.18$ from ~ 300 GS2 simulations obtained with several parameters scan; b) The other pinch coefficient C_P^C .

frequency ω_R for the wavenumber $k_y \rho_i = 0.18$. The points are obtained from ~ 300 GS2 simulations with several parameters scan to cover both the ITG and the TEM branch.

As expected from theory, we see that the thermodiffusion coefficient C_T^C is inward directed in TEMs and becomes outward directed in ITG, contrary to electrons as this pinch goes like $\sim 1/Z$. Its magnitude is also lower than the electrons one and it is limited to $C_T^C \approx -0.1 \div -0.15$ near the minimum.

The other pinch coefficient C_P^C can attain large negative (inward directed) values for strong ITG turbulence due to the k_{\parallel} -driven term. This contribution goes to zero at $\omega_R \sim 0$ and in TEM turbulence it can be outward directed. However here we find that the total C_P^C stays inward directed in TEM with values of $C_P^C \approx -2 \div -1$.

Considering both the ITG and the TEM branch, and assuming, as observed in the experiment, a $R/L_{Ti} \sim 7$, we obtain a range of variation of $0 \lesssim R/L_C (= -C_T^C R/L_{Ti} - C_P^C) \lesssim 3$ in the TEM branch and $1.5 \lesssim R/L_C \lesssim 4$ in the ITG branch.

We could already speculate that the behavior observed in the experimental current scan might be ascribed to the effect of the appearance, when sawteeth are small, of a large, inward directed, C_P^C term due to the background, strong ITG turbulence. However in the core region. i.e. in the range $\rho_{\psi} \sim 0.1 - 0.4$, the Ware pinch could play a role as discussed in subsection 5.4.4, such that the stationary state will be located near the ITG-TEM transition where the C_P^C term is not as strong as in ITG dominated turbulence. Or it might be that the Ware pinch is still not sufficient to produce a relevant upshift of the stationary state, namely if $|W_p| \ll |V_{\text{turb}}^e|$; in this case the low current cases can exhibit

core ITG-dominated turbulence and thus a large inward C_p^C pinch contribution to explain the experimental behavior. In this case however, as we have shown in subsection 5.4.3 and subsection 5.4.4, the total core stationary R/L_n is not at its maximum, and it might very well be significantly lower than the experimental value.

In the following Section we will put together all these elements and see in what range of parameters we can have quantitative agreement with the experimental values. However already from what has been shown in this subsection we expect the turbulent pinch to be moderate and not sufficient to explain the large peaking observed experimentally.

6.4 Interpretation of the experimental behavior

The set of simulations shown in table 6.1 is run to find the stationary profiles of electrons and carbon density normalized gradients as from equations (6.2), where the only external parameter is $\chi_e = \chi_e^{\text{PB}}$. In figure 6.10(a) we show the result for the Ohmic case (first three cases of table 6.1). In full circles we plot the stationary electron normalized gradient $[R/L_n]_{\text{stat}}$, while with the empty circles we plot the turbulent part alone given by $-\frac{RV_{\text{turb}}^e}{D_{\text{turb}}^e}$. With triangles, respectively full and empty, we show the stationary carbon normalized gradient $[R/L_C]_{\text{stat}}$ and its turbulent part alone. In figure 6.10(b) we plot the same quantities for the case with ECH heating (last three cases of table 6.1).

From these two figures we clearly see that for electrons the neoclassical part always provides a very small contribution. On the other hand, the carbon density profile is almost entirely sustained by neoclassical transport in the Ohmic case, and partially in the ECH case, where the profile is flattened all along the radial interval. Indeed, for electrons there is a flattening effect when going from the Ohmic to the ECH case, and that is mainly due to a reduction in the turbulence-driven inward pinch plus a small contribution from a reduced neoclassical pinch. For carbon, the flattening effect with ECH is mainly due to the reduction in the neoclassical term, namely the second contribution on the right hand side of equation (6.2), due to a reduction of V_{neo}^C and to an increase of both χ_e and D_{neo}^C . We now clarify the behavior of the different quantities in terms of turbulence behavior with respect to the dominant regime.

6.4.1 Detailed transport analysis

For each radial position of figures 6.10(a,b) we analyze the steady-state diagrams according to the definition given in subsection 5.2.3. We show the results for $\rho = 0.35$ in figures 6.11(a,b), respectively for the Ohmic and the ECH case, for $\rho = 0.5$ in figures 6.12(a,b), and for $\rho = 0.75$ in figures 6.13(a,b). In each figure we plot the behavior of R/L_n and R/L_C as calculated by the theoretical model as a function of R/L_n^{In} . The

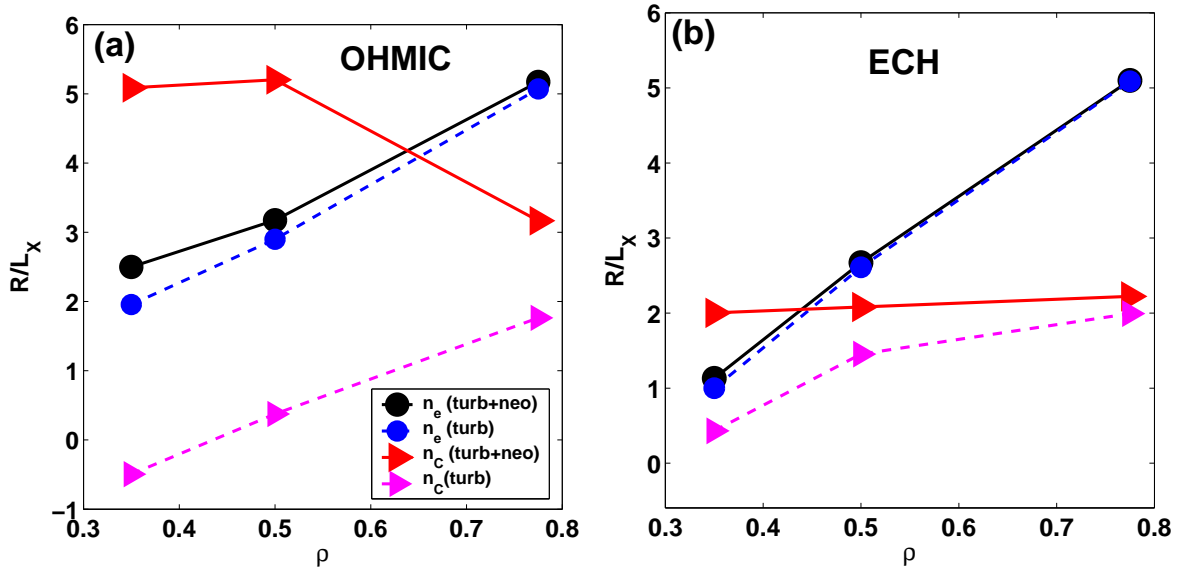


Figure 6.10: a) Stationary profiles of density normalized gradients for electrons without Ware pinch (circles, dashed) and with Ware pinch (circles, solid), and for carbon without neoclassical pinch (triangles, dashed) and with neoclassical pinch (triangles, solid) for the Ohmic heating case ; b) Same plot for the ECH case.

electron normalized gradient R/L_n is shown as the total of neoclassical+turbulent part (right triangles, solid line), and as the turbulent part alone (circles, dashed line). The carbon normalized gradient is shown in the same way: total (diamonds) and turbulent alone (left triangles). We also show the frequency ω_R of the mode with highest transport parameter $\gamma / \langle k_\perp^2 \rangle$ (pentagrams, dashed line). The stationary points are identified by the crossing of the different lines with the vertical dot-dashed line, determined by $[R/L_n]_{\text{stat}} = [R/L_n]_{\text{out,total}} = R/L_n^{\text{In}}$.

- $\rho = 0.35$, Ohmic, figure 6.11(a): first of all it is interesting to note the non-trivial effect when the Ware pinch is taken into consideration. In this case, $-RW_p/\chi_e^{\text{PB}}$ is not small as seen by comparing R/L_n^{turb} with $R/L_n^{\text{turb+neo}}$. The turbulent pinch alone would provide a stationary state at $R/L_n \approx 0.9$ (circles, dashed line, intersection with the diagonal) in the ITG regime ($\omega_R < 0$), while the total $[R/L_n]_{\text{stat}}$ is located at ≈ 2.5 in TEM regime ($\omega_R > 0$). Indeed, at the stationary point: $[R/L_n]_{\text{stat}} - [R/L_n^{\text{turb}}]_{\text{stat}} \approx 0.5$, i.e. smaller than $\approx 2.5 - 0.9 = 1.5$. Namely, the self-consistent state *with* the Ware pinch can be much larger than the stationary state *without* the Ware pinch, while at the steady-state point the portion of R/L_n carried by the Ware pinch can still be relatively small. Note also that the Ware pinch drastically changes the turbulence regime from an ITG to a TEM through $[R/L_n]_{\text{stat}}$. With regards to the behavior of carbon, we see that the turbulence provides an outward directed or very small inward directed pinch which does not sustain any relevant R/L_C . All the observed peaking is provided by neoclassical transport through V_{neo}^C .

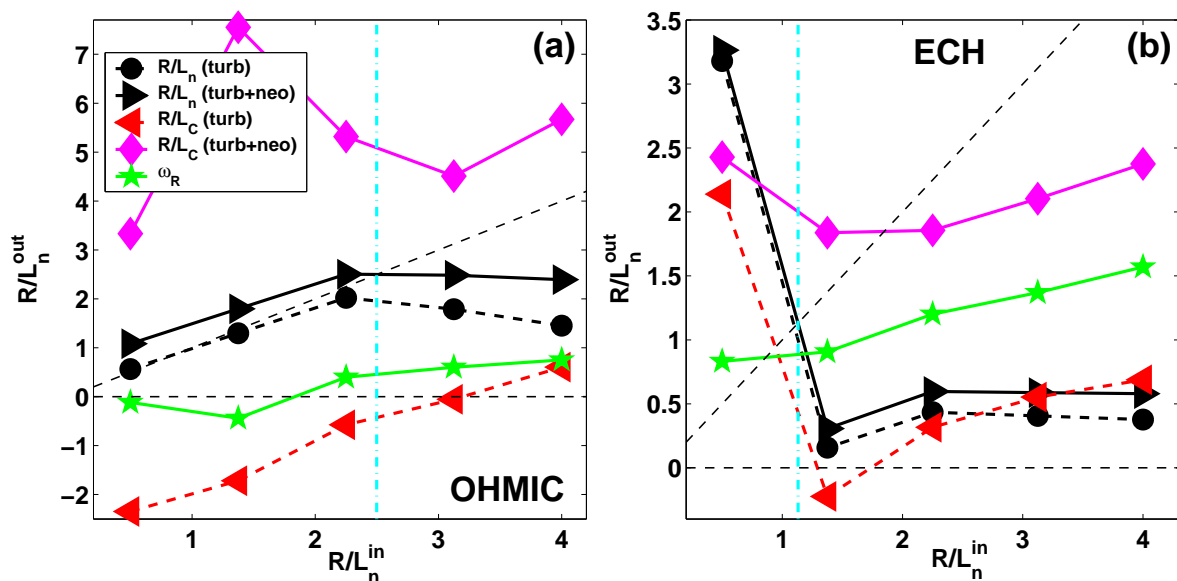


Figure 6.11: a) For the Ohmic heating case and $\rho = 0.35$, predicted normalized gradients versus input density gradient for electrons and carbon with and without neoclassical transport. The real frequency ω_R of the mode with highest transport is also shown (pentagrams, dashed line). The vertical dot-dashed line indicates the steady-state point; b) Same plot for the ECH case.

- $\rho = 0.35$, ECH, figure 6.11(b): the strong electron heating excites TEM which becomes the dominant instability all along the R/L_n^{in} scan. The Ware pinch provides negligible effect and the stationary state is located at a reduced value of R/L_n^{in} with respect to the Ohmic case. The carbon peaking is still mainly provided by neoclassical transport but at a reduced value through its dependence on $\sim 1/\chi_e$.

- $\rho = 0.5$, Ohmic, figure 6.12(a): in this case the stationary state is not significantly influenced by the addition of the Ware pinch. On the other hand, carbon neoclassical transport is still the main source of peaking for the carbon density profile.

- $\rho = 0.5$, ECH, figure 6.12(b): as for $\rho = 0.35$, the Ware pinch is negligible, and the stationary state is in TEM dominated turbulence. Neoclassical transport becomes important for carbon in TEM regime, and it provides about half of the observed peaking.

- $\rho = 0.75$, Ohmic, figure 6.13(a): the stationary state is located near the ITG-TEM transition region. Note that for carbon, neoclassical transport is negligible in the ITG region, while it becomes dominant in the TEM region. This behavior is due to the different behavior of $\delta_{eC}\lambda_D^e$: in ITG it is large and it suppresses the neoclassical part while in TEM it becomes small and allows neoclassical transport to become relevant.

- $\rho = 0.75$, ECH, figure 6.13(b): the picture is the same as for the Ohmic case, except now the neoclassical contribution is smaller due to an increase in χ_e .

We now look at the behavior of the coefficients ratio D_{turb}^C/χ_e and D_{turb}^e/χ_e to better

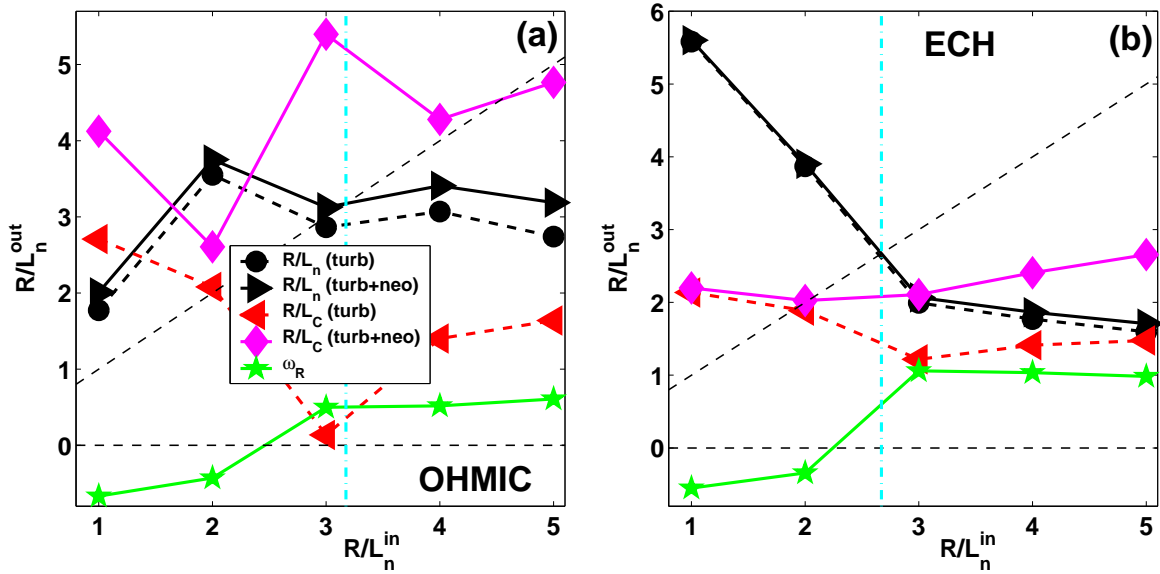


Figure 6.12: *a,b*) Same plots as in figure 6.11 but at radial position $\rho = 0.5$.

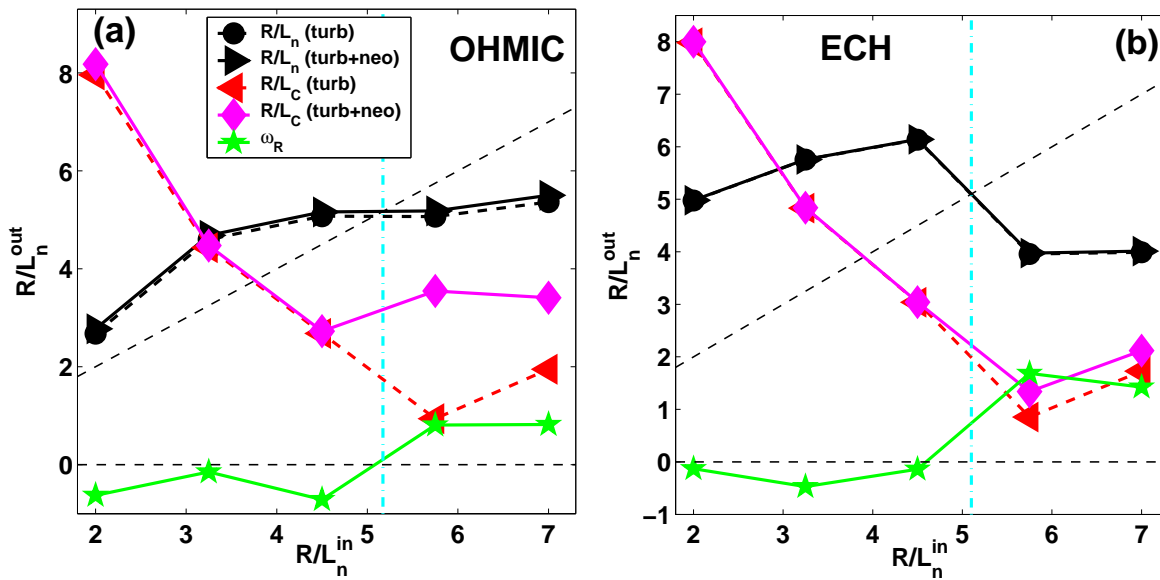


Figure 6.13: *a,b*) Same plots as in figure 6.11 but at radial position $\rho = 0.75$.

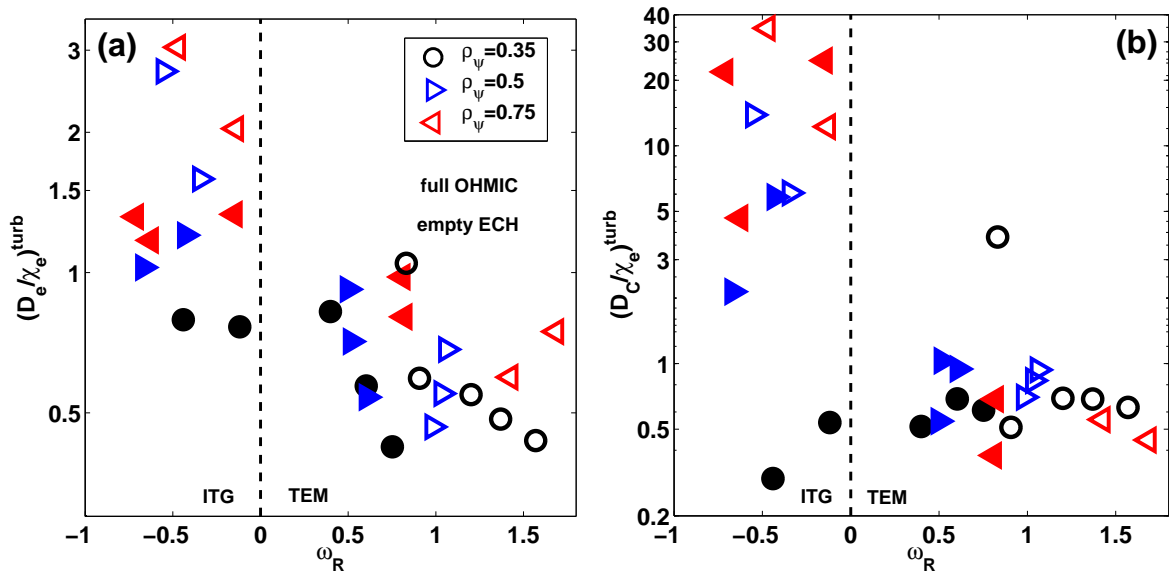


Figure 6.14: *a)* Particle to heat diffusivity ratio for electrons $(D_e/\chi_e)^{\text{turb}}$, as calculated by GS2, in logarithmic scale plotted versus the real frequency ω_R of the mode with highest $\gamma / \langle k_{\perp}^2 \rangle$. The different symbols represent different radial locations and pertain to the respective R/L_n^{In} scan. The full symbols are from the Ohmic case while the open symbols are from the ECH case; *b)* Same plot but for the carbon particle to electron heat diffusivity $(D_C/\chi_e)^{\text{turb}}$.

understand the results shown in figures 6.11-6.13. In figure 6.14(a,b) we plot respectively the ratio $(D_e/\chi_e)^{\text{turb}}$ for electrons (a) and $(D_C/\chi_e)^{\text{turb}}$ for carbon (b) versus the real frequency ω_R of the mode with highest $\gamma / \langle k_{\perp}^2 \rangle$. These quantities are such that $\delta_{eC}\lambda_D^e = (D_C/\chi_e)^{\text{turb}}$ and $\lambda_D^e = (D_e/\chi_e)^{\text{turb}}$ which enter in equations (6.2). We clearly see that in the very plasma core $\rho_{\psi} = 0.35$ the two quantities are in general lower than unity. In the outer region they are above unity in ITG-dominated turbulence while they drop to lower values below unity in TEM-dominated turbulence. In particular the carbon particle diffusivity becomes quite high compared to the electron heat diffusivity for ITG-dominated turbulence. This explains the behavior shown in figures 6.12-6.13, where we observe a drastic change in the role of the neoclassical pinch when R/L_n^{In} is sufficiently high to drive a stronger TEM turbulence.

In conclusion, we see that a complicated behavior is observed with an interplay between turbulence-driven and neoclassical pinch in frequency space. Depending on the dominant instability and on the local confinement through χ_e , neoclassical transport can play a role for either electrons and impurity, in a non-trivial way. In particular we can conclude that in Ohmic cases at low current the core region where χ_e is low is strongly influenced by Ware pinch, albeit the final state seems to show a small role of the neoclassical pinch for electrons. As we saw, this is clarified by the detailed analysis in R/L_n^{In} scan. The outer

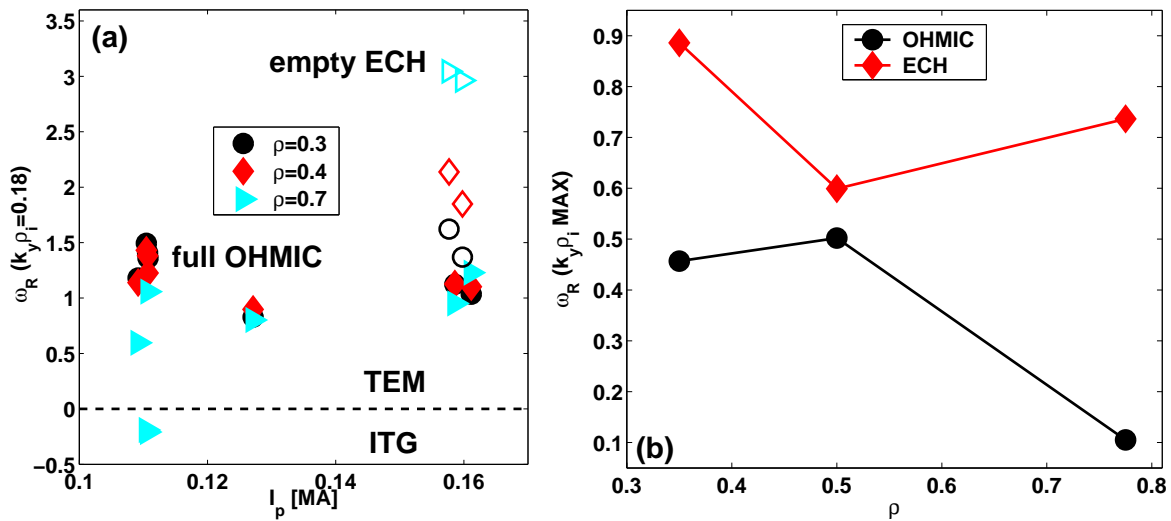


Figure 6.15: a) Mode real frequencies ω_R for the most unstable mode at $k_y \rho_i = 0.18$ plotted for some low current cases with Ohmic (full symbols) and ECH (open symbols) heating, at three radial positions (in legend); b) For Ohmic and ECH cases of figures 6.10(a,b), radial profile of the mode real frequency ω_R for the mode with highest mixing length estimate.

region, as well as when ECH is present, is dominated by the turbulence-driven pinch. This is not the case for carbon, for which we see that neoclassical transport is a dominant source all along the radial interval in Ohmic and ECH cases. In the latter, the flattening effect is thus simply a reduction of $|V_{\text{neo}}^C/\chi_e|$ through an increase of χ_e with ECH.

6.4.2 Comparison with experimental regime

From the previous subsection it can be deduced that the dominant instability in both Ohmic and ECH cases should be the TEM all along the radial interval. We compare this prediction with the outcome of the code calculations on low current cases but with only experimental input parameters. In figure 6.15(a) we plot the mode real frequency for wavenumber $k_y \rho_i = 0.18$ versus current for three different radial positions (in the legend). Full symbols indicate Ohmic cases while the open symbols are from an ECH case. As we see, the dominant mode is a TEM for all the points in the plasma core, the frequency being higher in the ECH case. In figure 6.15(b) we compare this result with the results from the stationary cases analyzed in the previous subsection. We show the radial profile of ω_R for the mode with highest value of $\gamma / \langle k_{\perp}^2 \rangle$ (which is located at $k_y \rho_i \approx 0.2$) for the Ohmic (circles) and the ECH (diamonds) case. The values have the same qualitative trends although the self-consistent state shows a lower frequency due to an underestimation of $[R/L_n]_{\text{stat}}$ with respect to the experimental value.

6.5 Summary

We have presented characteristic experimental observations on electrons and carbon particle transport in Ohmic and ECH cases with low plasma current. We find that carbon density peaking is always larger than electron density peaking in the plasma core, while the two normalized gradients are comparable in the outer plasma region.

This behavior is analyzed using the quasi-linear model described in Chapter 5, extended to cover the calculations of transport coefficients ratios for whatever species and to include neoclassical transport. The main results show that, for electrons, neoclassical transport plays an important and non-trivial role in the plasma core, in cases where χ_e is not large, while it becomes negligible in the outer plasma region or when ECH is applied. For carbon, the results suggest that the observed peaking is mainly provided by neoclassical transport in both Ohmic and ECH cases, being lower in amplitude in the latter regime. However the quantitative agreement is fragile and require more precise calculations of the neoclassical impurity pinch. In conclusion this study has to be considered preliminary and stimulating towards a full quantitative comparison. On the other hand, it shows that the interaction between turbulence-driven and neoclassical pinch is rather complex and depends not only on χ_e but also on the main turbulence modes.

Chapter 7

Conclusions

7.1 Main considerations

This thesis work has been devoted to the detailed theoretical understanding of particle and heat transport in TCV electron Internal Transport Barriers fully non-inductive scenario [21], with particular emphasis on the general theory of turbulent particle transport in the linear gyrokinetic theoretical framework.

Through the opening chapters, we have shown that the analysis of experimental data and their use in numerical codes requires several tools and accurate check of the consistency between the numerical results and the experimental data themselves. This has been done in Chapter 2 where we introduced the experimental set, the analysis tools, the numerical code ASTRA [29] for discharge simulation, and the theoretical tools to interpret the observed behavior in terms of first principle physics: gyrokinetic code GS2 [40] and Gyro-Landau-Fluid code GLF23 [37]. The former of the theoretical tools is suited for the calculation of basic turbulence properties in the linear phase and for calculation of stationary density profiles, while the latter is suited for fast global discharge simulations coupled with the ASTRA transport code.

7.2 Heat transport analysis of the eITB scenario

By means of the gyro-Landau-fluid code GLF23 coupled to the ASTRA transport code, the analysis of different TCV plasma scenarios has been carried out.

Several Ohmic and ECH heated L-mode plasmas are simulated. We find that the GLF23 formulation of the fluxes is not suited to explain the rapid increase of the observed heat transport coefficient from the core to the plasma periphery. In our analysis we discussed the possibility that this behavior could be due to the local gyro-Bohm scaling $\propto T_e^{3/2}$ explicit in the GLF23 formulation. In this sense, the GLF23 heat diffusivity, removing the $T_e^{3/2}$ dependence, is capable of reproducing different TCV cases over the whole radial interval with one additional free parameter. However the scaling itself is intrinsic in the

theoretical formulation, suggesting that the cause for the disagreement should instead be searched in the choice of the mixing length rule which is a free parameter in GLF23. This requires a dedicated study and it is not assessed in the present work.

The eITB fully–non inductive scenario is then analyzed with this re–normalized GLF23 model, with the $T_e^{3/2}$ dependence removed. The simulation is carried out on a typical stationary eITB through a scan in the total non–inductive current content I_{CD} . Increasing the percentage of off–axis non–inductive current results in a modification of the local magnetic shear which eventually becomes negative and attains large negative values. It is found that the predicted heat diffusivity χ_e decreases strongly when the local magnetic shear is decreased to negative values, allowing the sustainment of the eITB. The physical mechanism behind the improvement of confinement with the reversal of the q –profile is then elucidated assessing the role of the average magnetic curvature drift ω_d on the Trapped Electron Mode in the low $k_y\rho_i$ range [60, 59]. The reduction of ω_d due to its dependence on the magnetic shear s weakens the driver of the TEM and the turbulence spectrum peak shifts at higher values of $k_y\rho_i$, thus reducing the total energy transport.

7.3 Particle transport in the eITB scenario: experimental results

Novel experimental observations about stationary and transient particle transport in TCV eITB fully non–inductive scenario are reported in chapter 4.

When local confinement is sufficiently improved by means of the reversal of the safety factor profile and the creation of a region of negative magnetic shear, a strong correlation between the electrons density and temperature is observed, indicating that a relevant inward pinch of thermodiffusive nature might be the basic mechanism [22]. This is confirmed by both the global analysis of a large database of Ohmic/ECH L–modes and eITBs, and by the detailed discussion of several individual profiles on which the characteristics eITB features of correlated energy and particle barriers are evident. However the static database does not allow to estimate the particle diffusivity to discriminate the roles of neoclassical and turbulent transport in driving the observed density profiles.

To this purpose we turn to the analysis of transients, which allow the estimation of the particle diffusivity and of the off–diagonal convective term in the transport matrix. The results of this section reveal that neoclassical transport is still much smaller than the observed level of transport in the barrier region, suggesting that transport in the eITB region is still dominated by turbulence, although at a lower amplitude than in a standard L–mode with ECH heating [62].

7.4 Particle transport theory

The basic equations of particle transport in axisymmetric systems are presented in chapter 5 and a self-consistent model to evaluate the stationary density logarithmic gradient is built from first principles considering neoclassical and turbulent transport sources.

The turbulence-driven diffusive term, i.e. the diagonal term of the flux, and the turbulence-driven convective term, i.e. all the off-diagonal contributions, are formally calculated from the linear gyrokinetic theory. The linear relationship between the flux and the equilibrium gradients are such that two fundamental convective mechanisms, which arise from the background electrostatic microinstabilities, are identified: the thermodiffusion term (C_T), proportional to R/L_{Te} , and a pure convective off-diagonal term (C_P). Both contributions are found to be finite for unstable modes and their sign strongly depends on the type of dominant mode and on phase-space details [100].

The model predictions are then tested against known experimental observations in several cases through a series of parameter scans. We find that this model can explain qualitatively the observed density peaking maximization in the regime where the ITG and the TEM coexist with similar amplitudes. It also explains both the decrease of peaking in TEM dominated turbulence [63] and the decrease of peaking in ITG dominated turbulence [80] through different effects of the parameters on the two pinch terms. Specifically, we find that the thermodiffusive contribution $C_T R/L_{Te}$ is responsible for the decrease of peaking in TEM-dominated turbulence, while the other pinch term C_P is responsible for the flattening observed in ITG-dominated regime. We also find that the results can change when the quasi-linear rule for the sum over the wavenumber spectrum is chosen differently. In particular it is found that the result strongly changes for collisional plasmas when the rule is changed from the single-mode rule to a sum over modes where a large part of the spectrum is given a relevant role. Actually also for collisionless plasmas the result can change when modes with high $k_y \rho_i$ are given more weight. This is due to the fact that the particle flux driven by the low $k_y \rho_i$ is often of a different sign than the one driven by higher $k_y \rho_i$. Therefore the global result can depend on the quasi-linear rule used to take all these contributions together.

The magnetic shear dependence of the density peaking for low collisionality cases, and the apparent loss of this dependence at high collisionality, i.e. in strong ITG turbulence, is discussed and compared with known experimental results [85]. The results suggest that the shear dependence can emerge and play a dominant role only near the ITG-TEM transition region, i.e. when $\omega_R \approx 0$ where the shear-driven part of the pinch (appearing in both C_T and C_P) is more important than the collisionality-driven part (which gives strong importance to C_P).

The quasi-linear model is completed with the inclusion of neoclassical transport through

an ad-hoc diffusion coefficient to test the qualitative behavior when scanning the strength of neoclassical transport. In particular it is found that the inclusion of the Ware pinch can strongly increase the stationary density peaking in the case of dominant ITG turbulence. Our study indicates that when the Ware pinch is significant, a stationary (at zero flux) solution without Ware pinch and with ITG-dominated turbulence is shifted towards a stationary solution, with the Ware pinch included, which is TEM dominated, or near the ITG-TEM transition point. An example of a significant contribution of the Ware pinch was also seen in Ref. [79] in positive shear plasmas with off-axis ICRH. On the other hand, if the stationary solution without the Ware pinch is clearly in a TEM-dominated turbulence, then the addition of the Ware pinch has little effects.

7.5 Particle transport theory: interpretation of the eITB scenario

The quasi-linear gyrokinetic theoretical model is then applied to the interpretation of the eITB fully non-inductive scenario in TCV [69]. The simulations are first performed on a set of parameter scans.

We find that the model correctly predicts that, for experimentally relevant values of the stationary logarithmic gradients, a thermodiffusive inward directed pinch is the dominant mechanism responsible for the sustainment of a large density logarithmic gradient. In addition, in the collisionless case, the density peaking is found to be maximized when $L_{Te}/L_{Ti} \sim 1$, as also found for the monotonic q -profile cases. For regimes with dominant electron heating, with turbulence dominated by the TEM, which limits the value of R/L_n , one can expect that when the TEM is stabilized by some mechanism the value of $[R/L_n]_{stat}$ is increased. This explains why R/L_n increases with magnetic shear becoming more negative, since it stabilizes the TEM in eITBs. We have also shown that with finite collisionality the maximum value of R/L_n is predicted to be at values of L_{Te}/L_{Ti} smaller than one, of the order of 0.6 – 0.8 for collisionalities consistent with the experiment. We have seen that this is also due to the stabilizing effect of collisionality on the TEM.

The effect of impurities is then assessed through the inclusion of carbon ions with different values of the effective charge concentration. We find that when the carbon concentration is not small, i.e. $Z_{eff} \gtrsim 2$, the stationary electron density peaking is reduced.

The theoretical predictions are then tested on one typical TCV eITB case at different radial points, avoiding the $s \approx 0$ region since the ballooning approximation is not valid there. We find that the model qualitatively reproduces the radial profile of the stationary R/L_n , however quantitatively it tends to underestimate its value. Nevertheless, it correctly predicts the improvement of confinement inside the eITB region and the appearance of the particle transport barrier with a realistic value for $\sigma_e = L_{Te}/L_n$. Similarly

to what has been shown for the heat transport studies, we find again that the improved confinement regime is due to a reduction of TEM turbulence in the low $k_y \rho_i$ range.

7.6 Particle transport theory: interpretation of carbon behavior in TCV L-modes

Experimental observations from TCV Ohmic L-modes show that, at low values of the total plasma current when core sawtooth activity is very small or absent, the carbon density profile can be much more peaked than the electron density profile [88, 89], suggesting that a completely different physical mechanism is at play. In addition, when core electron heating is applied, both profiles are flattened, with the carbon density profile showing a stronger flattening. We address the problem of interpreting these observations again using the linear gyrokinetic model presented before with now the inclusion of neoclassical transport for both electrons and carbon ions species. The only free parameter of the model is the ratio between the electrons particle and heat diffusivity.

Linear gyrokinetic theory predicts two mechanisms for carbon density peaking, similarly to what has been found for electrons: a thermodiffusive type of pinch, and another off-diagonal pinch term which contains contributions from the parallel and the perpendicular dynamics [74]. Contrary to what was found for electrons, for carbon the first pinch is inward directed in TEM dominated turbulence and outward directed in ITG dominated turbulence, and it is small in absolute value; the second pinch term is inward directed in ITG turbulence and, either inward and small, or outward directed in TEM turbulence. It can be large in absolute value for ITG turbulence with large real frequency.

The gyrokinetic results are put together with neoclassical transport to find the self-consistent stationary state for both electrons, $[R/L_n]_{\text{stat}}$, and carbon ions, $[R/L_C]_{\text{stat}}$. This formalism is applied to a set of cases, extracted from the experimental database, representing a typical low current discharge with and without auxiliary heating. The main results can be divided in two parts:

- the core region where the electron heat diffusivity is small: the electrons local normalized density gradient $[R/L_n]_{\text{stat}}$ is sustained partly by the turbulent pinch and partly by the neoclassical Ware pinch. However their interplay is shown to be non-trivial and that in fact the Ware pinch plays an important role in this region, pushing the stationary state from an ITG-dominated to a TEM-dominated regime, although the final state seems to indicate a surprisingly negligible contribution from the Ware pinch. The role of the latter is strongly suppressed when ECH is applied, resulting in a local flattening of the profile. On the other hand, the carbon stationary $[R/L_C]_{\text{stat}}$ is found to be almost entirely sustained by the neoclassical pinch V_{neo}^C with only Ohmic heating. When ECH is applied, the neoclassical pinch is also strongly reduced, although it still plays an important role.

- the outer region where the electron heat diffusivity is moderate or large: the electrons local $[R/L_n]_{\text{stat}}$ is now sustained mostly by the turbulent pinch, while the neoclassical Ware pinch plays no significant role. On the opposite side, the carbon local $[R/L_C]_{\text{stat}}$ is still sustained mostly by the neoclassical pinch, and for this reason, when ECH is applied, the value is strongly reduced all along the radial interval.

Although the picture so far seems to fit the experimental observations, there is still some discrepancy between the predicted $[R/L_C]_{\text{stat}}$ and the experimental one in the outer region of the ECH case. In addition, the required neoclassical pinch is somewhat large and may not be realistic when more accurate calculations will be performed. Nevertheless we have shown that the turbulent pinch is largely insufficient to explain the observed carbon peaking, while it provides an electron density peaking which agrees with the experimental one. Therefore neoclassical contributions are important when analyzing carbon density profiles in these plasma conditions.

7.7 Open issues

This work has been devoted to the interpretation of experimental observations adopting first principles based models. However either of these models have drawbacks and limitations which could explain the discrepancy between the theoretical predictions and the experimental observations. In particular, for the particle transport modelling, different issues are still open and the two most challenging are listed here as stimulating for future works:

- non-linear effects: the model has been built from *linear* gyrokinetic theory, meaning that no information on the saturated values for the fields fluctuations is given, and a quasi-linear approach based on some choice of the mixing-length rule is required. Of course a benchmark of the rule can be done on non-linear calculations or on experimental data, but it will always be 'limited' to the range of parameters on which the benchmark is done. In addition, non-linear coupling between modes at different wavelengths could have an effect, especially when high $k_y \rho_i$ modes are highly unstable. A crucial point that we did not consider is the effect of taking only the fastest growing modes as done in linearized initial value codes like GS2. In fact, at a fixed $k_y \rho_i$, the sub-dominant modes could be as important for transport as the dominant mode in the non-linear stage. In this respect, using a spectral code, one could apply the quasi-linear rule to a full spectrum of modes in $k_y \rho_i$, where at each wavelength all the sub-dominant modes are taken into consideration. We speculate that this could make a difference in regimes where the dominant mode is of one type and the first sub-dominant mode is of another type, with the two modes having comparable growth rates. The resulting transport can be very different choosing both the modes compared to just taking the dominant mode;

- global effects: the model adopts the zero-order ballooning theory, which gives no information on the radial structure of the mode and thus on global effects which could be important, especially near $s = 0$ where slab modes are dominant.

In conclusion, there are still many open issues in the field of Tokamak particle transport, in particular with regards to the turbulent regime, for which a complete and closed mathematical model is difficult to realize, although highly sophisticated codes already exist and provide the plasma physicists a large amount of detailed understanding of the turbulent state and the induced transport. Still, the simple models can give deep physical insight and allow to span over a large range of parameters. In addition they are required to understand the non-linear results. The present work has hopefully fulfilled the goal of providing a coherent understanding of some "mysterious" aspects of electrons particle transport although the methodology was based on a linearized theory. Nevertheless this has proven to be an advantage to elucidate the basic mechanisms.

Bibliography

- [1] www.iter.org
- [2] R. Aymar *et al.*, Nucl. Fusion **41**, 1301 (2001)
- [3] F. L. Hinton and R. D. Hazeltine, Rev. Mod. Phys. **48** 2, 239 (1976).
- [4] W. Horton, Rev. Mod. Phys. **71** 3, 735 (1999).
- [5] R. C. Wolf, Plasma Phys. Control. Fusion **45**, R1 (2003).
- [6] J. W. Connor *et al.*, Nucl. Fusion **44**, R1 (2004).
- [7] X. Litaudon, Plasma Phys. Control. Fusion **48**, A1 (2006).
- [8] X. Garbet, Plasma Phys. Control. Fusion **43**, A251 (2001).
- [9] X. Garbet *et al.*, Phys. Plasmas **12**, 082511 (2005).
- [10] J. Nycander and V. V. Yankov, Phys. Plasmas **8** 2, 2874 (1995).
- [11] M. B. Isichenko *et al.*, Phys. Rev. Lett. **74** 22, 4436 (1995).
- [12] D. R. Baker and M. N. Rosenbluth, Phys. Plasmas **5**, 2936 (1998).
- [13] F. Miskane *et al.*, Phys. Plasmas **10**, 4197 (2000).
- [14] R. J. Buttery *et al.*, Plasma Phys. Control. Fusion **42**, B61 (2000).
- [15] B. Kadomtsev, Sov J. Plasma Phys. **1** 5, 389 (1975).
- [16] K. McGuire *et al.*, Phys. Rev. Lett. **50**, 891 (1983).
- [17] M. Psimopoulos, Phys. Lett. A **162**, 182 (1992).
- [18] F. Hofmann *et al.*, Plasma Phys. Control. Fusion **36**, B277 (1994).
- [19] S. Coda *et al.*, Plasma Phys. Control. Fusion **42**, B311 (2000).
- [20] I. Furno *et al.*, Phys. Plasmas **10**, 2422 (2003).

- [21] M. A. Henderson *et al.*, Plasma Phys. Control. Fusion **46**, A275 (2004).
- [22] E. Fable *et al.*, Plasma Phys. Control. Fusion **48** 9, 1271 (2006).
- [23] C. Angioni, Ph.D. Thesis, EPFL Library .
- [24] O. Sauter *et al.*, Phys. Rev. Lett. **84**, 3322 (2005).
- [25] A. G. Peeters, Plasma Phys. Control. Fusion **42**, B231 (2000).
- [26] S. Coda *et al.*, Phys. Plasmas **12**, 056124 (2005).
- [27] S. Coda *et al.*, IAEA, (2008).
- [28] P. H. Rebut *et al.*, Proc. 12th Int. Conf. of Plasma Physics and Controlled Fusion Research (Nice, 1988) Vol 2 (Vienna: IAEA) pag. 191 (1989).
- [29] G. V. Pereverzev *et al.*, ASTRA, An Automatic System for Transport simulations in a Tokamak, IPP Report 5/42 (August 1991).
- [30] O. Sauter *et al.*, Phys. Plasmas **6** 7, 2834 (1999).
- [31] C. Angioni and O. Sauter, Phys. Plasmas **7** 4, 1224 (2000).
- [32] F. Hoffmann and G. Tonetti, Nucl. Fusion **28**, 1871 (1988).
- [33] A. Zabolotsky *et al.*, Nucl. Fusion **46**, 594 (2006).
- [34] E. Fable and O. Sauter, Fortran90 routine available on CRPP servers.
- [35] F. Porcelli *et al.*, Plasma Phys. Control. Fusion **38**, 2163 (1996).
- [36] P. Nikkola *et al.*, Nucl. Fusion **43**, 1343 (2003).
- [37] R. E. Waltz *et al.*, Phys. Plasmas **2**, 2408 (1997).
- [38] G. W. Hammett and F. W. Perkins, Phys. Rev. Lett. **64** 25, 3019 (1990).
- [39] G. V. Pereverzev *et al.*, Nucl. Fusion **45**, 221 (2005).
- [40] M. Kotschenreuther *et al.*, Comput. Phys. Commun. **88**, 128 (1995).
- [41] A. J. Brizard and T. S. Hahm, Rev. Mod. Phys. **79**, 421 (2007).
- [42] J. Candy *et al.*, Phys. Plasmas **13**, 074501 (2006).
- [43] F. L. Hinton and R. E. Waltz, Phys. Plasmas **13**, 102301 (2006).

- [44] E. A. Frieman and Liu Chen, *Phys. Fluids* **25**, 502 (1982).
- [45] J. W. Connor *et al.*, *Proc. R. Soc.* **A365**, 1 (1979).
- [46] E. A. Frieman *et al.*, *Phys. Fluids* **23** 9, 1750 (1980).
- [47] J. W. Connor *et al.*, *Phys. Fluids B* **4** 1, 56 (1992).
- [48] J. W. Connor and H. R. Wilson, *Plasma Phys. Control. Fusion* **36**, 719 (1994).
- [49] Y. Idomura *et al.*, *Phys. Plasmas* **7**, 2456 (2000).
- [50] X. Garbet, *Plasma Phys. Control. Fusion* **43**, A251 (2006).
- [51] R. E. Waltz *et al.*, *Phys. Plasmas* **1**, 2408 (1995).
- [52] M. A. Beer *et al.*, *Phys. Plasmas* **2**, 2687 (1995).
- [53] J. Weiland and A. Hirose, *Nucl. Fusion* **30**, 938 (1992).
- [54] F. Jenko *et al.*, *Plasma Phys. Control. Fusion* **47**, B195 (2005).
- [55] Y. Camenen *et al.*, *Plasma Phys. Control. Fusion* **47**, 1971 (2005).
- [56] A. A. Galeev and R. Z. Sagdeev, *Soviet Phys. JETP* **26**, 233 (1968).
- [57] T. Dannert and F. Jenko, *Phys. Plasmas* **12**, 072309 (2005).
- [58] T. P. Goodman *et al.*, *Plasma Phys. Control. Fusion* **47** 12B, B107 (2005).
- [59] A. Bottino *et al.*, *Plasma Phys. Control. Fusion* **48** 2, 215 (2006).
- [60] M. A. Beer and G. W. Hammett, *Phys. Plasmas* **3** 11, 4018 (1996).
- [61] F. Ryter *et al.*, *Phys. Rev. Lett.* **95** 8, 085001 (2005).
- [62] E. Fable *et al.*, 32nd EPS Conference on Plasma Phys. Tarragona, 27 June - 1 July 2005 ECA Vol.29C, P-1.051 (2005).
- [63] C. Angioni *et al.*, *Nucl. Fusion* **44**, 827 (2004).
- [64] M. Romanelli *et al.*, *Plasma Phys. Control. Fusion* **49** 6, 935 (2007).
- [65] A. Zabolotsky and H. Weisen, *Plasma Phys. Control. Fusion* **46** 5, 594 (2006).
- [66] C. Zucca *et al.*, *Plasma Phys. Control. Fusion* **51** , 015002 (2008).
- [67] K. W. Gentle *et al.*, *Plasma Phys. Control. Fusion* **29**, 1077 (1987).

- [68] D. R. Baker *et al.*, Nucl. Fusion **38**, 485 (1998).
- [69] E. Fable *et al.*, 34th EPS Conference on Plasma Phys. Warsaw, 2 - 6 July 2007 ECA Vol.31F, P-1.100 (2007).
- [70] E. Poli *et al.*, AIP Conf. Proc. **871**, 400 (2006).
- [71] A. A. Ware, Phys. Rev. Lett. **25**, 916 (1970).
- [72] X. Garbet *et al.*, Phys. Rev. Lett. **91**, 035001-1 (2003).
- [73] G. M. Staebler *et al.*, Phys. Plasmas **12**, 102508 (2005).
- [74] C. Angioni and A. G. Peeters, Phys. Rev. Lett. **96**, 095003 (2006).
- [75] L. D. Horton *et al.*, Nucl. Fusion **45**, 856 (2005).
- [76] K. Hallatschek and W. Dorland, Phys. Rev. Lett. **95**, 055002 (2005).
- [77] C. Bourdelle *et al.*, Phys. Plasmas **14**, 055905 (2007).
- [78] G. T. Hoang *et al.*, Phys. Rev. Lett. **93**, 135003 (2004).
- [79] D. R. Ernst *et al.*, Phys. Plasmas **11** 5, 2637 (2004).
- [80] C. Angioni *et al.*, Phys. Rev. Lett. **90** 20, 205003-1 (2003).
- [81] M. Greenwald *et al.*, Nucl. Fusion **47**, L26 (2007).
- [82] C. Angioni *et al.*, Phys. Plasmas **12**, 040701 (2005).
- [83] M. Romanelli *et al.*, Phys. Plasmas **11**, 3845 (2004).
- [84] C. Angioni, private communication.
- [85] H. Weisen *et al.*, Nucl. Fusion **45** 2, L1-L4 (2005).
- [86] G. T. Hoang *et al.*, Phys. Rev. Lett. **90**, 155002 (2003).
- [87] E. Fable *et al.*, Plasma Phys. Control. Fusion **50**, 115005 (2008).
- [88] E. Scavino *et al.*, Plasma Phys. Control. Fusion **46**, 857 (2004).
- [89] A. Zabolotsky *et al.*, 33rd EPS Conference on Plasma Phys. Rome, 19 - 23 June 2006 ECA Vol.30I, P-1.145 (2006).
- [90] M. Z. Tokar *et al.*, Plasma Phys. Control. Fusion **37**, 1691 (1997).

- [91] V. A. Soukhanovskii *et al.*, Plasma Phys. Control. Fusion **44**, 2339 (2002).
- [92] J. Stober *et al.*, Plasma Phys. Control. Fusion **44**, A159 (2002).
- [93] H. Weisen *et al.*, Nucl. Fusion **42**, 136 (2002).
- [94] A. Zabolotsky and H. Weisen, Plasma Phys. Control. Fusion **45**, 735 (2003).
- [95] A. Zabolotsky, Ph.D. Thesis, EPFL Library .
- [96] G. Fussman *et al.*, Plasma Phys. Control. Fusion **33**, 1677 (1991).
- [97] R. Dux, STRAHL user Manual, Preprint IPP 10/30 (2006).
- [98] C. Angioni *et al.*, Plasma Phys. Control. Fusion **49** 12, 2027 (2007).
- [99] C. Angioni *et al.*, Phys. Plasmas **14**, 055905 (2007).
- [100] E. Fable, C. Angioni and O. Sauter, AIP Conf. Proc. **1069**, 64 (2008).

List of common symbols and definitions

Mathematical

i – Imaginary unit: $i = \sqrt{-1}$

\Re – Real part of a complex variable

\Im – Imaginary part of a complex variable

$\langle \dots \rangle$ – Generic average operator (to be contextually specified)

Plasma macroscopic physical quantities

r – Minor radius

a – Plasma boundary, i.e. minor radius of the last closed flux surface

R_0 – Major radius of the geometrical magnetic axis of the plasma column

R – Defined as $R = R_0 + \Delta_s$ where Δ_s is the (mid-plane) Shafranov-shift of the local flux surface. Another definition is $R = \frac{R_{\max} - R_{\min}}{2}$.

B_0 – Toroidal magnetic field at R_0

ϵ – Local aspect ratio defined as $\epsilon = r/R$

κ, δ – Plasma elongation, triangularity

ψ – Poloidal magnetic flux, defined as $\psi = \int \mathbf{B} \cdot d\mathbf{S}_\theta$

ρ – Generic flux surface label (or radial coordinate)

ρ_ψ – Radial coordinate defined as $\rho = \sqrt{\psi/\psi_b}$

ρ_V – Radial coordinate defined as $\rho_V = \sqrt{V/V_b}$

V – Flux surface enclosed plasma volume

Z – Species charge normalized to the fundamental proton charge

Z_{eff} – Effective charge defined as $Z_{\text{eff}} = \sum_j n_j Z_j^2 / \sum_j n_j$

m_i – Main ion species mass

n – Species density. If not specified: electron density

n_e, n_i, n_C – Electron, main ion, carbon density

R/L_X – Normalized inverse length scale of field X : $R/L_X = - \langle |\nabla\rho| \rangle \partial \log X / \partial \rho$

T – Species temperature

T_e, T_i – Electron, main ion species temperature

τ – Ion to species temperature ratio $\tau = T_i/T$

ν_{ei} – Electron-ion collisional frequency, defined as $\nu_{ei} = 0.00279 \Lambda n_e / T_e^{3/2}$ where Λ is the Coulomb logarithm, n_e is in units of 10^{19} m^{-3} and T_e is in keV.

c_s – Ion sound speed defined as $c_s = \sqrt{T_i/m_i}$

ν_{eff} – Effective collisionality defined as ν_{eff}/c_s

P_{ECH} – ECH absorbed power density

ρ_{ECH} – ECH deposition location in ρ

P_{EQ} – Equipartition power density defined as $P_{\text{EQ}} = n_e \nu_{ei} (T_i - T_e)$

P_{OH} – Ohmic power density

V_{loop} – Plasma boundary loop voltage

I_{p} – Plasma total toroidal current

q – Safety factor profile

s – Magnetic shear

q_{95} – Value of the safety factor at 95% of the enclosed poloidal magnetic flux

β – Normalized plasma pressure $\beta = p/p_{\text{B}}$ where $p_{\text{B}} = B_0^2/(2\mu_0)$ is the magnetic 'pressure'.

α – Shafranov-shift parameter defined as $\alpha = -Rq^2 d\beta/dr$

ρ_{inv} – Radial position of the sawtooth inversion radius, i.e. where $q = 1$.

ρ_{mix} – Radial position of the sawtooth mixing radius, i.e. where the modified poloidal flux $\psi^* = 0$.

j_{\parallel} – Parallel total current density

$j_{\text{OH}}, j_{\text{BS}}, j_{\text{CD}}$ – Ohmic, bootstrap, ECRF-driven (ECCD) current density

f_{BS} – Bootstrap current fraction

Plasma microscopic quantities

f_{t} – Trapped particle fraction

v_{\parallel} – Particle gyrocenter parallel velocity

v_{\perp} – Particle gyrocenter perpendicular velocity

ρ_{i} – Ion Larmor radius

\mathbf{k} – Wavenumber vector

k_{y} – Poloidal wavenumber

k_{\perp} – Perpendicular wavenumber

$\langle k_{\perp}^2 \rangle$ – Ballooning averaged of the square of the perpendicular wavenumber

k_{\parallel} – Parallel wavenumber

ω_{d} – Magnetic curvature drift frequency, equation (2.24)

ω_{*} – Diamagnetic frequency, equation (2.24)

ω – Mode complex frequency: $\omega = \omega_{\text{R}} + i\gamma$

γ – Mode growth rate

ω_{R} – Mode pulsation or real frequency

Transport related quantities

Γ – Particle flux

Q – Heat flux

χ – Heat transport coefficient

D – Particle diffusivity

V – Particle convection velocity

Acronyms

'neo' – Neoclassical-driven transport

'turb' – Turbulence-driven transport

eITB – electron Internal Transport Barrier

EC – Electron Cyclotron

ECH – Electron Cyclotron Heating

ECCD – Electron Cyclotron Current Drive

Acknowledgments

To start with the *remerciements* I would like to acknowledge Prof. Franco Porcelli who has supervised my Laurea work at the university and introduced me in the field of plasma physics, following with Dr. Kurt Appert, Prof. Minh Quang Tran and Prof. Ambrogio Fasoli who invited me to work at CRPP and perform my research work on TCV.

This thesis work has been supervised by Dr. Olivier Sauter who I thank for the many discussions and suggestions to improve and affine my scientific methodology. I also thank Dr. Clemente Angioni for his very fruitful (and still ongoing) collaboration in the framework of particle transport to which he brought relevant and novel contributions. I thank Dr. Francois Ryter of IPP–Garching for his kindness in providing me with several experimental sessions at the ASDEX–Upgrade facility.

I would like to mention the help I received from different people to whom my appreciation for their scientific knowledge goes, especially in the framework of gyrokinetic theory and theoretical interpretation of experimental results, together with people from the experimental part who helped me with the raw data and the diagnostics. I also thank people from the secretary who helped me with the administrative part and so on.

A VERY big thank goes to the people that supported me along these 5 years of thesis, either for the work itself or in other ways: Egle, Alan, Miss O. Time, and the cats.

This work was supported in part by the Swiss National Science Foundation.

Curriculum Vitae of Emiliano Fable

Italian, date of birth: June 27th 1978

CRPP-EPFL, Station 13, PPB,

1015 Lausanne, Switzerland.

Telephone : +41 21 6934561

E-mail : emiliano.fable@epfl.ch

Education

December 2003 - December 2008 : **Ecole Polytechnique Fédérale de Lausanne (EPFL), Switzerland.**

Ph.D. Thesis - "*Experimental and theoretical study of particle transport in the TCV tokamak*", Thesis supervisor: Dr. Olivier Sauter.

September 1997 - June 2003 : **Politecnico di Torino, Department of Energetics, Italy**

Degree: **Laurea** in Nuclear Engineering with mention of 110/110 *cum laude* "*Magnetic reconnection in liquid metals*", Supervisor: Prof. F. Porcelli.

Postgraduate courses

March 2004 - July 2004 : "*Physique des plasmas confinés magnétiquement*",

Oct. 2005 - Febr. 2006 : "*Advanced Plasma Physics*",

Oct. 2007 - Febr. 2007 : "*Plasma Physics Applications*",
at CRPP, EPFL, Lausanne.

Work Experience

December 2003 - December 2008 : **Centre de Recherches en Physiques des Plasmas, EPFL.**

• Assistant / Doctoral Student

- Implementation and usage of ASTRA transport code for simulation of TCV eITB discharges.

- Implementation and usage of gyrofluid GLF23 and gyrokinetic GS2 codes.

- Implementation of a Fortran95 module for the modeling of sawtooth crash on plasma evolution to be used in the IMP-2 task force.

• Supervision of general physics courses for Engineers of the EPFL, in support to the didactic activity of the CRPP.

Sept. 2003 - Dec. 2003 : Collaboration with Prof. F. Porcelli at the Politecnico di Torino in research on magnetic reconnection.

Summer 1999 : Builder.

Language Skills

Italian : Mother tongue

French : fluent

English : fluent

Computer Skills

Operating Systems : Windows, UNIX, basic knowledge of VMS.

Languages : MATLAB, MAPLE, FORTRAN, HTML.

Word-processing : L^AT_EX, Microsoft Word, MS Power-Point.

Publications and Conference Contributions

Publications in refereed journals as main author

- [1] **E. Fable** *et al.*, Inward thermodiffusive particle pinch in electron internal transport barriers in TCV, *Plasma Phys. Control. Fusion* **48** (9), 1271 (2006).
- [2] **E. Fable** *et al.*, Gyrokinetic calculations of steady-state particle transport in electron internal transport barriers, *Plasma Phys. Control. Fusion* **50**, 115005 (2008).

Conference proceedings

- [1] **E. Fable** and O. Sauter, Transport simulations of electron internal transport barriers in TCV, in *Theory of Fusion Plasmas*, Proceedings Joint Varenna-Lausanne Int. Workshop 2004, J.W. Connor, E. Sindoni and J. Vaclavik Eds, Ed. Compositori, Bologna (2004), p. 403.
- [2] **E. Fable** *et al.*, Density behavior during electron internal transport barriers in TCV fully non-inductive discharges, 32nd EPS Conference on Plasma Phys. Tarragona, 27 June - 1 July 2005 ECA Vol.29C, P-1.051 (2005).
- [3] **E. Fable** *et al.*, Theoretical study of particle transport in electron internal transport barriers in TCV E. Fable, *AIP Conf. Proc.* **871**, 318 (2006).
- [4] **E. Fable** *et al.*, The role of electron-driven microinstabilities in particle transport during electron Internal Transport Barriers, 34th EPS Conference on Plasma Phys. Warsaw, 2 - 6 July 2007 ECA Vol.31F, P-1.100 (2007).
- [5] **E. Fable**, C. Angioni and O. Sauter, Parametric dependence of particle pinch coefficients for electron particle transport in linear gyrokinetic theory, *AIP Conf. Proc.* **1069**, 64 (2008).

Other publications in refereed journals

- [1] G. L. Delzanno, **E. Fable** and F. Porcelli, Driven reconnection about a magnetic X-point in weakly collisional plasmas, *Phys. Plasmas* **11**, 5212 (2004).
- [2] C. S. Carey *et al.* (including **E. Fable**), Application of the singular value decomposition method for inversion of interferometer measurements in fusion plasmas, *Rev. Sci. Instr.* **75** (10), 3411 (2004).
- [3] M. A. Henderson *et al.* (including **E. Fable**), Rapid electron internal transport barrier formation during magnetic shear reversal in fully non-inductive TCV discharges, *Nucl. Fusion* **45** (12), 1642 (2005).
- [4] I. Furno *et al.* (including **E. Fable**), A new method for the inversion of interferometry data using basis functions derived from singular value decomposition of local measurements in tokamak plasmas, *Plasma Phys. Control. Fusion* **47** (1), 46 (2005).
- [5] O. Sauter *et al.* (including **E. Fable**), Inductive current density perturbations to probe electron internal transport barriers in tokamaks, *Phys. Rev. Lett.* **94** (10), 105002 (2005).
- [6] S. Coda *et al.* (including **E. Fable**), High bootstrap, non-inductively sustained electron internal transport barriers in the Tokamak a Configuration Variable, *Phys. Plasmas* **12** (5), 056124 (2005).

- [7] T. P. Goodman *et al.* (including **E. Fable**), Safety factor profile requirements for electron ITB formation in TCV, *Plasma Phys. Control. Fusion* **47** (12B), B107 (2005).
- [8] A. Bottino *et al.* (including **E. Fable**), Linear stability analysis of microinstabilities in electron internal transport barrier noninductive discharges, *Plasma Phys. Control. Fusion* **48** (2), 215 (2006).
- [9] C. Angioni *et al.* (including **E. Fable**), Non-adiabatic passing electron response and outward impurity convection in gyrokinetic calculations of impurity transport in ASDEX Upgrade plasmas, *Plasma Phys. Control. Fusion* **49**, 2027 (2007).
- [10] S. Coda *et al.* (including **E. Fable**), The physics of electron internal transport barriers in the TCV tokamak, *Nucl. Fusion* **47**, 714 (2007).
- [11] V. S. Udintsev *et al.* (including **E. Fable**), Recent electron cyclotron emission results on TCV, *Fusion Science and Technology* **52**, 161 (2007).
- [12] G. Turri, *et al.* (including **E. Fable**), MHD as trigger of plasma oscillations in ECCD driven discharges in TCV, *Plasma Phys. Control. Fusion* **50**, 065010 (2008).
- [13] C. Zucca, *et al.* (including **E. Fable**), Current density evolution in electron internal transport barrier discharges in TCV, *Plasma Phys. Control. Fusion* **51**, 015002 (2008).

Contributions to conference proceedings

- [1] A. Pochelon *et al.* (including **E. Fable**), Effect of plasma shape on electron heat transport in the presence of extreme temperature gradients variations in TCV, in *Proceedings of 20th IAEA-FEC conference*, EX/9-1, Villamoura, Portugal (2004).
- [2] A. Pochelon *et al.* (including **E. Fable**), Recent physics results with electron cyclotron heating in TCV, in *Proceedings of 6th Int. Workshop "Strong Microwaves in Plasmas"*, Nizhny Novgorod (2005), *Institute of Applied Physics* **2**, 421 (2006).
- [3] T. P. Goodman *et al.* (including **E. Fable**), Inductive Current Perturbations to Steady-State eITBs, in *31st EPS Conference on Plasma Phys. London, 28 June - 2 July 2004 ECA Vol.28G, O-2.05* (2004).
- [4] M. A. Henderson *et al.* (including **E. Fable**), Control of the eITB formation and performance in fully non-inductively sustained ECCD discharges in TCV, *AIP Conf. Proc.* **787**, 399 (2005).
- [5] S. Coda *et al.* (including **E. Fable**), The physics of electron internal transport barriers in the TCV tokamak, in *Proceedings of the 21st IAEA-FEC in Chengdu, China (2006)*, *Nucl. Fusion* **47**, 714 (2007).
- [6] E. Asp *et al.* (including **E. Fable**), On the ECCD current density profile with particle diffusion in eITBs and its impact on the q-profile, *AIP Conf. Proc.* **871**, 283 (2006).
- [7] C. Zucca *et al.* (including **E. Fable**), Safety-factor profile tailoring by improved electron cyclotron system for sawtooth control and reverse shear scenarios in ITER, *AIP Conf. Proc.* **1069**, 361 (2008).

- [8] C. Angioni *et al.* (including **E. Fable**), Gyrokinetic simulations of impurity, He ash and α particle transport and consequences on ITER transport modelling, in *Proceedings of 22nd IAEA-FEC conference*, TH/8-3, Geneva, Switzerland (2008).
- [9] V. S. Udintsev *et al.* (including **E. Fable**), Global plasma oscillations in electron internal transport barriers in TCV, in *Proceedings of 35th EPS conference*, Plasma Phys. Control. Fusion **50**, 124052 (2008).